

JOURNAL OF SCIENCE

PART A: ENGINEERING AND INNOVATION



Year | 2023

Volume | 10

Issue | 2

e-ISSN 2147-9542



| Owner |

on behalf of Gazi University

Rector

Prof. Dr.

Musa YILDIZ

| Publishing Manager |

Prof. Dr.

Cevriye GENCER

Gazi University

| Chief Editor |

Prof. Dr.

Sema Bilge OCAK

Gazi University

| Managing Editor |

Prof. Dr.

Mustafa Gürhan YALÇIN

Akdeniz University



| Editorial Board |

Prof. Dr. Gazi University
Adem TATAROĞLU Physics

Prof. Dr. Gazi University
Adnan SÖZEN Energy Systems Engineering

Prof. Dr. Çukurova University
Ali KESKİN Automotive Engineering

Prof. Dr. Ankara University
Ali Osman SOLAK Chemistry

Prof. Dr. Gazi University
Alper BÜYÜKKARAGÖZ Civil Engineering

Prof. Dr. Gazi University
Atilla BIYIKOĞLU Mechanical Engineering

Prof. Dr. Akdeniz University
Aynur KAZAZ Civil Engineering

Prof. Dr. Bilecik Şeyh Edebali University
Çağlayan AÇIKGÖZ Chemical Engineering

Prof. Dr. Hitit University
Çetin ÇAKANYILDIRIM Chemical Engineering

Prof. Dr. Ankara University
Demet CANSARAN DUMAN The Institute of Biotechnology

Prof. Dr. Gazi University
Elif ORHAN Physics

Prof. Dr. Gazi University
Erdal IRMAK Electrical-Electronic Engineering

Prof. Dr. Atatürk University
Fatih ÖZ Food Engineering

Prof. Dr. Nevşehir Hacı Bektaş Veli University
Feyza DİNÇER Geological Engineering

Prof. Dr. Gazi University
Gürhan İÇÖZ Mathematics



| Editorial Board |

Prof. Dr. Gazi University
Hacer KARACAN Computer Engineering

Prof. Dr. Gazi University
Hakan ATEŞ Metallurgical and Materials Engineering

Prof. Dr. Gazi University
Hüseyin Serdar YÜCESU Automotive Engineering

Prof. Dr. Gazi University
Meltem DOĞAN Chemical Engineering

Prof. Dr. Gazi University
Metin GÜRÜ Chemical Engineering

Prof. Dr. Gazi University
Mine TÜRKTAŞ Biology

Prof. Dr. Aksaray University
Murat KAYA Biotechnology and Nanotechnology

Prof. Dr. Ege University
Nalan KABAY Chemical Engineering

Prof. Dr. Ankara Hacı Bayram Veli University
Nazife ASLAN Chemistry

Prof. Dr. Akdeniz University
Niyazi Uğur KOÇKAL Civil Engineering

Prof. Dr. Eskişehir Technical University
Nuran AY Materials Science and Engineering

Prof. Dr. Akdeniz University
Nurdane İLBEYLİ Geological Engineering

Prof. Dr. Gazi University
Nursel AKÇAM Electrical-Electronic Engineering

Prof. Dr. İstanbul Technical University
Ömer ŞAHİN Chemical Engineering

Prof. Dr. Gazi University
Selim ACAR Physics



| Editorial Board |

Prof. Dr. Konya Technical University
Şükrü DURSUN Environmental Engineering

Prof. Dr. Ankara Yıldırım Beyazıt University
Veli ÇELİK Mechanical Engineering

Prof. Dr. Akdeniz University
Yılmaz ŞİMŞEK Mathematics

Prof. Dr. Kahramanmaraş Sütçü İmam University
Yusuf URAS Geological Engineering

Prof. Dr. TOBB University of Economics and Technology
Yücel ERCAN Mechanical Engineering

Prof. Dr. Middle East Technical University
Zafer EVİS Engineering Sciences

Assoc. Prof. Dr. Ankara University
Defne AKAY Physics

Assoc. Prof. Dr. Gazi University
Uğur GÖKMEN Metallurgical and Materials Engineering

Assoc. Prof. Dr. Akdeniz University
Yasemin LEVENTELİ Geological Engineering

Assist. Prof. Dr. Akdeniz University
Emine Şükran OKUDAN Basic Sciences Fisheries

Assist. Prof. Dr. Akdeniz University
Füsun YALÇIN Mathematics

Assist. Prof. Dr. Marmara University
Senai YALÇINKAYA Mechanical Engineering

Dr. Gazi University
Murat AKIN Computer Technologies

Dr. Gazi University
Silver GÜNEŞ Chemical Engineering



| Foreign Editorial Advisory Board |

Prof. Dr. **Abdelmejid BAYAD** Université d'Évry Val d'Essonne **FRANCE**

Prof. Dr. **Ali Behcet ALPAT** Istituto Nazionale di Fisica Nucleare (INFN) **ITALY**

Prof. Dr. **Azra SPAGO** Dzemal Bijedic University of Mostar **BOSNIA AND HERZEGOVINA**

Prof. Dr. **Bektay YERKIN** Satbayev University **KAZAKHSTAN**

Prof. Dr. **Burçin BAYRAM** Miami University **USA**

Prof. Dr. **Daeyeoul KIM** Jeonbuk National University **SOUTH KOREA**

Prof. Dr. **Elvan AKIN** Missouri University of Science and Technology **USA**

Prof. Dr. **Filiz DİK** Rockford University **USA**

Prof. Dr. **Homer RAHNEJAT** Loughborough University **UNITED KINGDOM**

Prof. Dr. **Loksha VEERABHADRIAH** Vijayanagara Sri Krishnadevaraya University **INDIA**

Prof. Dr. **Mehmet DİK** Rockford University **USA**

Prof. Dr. **Nedim SULJIĆ** University of Tuzla **BOSNIA AND HERZEGOVINA**

Prof. Dr. **Rob DWYER-JOYCE** The University of Sheffield **UNITED KINGDOM**

Prof. Dr. **Snezana KOMATINA** University Novi Sad **SERBIA**

Prof. Dr. **Toni NIKOLIC** University Džemal Bijedić Mostar **BOSNIA AND HERZEGOVINA**

Prof. Dr. **Turysbekova Gaukhar SEYTKHANOVNA** Satbayev University **KAZAKHSTAN**

Assoc. Prof. Dr. **Burcin ŞİMŞEK** Associate Director Biostatistics (Oncology) at Bristol Myers Squibb **USA**

Assist. Prof. Dr. **Alisa BABAJIC** University of Tuzla **BOSNIA AND HERZEGOVINA**

Dr. **Daniel Ganyi NYAMSARI** Mining Company Researcher **CAMEROON**



| English Language Editors |

Lecturer Gazi University
Gizem AÇELYA AYKAN School of Foreign Languages

Lecturer Gazi University
Tuğçe BÜYÜKBAYRAM School of Foreign Languages

| Technical Editors |

Dr.
Fatih UÇAR Akdeniz University

Research Assistant
Özge ÖZER ATAKOĞLU Akdeniz University



| Correspondence Address |

Gazi University Graduate School of Natural and Applied Sciences
Emniyet Neighborhood, Bandırma Avenue, No:6/20B, 06560, Yenimahalle - ANKARA
B Block, Auxiliary Building

| e-mail |

gujsa06@gmail.com

| web page |

<https://dergipark.org.tr/tr/pub/gujsa>

Gazi University Journal of Science Part A: Engineering and Innovation
is a peer-reviewed journal.

| INDEXING |



| ACCESSIBILITY |



This work are licensed under a Creative Commons Attribution-ShareAlike 4.0 International License.

| CONTENTS |

Page | Articles

113-130	Effect of Wall Stiffness on Excavation -Induced Horizontal Deformations in Stiff- Hard Clays G. Üçdemir  S. O. Akbaş  Research Article Civil Engineering	10.54287/gujisa.1244790
131-139	Analysis of Dislocation Density for GaN Based HEMTs in Screw Mod Ö. Bayal  E. Balcı  A. K. Bilgili  M. K. Öztürk  S. Özçelik  E. Özbay  Research Article Physics	10.54287/gujisa.1215224
140-148	A Sustainable Building Material Developed from Low-Temperature Sintering of Mining Waste with an Alkali-Silicate Solution P. O. Odewole  Research Article Metallurgical and Materials Engineering	10.54287/gujisa.1245213
149-156	Self-Powered Mechanical Energy Sensor Application of SnO₂/Ag and PMMA/ITO Nanocomposites via Triboelectric Effect G. Durak Yüzüak  M. Çetin  E. Yüzüak  Research Article Energy Systems Engineering	10.54287/gujisa.1247152
157-165	Investigation of Mechanical Properties of Aluminum 7075 Alloy via Surface Engineering G. Altuntaş  G. Yazbahar  B. Bostan  Research Article Metallurgical and Materials Engineering	10.54287/gujisa.1259370



| CONTENTS |








Page | Articles

	Asphaltite Pyrolysis in Fluidized Bed Reactor	
166-175	S. Moghanirahimi  H. Topal 	
	Research Article	
	Mechanical Engineering	10.54287/gujisa.1256330
<hr/>		
	Comparison of the Number of Particle History for Monte Carlo Codes in Gamma-Ray Spectroscopy	
176-183	E. Uyar  Z. A. Günekbay 	
	Research Article	
	Physics	10.54287/gujisa.1276486
<hr/>		
	Evaluation of Range Estimation Performance of FLIR with Field Requirements Criteria	
184-195	B. Akın 	
	Research Article	
	Physics	10.54287/gujisa.1264848
<hr/>		
	Convergence Properties of a Kantorovich Type of Szász Operators Involving Negative Order Genocchi Polynomials	
196-205	E. Ağyüz 	
	Research Article	
	Mathematics	10.54287/gujisa.1282992
<hr/>		
	A Control Scheme for a Quasi-Z Source Three-Phase Inverter	
206-221	Z. Ortatepe  S. Özdemir 	
	Research Article	
	Electrical & Electronics Engineering	10.54287/gujisa.1303347



| CONTENTS |

Page | Articles

222-231	The Investigation of CO₂ Gas Sensing Performance of ZnO Nanorods Growth on RF Sputtered Seed Layer F. Bulut  Ö. Öztürk  S. Acar  Research Article 10.54287/gujisa.1302064 <i>Metallurgical and Materials Engineering</i>
232-240	Identities for a Special Finite Sum Related to the Dedekind Sums and Fibonacci Numbers E. Çetin  Research Article 10.54287/gujisa.1280707 <i>Mathematics</i>
241-261	Process Improvement Between Company Departments with the Integration of ERP and CRM Software Programs M. Ulusoy Yılmaz  B. Özyörük  S. Bilge Ocak  Research Article 10.54287/gujisa.1255461 <i>Industrial Engineering</i>



Gazi University

Journal of Science

PART A: ENGINEERING AND INNOVATION

<http://dergipark.org.tr/guj.1244790>

Effect of Wall Stiffness on Excavation-Induced Horizontal Deformations in Stiff-Hard Clays

Gamze ÜÇDEMİR^{1,2*} Sami Oğuzhan AKBAŞ³¹Gazi University, Graduate School of Natural and Applied Sciences, Ankara, Türkiye²Atatürk University, Faculty of Engineering, Civil Engineering Department, Erzurum, Türkiye³Gazi University, Faculty of Engineering, Civil Engineering Department, Ankara, Türkiye**Keywords**Anchored Deep
Excavation
Horizontal
Displacement
Stiff-Hard Clay
Support System
Stiffness**Abstract**

Excavation-induced ground movements are affected by the stiffness of the support system as well as the soil properties. Displacement estimations of deep excavations are generally made using the finite element method (FEM). However, the accuracy and reliability of the results obtained from the finite element calculations will change significantly in proportion with the quality of the parameters employed in the program, thus, the use of probabilistic analysis that considers soil variability's impact has become a popular approach in recent studies. Based on these considerations, this study aims to investigate the influence of wall bending stiffness on excavation-induced lateral displacements for deep excavations in stiff to hard clays and provide a practical methodology to be used in preliminary design. For this purpose, finite element analyses were carried out using various practically achievable support system stiffness values and soil parameters. Considering the inherent variability of the soil, effective stress friction angle and effective cohesion of the soil were randomly generated by Monte Carlo simulations to be used in the finite element analyses. The performance of the analyses was evaluated using results from 22 case histories from deep excavations in stiff-hard clays. The results indicate that, lateral movement in excavations in stiff-hard clays is minimally affected by the stiffness of the wall. Soil variability was found to have a significant impact on the outcome of Monte Carlo simulations, resulting in a wide range of normalized maximum lateral deformations for a given wall stiffness. A new stiffness factor has been proposed that incorporates the horizontal spacing of the support elements, which is capable of covering a wider range of excavation support system types, thus enhancing the accuracy of the analyses.

Cite

Üçdemir, G., & Akbaş, S. O. (2023). Effect of Wall Stiffness on Excavation-Induced Horizontal Deformations in Stiff-Hard Clays. *GU J Sci, Part A, 10(2)*, 113-130. doi:10.54287/guj.1244790

Author ID (ORCID Number)

0000-0002-4274-5823 Gamze ÜÇDEMİR
0000-0002-7872-1604 Sami Oğuzhan AKBAŞ

Article Process

Submission Date 30.01.2023
Revision Date 07.04.2023
Accepted Date 10.04.2023
Published Date 03.05.2023

1. INTRODUCTION

Deep excavation-induced ground movements can cause severe harm to nearby infrastructure in urban areas if they exceed acceptable limits. Ground movements caused by deep excavations depend on many factors such as soil properties, the type and structural characteristics of the support system, which is usually denoted numerically by its stiffness. Excavation support system stiffness is a variable that is a combination of many factors such as the stiffness of the wall, the horizontal and vertical spacing of the support elements besides the structural strength, and the type of connection between the support elements and the wall (Bryson & Zapata-Medina, 2012).

Prediction of deep excavation-induced displacements are generally made using the finite element method (FEM). But, in engineering practice, simplified charts or empirical design equations are still popular to estimate approximate values of wall deformations, especially before the detailed design phase. Moreover, it is clear that

*Corresponding Author, e-mail: gamzeucdemir@atauni.edu.tr

the accuracy and reliability of the results obtained from the FEM will significantly change as a function of the quality of the parameters employed in the program, thus the incorporation of the impact of soil variability in conjunction with probabilistic analysis has become popular in recent studies. Based on these considerations, this study was performed to investigate the effect of wall rigidity on lateral deformations for excavations in stiff to hard clays. The main aim is to provide a practical methodology to be used in preliminary design. For this purpose, a range of finite element analyses were performed that involve a practical range of support system stiffness values, as well as stiff-hard clay strength parameters. Considering the inherent variability of the soil, the effective stress friction angle (ϕ) and effective cohesion (c') of the clay were randomly generated using Monte Carlo simulations to be automatically inserted into the finite element analyses using Python programming language. Finally, the performance of the analyzes was evaluated comparatively using measurements reported in 22 well-documented case histories from deep excavations in stiff-hard clays.

This paper is intended to examine the effect of the wall elasticity modulus, which is the support system stiffness parameter, and the soil variability on the displacements. This was achieved by analyzing a range of wall elasticity moduli along with the different soil parameters created separately by Monte Carlo simulations. A novel approach was undertaken by carrying out finite element analyses considering the soil variability, and thus the practical range of the results can be observed. In addition, the obtained data was compared both with other theoretical studies and measurements from case histories, and the adequacy of the system stiffness proposed by Clough et al. (1989), which is widely-used in practice was examined.

This study stands out from others by not only examining the effect of wall flexural stiffness on displacement but also by including the variability in both cohesion and internal friction angle of the soil in the analyses. Additionally, a new stiffness factor has been proposed that incorporates the horizontal spacing of the support elements, which enables covering a wider range of excavation support system types, thus enhancing the accuracy of the preliminary analyses.

2. PREVIOUS STUDIES

One of the most widely-accepted methods to determine excavation-induced displacements was presented by Clough et al. (1989). This method was developed based on excavations in soft clays, and later it was reported to be approximately valid for other soil types. It has the advantage of handling the characteristics of the soil, wall, and the support system together. As a result of studies by Clough et al. (1989), a simple design chart has been proposed for soft to medium stiff clays based on the rigidity of the support system and the factor of safety against basal heave (FOS_{base}). According to this design chart, the support system stiffness, which is defined as a function of wall modulus (E), modulus of inertia (I), and vertical spacing of support elements (s_v) as $EI/\gamma_w s_v^4$, has a significant effect on the wall movement in excavations made in soft-medium stiff clays especially for cases where the factor of safety against basal heave is low. In excavations made in stiff clays with high FOS_{base} , the support system stiffness has a less pronounced effect on the wall movement (Clough & O'Rourke, 1990).

The results of the study by Clough et al. (1989) was later updated with the help of a larger database developed by Long (2001). Long (2001) classified the database he created according to low and high FOS_{base} and generated a chart of normalized maximum horizontal displacement as a function of support system stiffness. According to the results obtained in that study, the horizontal displacements of excavations in hard clays are largely distinct of the wall strength and the characteristics of the support elements. In addition, the findings indicate that the support system stiffness has an important effect on the excavations displacement in soft clays with low FOS_{base} , while the influence on systems with high FOS_{base} is less.

Moormann (2004) created an international case history database on deep excavations mostly in soft soils to evaluate the accuracy and reliability of the chart prepared by Clough et al. (1989). According to his analyses, wall lateral displacement was largely independent of the support system stiffness. However, there is no detailed information in the study on factors such as circumambient buildings, geometrical irregularities, quality of workmanship, soil properties at the embedded part of the wall, unforeseen events, ground water circumstances, prestressing of support elements. Because of these uncertainties, Bryson and Zapata-Medina (2012) claimed that the effect of system stiffness on lateral movements should further be investigated by numerical analyses.

In their study, Bryson and Zapata-Medina (2012) created 3-D numerical models that realistically represented the action of the excavation and excavation support systems, to eliminate the uncertainties caused by the lack of information in the Long (2001) and Moormann (2004) databases. In these finite element models, the influences of the wall stiffness, the characteristics of the support elements and different soil conditions on the lateral movement were investigated. Their analyzes showed that in hard clays, the deformations are mostly independent of the support system stiffness at sufficient FOS_{base} , although in soft-medium stiff clays it was greatly affected by the stiffness of the system at low FOS_{base} . Therefore, the results indicate that the effect of the excavation support system on deformations is related to the soil strength.

As can be seen from the results of previous studies, there is a debate on the extent of effect of wall stiffness on excavation-induced displacements, especially as a function of soil strength in stiff-hard clays. In addition, not much effort has been put into investigating the impact of soil variability on the results. These points comprise the main focus of the study presented herein.

3. METHODOLOGY

3.1. Finite Element Modelling

In this study, finite element analyses for deep excavation systems were performed using Plaxis 2D Ultimate software, version 2022. Among the many material models available for modeling soil in the software, the hardening soil (HS), which is an elastoplastic multi-yield surface model (Bryson & Zapata-Medina, 2012) was used. The model uses compression hardening to imitate the permanent compaction of soil during primary compression. Hyperbolic stress-strain relationship showing model behavior is presented in Figure 1 (Plaxis 2D Material Models Manual, 2022).

In this model, when the soil is subjected to primary deviatoric loading, soil strength decreases, and permanent deformation occurs in the soil simultaneously (Bryson & Zapata-Medina, 2012). Soil moduli based on the HS model are determined with the help of the following equations:

$$E_{50} = E_{50}^{ref} \left(\frac{c \cos\varphi - \sigma'_3 \sin\varphi}{c \cos\varphi + p^{ref} \sin\varphi} \right)^m \quad (1)$$

$$E_{oed} = E_{oed}^{ref} (\sigma/p^{ref})^m \quad (2)$$

$$E_{ur} = E_{ur}^{ref} \left(\frac{c \cos\varphi - \sigma'_3 \sin\varphi}{c \cos\varphi + p^{ref} \sin\varphi} \right)^m \quad (3)$$

in which, E_{50} = secant stiffness at the point of 50% of the maximum deviatoric stress, E_{oed} = tangent stiffness for primary oedometer loading, E_{ur} = unloading/reloading stiffness, p_{ref} = reference stress equal to 1 atm, m = power for stress-level dependency of stiffness, E_{50}^{ref} =triaxial loading stiffness modulus at reference pressure p_{ref} , E_{oed}^{ref} = oedometer loading stiffness module at reference pressure, and E_{ur}^{ref} = unloading/reloading stiffness module at reference pressure (Plaxis 2D Material Models Manual, 2022). The stress dependent stiffness parameter m used in Eq.1, Eq.2 and Eq.3 varies between 0.5-1.0, with m being 1.0 in soft clay soils and 0.5 in Norwegian sands and silts (Plaxis 2D Material Models Manual, 2022).

The effect of soil variability was also considered in the analyses. In a comprehensive study conducted by Akbaş and Kulhawy (2010) the variability of Ankara Clay (Table 1) was investigated. Ankara Clay is a stiff to hard, semi-saturated, plastic clay red brown in color. It becomes stiffer with depths (Bozkurt, 2017). In the study, the analyses results summarized in Table 1, which can be safely assumed to be representative of hard-stiff clays, was used to determine the mean and coefficient of variation (COV) of the undrained shear strength (c_u) of the clay. The data from the literature was used for estimating the COV of the φ of the clay. In studies by Harr (1984), and Kulhawy (1992), the coefficient of variation of effective stress friction angle varies between 2% and 13%. COV and mean values of c_u and φ used in this study are shown in Table 2.

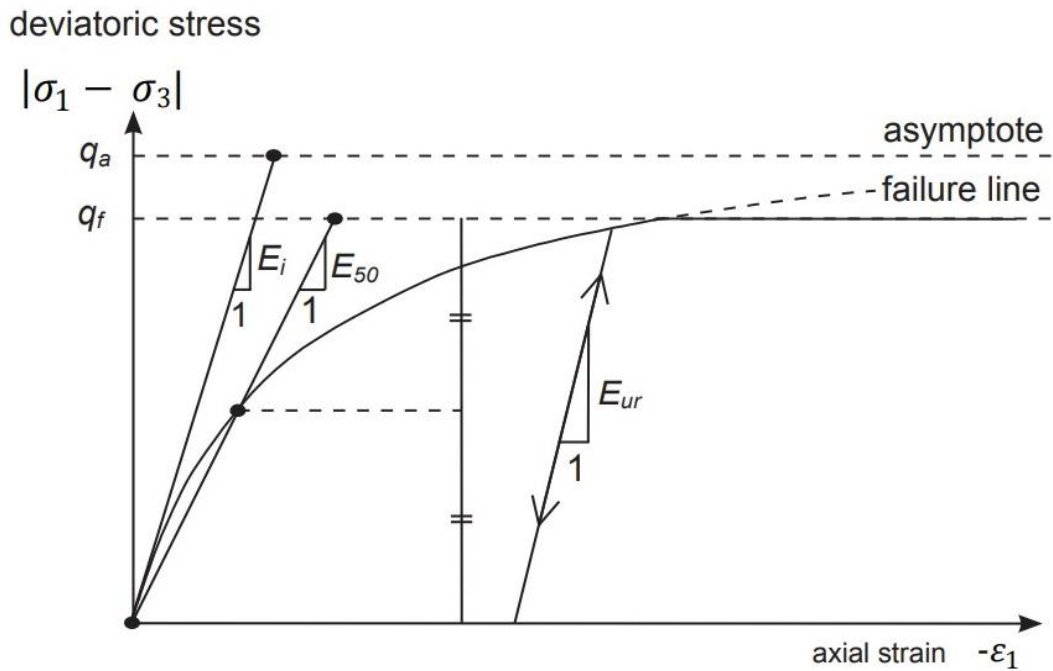


Figure 1. Hyperbolic Stress-Strain Relation in Primary Loading for a Standard Drained Triaxial Test (Plaxis 2D Material Models Manual, 2022)

Table 1. Inherent Variability of Some Geotechnical Properties of Ankara Clay (Akbaş & Kulhawy, 2010)

Property	No. of data groups	No. of tests per group	Property value		Property COV(%)	
				Mean	Range	Mean
w _L (%)	25	4-24	50-79	64	9-22	14
w _P (%)	25	4-25	20-35	26	6-19	12
w _n (%)	26	4-18	23-37	29	12-22	14
PI (%)	25	4-24	21-52	38	13-28	19
e ₀	14	4-25	0,65-0,98	0,84	3-16	9
Y _d (kN/m ³)	20	3-12	14-17	15,8	2-8	5
c _u (kN/m ³)	9	4-8	106-186	148	11-35	23
C _c	7	3-8	0,18-0,38	0,26	14-35	26
SPT N	12	6-31	23-60	38	10-46	29

Table 2. Mean and COV Values for c_u and φ

Parametre	Mean Value	COV (%)
c _u (kPa)	100	23
φ (°)	28	13

After estimating the statistical parameters, Monte Carlo simulations was carried out within the finite element model of the deep excavation system using Plaxis Remote scripting through the Plaxis-Python code software interaction interface (Figure 2).

```

Iteration Codes
Logout

File Edit View Insert Cell Kernel Navigate Widgets Help Trusted | PLAXIS Python 3 O

Contents
In [1]: import imp
        from math import pi
        from math import log
        from math import sqrt
        from math import pow
        from math import sin
        import random
        import numpy as np

In [2]: # Python-Plaxis Link
        localhostport_input = 10000
        localhostport_output = 10001
        plaxis_path = r"C:\ProgramData\Bentley\Geotechnical\PLAXIS Python Distribution V1\python\Lib\site-packages"
        found_module = imp.find_module('plxscripting', [plaxis_path])
        plxscripting = imp.load_module('plxscripting', *found_module)
        from plxscripting.easy import *
        s_i, g_i = new_server('localhost', localhostport_input, password = 'yc8KA7wv~-C5#WV1')
        s_o, g_o = new_server('localhost', localhostport_output, password = 'yc8KA7wv~-C5#WV1')

In [3]: g_i.SoilContour.initializeRectangular(-40, -65, 65, 65)
        g_i.setproperties(
            "Title", "Derinkazi",
            "Comments", "",
            "UnitForce", "kN",
            "UnitLength", "m",
            "UnitTime", "day",
            "Waterweight", 10,
            "ModelType", "PlaneStrain",

```

Figure 2. Plaxis Commands in Python

In the Monte Carlo simulation method, a variable mathematical or empirical parameter is generated randomly within a certain distribution. The normal or Gaussian distribution is the most usually used type of distribution to determine random variability in a data set in many science disciplines, especially for natural phenomena. However, in asymmetrical distributions, and for cases where negative values are inadmissible, log-normal distribution is more versatile to capture the uncertainty behavior. For this reason, it would be more appropriate to model soil properties as random variables with only positive values using log-normal distribution (Bozkurt, 2017). Therefore, in the analyzes performed in this study, the soil parameter variability was modelled with a log-normal distribution using the aforementioned mean and COV values.

3.2. Case Study and Soil Properties

The case of a braced excavation with a depth of approximately 19 m in Istanbul has been examined within the scope of this study. For the in-situ wall, 65 cm diameter drilled shafts were installed at 120 cm center to center distance. The deep excavation was supported by 6 rows of prestressed soil anchors with vertical and horizontal spacings of 2.52 m and 1.8 m, respectively (Figure 3). The prestressing load for the anchor strands was determined as 40 tons (Şahin, 2017).

In the field, the exploratory boreholes indicate that, very stiff to hard sandy-silty clay containing yellow-brown fine quartzite pebbles with a thickness of approximately 18 m underlies a fill layer of approximately 3 m from the ground surface. Below the silty clay, a weathered limestone-claystone unit in bluish greenish blackish gray tones was observed as bedrock (Şahin, 2017).

The geometry of the anchored deep excavation is shown as modeled in the finite element model in Figure 4. According to inclinometer readings carried out in the field, it was observed that the maximum horizontal deformations of the in-situ wall in the case of full excavation is approximately 18 mm (Figure 5).

Back analysis of the deep excavation was carried out to obtain the elasticity modulus values reflecting the behavior observed in the inclinometer readings. Duncan and Buchignani (1976) equation was used to obtain the initial modulus of elasticity of the silty clay soil layer:

$$E_u = (300 - 1000) \cdot c_u \quad (4)$$

Using the mean value of the c_u of 100 kPa, a reasonable first assumption for the E_u value was made as 60000 kPa. As a result, initial values for back analyses are shown in Table 3.

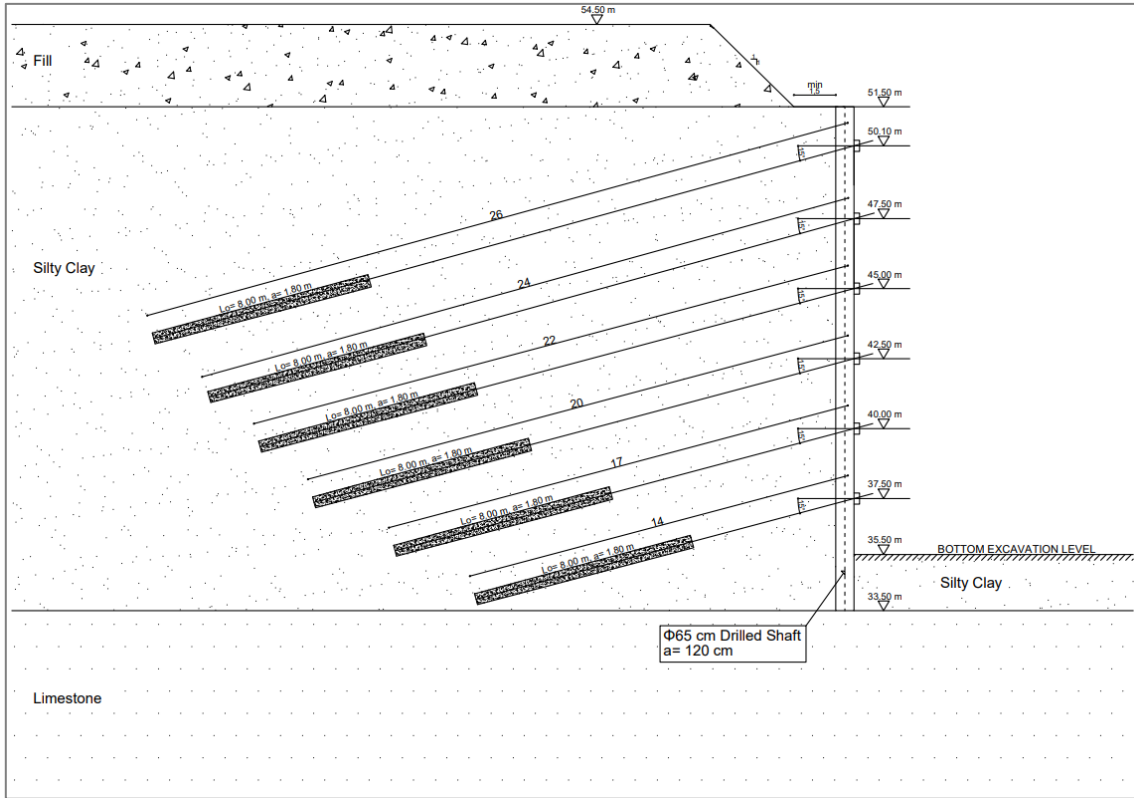


Figure 3. Cross Sectional View of the Shoring System

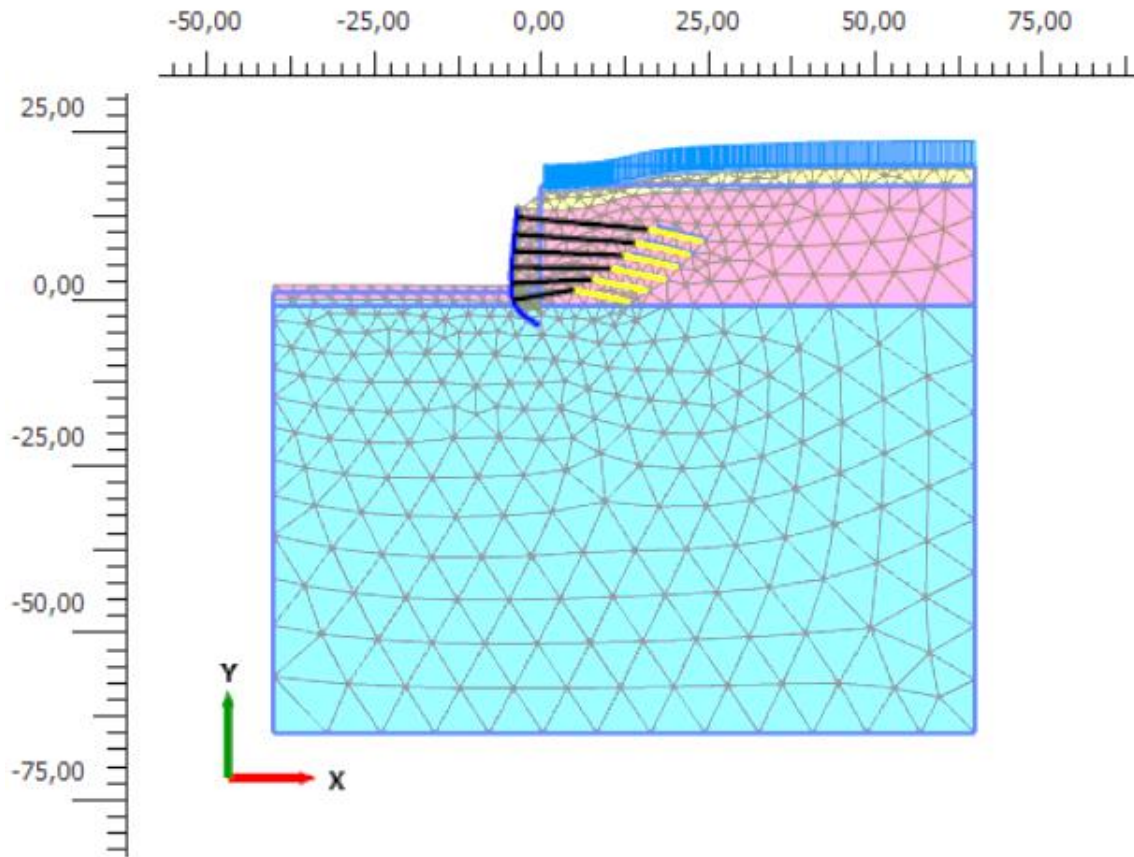


Figure 4. Finite Element Model of Anchored Deep Excavation

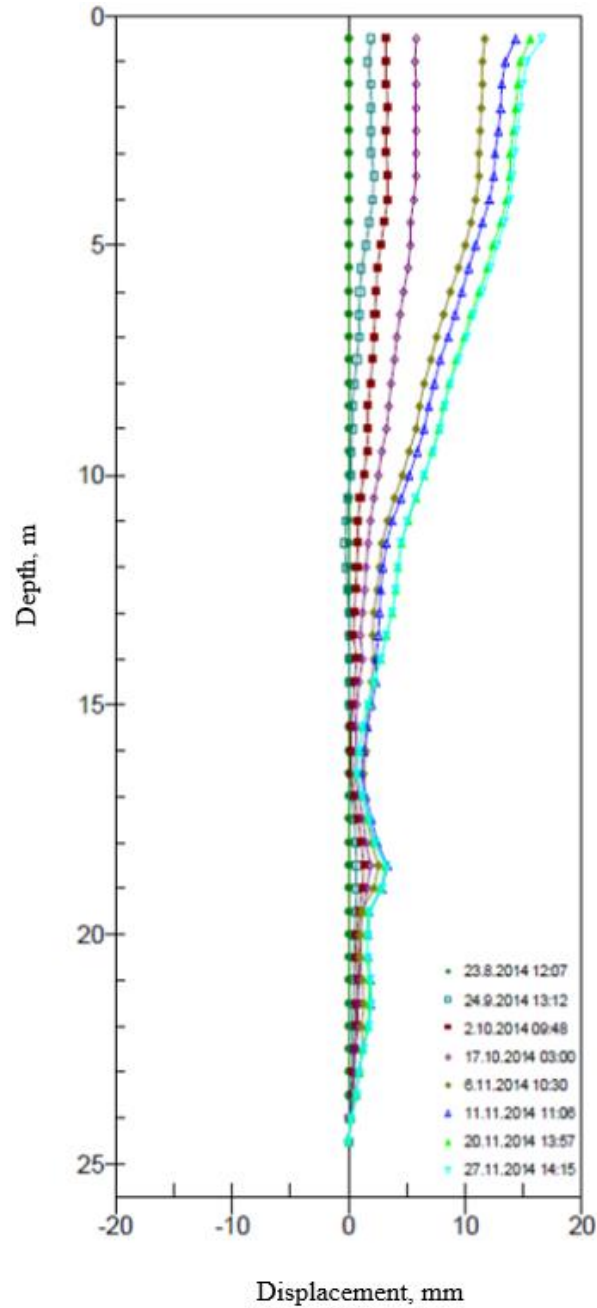


Figure 5. Deep Excavation Inclinometer Readings (Şahin, 2017)

Table 3. Initial Estimates Used in Case Back Analyses (Şahin, 2017)

Parameter	Fill	Silty Clay	Limestone	Unit
Material Model	Hardening Soil (HS)	Hardening Soil (HS)	Hardening Soil (HS)	-
Drainage Type	Drained	Drained	Drained	-
c'	5	10	25	kN/m ²
ϕ'	27	28	35	°
E_{50}^{ref}	12000	42000	200000	kN/m ²
E_{oed}^{ref}	12000	42000	200000	kN/m ²
E_{ur}^{ref}	36000	126000	600000	kN/m ²

The empirical correlations used for the estimation of the geotechnical parameters of the silty clay unit used in the iterative analyzes are presented in Table 4.

Table 4. Correlations Used in the Determination of Silty Clay Unit Parameters

Parameter	Silty Clay	Source
E'	$0.7 \times E_u$	Craig, 2004
E_u	$600 \times c_u$	Duncan & Buchignani, 1976
c'	$c_u \times 0.1$	Sorensen & Okkels, 2013

As a result of the back analysis, it was detected that the deformation behavior can be realistically simulated only if the correlation $E_u/c_u \approx 776$ value is used for the silty clay unit, as with this value a horizontal deformation of about 18 mm that was observed in the field has also been determined by the finite element analysis (Figure 6). The calculations of the reference elasticity moduli besides the geotechnical parameters obtained as a result of back analysis and used in finite element analyses are presented in Table 5.

Table 5. Parameters Found as a Result of Case Back Analysis

Parameter	Fill	Silty Clay	Limestone	Back Analysis Correlations/Calculations
Material Model	Hardening Soil (HS)	Hardening Soil (HS)	Hardening Soil (HS)	$c'=0.1c_u$ $c_u=100$ kPa
Drainage Type	Drained	Drained	Drained	$E_u/c_u=776$
γ (kN/m ³)	18	19	21	$E_u=100*776=77600$
c' (kN/m ²)	5	10	25	$E_u/E'=0.7$
ϕ' (°)	27	28	35	$E'=0,7*776000 \approx 54350$
E_{50}^{ref} (kN/m ²)	12000	54350	200000	$E_{50}^{ref}=E'=54350$
E_{oed}^{ref} (kN/m ²)	12000	54350	200000	$E_{oed}^{ref}=E_{50}^{ref}$
E_{ur}^{ref} (kN/m ²)	36000	163050	600000	$E_{ur}^{ref}=3E_{50}^{ref}$
Power (m)	0.5	0.5	0.5	-
R_{inter}	0.7	0.8	0.8	-



Figure 6. Lateral Displacement of Drilled Shaft Wall as Obtained from the Back-Analysis
($\delta_{maxlateral} \cong 18$ mm)

4. RESULTS AND DISCUSSION

4.1. Influence of Wall Bending Stiffness

In this study, 8 different coefficients called α as defined by Bryson and Zapata-Medina (2012) were used to represent walls with various rigidities that can be constructed in the field. The drilled shaft rigidity was determined according to the α coefficients produced. The typical drilled shaft wall conditions and geometries used to determine the lower and upper limits of the α coefficient are given in Table 6. Based on Table 6, the α coefficient range was determined to have a range between 0.05 and 50.

Table 6. Upper and Lower Limits for α Coefficient

Drilled Shaft Properties	Upper Limit for α	Lower Limit for α
Concrete Class	C35	C16
Pile Diameter (cm)	$\phi 160$	$\phi 30$
Pile Spacing (m)	0.8	1.5
I: Moment of Inertia (m ⁴)	0.3217	$3.9761 \cdot 10^{-4}$
E: Elasticity Module (kN/m ²)	33200000	27000000
Rigidity: EI (kNm ² /m)	13350512.14	7156.94
Baseline EI (kNm ² /m)	220000	220000
$\alpha = EI / \text{Baseline EI}$	60	0.04

For each of the wall rigidity determined using 8 different α coefficients, 100 Monte Carlo simulation-based finite element analyzes, that is, a total of 800 anchored deep excavation analyzes, were carried out to also determine the influence of soil variability on the results. In the analyzes carried out for the anchored deep excavation, the bored pile element is modeled as a solid element, which has both bending and axial rigidity, and is assumed to exhibit linear elastic behavior. With the assumption of elastic behavior, high moment capacity (Mp) and axial capacity (Np) values are automatically assigned to the wall element by the finite element program, so that the solid element exhibits elastic behavior in all cases, regardless of the section effects.

In the study, the wall bending stiffness values were obtained by multiplying the bending stiffness in the sample case with different α coefficients determined by considering the possibility of the various wall geometries and construction qualities that can be realized in the field. The baseline bending stiffness value used to improve the various wall stiffness is 220000 kNm²/m. Table 7 displays the wall stiffness values utilized in the probabilistic analyses.

Table 7. Wall Bending Stiffness Values

α	$\alpha \times EI$ (kN.m ² /m)
0.05	11000
0.5	110000
0.75	165000
1	220000
5	1100000
10	2200000
25	5500000
50	11000000

Note: Baseline EI = 220000 kNm²/m

While evaluating the impact of wall stiffness on displacement, Clough et al. (1989) used a variable named as the system stiffness factor, which is defined as $EI / \gamma_w s_v^4$ where E =Young's modulus of the wall, I =moment of inertia per unit length of the wall, s_v =average vertical support spacing, and presented its relationship with lateral wall movement normalized with excavation depth (Figure 6). In this study, first, the Clough et al. (1989) design chart shown in Figure 7 was compared with the deterministic analysis of the deep excavation (Figure 8). Note that stiffness-normalized horizontal displacement is defined as $\delta_H(\max) / H$, where $\delta_H(\max)$ is the maximum horizontal wall movement, and H is the maximum excavation depth.

Deep excavation FOS_{base} can be calculated by

$$FOS_{base} = \frac{N_c c_u + \sqrt{2} c_u \left(\frac{H+D}{B} \right) + 2 c_u \left(\frac{D}{B} \right)}{\gamma H} \quad (5)$$

where N_c is the bearing capacity factor, c_u is the average undrained shear strength of the retained soil, H is the height of the excavation; B is the width of the excavation; D is the depth of embedment below the excavation bottom, and γ is the unit weight of the soil above the excavation (Carswell & Siebert, 2021). Since the length of the excavation is not known, it is assumed to be infinite. But the width, B , is restricted because a stiff stratum, i.e., weathered limestone-claystone is near the bottom of the excavation (Sabatini et al., 1999). Therefore, B is equal to depth $D = 2$ m. The minimum N_c value is determined as 5.14 according to the continuous foundation property and conservatively assuming $H/B=0$. As a result, the deep excavation FOS_{base} is calculated to be approximately as 6.

Current practice is to use a FOS_{base} greater than 2.5 for permanent works and 1.5 for support of excavation works (Sabatini et al., 1999). The FOS_{base} calculated indicates that the deep excavation is very safe against basal heave.

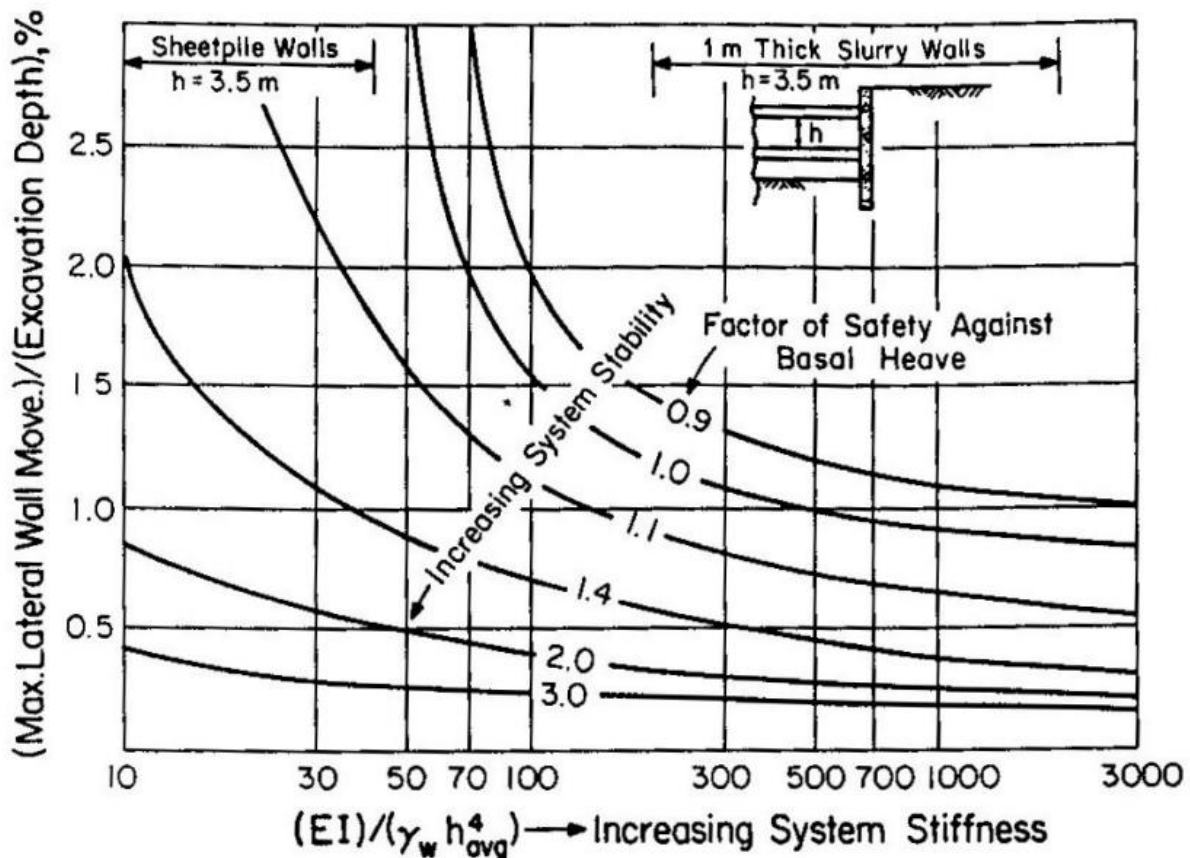


Figure 7. System Stiffness-Normalized Maximum Lateral Deformation (Clough et al., 1989)

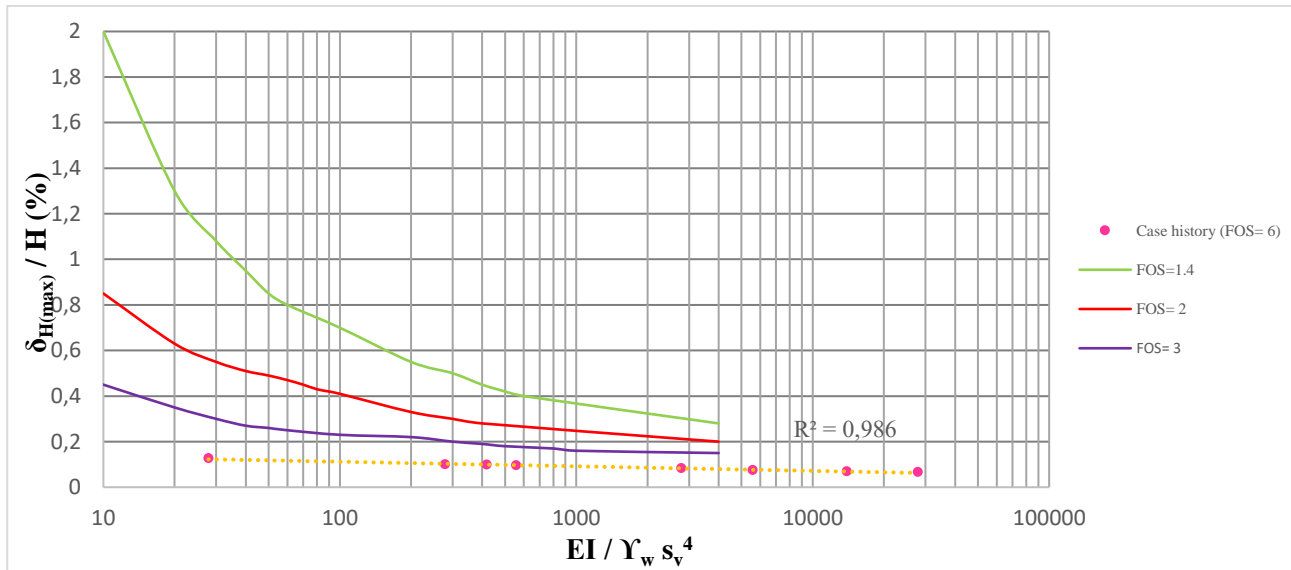


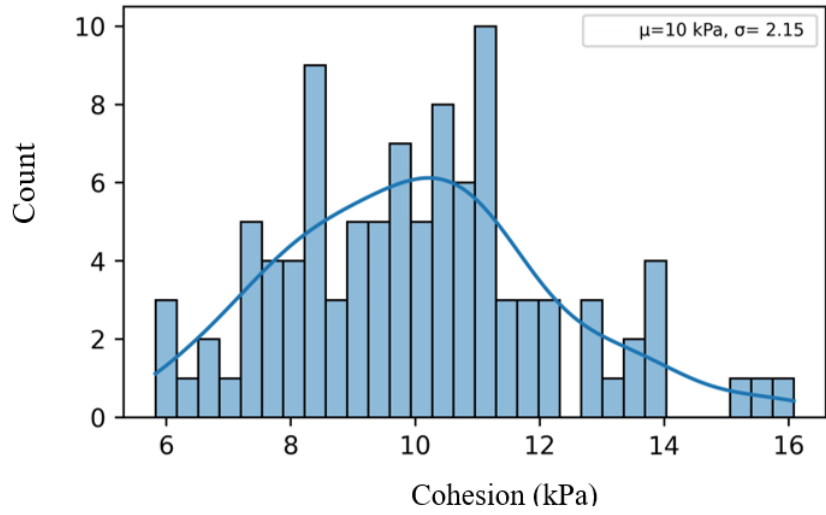
Figure 8. Comparison of the Deterministic Analysis with the Clough et al. (1989) Design Chart

As can be seen from Figure 8, the design curve obtained as a result of deterministic finite element calculations has a similar trend with those asserted by Clough et al. (1989) for hard-stiff clays, i.e. those with high FOS_{base} values. Note that for the cases investigated herein the system stiffness varies between about 27.8-27800, while the displacement value varies within a very low range of about 0.126%-0.066%, as expected. As can be seen from these results, stiffness of the support system has a very low effect on displacements in stiff-hard clays for all practical purposes.

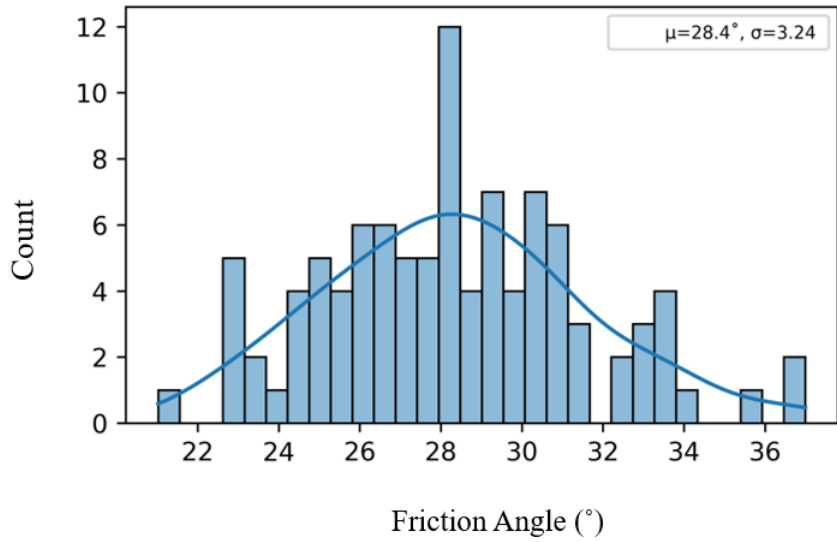
The deterministic analysis results indicate that, as the system stiffness factor increases 1000 fold, the normalized lateral deformation decreases only from 0.13% to 0.07%. The results obtained support the findings of Clough and O'Rourke (1990), who stated that wall stiffness and support element spacing have a minimal effect on wall lateral movement in stiff-hard clays.

In addition, for estimating the effect of soil variability on deformations, 100 analyzes performed for each wall stiffness, i.e., for each α value using Monte Carlo simulations. The distribution of simulated values for soil modulus as well as the horizontal displacements are shown in Figure 9 for $\alpha = 5$ and the results for all α are plotted on Figure 10 in terms of system stiffness vs. normalized maximum lateral deformation. As can be seen from Figure 10, soil variability, which is inevitable, results in quite a large range in the obtained values of normalized maximum lateral excavation deformation for any given wall stiffness. To compare the analytical results with those measured from case histories, data reported from anchored deep excavations in stiff clays obtained from different studies (Table 8) as well as the results of the parametric study by Bryson and Zapata-Medina (2012) (Table 9) are also plotted on the Figure 10.

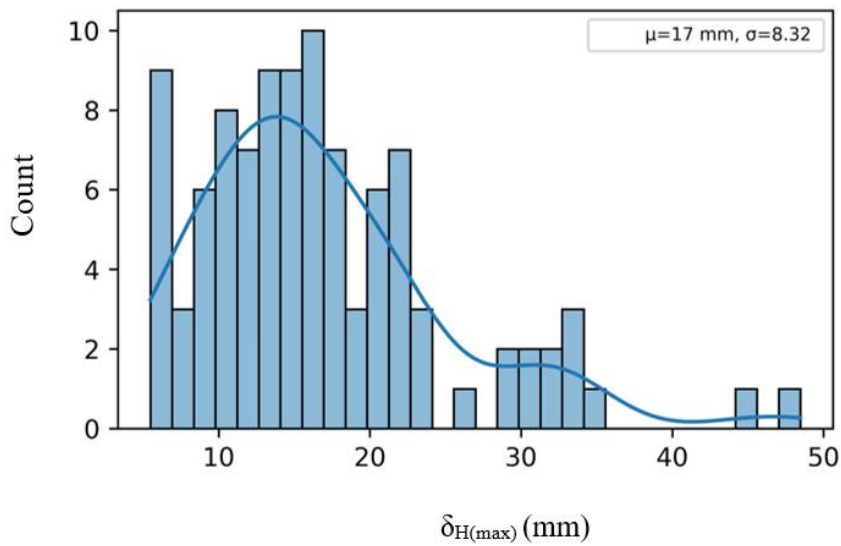
A close look at Figure 10 indicates a similar trend of slightly decreasing normalized maximum deformation with increased system stiffness both for finite element analysis results and case histories for stiff-hard clays. It is interesting to observe that the boundaries defined by the probabilistic analyses captures most of the deviation from the trend lines observed for the case histories, except two of them. Note that in one of these outliers $\delta_{H(max)}/H$ value is 0.62, which corresponds to a high horizontal deformation of 125 mm, even though the support type is a quite rigid diaphragm wall. A close look at this case history indicates that, although the clay was classified as stiff-hard, the undrained modulus is reported to be only 15300 kPa, which may be the reason for this relatively large displacement. A similar conclusion was reached for the second outlier in the data with $\delta_{H(max)}/H$ value of 0.51. For the results of the parametric study carried out by Bryson and Zapata-Medina (2012), it is seen that except for three, the data lies within the borders defined by probabilistic analysis. The three values that are left out has α coefficients that are out of the range employed herein. For the data points with normalized displacement values of 0.253% and 0.268%, the sheet pile walls behaved quite flexibly, and for the data point with a low normalized displacement value of 0.066%, the thick diaphragm wall is extremely rigid.



(a)



(b)



(c)

Figure 9. 100 Analyzes Histograms for $\alpha = 5$
 a) Cohesion, b) Friction Angle, c) Maximum Lateral Displacement

Table 8. *Extracted Case History Data*

References	c_u (kN/m ²)	EI (kNm ² /m)	s_v (m)	s_h (m)	H (m)	$\delta_{H(max)}$ (mm)
Bahadır & Onur, 2018	100	328000	2.4	1.6	19	21.86
Bahadır & Onur, 2018	150	219000	3.25	1.8	17	12.96
Bahadır & Onur, 2018	150	219000	3.25	1.8	14.5	5.8
Bryson & Zapata-Medina, 2012	140	970313	2.45	2.45	12.2	14.75
Bryson & Zapata-Medina, 2012	190	2500000	3.08	3.08	18.5	30
Bryson & Zapata-Medina, 2012	76.5	2300000	3.8	3.8	20	124.76
Bryson & Zapata-Medina, 2012	105	468000	3.3	3.3	11.8	44.53
Bryson & Zapata-Medina, 2012	77.5	1177600	2.65	1.92	15.7	81.37
Cavlaz, 2017	125	312161	2.5	1.87	18	12
Cavlaz, 2017	200	477522	2.5	1.3	29.5	50
Çalışan, 2009	200	263000	2.5	2	20	26
Engin, 2019	95	573027	2	1.7	25	35
Karatağ, 2012	200	263000	2.5	2	13.6	8.6
Kökten & Yıldız, 2018	190	249728.5	2.5	2	13.6	13
Özyürek, 2019	190	603200	2.125	1.63	33	23
Şahin, 2017	100	220000	2.5	1.8	18.5	18
Şahin, 2017	100	220000	2.2	1.5	20	15
Şahin, 2017	100	220000	2.52	1.8	19	18
Ünver & Ünver, 2021	170	520933.2	2.8	1.1	25	42
Ünver & Ünver, 2021	170	520933.2	2.8	1.1	24	40
Ünver & Ünver, 2021	170	520933.2	2.8	1.1	19	65
Yeler, 2019	200	280400	2.5	2	14	12.7

Table 9. *Parametric Study by Bryson and Zapata-Medina (2012)*

Stiff Clay ($c_u=125$ kPa, $E_s=14847$ kPa, $FOS_{base}=3.52$)			
Model	$EI/Y_w s_v^4$	$s_v s_H Y_w H^2/EI$	$\delta_{H(max)}$ (mm)
1	264	61.53	24.64
2	264	39	22.69
3	264	78	26.09
4	2150	36.46	22.07
5	897	45.37	23.01
6	4229	30.79	21.29
7	897	45.37	23.07
8	13	1231.45	32.67
9	26	615.73	30.93
10	66	246.29	28.52
11	132	123.15	26.56
12	1322	12.31	20.06
13	2643	6.16	17.83
14	6608	2.46	14.79
15	66080	0.25	8.07

Note: System stiffness factors were calculated using the following values: $H=12.2$ m; $s_v=3.8$ m; $s_H=6$ m

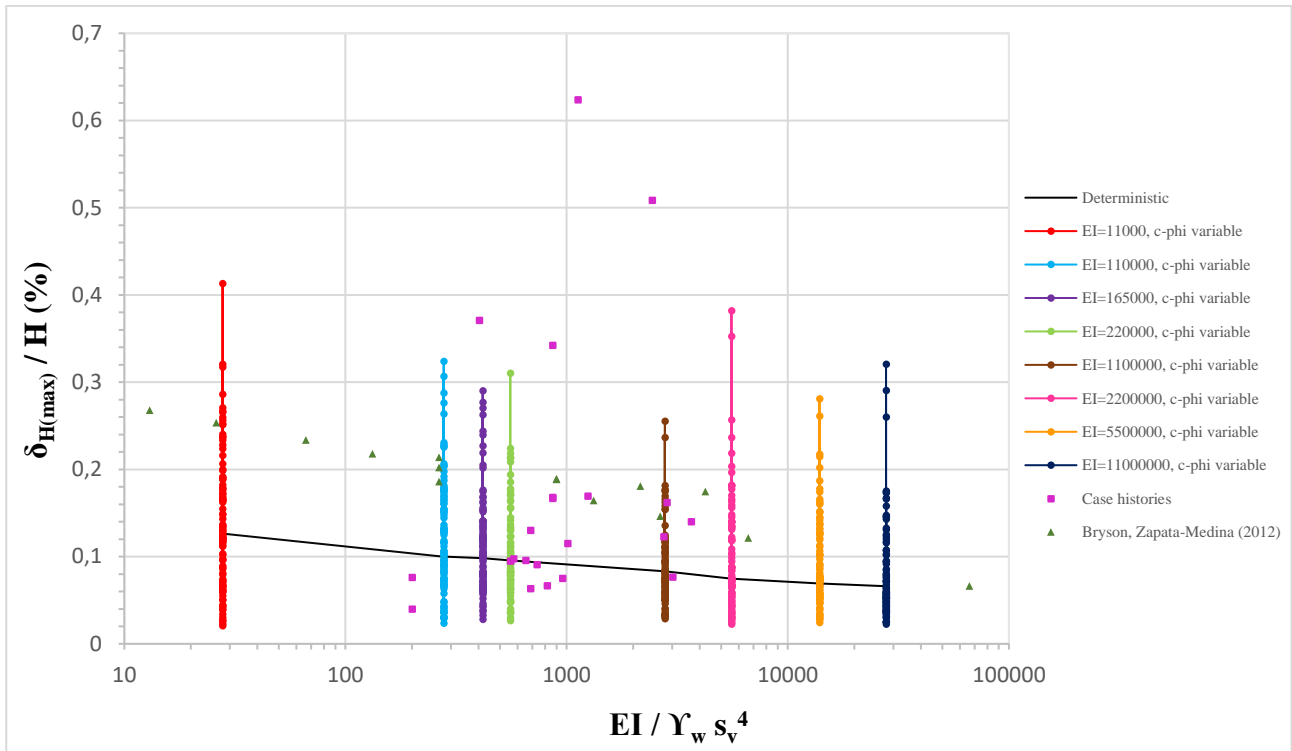


Figure 10. $\delta_{H(max)} / H$ (%) - $EI / \gamma_w s_v^4$ Graph of all Data

It is important to note that the Clough et al. (1989)-defined system stiffness factor, which was also used in the preparation of Figure 10, may not be able to fully symbolize the real nature of deep excavation behavior, because this factor uses just the vertical spacing of the support elements. The Clough et al. (1989)-suggested system stiffness factor includes the wall stiffness and the support element vertical spacing, but not the horizontal spacing. Figure 11 illustrates the relationship between the horizontal distance between anchors and the lateral deformation of the deep excavation examined. According to the results of the analysis, when the horizontal spacing of the anchor is reduced by about 1 m, the lateral deformation is reduced by about 16 mm. Considering that the maximum horizontal deformation as recorded by the inclinometer measurements for the excavation was 18 mm, the horizontal spacing of the anchor seems to have about as much effect as the vertical spacing on the lateral deformations. Since Clough et al. (1989) uses only the vertical spacing of support element in the system stiffness factor, this approach can be considered only as a 2D approach. However, as seen in Figure 11, it is more likely that the system stiffness factor is 3D due to the effect of horizontal spacing (Bryson & Zapata-Medina, 2012).

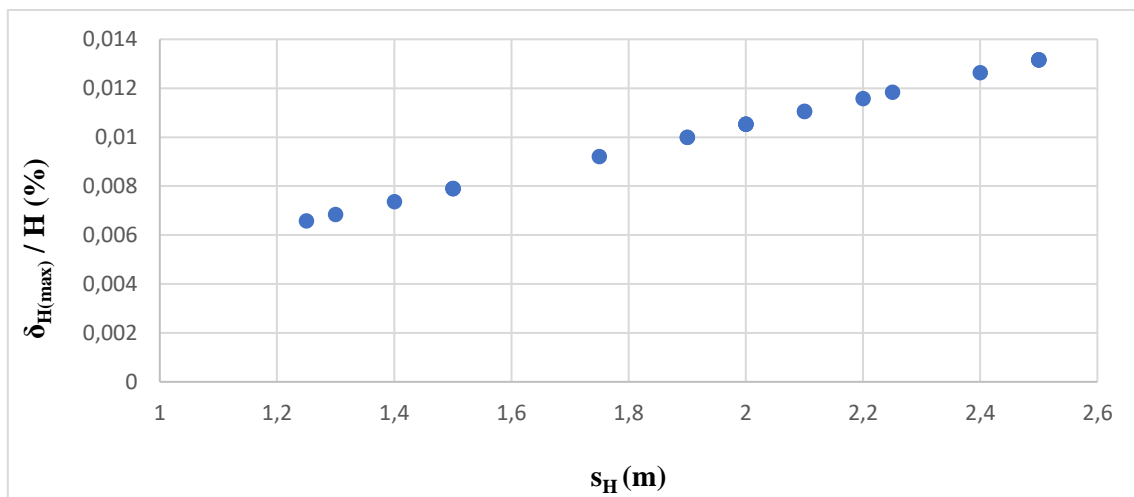


Figure 11. Influence of Horizontal Support Element Spacing on Deep Excavation Lateral Deformation

The relationship between the normalized displacement and a suggested updated system stiffness factor in the form of $s_v s_H \gamma_w H^2 / EI$, which includes support element horizontal spacing s_H and maximum excavation height H are presented in Figure 12. A comparison of Figure 12 with Figure 10, which is created with Clough et al. (1989)-proposed system stiffness factor, firstly indicates that the two outliers aforementioned above could not be captured by the newly defined system stiffness factor also. Thus, these two cases, as previously indicated, have some unusual behavior, which cannot be reasonably explained theoretically. On the other hand, with the use of the newly proposed system stiffness, all the data from the parametric studies performed by Bryson and Zapata-Medina (2012), except one, are now within the limits of finite element analysis results. The diaphragm wall with high stiffness remains out of the range for the same reason. But the case histories with flexible sheet pile walls moved inside the smaller range since the horizontal spacing of the support elements is 6 m, and the vertical spacing is approximately 4 m. Thus, a larger range and different types of support elements are now more easily captured, meaning that proposed the new definition is a more meaningful way to describe design results as illustrated with case histories.

Table 10 shows a statistical evaluation of the system stiffness factor for the case histories. If the system stiffness factors are to be evaluated according to statistical parameters, the range of the system stiffness value suggested by Clough et al. (1989) is 3450.7, while that of the new system stiffness factor is 66.7. In addition, while the standard deviation and the coefficient of variation of the system stiffness value suggested by Clough et al. (1989) are 998.43 and 81.03%, respectively, the standard deviation and the coefficient of variation of the new system stiffness factor are 20.76 and 48.86%, in order. As it can be understood from here, the new system stiffness factor changes within a narrower range and when the standard deviation and coefficient of variation are taken into account, the values are closer to each other.

Thus, with the use of the newly proposed system stiffness factor, unlike the Clough et al. (1989) proposition, most of the case histories, i.e. typical designs, are concentrated in the range where the system stiffness is between 14.6 and 73, with a normalized displacement of approximately 0.04% ~ 0.18%. Thus, successful designs in practice can be expected to lie within this smaller range for stiff-hard clays, which is a useful information for preliminary calculations.

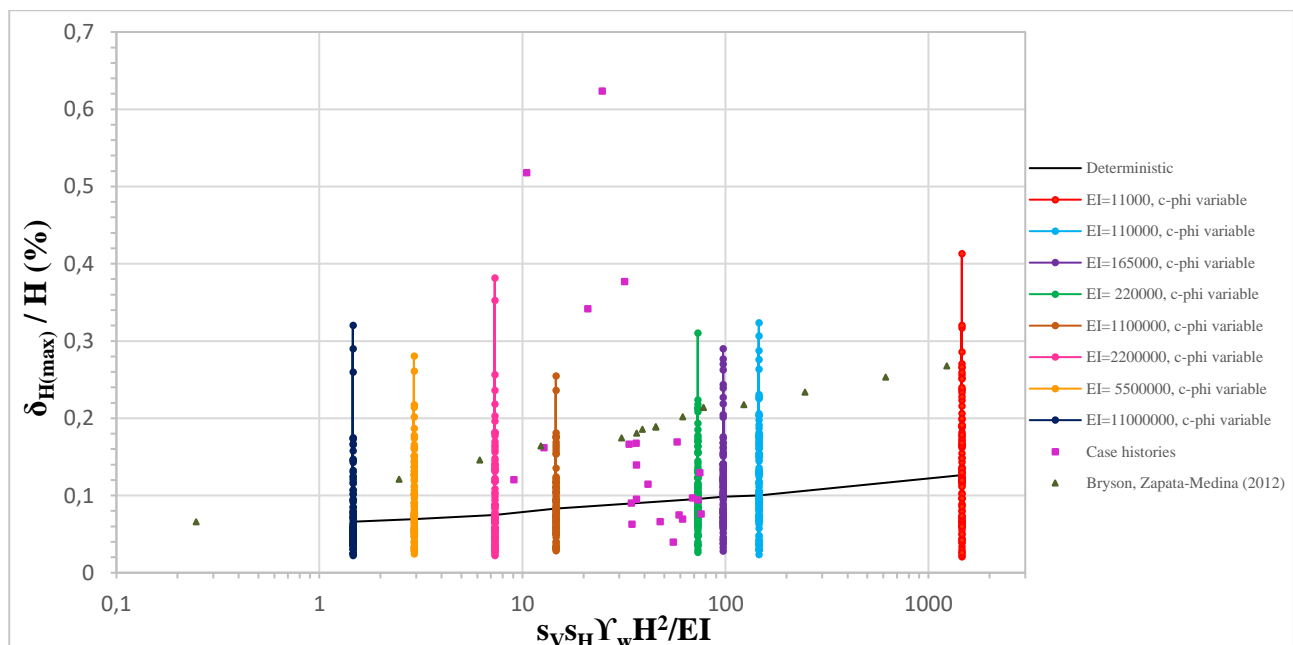


Figure 12. The Newly Created System Stiffness and Normalized Lateral Deformation Graph for all Data

Table 10. Statistical Evaluation of the System Stiffness Factors

Statistical Parameters	$EI/\gamma_w s_v^4$	$s_v s_H \gamma_w H^2/EI$
Range	3450.7	66.7
Mean	1232.2	42.5
Standard Deviation	998.43	20.76
Coefficient of Variation (%)	81.03	48.86

5. CONCLUSION

In this study, the effect of wall stiffness on lateral displacements was investigated for excavations in stiff to hard clays. For this purpose, a series of systematic finite element analyses were carried out that involve a practical range of support system stiffness values, as well as stiff-hard clay geotechnical parameters. A practical methodology in terms of a chart to be used in preliminary design was presented. Considering the inherent variability of the soil, the ϕ and c' of the clay were randomly generated using Monte Carlo simulations to be automatically inserted into the finite element analyses using Python programming language. Finally, the performance of the analyzes was evaluated comparatively using measurements reported in 22 well-documented case histories from deep excavations in stiff-hard clays.

The results indicate that for a 1000-fold heighten in the system stiffness factor, the decrease in the mean normalized lateral deformation is only about 0.06%. Thus, wall stiffness and spacing of support elements have a small influence on wall lateral movement in stiff-hard clays. On the other hand, Monte Carlo simulations demonstrated that soil variability has a large influence, and results in quite a large range in the obtained values of normalized maximum lateral excavation deformation for a given wall stiffness. This range was observed to explain the variability of the lateral deformations observed in well-documented case histories.

Finite element analyses designate that the horizontal spacing of the anchor has about as much effect as the vertical spacing on the lateral deformations. Widely-used Clough et al. (1989) definition of system stiffness uses only the horizontal center-to-center spacing, thus can be considered as a 2D approach. A new definition of system stiffness is recommended in this study, and it captures a larger range and different types of support elements are now more easily captured, and thus can be considered as a more robust and simple approach to describe the expected performance of excavation wall design.

In deep excavations in stiff-hard clays, the main factor affecting the maximum lateral wall displacement is the soil parameters, regardless of the bending stiffness of the support system. In fact, this study has indicated clearly that relying solely on the stiffness of the support system to determine the lateral displacement in deep excavations may not be reliable. Another contribution of this study is to demonstrate that the variability of soil parameters and the support system stiffness can lead to significant variations in the expected displacements. Therefore, probabilistic analyses that consider the variability in both soil parameters and support system stiffness should be conducted during the design phase to determine the magnitude of displacements and appropriate measures should be taken accordingly.

CONFLICT OF INTEREST

The authors declare no conflict of interest.

REFERENCES

- Akbaş, S. O., & Kulhawy, F. H. (2010). Characterization and estimation of geotechnical variability in Ankara clay: a case history. *Geotechnical and Geological Engineering*, 28(5), 619-631. doi:[10.1007/s10706-010-9320-x](https://doi.org/10.1007/s10706-010-9320-x)
- Bahadır, A. A., & Onur, M. İ. (2018). “Derin Kazı Analizlerinde Küçük Şekil Değiştirme Rijitliğinin Etkisi”. *El-Cezeri*, 5(1), 96-106. doi:[10.31202/ecjse.364289](https://doi.org/10.31202/ecjse.364289)
- Bozkurt, S. (2017). *Application of finite element method in geotechnical risk analysis: An application for supported deep excavations* (in Turkish). MSc Thesis, Gazi University, Ankara, Türkiye.

- Bryson, L. S., & Zapata-Medina, D. G. (2012). Method for estimating system stiffness for excavation support walls. *Journal of Geotechnical and Geoenvironmental Engineering*, 138(9), 1104-1115. doi:[10.1061/\(ASCE\)GT.1943-5606.0000683](https://doi.org/10.1061/(ASCE)GT.1943-5606.0000683)
- Carswell, W., & Siebert, D. R. (2021, May 10-14). *Factor of Safety against Basal Heave and the Evaluation of Global Soil Movements*. In: C. E. Mohtar, S. Kulesza, T. Baser, & M. D. Venezia (Eds.), Selected Papers from the Sessions of the International Foundations Congress and Equipment, Earth Retention, Ground Improvement, and Seepage Control (IFCEE 2021), (pp. 123-132). doi:[10.1061/9780784483411.012](https://doi.org/10.1061/9780784483411.012)
- Cavlaz, C. R. (2017). *Comparison of the instrumentation results obtained from supported deep excavation case histories with finite element analyses* (in Turkish). MSc Thesis, Gazi University, Ankara, Türkiye.
- Clough, G. W., Smith, E. M., & Sweeney, B. P. (1989, June 25-29). *Movement Control of Excavation Support Systems by Iterative Design*. In: F. H. Kulhawy (Eds.), Proceedings of the Foundation Engineering Congress on Current Principles and Practices, Vol. 2, (pp. 869-884), ASCE, New York.
- Clough, G. W., & O'Rourke, T. D. (1990, June 18-21). *Construction Induced Movements of Insitu walls*. In: P. C. Lambe, & L. A. Hansen (Eds.), Proceedings of the Specialty Conference on Design and Performance of Earth Retaining Structures, (pp. 439-470), ASCE, New York.
- Craig, R. F. (2004). *Craig's soil mechanics*. CRC press.
- Çalışan, O. (2009, September 23). "Ankara Kilinde Yapılan 20 m Derinliğindeki Bir Kazının Geri Analizi", In: Proceedings of 5. METU Geotechnical Symposium, (pp. 1-12), Ankara.
- Duncan, J. M., & Buchignani, A. L. (1976). *An engineering manual for settlement studies*. Berkeley: Department of Civil Engineering, University of California.
- Engin, A. T. (2019). *Finite element analysis of a deep excavation: A case study*. MSc Thesis, Middle East Technical University, Ankara, Türkiye.
- Harr, M. E. (1984). *Reliability-based design in civil engineering* (Vol. 20). Department of Civil Engineering, School of Engineering, North Carolina State University.
- Karatağ, H. (2012). *The comparison of the calculated and observed behavior of an anchored retaining wall* (in Turkish). MSc Thesis, Gazi University, Ankara, Türkiye.
- Kökten, Ö., & Yıldız, E. (2018). A study on the reliability analysis of a deep excavation supported with anchored pile walls. *ce/papers*, 2(2-3, Special Issue), 463-468. doi:[10.1002/cepa.714](https://doi.org/10.1002/cepa.714)
- Kulhawy, F. H. (1992). On the evaluation of soil properties. ASCE Geotechnical Special Publications, Vol. 31, (pp. 95-115).
- Long, M. (2001). Database for Retaining Wall and Ground Movements Due to Deep Excavations. *Journal of Geotechnical and Geoenvironmental Engineering*, 127(3), 203-224. doi:[10.1061/\(ASCE\)1090-0241\(2001\)127:3\(203\)](https://doi.org/10.1061/(ASCE)1090-0241(2001)127:3(203))
- Moormann, C. (2004). Analysis of Wall and Ground Movements Due to Deep Excavations in Soft Soil Based on a New Worldwide Database. *Soils and Foundations*, 44(1), 87-98. doi:[10.3208/sandf.44.87](https://doi.org/10.3208/sandf.44.87)
- Özyürek, Y. E. (2019). *Two dimensional finite element modeling for the multi tier pile wall with anchor shoring system*. MSc Thesis, Middle East Technical University, Ankara, Türkiye.
- PLAXIS 2D Material Models Manual (2022). Bentley Systems. [URL](#)
- PLAXIS 2D Ultimate [Software] (2022). Bentley Systems.
- Python version 3.11 [Programming Language] (2022, October 24). The Python Software Foundation. [URL](#)
- Sabatini, P. J., Pass, D. G., & Bachus, R. C. (1999). Ground anchors and anchored systems (Report No. FHWA-IF-99-015). United States Department of Transportation, Federal Highway Administration, Office of Bridge Technology.
- Sorensen, K. K., & Okkels, N. (2013, September 2-6). Correlation between drained shear strength and plasticity index of undisturbed overconsolidated clays. In: P. Delage, J. Desrues, R. Frank, A. Puech, & F.

Schlosser (Eds.), Proceedings of the 18th International Conference on Soil Mechanics and Geotechnical Engineering (ICSMGE), Vol. 1, (pp. 423-428).

Şahin, M. (2017). *The investigation of an instrumentally observed deep excavation by numerical analyses* (in Turkish). MSc Thesis, Yıldız Technical University, Istanbul, Türkiye.

Ünver, M., & Ünver, İ. S. (2022). Monitoring of a deep excavation supported by anchored retaining walls. *Indian Geotechnical Journal*, 52(1), 227-236. doi:[10.1007/s40098-021-00544-5](https://doi.org/10.1007/s40098-021-00544-5)

Yeler, M. (2019). *Comparison of design deformations calculated with finite element method an inclinometer measurement in excavation support system with bored pile* (in Turkish). MSc Thesis, Yıldız Technical University, Istanbul, Türkiye.









Gazi University

Journal of Science

PART A: ENGINEERING AND INNOVATION

<http://dergipark.org.tr/guj.1215224>

Analysis of Dislocation Density for GaN Based HEMTs in Screw Mod

Özlem BAYAL^{1*}  Esra BALCI²  A. Kürşat BİLGİLİ³  M. Kemal ÖZTÜRK³  Süleyman ÖZÇELİK⁴  Ekmel ÖZBAY⁵ 

¹Photonics Application and Research Center, Gazi University, Ankara, Türkiye

²Department of Physics, Ankara Hacı Bayram Veli University, Ankara, Türkiye

³Department of Physics, Faculty of Science, Gazi University, Ankara, Türkiye

⁴Department of Photonics, Faculty of Science, Gazi University, Ankara, Türkiye

⁵NANOTAM, Bilkent University, Ankara, Türkiye

Keywords	Abstract
Screw Dislocation HEMT III-V Group Nitrid MOCVD HRXRD	Quick response is an important feature in design of optoelectronic cards. So, in this study, structural properties of GaN/AlN/AlGaIn HEMTs structures grown on sapphire by the chemical vapor adjustment method are analyzed by the X-ray diffraction method. The main property of these kind of materials is that they are resistant to high voltage, temperature, and pressure. Although their performance is worse compared silicon, for forcing limit standards, they present wide research field. In this study, the focus of investigation is dislocation density stemming from lattice mismatch between layers and wafer causing cracks on the surface. In HEMT structure calculation of dislocation density for GaN and AlN represents all structure. High dislocation density for AlN layer is determined because of aggressive behavior of Al element in the structure. Also, quantized GaN layers stop moving of dislocations and prevents surface cracks.

Cite

Bayal, Ö., Balci, E., Bilgili, A. K., Öztürk, M. K., Özçelik, S., & Özbay, E. (2022). Analysis of Dislocation Density for GaN Based HEMTs in Screw Mod. *GU J Sci, Part A, 10(2)*, 131-139. doi:[10.54287/guj.1215224](https://doi.org/10.54287/guj.1215224)

Author ID (ORCID Number)	Article Process
0000-0003-0718-9734	Submission Date 06.12.2022
0000-0003-0217-9481	Revision Date 23.01.2023
0000-0003-3420-4936	Accepted Date 21.02.2023
0000-0002-8508-5714	Published Date 22.05.2023
0000-0002-3761-3711	
0000-0003-2953-1828	

1. INTRODUCTION

Today, III-V group semiconductor nitrides such as AlN, GaN and AlGaIn and their alloys forms the base of electronic and opto-electronic devices as light emitting diodes (LED), laser diodes, UV sensors and high electron mobility transistors (HEMT) because of their physical properties (Kapolnek et al., 1995; Heinke et al., 2000). These semiconductor nitrides and their alloys crystallize both in wurtzite and zinc-blende structures (Strite & Morkoç, 1992; Vurgaftman et al., 2001). The basic difference between these two structures is the rank of planes. Wurtzite structure is regulated as triangle (0001) tightly packed planes. Zincblende structure is formed as tightly packed atoms in (111) plane as triangles along $\langle 111 \rangle$ direction. III-V group semiconductor nitrides have direct and wide band gaps. In semiconductors with direct band gap, recombination of electrons and holes comes out in $\delta k=0$ without a change in momentum. This situation implies III-V group semiconductor nitrides that are effective for photon producers (Chen et al., 2020). At the same time, mobility increases if conduction conditions are maintained because of direct band transition. Band gaps of III-V group semiconductor nitrides are 0.7, 3.4, and 6.1 eVs for InN, GaN and AlN respectively (Elhamri et al., 1998). Because working principle of electronic and opto-electronic devices are dependent on physical properties of materials forming the device. Direct band transition feature gives hand to many different applications in a wide wavelength range (Wu et al., 2002). For instance, in billboards, traffic lamps or cell phones using nitrite based HEMTs, maintains many advantages in terms of power depletion, cost and efficiency. On the other hand,

nitrites can operate at high temperatures with low noise because of their good thermal conductivity. Also, III-V group nitrites have the property of well electron carrying, good mobility value and saturation speed. These features enable GaN based HEMTs to be used in radars, rockets and satellite systems those require high temperature and high power (Bayrak, 2003). III group nitrites are also convenient for quantum wells, modulation doped hetero interfaces, heterojunction structures and hetero structure technology (Morkoç, 1999).

Because of difficulties in growth of GaN crystal, GaN/AlGaN heterojunction structures are grown on sapphire (Al_2O_3) wafers despite there is low thermal and structural match (Kapolnek et al., 1995). The reason of choosing sapphire is its hexagonal symmetry, easy handling, easy cleaning procedure before growth and low cost. Also, melting point of sapphire is 2040°C and this property makes it chemically stable at even very high temperatures. But sapphire is not an ideal wafer for commercial applications. The reason for this is high dislocation density stemming from great lattice mismatch between sapphire and III-V group nitrites and mismatch between thermal expansion coefficients. Lattice mismatch is about 14-16% and thermal expansion coefficient mismatch is about 34% (Bernardini et al., 1997).

In this study, structural properties and mosaic defects of AlN/GaN/AlGaN structure are investigated on three different samples. It is seen that gained data and analysis concluded with great accordance with literature. Investigation of this type of samples are rare in literature, so this study may play a key role for researchers for their future studies. The defect nature of these structures is predominantly attributed to the dislocation density. Finding the dislocation in monolayer structures is easy (Feaugas & Delafosse, 2019). Although finding the dislocation density of interfaces in a multi-quantum HEMT structure sheds light on an important problem. In this study, we aim to find the defect factors and increase the quality of the HEMT structure.

2. MATERIAL AND METHOD

GaN/AlN/AlGaN HEMT samples were grown on sapphire wafer by the MOCVD technique. Al pre-deposition did not applied and the growth process can be summarized as follows. Surfaces were clean and mirror like, there were colourful crowding fields on the surface. GaN thin film is deposited on 520 nm thick AlN layer. Over this GaN buffer layer 2 nm thick AlN inter layer is grown. Later 25 nm thick AlGaN layer is grown on AlN inter layer. AlGaN layer is grown at 1075°C - 1140°C temperature range under NH_3 flow and 50 mbar medium pressure 3 nm thick GaN cap layer is grown at the last step of sample growth.

Deposition is made at 1050°C for 15 minutes. During preparation of samples sapphire is used as a wafer. To construct high electron mobility transistor (HEMT), AlGaN layer is deposited on AlN nucleation layer in MOCVD. This structure is grown as stable as possible. Five layers of quantized GaN layers are used to prevent or reduce dislocations. Schematic diagram of samples is shown in Figure 1. in experimental section. To prevent dislocations stemming from lattice mismatch between sapphire and GaN buffer layer AlN nucleation layer and AlN buffer layers are grown at high temperature. AlN inter layer is grown in 1075°C and 1140°C temperature range with triethylaluminium TMAI sources under NH_3 flow with flow speed of 200 sccm and 10 sccm respectively under 50 mbar pressure in a duration of 3 minutes. Nucleation layer is grown at 550 - 560°C temperature that ranges under 50 mbar pressure with NH_3 flow at speed of 1000 sccm and TMAI source with flow speed of 15 sccm.

In the expectation that GaN/AlGaN HEMT structures in detail, High Resolution X-Ray Diffraction (HRXRD), noncontact Hall measurement, and Atomic Force Microscopy (AFM) (Nanomagnetic Instruments) in dynamic mode scanning measurement were examined in this study.

XRD analysis is made with Bruker D-8 discovery HRXRD diffractometer. This device uses X- rays with a wavelength of 0.54056 nm with pure $\text{CuK}\alpha_1$ source and four channel Ge monochromator. Scans for samples are made on (101), (102), (103), (105), (106), (112), (114), (121), (122), (123), (124), (201), (202), (203), (204), (211), (212), (213), (301), (302) symmetric and asymmetric planes. These plane scans are made for AlGaN, AlN and GaN individually. The surface morphology of samples was characterized by Atomic Force Microscopy (AFM) (Nanomagnetic Instruments) in dynamic mode scanning.

GaN cap layer	t ~ 3 nm	GaN cap layer	t ~ 3 nm	GaN cap layer	t ~ 3 nm
AlGaIn	t ~ 25 nm	AlGaIn	t ~ 25 nm	AlGaIn	t ~ 25 nm
AlN interlayer	t ~ 1-2 nm	AlN interlayer	t ~ 1-2 nm (3.00min)	AlN interlayer	t ~ 1-2 nm (7.00min)
GaN buffer layer [5]	t ~ 150 nm	GaN Layer	t ~ 5 nm	GaN Layer	t ~ 5 nm
GaN buffer layer [4]	t ~ 300 nm	InGaIn Layer	t ~ 1 nm	InGaIn Layer	t ~ 1 nm
GaN buffer layer [3]	t ~ 60 nm	GaN buffer layer [5]	t ~ 150 nm	GaN buffer layer [5]	t ~ 150 nm
GaN buffer layer [2]	t ~ 700 nm	GaN buffer layer [4]	t ~ 300 nm	GaN buffer layer [4]	t ~ 300 nm
GaN buffer layer [1]	t ~ 60 nm	GaN buffer layer [3]	t ~ 110 nm	GaN buffer layer [3]	t ~ 110 nm
HT AlN buffer layer	t ~ 520 nm	GaN buffer layer [2]	t ~ 800 nm	GaN buffer layer [2]	t ~ 800 nm
AlN NL	[3.00 min]	GaN buffer layer [1]	t ~ 90 nm	GaN buffer layer [1]	t ~ 90 nm
		HT AlN buffer layer	t ~ 520 nm	HT AlN buffer layer	t ~ 520 nm
		AlN NL	[3.00 min]	AlN NL	[3.00 min]

Figure 1. The schematic diagrams of samples

3. RESULTS AND DISCUSSION

In defected epilayers, FWHM of ω curves are formed by support of tilt, twist, mean size of grains and inhomogeneous stress and strain dispersion. In principle expansion may be important because of limited field dimension and strain but in present system it is determined that it has a little effect. Here to reduce or prevent expansion stemming from inhomogeneous strain and limited grain dimension, a slit with a 0.5 mm width is inserted in front of detector during use of double axis ω scans. Also, samples present 10"-30" FWHM both with triple axis 2 theta scans and non-zero h_k orientation in (00.2) reflection. Moreover, for all experimental reflections both inward expansion of crystal reflection and expansion stemming from device can be neglected. Because these effects take only a few arc seconds. Expansion caused by twist angle can be analyzed using reflections in screw geometry.

Nitride materials are well-known with their cubic hexagonal structure. Nano structures has many advantages for opto-electronic devices in terms of optical and electrical properties. Nitride materials have the advantage of operating at high voltage, temperature, and frequency. For instance, nitride-made transformers can operate for a long time without getting out of order (Yang et al., 2022). In space works, these materials resist to high temperature very well and maintains operation of device for a long time. The reasons for this situation are point, line and volume defects spreading all over the structure. There are some methods to reduce these defects. In samples five layers of GaN are used to reduce defects. Tilt twist, grain size and dislocations can be given as examples of defects supporting broadening of FWHM. Broadening of FWHM stemming from device is enough to determine twist angle in screw geometry. In this situation grain size at some arc seconds dimension and inhomogeneous strain may be neglected and this makes calculation of twist angle, screw, and edge type dislocations available.

Sapphire is used as a wafer. Lattice mismatch between this layer and GaN is caused by clean mirror-like image of surface. Three samples are grown to examine defect properties by changing thickness of GaN layers and buffer AlN layer (Kato et al., 2021). Defect structure is examined in electrical, optical, and structural terms. To examine HEMTs, especially mobility is important gained by Hall device.

Figure 2 shows Φ scan of samples. Curves belonging to different samples are shown with different colors. Φ scan angles show optimized Φ angle value for Φ scan of planes. Because there is diffraction at every edge of hexagonal structure in Φ scan, there are six peaks between 60° and 360° range. Φ scan gives right value in pdf card for high quality GaN because Φ scan is optimized. For cubic systems there are four different peaks in Φ scan. Peak is optimized for Φ scan (Nand et al., 2022).

Figure 3. shows increasing FWHM for Φ and ω scans for three samples. FWHM of Φ and ω scans are gained by using pseudo-voigt function from rocking curves. FWHM of a scan in Figure 3. decrease with an increase in Φ . On the other hand, (12.1) reflections approach each other because they are 78.8° in percentage. In fact, they should be equal when Φ angle reaches 90° . Diffraction geometry is shown in Figure 4. With the

cause of too thin films reflection is impossible in 90° lattice plane tilt. Here it can be seen that in wurtzite structure and on (12.1) plane there are 12 similar planes.

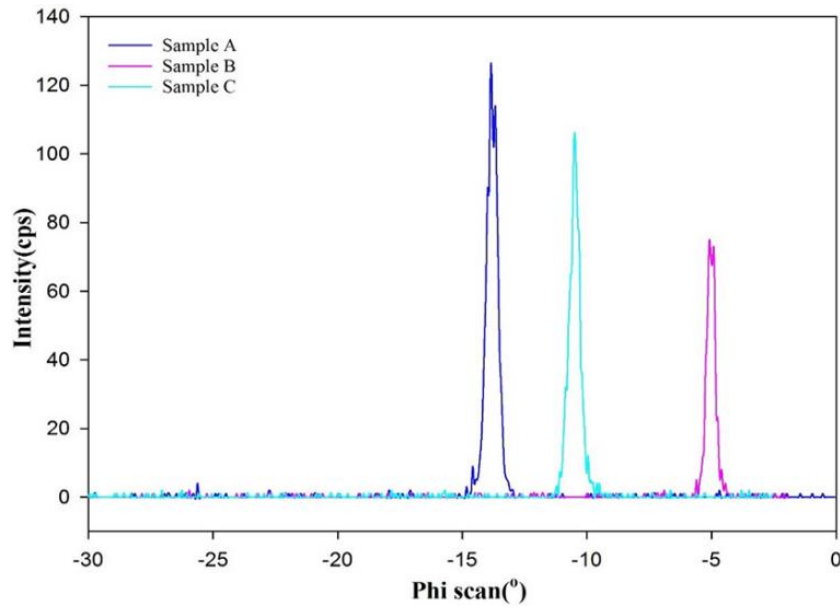


Figure 2. Φ scan of crystal planes for samples A, B and C

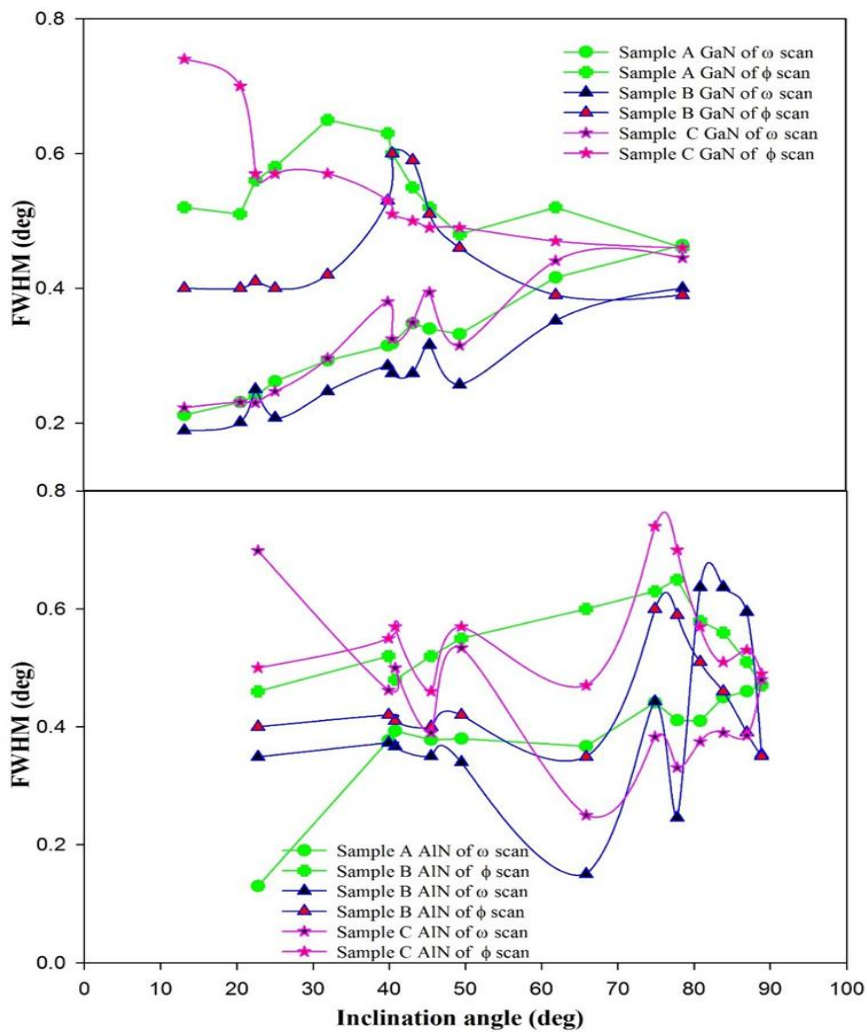


Figure 3. Φ and ω scans for GaN and AlN films in three samples

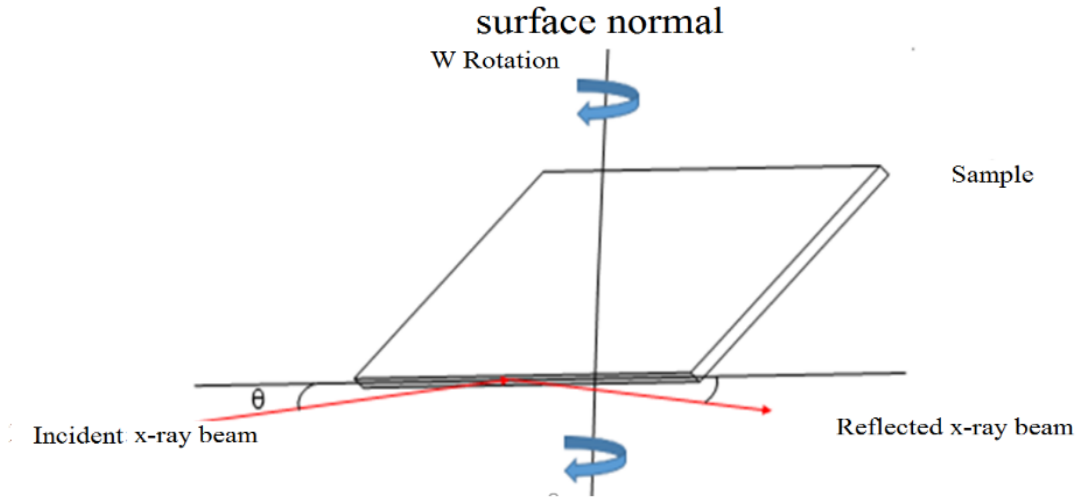


Figure 4. Screw dislocation of HEMT on HRXRD

Reflection peaks do not iterate at each 30° azimuth angle. Group six peaks iterate at every 60° azimuth angle and other groups behave similar but FWHM values of Φ and ω scans are equal. Although lattice have different hexagonal crystal structure on (12.1) diffraction plane twist angles are different for GaN and AlN layers. Quantized growth reduced dislocations. In addition, on tilt angle which the reflection is seen (78.8°) FWHM of Φ and ω scans are almost the same. These results imply width of rocking curves approach twist angle in Φ and ω scans at higher ksi angles. Also, difference in FWHM of scans are larger than ksi scans. For this reason, mean twist angle should be between FWHM and ksi= 78.8° . In this situation, average value of FWHM and ksi= 78.8° can be taken as mean twist angle.

In order to test validity of results, when compared with Srikant and co-workers' method, it is seen that they correspond each other (Heinke et al., 2000). Appear to be compatible with each other. Little difference between twist angle calculated in this study and twist angle value in literature can be calculated as $\pm 0.005^\circ$. This result is in borders of instrumental resolution. To determine twist angle of different defected structures is also possible with this method.

To compare GaN and AlN on (002) plane rocking curves are given in Figure 5. While GaN layers are in a uniform width position AlN is fluctuating with a strain value. This means that for all three samples (002) plane is crystallized and (002) orientations are in texture structure. On (004) plane there are differences in crystallite GaN structures. For AlN GaN in sample A there is low peak intensity but high FWHM. On these planes GaN lattice match is seen and AlN strain fluctuations are expanded. On (006) plane GaN layer is well crystallized and for sample A AlN is extremely fluctuated with strain.

As can be seen in Table 1 twist angles increase with a decrease in tilt angles. Estimated dislocation density values can be calculated with Equations (1), (2) and (3).

$$D_{screw} = \frac{\beta_{(00.2)}^2}{9b_{screw}^2} \quad (1)$$

$$D_{edge} = \frac{\beta_{(12.1)}^2}{9b_{edge}^2} \quad (2)$$

$$D_{dis} = D_{screw} + D_{edge} \quad (3)$$

Beta is FWHM of rocking curves and b screw and edge are the length of burgers vector. As known before, twist range of lattice planes for wurtzite GaN films uses burgers vector $b = [001]$ and screw type dislocations (Gay et al., 1953; Look & Sizelove, 1999). Tilt range of lattice plane shows details of burgers vector and edge type dislocation density. Number of samples versus dislocation density plot is shown in Figure 6. Dislocation densities of GaN films are too different from each other. It is still being investigated how these dislocations effect electrical and optical features of device.

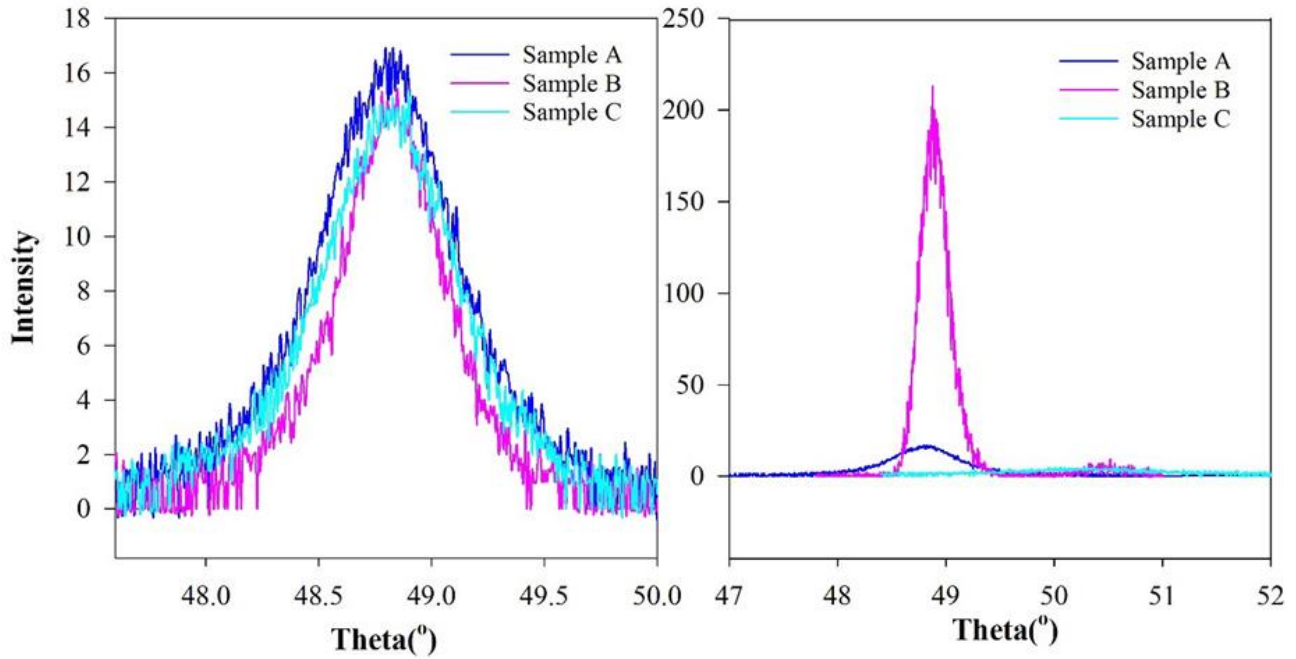


Figure 5. HRXRD omega curves of (002) miller plane of GaN and AlN layers in HEMT structures.

Table 1. GaN films are the rocking curves of Φ and ω scans of experimental results

Samples		Measurement results			
		FWHM (deg)			
		(00.2) reflection	ω scan of (12.1) reflection	Φ scan of (12.1) reflection	Twist angle with error correction (deg)
GaN	A	0.08	0.28	0.52	0.54
	B	0.07	0.20	0.46	0.43
	C	0.09	0.21	0.57	0.49
AlN	A	0.21	0.235	0.41	0.44
	B	0.17	0.175	0.34	0.35
	C	0.22	0.305	0.62	0.62

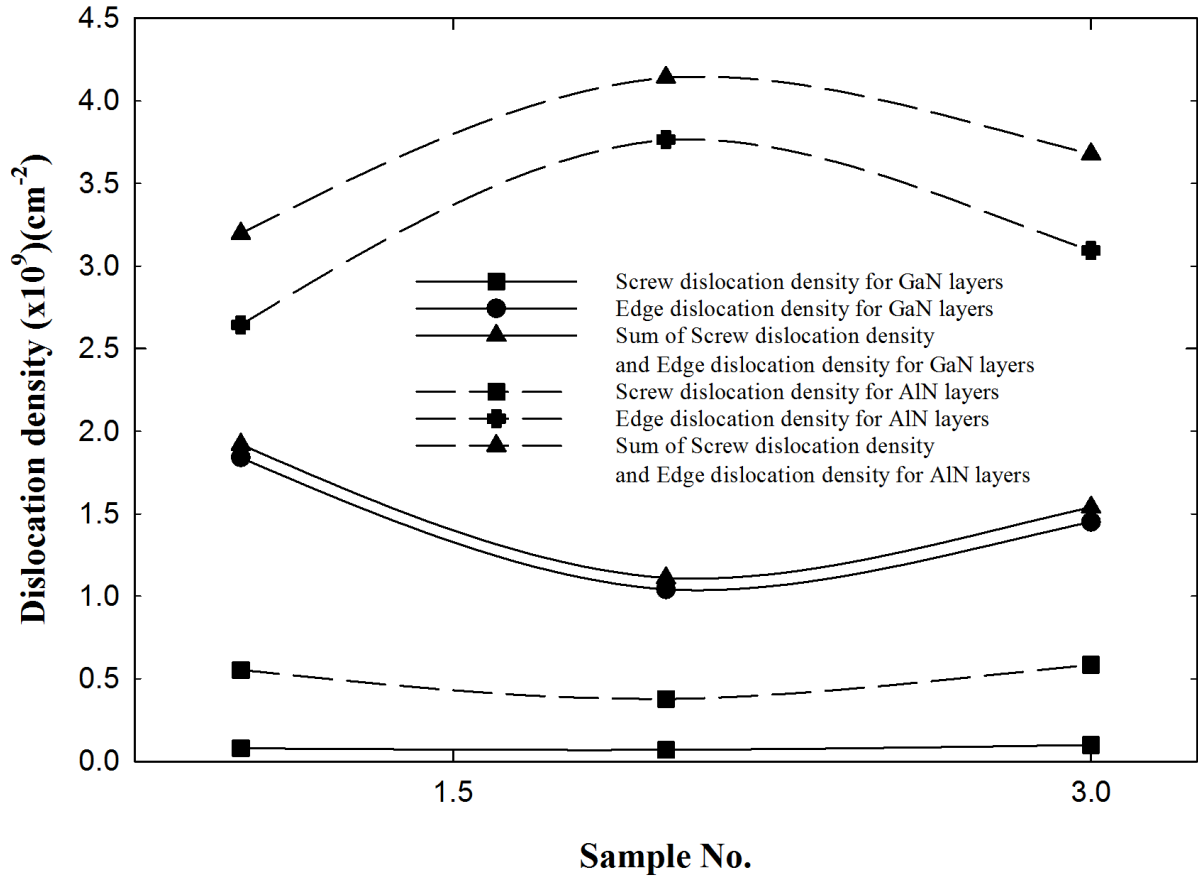


Figure 6. Presentation of calculated screw and edge type dislocations

Twist angle of AlN is larger than other layers. Fluctuations in samples show that there is no linear behavior. It can clearly be seen that defect structure difference is large for AlN/GaN crystallite size. Al dislocations show screw and edge dislocations. It is higher than the GaN dislocation value. Because AlN is an aggressive material, there is a mismatch incompatibility with GaN.

It is clearly seen in Figure 7, for sample A the exposed AlN surface is smooth with the surface roughness of 2.14 nm. sharp rocky mountain-like morphological structure but macro grain crystal structures are observed in sample A. In sample B with a lot of grain and high roughness. Sample B with the rms value is 1.00 nm has more smooth surface than Sample A. The sample C which has moderate grain structures with rms value is 4.21 nm. Dielectric layer between metal and semiconductor converts metal-semiconductor (MS) structure to metal insulator semiconductor (MIS) structure. The interface layer with increasing thickness is in equilibrium with the semiconductor. (Bilgili et al., 2022)

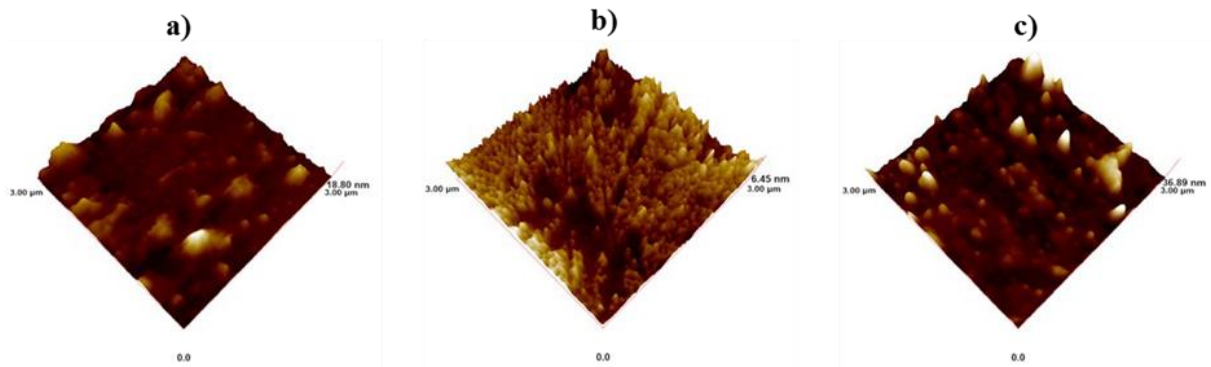


Figure 7. AFM images of a) sample A, b) sample B and c) sample C

4. CONCLUSION

HRXRD makes investigation of line defects for inter-layers available for HEMT structure with this method. Defect reduction of optoelectronic devices plays an important role in improving the performance of crystal structure properties in IV characterization of mobility movements. In addition to being stable at high voltage current frequency values, HEMTs LEDs Diodes door switches with effective selectable wavelengths provide advantages in many optoelectronic devices (Subramanian et al., 2020). For this purpose, defect analysis in HEMT structure was analyzed with HRXRD with weighted dislocation density. According to the analysis result, AlN and GaN dislocation densities were calculated with high precision according to the surface and interface densities. Both AlN and GaN dislocation densities showed similar type properties in the increasing sample. AlN defect structures of these structures are gradually seen in GaN. We see that this harmony remains within the dislocation of the GaN wafer layers, which is about $4 \times 10^9 \text{cm}^{-1}$. Dislocation densities are compatible with the amplification mobility of our sample.

ACKNOWLEDGEMENT

This work was supported by Presidency Strategy and Budget Directorate (Grant Number: 2016K121220)

Data availability statement: All data used in this work are available from the author.

Author contributions: Özlem Bayal, wrote the manuscript, Esra Balcı, made the measurements, made the calculations, Mustafa Kemal Öztürk, Süleyman Özçelik, Ekmel Özbay maintained device support.

CONFLICT OF INTEREST

The authors declare no conflict of interest.

REFERENCES

- Bayrak, S. T. (2003) *AlxGa1-xN/GaN hetero yapılarıdaki 2BEG'nin elektriksel ve optiksel karakterizasyonu* MSc Thesis, Balıkesir University.
- Bernardini, F., Fiorentini, V., & Vanderbilt, D. (1997). Spontaneous polarization and piezoelectric constants of III-V nitrides *Physical Review B*, 56(16), R10024. doi:[10.1103/PhysRevB.56.R10024](https://doi.org/10.1103/PhysRevB.56.R10024)
- Bilgili, A. K., Çağatay, R., Öztürk, M. K., & Özer, M. (2022). Investigation of Electrical and Structural Properties of Ag/TiO₂/n-InP/Au Schottky Diodes with Different Thickness TiO₂ Interface. *Silicon*, 14(6), 3013-3018. doi:[10.1007/s12633-021-01093-5](https://doi.org/10.1007/s12633-021-01093-5)
- Chen, Y., Liu, J., Zeng, M., Lu, F., Lv, T., Chang, Y., Lan, H., Wei, B., Sun, R., Gao, J., Wang, Z., & Fu, L. (2020). Universal growth of ultra-thin III–V semiconductor single crystals. *Nature Communications*, 11(1), 3979. doi: [10.1038/s41467-020-17693-5](https://doi.org/10.1038/s41467-020-17693-5)
- Elhamri, S., Newrock, R. S., Mast, D. B., Ahoujja, M., Mitchel, W. C., Redwing J. M., Tischler, M. A., & Flynn, J. S. (1998). Al_{0.15}Ga_{0.85}N/GaN heterostructures: Effective mass and scattering times. *Physical Review B*, 57(3), 1374-1377. doi:[10.1103/PhysRevB.57.1374](https://doi.org/10.1103/PhysRevB.57.1374)
- Feugas, X., & Delafosse, D. (2019). Hydrogen and crystal defects interactions: Effects on plasticity and fracture. In: C. Blanc, & I. Aubert (Eds.), *Mechanics - Microstructure - Corrosion Coupling Concepts, Experiments, Modeling and Cases* (pp. 199-222). Elsevier. doi:[10.1016/B978-1-78548-309-7.50009-0](https://doi.org/10.1016/B978-1-78548-309-7.50009-0)
- Gay, P., Hirsch, P. B., & Kelly, A. (1953). The estimation of dislocation densities in metals from X-ray data. *Acta Metallurgica*, 315(3), 315-319. doi:[10.1016/0001-6160\(53\)90106-0](https://doi.org/10.1016/0001-6160(53)90106-0)
- Heinke, H., Kirchner, V., Einfeldt, S., & Hommel, D. (2000). X-ray diffraction analysis of the defect structure in epitaxial GaN. *Applied Physics Letters*, 77(14), 2145-2147. doi:[10.1063/1.1314877](https://doi.org/10.1063/1.1314877)
- Kapolnek, D., Wu, X. H., Heying, B., Keller, S., Keller, B. P., Mishra, U. K., DenBaars, S. P., & Speck, J. S. (1995). Structural evolution in epitaxial metalorganic chemical vapor deposition grown GaN films on sapphire. *Applied Physics Letters*, 67(11), 1541-1543. doi:[10.1063/1.114486](https://doi.org/10.1063/1.114486)

- Kato, M., Asada, T., Maeda, T., Ito, K., Tomita, K., Narita, T., & Kachi, T. (2021). Contribution of the carbon-originated hole trap to slow decays of photoluminescence and photoconductivity in homoepitaxial n-type GaN layers. *Journal of Applied Physics*, 129(11), 115701. doi:[10.1063/5.0041287](https://doi.org/10.1063/5.0041287)
- Look, D. C., & Sizelove, J. R. (1999). Dislocation Scattering in GaN. *Physical Review Letters*, 82(6), 1237-1240. doi:[10.1103/PhysRevLett.82.1237](https://doi.org/10.1103/PhysRevLett.82.1237)
- Morkoç, H. (1999). General Properties of Nitrides. In: *Nitride Semiconductors and Devices* (pp. 8-44), (Springer Series in Materials Science, 32). Springer. doi:[10.1007/978-3-642-58562-3_2](https://doi.org/10.1007/978-3-642-58562-3_2)
- Nand, M., Tripathi, S., Rajput, P., Kumar, M., Kumar, Y., Mandal, S. K., Urkude, R., Gupta, M., Dawar, A., Ojha, S., Rai, S. K., & Jha, S. N. (2022). Different polymorphs of Y doped HfO₂ epitaxial thin films: Insights into structural, electronic and optical properties. *Journal of Alloys and Compounds*, 928, 167099. doi:[10.1016/j.jallcom.2022.167099](https://doi.org/10.1016/j.jallcom.2022.167099)
- Strite, S., & Morkoç, H. (1992). Microelectronics and Nanometer Structures Processing, Measurement, and Phenomena. *Journal of Vacuum Science & Technology B*, 10(4), 1237-1266. doi: [10.1116/1.585897](https://doi.org/10.1116/1.585897)
- Subramanian, B., Anandan, M., Veerappan, S., Panneerselvam, M., Wasim, M., Radhakrishnan, S. K., Pechimuthu, P., Verma, Y. K., Vivekanandhan, S. N., & Raju, E. (2020). Switching transient analysis and characterization of an E-mode B-doped GaN-capped AlGaN DH-HEMT with a freewheeling Schottky barrier diode (SBD). *Journal of Electronic Materials*, 49(7), 4091-4099. doi:[10.1007/s11664-020-08113-x](https://doi.org/10.1007/s11664-020-08113-x)
- Vurgaftman, I., Meyer, J. R., & Ram-Mohan, L. R. (2001). Band parameters for III-V compound semiconductors and their alloys. *Journal of Applied Physics*, 89(11), 5815-5875. doi:[10.1063/1.1368156](https://doi.org/10.1063/1.1368156)
- Wu, J., Walukiewicz, W., Shan, W., Yu, K. M., Ager III, J. W., Haller, E. E., Lu, H., & Schaff, W. J. (2002). Effects of the narrow band gap on the properties of InN. *Physical Review B*, 66(20), 201403. doi:[10.1103/PhysRevB.66.201403](https://doi.org/10.1103/PhysRevB.66.201403)
- Yang, Z., Zhong, Y., Zhou, X., Zhang, W., Yin, Y., Fang, W., & Xue, H. (2022). Metal-organic framework-based sensors for nitrite detection: a short review. *Journal of Food Measurement and Characterization*, 16(2), 1572-1582. doi: [10.1007/s11694-021-01270-5](https://doi.org/10.1007/s11694-021-01270-5)



Gazi University

Journal of Science

PART A: ENGINEERING AND INNOVATION

<http://dergipark.org.tr/guj.1245213>

A Sustainable Building Material Developed from Low-Temperature Sintering of Mining Waste with an Alkali-Silicate Solution

Peter Oluwagbenga ODEWOLE^{1*} ¹College of Engineering and Environmental Sciences, Olabisi Onabanjo University, Ogun State, Nigeria

Keywords	Abstract
Glass-Ceramic Foam	The development of glass-ceramic foam has received significant attention in building and construction, given its potential for sustainability. This study investigated the low-temperature route of fabricating glass-ceramic foams from mining waste. The feasibility of one-step or chemical-aided sintering of glass-ceramic foams using granite powder, a naturally sourced mining waste, rather than using already heat-treated wastes such as glass and fly ash has been explored in this study. Glass-ceramic foam samples were synthesized from a homogenous blend of constant percentage by weight of granite-clay mix with varying amounts of alkali-silicate solution. The influence of the alkali-silicate solution on the physicomaterial and microstructural properties of the synthesized samples sintered at 850°C was investigated. The results showed water absorption of 9.5-33.3%, apparent porosity of 18.2-56.7%, bulk density of 1.7-1.91 g/cm ³ , and compressive strength of 20.7-26.3MPa. The glass-ceramic foam developed in this research can be suitably used for the thermal insulation of buildings.
Sustainable Building Material	
Physicomaterial Properties	
Microstructure	
Low-Temperature Sintering	

Cite

Odewole, P. O. (2023). A Sustainable Building Material Developed from Low-Temperature Sintering of Mining Waste with an Alkali-Silicate Solution. *GU J Sci, Part A, 10(2)*, 140-148. doi:10.54287/guj.1245213

Author ID (ORCID Number)	Article Process
0000-0002-0977-2993	<p>Peter Oluwagbenga ODEWOLE</p> <p>Submission Date 31.01.2023</p> <p>Revision Date 20.03.2023</p> <p>Accepted Date 27.03.2023</p> <p>Published Date 09.06.2023</p>

1. INTRODUCTION

Glass-ceramic foams are gaining significant research attention given their exciting properties, including low density, high perviousness, and appropriate moisture absorption (Khamidulina et al., 2017). Glass-ceramic foams are porous materials with many valuable applications as thermal and sound insulators, architectural panels, filters, gas sensors, absorbers, lightweight concrete aggregates, and more (Dragoescu et al., 2018). Unlike polymeric foams such as polystyrene and polyurethane, glass-ceramic foams are nonflammable, non-toxic, and chemically inert; thus, they substitute for polymeric foams as building insulation materials owing to their ability to provide aid in reducing damages during a fire outbreak (Dragoescu et al., 2018). Apart from the unique features of glass-ceramic foams that qualify it as a suitable thermal insulation material in numerous applications, its cost-effectiveness is another area of interest. In this regard, current research efforts on glass-ceramic foams are channeled toward two essential areas: waste valorization and low-cost fabrication routes.

Zhang et al. (2022), Yu (2022), Hujova et al. (2020), Paunescu et al. (2020), Hisham et al. (2021), and Ma et al. (2018), prepared glass-ceramic foams based on industrial wastes showing the possibility of converting wastes into valuable materials at a low cost. Glass-ceramic foam production is commonly based on secondary wastes obtained from manufacturing industries, including waste glass, bottom ash, and fly ash. However, in developing countries with limited industries, using these industrial wastes for glass-ceramic foams' mass production requires much work. For instance, the extensive use of glass cullet is stunted by their insufficient amounts and the variation of the chemical composition (Ivanov, 2018). Given waste glass's inadequate

*Corresponding Author, e-mail: peterodewole@gmail.com

availability, alternative raw materials, such as naturally-sourced minerals for glass-ceramic foam production, are necessary (Sedlačík et al., 2022). Hence, the utilization of primary or naturally sourced industrial wastes such as granite powder, which are abundantly obtainable and suitable for producing glass-ceramic foams, is crucial. Accumulating granite powder as mining waste can cause environmental problems (Arivumangai & Felixkala, 2014). Reducing environmental impact is, therefore, a significant issue for granite industries (Ayodele et al., 2014). This necessitated the use of granite powder in this research.

Different techniques have been used to fabricate porous glass ceramics, including gas foaming, phase separation, sol-gel, and sintering (M. H. Ibrahim et al., 2022). Among other methods, fabricating glass-ceramic by sintering technique is widely used since it is convenient and cheap (M. H. Ibrahim et al., 2022). Foaming by the sintering technique of glass ceramic foam production can be achieved through either two-step sintering or one-step sintering. The two-step method involves double heat treatments. The two-step sintering method of glass-ceramic foam production entails the preparation of base glass material at a higher temperature, followed by foaming at a much lower temperature (Kim et al., 2017).

On the other hand, the one-stage or one-step sintering mechanism of obtaining glass-ceramic foam is achievable without needing a prior heat treatment to prepare the glassy base. If done this way, the crystallization and the foaming procedure are performed in one step. The two-step method effectively controls the glass ceramic foams' pore structure (Chen et al., 2017). However, significant energy input is required for developing a glassy base material, meaning that more substantial venture expenses are involved than in the single-step method (Chen et al., 2017). Merging the two steps into one operation by mixing the raw materials and heating directly to form the foamed material is more economically satisfactory since the glassy phase development and its foaming is carried out in a one-step process (Ivanov, 2018). Therefore, using one-step sintering to synthesize glass-ceramic foam helps reduce production costs (Yuan et al., 2018).

One-step sintering can be classified into two types: (i) indirect one-step sintering and (ii) direct one-step sintering. Indirect one-step sintering involves the using waste glass powder with or without other wastes that are by-products of high-temperature industrial activities or combustion processes, such as fly ash and slag, and with or without foaming agent addition. Mustaffar and Mahmud (2018) prepared glass-ceramic foams from a mixture of waste glass, fly ash, and SiC (foaming agent). Ma et al. (2018) obtained glass-ceramic foam from coal fly ash and calcium carbonate (CaCO_3) sintered at four varying temperatures of 1100°C, 1150°C, 1200°C, and 1250°C. Lardizábal-G et al. (2020) also fabricated glass-ceramic foam from glass waste, 5-15% pumice, and 5% limestone sintered at different temperatures of 700°C, 750°C, 800°C, and 850°C, respectively. Hisham et al. (2021) obtained foam glass-ceramic from waste glass and ark clamshell sintered at temperatures of 700°C, 800°C, and 900°C, respectively. Zhang et al. (2022) developed glass-ceramic foam from a mixture of fly ash, bottom ash, and pickling sludge, with borax (fluxing agent) and CaCO_3 (foaming agent), sintered at 1180°C and annealed at 500°C.

However, direct one-step sintering of glass-ceramic foams involves the using natural inorganic materials such as mining wastes, amorphous silica, or other rock minerals as base glass material with the addition of a foaming agent. Tian et al. (2016) developed thermal insulating foams at 650°C to 1200°C using shale as a glass-former, feldspar (fluxing agent), SiC (foaming agent), and walnut shell (pore-forming or internal combustion agent). Chemical-aided fabrication involves using chemicals (such as NaOH and Na_2SiO_3) to facilitate the one-step sintering of glass-ceramic foams. Previous studies reviewed in this respect are presented as follows. Ivanov (2018) manufactured glass-ceramic foams from diatomite and 40% NaOH solution (foaming agent), constantly heated at 775°C. da Silva et al. (2019) prepared foam glass from glass waste using NaOH as the foaming agent. Owoeye et al. (2020) prepared glass foam from waste glasses using 15wt-% Na_2SiO_3 as the foaming agent. Sedlačík et al. (2022) developed glass-ceramic foams from diatomaceous earth (clay-rich waste) through a hydrate mechanism using 50 wt-% NaOH solution as the foaming agent. J. E. F. M. Ibrahim et al. (2022) fabricated glass-ceramic foams from zeolite-rich clay and sawdust based on alkali activation using 15wt-% NaOH.

To the best of the knowledge of the author of this study through literature review, only Odewole (2022) has used a mix of NaOH and Na_2SiO_3 as a foaming agent. However, Odewole (2022) used an agricultural waste (maize cob) as a pore-forming agent. The novelty of this study is based on evaluating the effect of an alkali-

silicate solution (obtained by mixing NaOH and Na₂SiO₃) on mining waste (granite powder) without adding any carbonaceous or combustible material as a pore-forming agent.

2. MATERIAL AND METHOD

2.1. Sourcing of Starting Raw Materials

Granitic powder, ball clay, sodium silicate (Na₂SiO₃), and caustic soda (NaOH) were used in this study. Dotmond Quarry, Ita-Ogbolu, Ondo State, Nigeria, provided the granite powder used as the primary glassy material. Ire Clay Products Limited, Ire Ekiti, Ekiti State, Nigeria, provided the ball clay used as the binder. Qualikems Fine Chemicals Pvt. Ltd. supplied the sodium silicate (Na₂SiO₃), which contained about 12% Na₂O and 30% SiO₂. May & Baker Ltd., Dagenham, England, supplied the sodium hydroxide (NaOH) pellets with a minimum assay of 98.9%. This study used the mixture of Na₂SiO₃ and NaOH to form an alkaline silicate solution as the pore-forming agent.

2.2. Sample Preparation

The granite powder and ball clay used in this study were screened to pass a 300µm British standard sieve. The granite powder-clay mix prepared by mixing granite powder and ball clay in a ratio of 3:1 served as the starting material for the glassy phase. The addition of ball clay was mainly to serve as a binder since granite powder is a non-plastic material. The Alkali-silicate solution prepared from the mixture of Na₂SiO₃ and 10M NaOH solution in a ratio of 1:1 served as the foaming agent. 10M sodium hydroxide has been found to exhibit desirable effects when used to prepare alkali activators in the production of metakaolin geopolymers (Jaya et al., 2018; Vitola et al., 2020). Three different samples of glass-ceramic foam were formulated by adding 15vol%, 20vol%, and 25vol% of the alkali-silicate solution to 100g of granite powder-clay mix, labeled as samples 1-3. The prepared samples were carefully mixed. The homogenized blend was transferred into steel molds (5 x 5 x 5 cm) and pressed at 10MPa into cubic shapes. The formulated samples were oven-dried at 110°C for 6hr., heat-treated in a gas-fired kiln at 850°C for 3hr., and held for 2hr.

2.3. Materials and Samples' Characterization

X-ray fluorescence analysis done with Skyray Instrument, Model: EDX3600B, to obtain the chemical composition of the granite powder and ball clay used in this study are presented in Table 1. The sintered samples' apparent porosity, bulk density, and water absorption (physical properties) were estimated according to ASTM C20-00 (2022). The samples' compressive strength (mechanical properties) was measured according to ASTM C240-97 (2017) using Instron 3369 universal testing machine. The samples' microstructural properties were investigated using Nikon SMZ745T Stereomicroscope.

Table 1. Chemical composition of granite powder and ball clay

Raw Materials	Constituent (wt%)										
	Al ₂ O ₃	SiO ₂	P ₂ O ₅	SO ₃	K ₂ O	CaO	TiO ₂	Fe ₂ O ₃	SnO ₂	Sb ₂ O ₃	LOI
Granite Powder	12.82	59.72	0.44	0.82	5.74	5.67	0.35	11.29	1.14	1.10	0.91
Ball Clay	21.60	58.15	0.21	0.71	2.30	0.15	1.81	14.40	-	-	0.67

3. RESULTS AND DISCUSSION

3.1. Physical Observation of Samples after Sintering

Different properties were perceived in the glass-ceramic foams' sintered samples. These properties were noted to have been impacted by the varying amounts of the alkali solution added to the granite powder-clay mix to facilitate one-step foaming by sintering. From the physical appearance of the samples, as shown in Figure 1, it was noticed that the foaming of the samples appears to increase with rising amounts of the alkali-silicate solution.



Figure 1. Glass-ceramic foams sintered at 850°C with different amount of alkali-silicate solution; **a)** 15vol%; **b)** 20vol%; **c)** 25vol%

3.2. Physical, Mechanical, and Thermal Properties

Figures 2a, 2b and 2c reveal an increasing trend in the apparent porosity and water absorption and a decline in bulk density of the sintered samples from 1 to 3, respectively, with the rise in the amount of alkali-silicate solution (ASS). Water absorption rose by 98% from 9.5% in sample 1 containing 15vol% ASS to 18.8% in sample 2 containing 20vol% ASS and by 77% from 18.8% in sample 2 to 33.3% in sample 3 containing 25vol% ASS. The apparent porosity increased by 83% from 18.2% in sample 1 to 33.3% in sample 2 and by 70% from 33.3% in sample 2 to 56.7% in sample 3. The bulk density decreased by 68% from 1.91g/cm³ in sample 1 to 1.78 g/cm³ in sample 2 and by 45% from 1.78 g/cm³ in sample 2 to 1.70 g/cm³ in sample 3. This trend could result from the rise in NaOH content resulting from increased ASS added to the glass-ceramic foam samples as the foaming agent. da Silva et al. (2019) observed that increased NaOH content reduced the density of the produced glass-ceramic foam but increased its open (apparent) porosity.

Figure 2d shows that the samples' compressive strength increased by 12% from 20.7 MPa in sample 1 to 23.1 MPa in sample 2 and by 14% from 23.1 MPa in sample 2 to 26.3 MPa in sample 3. The increasing values of compressive strength of the samples were supposed to correspond to increasing bulk density and decreasing porosity, which is generally expected according to Zakaria et al. (2020). However, in this study, there is a contrastive decrease in bulk density with a rise in compressive strength even though there was an increase in apparent porosity. It is noteworthy that a similar occurrence of contrast between compressive strength and bulk density of foam glass was noted by Owwoeye et al. (2020), in which the samples' compressive strength and apparent porosity increased while the bulk density decreased. Although Owwoeye et al. (2020) attributed this compressive strength-bulk density anomaly to the decline in the average pore size coupled with the rise in the quantity of liquid glassy phase attained at increased temperature, it can be observed that temperature is kept constant in this study, while varying the amount of foaming agent. Therefore, the compressive strength-bulk density anomaly observed in the samples could be due to the increasing tendency of the samples to vitrify at 850°C, forming a glassy phase which is accounted for by the rising amount of the alkali-silicate solution used as a foaming agent.

The results of the prepared glass-ceramics foam by Odewole (2022), involving the use of an agricultural waste (maize cob powder) and alkali silicate solution (mixture of Na₂SiO₃ and NaOH) as the pore-forming agent revealed water absorption of 25.6–46.7%, apparent porosity of 43.5–75%, bulk density of 1.45–1.9 g/cm³, and compressive strength of 0.7–9.7 MPa, respectively. On the other hand, the results of this study conducted using an alkali silicate solution (mixture of Na₂SiO₃ and NaOH) only, without the addition of any agricultural waste as a pore-forming agent, showed water absorption of 9.5–33.3%, apparent porosity of 18.2–56.7%, bulk density of 1.7–1.91 g/cm³, and compressive strength of 20.7–26.3 MPa, respectively. Comparing these results, we deduced that glass-ceramic foams of higher compressive strengths were obtained without including any carbonaceous material as a pore-forming agent.

The compressive strengths of all three samples obtained in this study are significantly higher than the 0.8–3.5MPa recommended range for a typical foam glass (Khamidulina et al., 2017) but compare favourably with over 20 MPa of porous concrete obtained by Alemu et al (2021). Nevertheless, sample 3, produced by adding 25 vol% of the alkaline-silicate solution, is considered the optimum sample for this study, given that its

compressive strength is close to 28 MPa, specified as the minimum standard value for concrete (Alemu et al., 2021). Hence, this implies that the glass-ceramic foam obtained in this study can be used in building applications requiring a load-bearing material.

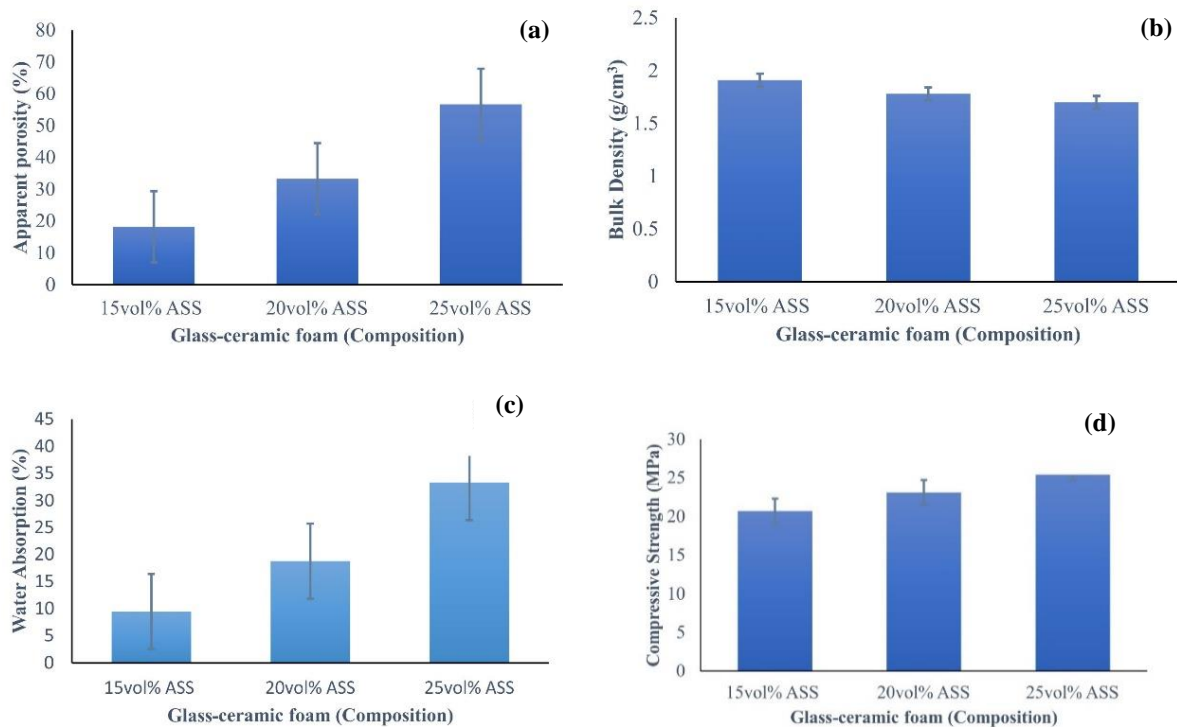


Figure 2. Physical and mechanical properties of the obtained glass-ceramic foam samples; **a)** Apparent porosity; **b)** Bulk density; **c)** Water absorption; **d)** Compressive strength

3.3. Microstructural Properties

The glass ceramic foams' physicochemical properties are substantially influenced by pore morphology (Zhang et al., 2022). In this regard, Figures 3a-c show the microstructural properties of the samples sintered at 850°C. The micrographs reveal varying morphological features of different degrees of agglomeration and porosity. The lighter areas illustrate the densification and aggregation of the samples' grains, showing the solid phase characteristic of glassy materials. The samples were observed to have a non-uniform pore size distribution and an open-celled morphology. The degree of open porosity and the morphology and dimensions of pores generated in glass-ceramic foams are influenced by the quantity of foaming agents introduced. This is supported by a study by Osfouri and Simon (2022), where varying amounts of SiC used as the foaming agent were added to a glass to produce foams with various pore characteristics. The results showed that increasing the volume of foaming agents resulted in higher porosity and larger pore sizes in the resulting foam. This finding is consistent with the research on ceramic foams conducted by Zakaria et al. (2020). Therefore, the amount of foaming agents utilized plays a substantial role in influencing the open porosity and pore characteristics of glass-ceramic foams.

According to Sazegaran and Nezhad (2021), pore morphologies considerably affect the mechanical properties of porous materials. The influence of pore morphology on the compressive strength of foamed materials revealed that their pore shapes had a higher impact on their mechanical properties than the pore size (Parveez et al., 2022). Therefore, the interconnected network of pores in the open-celled morphology and its ability to absorb energy under compressive loading could be responsible for the high compressive strength of the developed samples in this study.

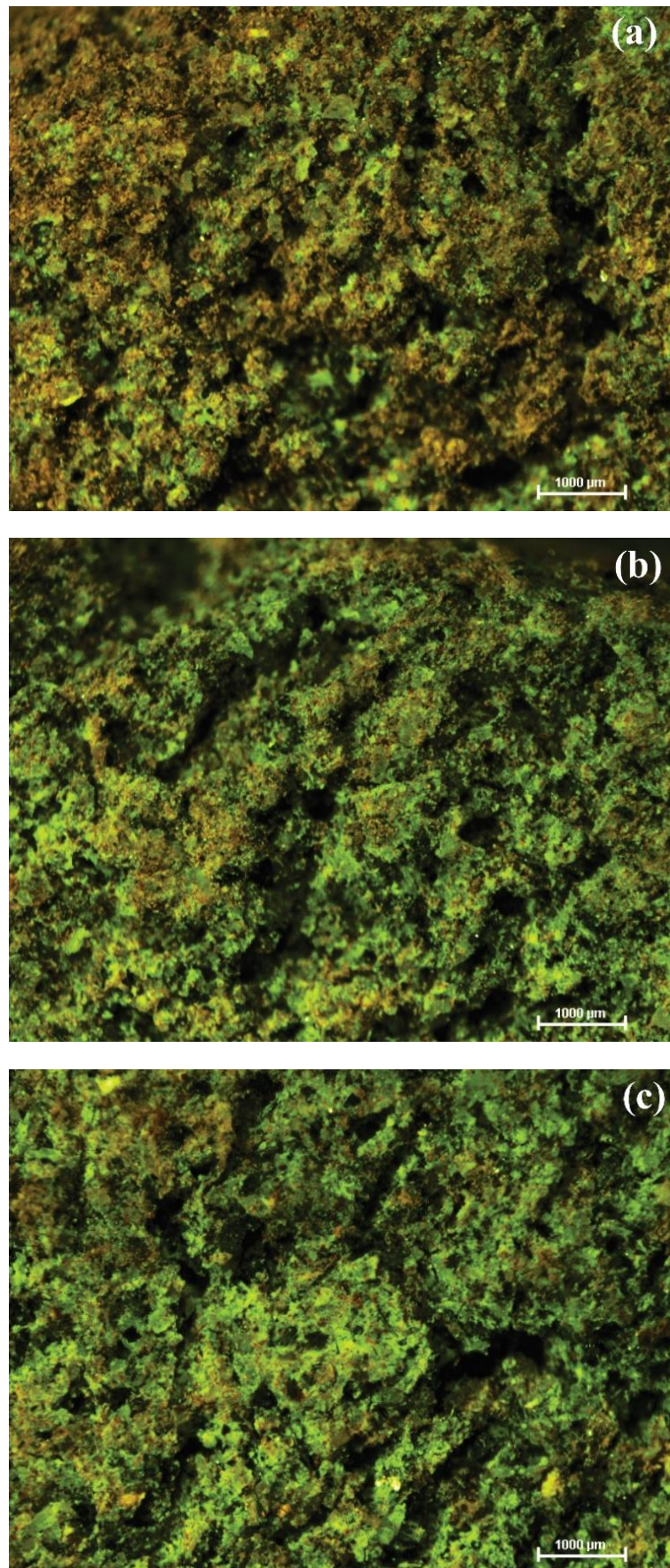


Figure 3. Micrographs of the prepared glass-ceramic foam samples sintered at 850°C with varying quantities of alkali-silicate solution; **a)** 15vol%; **b)** 20vol%; **c)** 25vol% (each at 1000 µm)

4. CONCLUSION

The viability of synthesizing glass-ceramic foams from a granite powder-clay mixture by one-step sintering has been explored in this study. The variation in the performance properties of the developed glass-ceramic foam samples was observed to have been due to the varying amounts of alkali-silicate solution used as the foaming agent. It was observed that with the rise in the foaming agent addition, water absorption increased linearly with apparent porosity values in the obtained glass-ceramic foam samples. In contrast, bulk density decreased linearly with a contrastive rise in the samples' compressive strength, which was traceable to the growing tendencies of the samples to vitrify at 850°C. The result obtained in this study and other pertinent studies showed that chemical reagents could serve as a sintering aid, foaming agent, or both, as the case may be when fabricating glass-ceramic foam from mining wastes, and provides an alternative cost-effective production route. According to Yu (2022), glass-ceramic foams have found practical applications in traditional buildings' thermal insulation. Therefore, the obtained glass-ceramic foam samples in this research can be suitable as a sustainable material in the thermal insulation of buildings. The results of the physicochemical tests conducted on the glass-ceramic foams gotten in this study showed water absorption of 9.5-33.3%, apparent porosity of 18.2-56.7%, bulk density of 1.7-1.91 g/cm³, and compressive strength of 20.7-26.3MPa. Sample 3, produced by adding 25 vol% of the alkaline-silicate solution, is considered the optimum sample for this study, given that its compressive strength is close to 28 MPa, specified as the minimum standard value for concrete, and hence, can be used in building applications requiring a load-bearing material.

ACKNOWLEDGEMENT

The author would like to thank Mr. J.O. Oke of The Federal University of Technology, Akure, Nigeria, for offering technical assistance in the laboratory during the preparation of samples, Dr. O.S. Adelabu of The University of Johannesburg, South Africa, for helping to convey the samples to South Africa, and Dr. M.O. Bodunrin of The University of the Witwatersrand, South Africa for helping to carry out the microstructural analysis on the samples.

CONFLICT OF INTEREST

The author declares no conflict of interest.

REFERENCES

- Alemu, A. S., Yoon, J., Tafesse, M., Seo, Y.-S., Kim, H.-K., & Pyo, S. (2021). Practical considerations of porosity, strength, and acoustic absorption of structural pervious concrete, *Case Studies in Construction Materials*, 15, e00764. doi:[10.1016/j.cscm.2021.e00764](https://doi.org/10.1016/j.cscm.2021.e00764)
- Arivumangai, A., & Felixkala, T. (2014). Strength and durability properties of granite powder concrete. *Journal of Civil Engineering Research*, 4(2A), 1-6. doi:[10.5923.c.jce.201401.01](https://doi.org/10.5923.c.jce.201401.01)
- ASTM C20-00 (2022). *Standard test methods for apparent porosity, water absorption, apparent specific gravity, and bulk density of burned refractory brick and shapes by boiling water*. ASTM International, West Conshohocken, PA. doi:[10.1520/C0020-00R22](https://doi.org/10.1520/C0020-00R22)
- ASTM C240-97 (2017). *Standard test methods of testing cellular glass insulation block*. ASTM International, West Conshohocken, PA. doi:[10.1520/C0240-97](https://doi.org/10.1520/C0240-97)
- Ayodele, O. J., Shittu, O. S., & Balogun, T. (2014). Heavy metal pollution assessment of granite quarrying operations at Ikole-Ekiti, Nigeria. *International Journal of Environmental Monitoring and Analysis*, 2(6), 333-339. doi:[10.11648/j.ijema.20140206.16](https://doi.org/10.11648/j.ijema.20140206.16)
- Chen, C., Feng, K., Zhou, Y., & Zhou, H. (2017). Effect of sintering temperature on the microstructure and properties of foamed glass-ceramics prepared from high-titanium blast furnace slag and waste glass, *International Journal of Minerals, Metallurgy and Materials*. 24(8), 931-936. doi:[10.1007/s12613-017-1480-8](https://doi.org/10.1007/s12613-017-1480-8)
- da Silva, R. C., Kubaski, E. T., & Tebcherani, S. M. (2019). Glass foams produced by glass waste, sodium hydroxide, and borax with several pore structures using factorial design. *International Journal of Applied Ceramic Technology*, 17, 75-83. doi:[10.1111/ijac.13210](https://doi.org/10.1111/ijac.13210)

- Dragoescu, M. F., Paunescu, L., Axinte, S. M., & Fiti, A. (2018). Influence of the color of bottle glass waste on the characteristics of foam glass produced in the microwave field. *International Journal of Science and Engineering Investigations*, 7(72), 95-100.
- Hisham, N. A. N., Zaid, M. H. M., Aziz, S. H. A., & Muhammad, F. D. (2021). Comparison of foam glass-ceramics with different compositions derived from ark clamshell (ACS) and soda lime silica (SLS) glass bottles sintered at various temperatures. *Materials*, 14(3), 570. doi:[10.3390/ma14030570](https://doi.org/10.3390/ma14030570)
- Hujova, M., Monich, P. R., Sedlacek, J., Hnatko, M., Kraxner, J., Galusek, D., & Bernardo, E. (2020). Glass-ceramic foams from alkali-activated vitrified bottom ash and waste glasses. *Applied Sciences*, 10(16), 5714. doi:[10.3390/app10165714](https://doi.org/10.3390/app10165714)
- Ibrahim, M. H., Mustaffar, M. I., Ismail, S. A. & Ismail, A. N. (2022). A review of the porous glass-ceramic production process, properties, and applications. *Journal of Physics: Conference Series*, 2169, 012042. doi:[10.1088/1742-6596/2169/1/012042](https://doi.org/10.1088/1742-6596/2169/1/012042)
- Ibrahim, J. E. F. M., Tihtih, M., Kurovics, E., Gömze, L. A., & Kocserha, I. (2022). Innovative glass-ceramic foams prepared by alkali activation and reactive sintering of clay containing zeolite (zeolite-poor rock) and sawdust for thermal insulation. *Journal of Building Engineering*, 59, 105160. doi:[10.1016/j.job.2022.105160](https://doi.org/10.1016/j.job.2022.105160)
- Ivanov, K. S. (2018). Preparation and properties of foam glass-ceramic from diatomite. *Journal of the Wuhan University of Technology-Mater. Sci. Ed.*, 33, 273-277. doi:[10.1007/s11595-018-1817-8](https://doi.org/10.1007/s11595-018-1817-8)
- Jaya, N. A., Yun-Ming, L., Abdullah, M. M. A., Cheng-Yong, H., & Hussin, K. (2018). Effect of sodium hydroxide molarity on physical, mechanical, and thermal conductivity of metakaolin geopolymer. *IOP Conf. Series: Materials Science and Engineering*, 343, 012015. doi:[10.1088/1757-899X/343/1/012015](https://doi.org/10.1088/1757-899X/343/1/012015)
- Khamidulina, D. D., Nekrasova, S. A., & Voronin, K. M. (2017). Foam glass production from waste glass by compression. *IOP Conf. Series: Materials Science and Engineering*, 262, 012008. doi:[10.1088/1757-899X/262/1/012008](https://doi.org/10.1088/1757-899X/262/1/012008)
- Kim, Y., Sun, C., & Nuguzhinov, Z. (2017). Produce foam glass crystalline insulating material based on anthropogenic raw materials in Kazakhstan according to China's experience. *International Journal of Structural and Civil Engineering Research*, 6(2), 159-163. doi:[10.18178/ijscer.6.2.159-163](https://doi.org/10.18178/ijscer.6.2.159-163)
- Lardizábal-G, D., Estrada-Guel, I., Montes, J. A., Ramirez-Balderrama, K. A., Soto-Figueroa, C., & Santos, R. R. (2020). Synthesis and characterization of low-cost glass-ceramic foams for insulating applications using glass and pumice wastes, *Journal of Applied Research and Technology*, 18(2), 44-50. doi:[10.22201/icat.24486736e.2020.18.2.994](https://doi.org/10.22201/icat.24486736e.2020.18.2.994)
- Ma, Q., Wang, Q., Luo, L., & Fan, C. (2018). Preparation of high-strength and low-cost glass ceramic foams with extremely high coal fly ash content. *IOP Conf. Series: Materials Science and Engineering*, 397, 012071. doi:[10.1088/1757-899X/397/1/012071](https://doi.org/10.1088/1757-899X/397/1/012071)
- Mustaffar, M. I., & Mahmud, M. H. (2018). Processing of highly-porous glass-ceramic from glass and fly ash wastes. *AIP Conference Proceedings*, 2031, 020010. doi:[10.1063/1.5066966](https://doi.org/10.1063/1.5066966)
- Odevole, P. O. (2022). Properties of glass-ceramics foam based on granite dust-clay-maize cob composite as a sustainable building material. *Journal of Sustainable Construction Materials and Technologies*, 7(1), 1-8. doi:[10.14744/jscmt.2022.07](https://doi.org/10.14744/jscmt.2022.07)
- Osfouri, M. & Simon, A. (2022). Study on the thermal conductivity and density of foam glass, *Pollack Periodica*, 18(1), 126-131. doi:[10.1556/606.2022.00591](https://doi.org/10.1556/606.2022.00591)
- Owoeye, S. S., Mathew, G. O., Oviemhanda, F. O., & Tunmilayo, S. O. (2020). Preparation and characterization of foam glass from waste container glasses and water glass for application in thermal insulations. *Ceramic International*, 46(8 Part B), 11770-11775. doi:[10.1016/j.ceramint.2020.01.211](https://doi.org/10.1016/j.ceramint.2020.01.211)
- Parveez, B., Jamal, N. A., Anuar, H., Ahmad, Y., Aabid, A., & Baig, M. (2022). Microstructure and mechanical properties of metal foams fabricated via melt foaming and powder metallurgy technique: A review. *Materials*, 15(15), 5302. doi:[10.3390/ma15155302](https://doi.org/10.3390/ma15155302)

- Paunescu, L., Axinte, S. M., Dragoescu, M. F., & Cosmulescu, F. (2020). Glass-ceramic foams are made of very high coal fly ash weight ratio by the direct microwave heating technique. *Journal La Multiapp*, 1(4), 33-42. doi:[10.37899/journallamultiapp.v1i4.242](https://doi.org/10.37899/journallamultiapp.v1i4.242)
- Sazegaran, H., & Nezhad S. M. M. (2021). Cell morphology, porosity, microstructure and mechanical properties of porous Fe–C–P alloys, *International Journal of Minerals, Metallurgy and Materials*, 28(2), 257-265. doi:[10.1007/s12613-020-1995-2](https://doi.org/10.1007/s12613-020-1995-2)
- Sedlačík, M., Nguyen, M., Opravil, T., & Sokolář, R. (2022). Preparation and Characterization of Glass-Ceramic Foam from Clay-Rich Waste Diatomaceous Earth. *Materials*, 15(4), 1384. doi:[10.3390/ma15041384](https://doi.org/10.3390/ma15041384)
- Tian, Y., Li, S., Xu, C.-W., Li, J.-W., Sun, S.-B., Qi, H., Ma, C.-X., & Cao, M.-P. (2016). Process and properties study of porous thermal insulation building materials based on a walnut shell. *Advances in Engineering Research*, 103, 262-268. doi:[10.2991/icmea-16.2016.43](https://doi.org/10.2991/icmea-16.2016.43)
- Vitola, L., Pundiene, I., Pranckeviciene, J., & Bajare, D. (2020). The impact of the amount of water used in the activation solution and the initial temperature of paste on the rheological behaviour and structural evolution of metakaolin-based geopolymer pastes. *Sustainability*, 12(19) 8216. doi:[10.3390/su12198216](https://doi.org/10.3390/su12198216)
- Yu, Q. (2022). Application of foam glass-ceramic composite thermal insulation material in traditional buildings. *Journal of Chemistry*, 2022, 9662805. doi:[10.1155/2022/9662805](https://doi.org/10.1155/2022/9662805)
- Yuan, H., Wu, H., & Guan, J. (2018). Synthesis of foam glass-ceramic from CRT panel glass using one-step powder sintering. *IOP Conf. Series: Earth and Environmental Science*, 186, 012020. doi:[10.1088/1755-1315/186/2/012020](https://doi.org/10.1088/1755-1315/186/2/012020)
- Zakaria, S. K., Zulkifli, M. L. H., Taib, M. A. A., Budiman, F., Mohamed, M., Ali, A., Yusoff, A. H., & Teo, P. T. (2020). Recycling of wood saw dust waste as green pore forming agent for porous ceramic, *IOP Conf. Series: Earth and Environmental Science*, 596, 012017. doi:[10.1088/1755-1315/596/1/012017](https://doi.org/10.1088/1755-1315/596/1/012017)
- Zhang, J., Zhang, X., Liu, B., Ekberg, C., Zhao, S., & Zhang, S. (2022). Phase evolution and properties of glass ceramic foams prepared by bottom ash, fly ash, and pickling sludge. *International Journal of Minerals, Metallurgy and Materials*, 29(3), 563-573. doi:[10.1007/s12613-020-2219-5](https://doi.org/10.1007/s12613-020-2219-5)



Gazi University

Journal of Science

PART A: ENGINEERING AND INNOVATION

<http://dergipark.org.tr/guj.1247152>

Self-Powered Mechanical Energy Sensor Application of SnO₂/Ag and PMMA/ITO Nanocomposites via Triboelectric Effect

Gizem DURAK YÜZÜAK¹ Mehmet ÇETİN² Ercüment YÜZÜAK^{2*}

¹Munzur University, Rare Earth Elements Application and Research Center, Tunceli, Türkiye

²Recep Tayyip Erdoğan University, Faculty of Engineering and Architecture, Rize, Türkiye

Keywords	Abstract
Triboelectric Nanotechnology Nano-Energy Self-Electric Contact Dedector (SPCS)	The triboelectric nanogenerator is a state-of-the-art device for addressing the growing problem of meeting the world's ever-increasing energy needs by converting mechanical energy into electrical energy. Using the popular semiconductor SnO ₂ nanostructured thin films as a triboelectric layer over contact regions, as opposed to polymers with lesser performance, increases the output power and life time of nanogenerators. In order to design a triboelectric nanogenerator, deposited thin film SnO ₂ is used as a friction layer with Ag electrode after heat-treatment at 623 K with a contrary layer of PMMA poly (methyl-methacrylate) with ITO electrode. The structural and electrical properties were analyzed by using scanning electron microscopy (SEM), electro-impedance spectroscopy (EIS) and atomic force microscopy (AFM) measurements. The increased output power of the triboelectric nanogenerator is attributed to the nanoscale PMMA contact charge created by tunneling electrons in the SnO ₂ /Ag nanocomposite thin film layer. Due to its proximity to the PMMA/ITO surface, the SnO ₂ /Ag layer causes electron field emission, and tapping the SnO ₂ /Ag layer may result in electron cloud overlap. Similar to a semiconductor/insulator interface, the Fermi level of SnO ₂ plays a crucial role in electron transport. The system efficiency stated as a touch detector in a conventional keyboard that generates its own power is revealed in part by an analysis of its operating state up to the 4V.

Cite

Yüzüak, G. D., Çetin, M., & Yüzüak, E. (2023). Self-Powered Mechanical Energy Sensor Application of SnO₂/Ag and PMMA/ITO Nanocomposites Via Triboelectric Effect. *GU J Sci, Part A, 10(2)*, 149-156. doi:10.54287/guj.1247152

Author ID (ORCID Number)	Article Process
0000-0002-2358-8789	Gizem DURAK YÜZÜAK
0000-0001-6422-4634	Mehmet ÇETİN
0000-0002-2521-9362	Ercüment YÜZÜAK
	Submission Date 03.02.2023
	Revision Date 27.03.2023
	Accepted Date 03.04.2023
	Published Date 12.06.2023

1. INTRODUCTION

Scientists have been conducting a variety of studies for years in an effort to find a solution to the world's energy dilemma by uncovering new forms of energy. One of the current issues in renewable and clean-energy generation is the development of new methods that can compare various energy sources. Artificial forces, including wind and rain (also known as variable forces), or other forces resulting from human activities have the characteristics of being waste and may be recovered to provide electricity (Xia et al., 2019). The triboelectric effect (TEE) is a natural phenomenon that facilitates the design of simple and cheap devices for transforming mechanical energy into electrical power (Wang, 2020). Through the frictional charging method, mechanical energy may be converted into electrical power, allowing for the operation of tiny electronic devices within the context of a low-cost, straightforward, and efficient strategy via the triboelectric nanogenerator (TENG). A surface charge is generated at the interface between two dissimilar dielectrics. As the separation between the two dielectrics grows, so does the rate at which electrons may move from one electrode to the other. Originally, TENGs have had electrodes connected to both the above and bottom sides of two dissimilar layers that face each other (Wang, 2020). The triboelectric effect is its primary mechanism for accomplishing this purpose. On the basis of this working feature, TENGs are used

*Corresponding Author, e-mail: ercument.yuzuak@erdogan.edu.tr

as: a) mechanical energy harvesting structure from the vibration source as a form of mechanical energy capture devices (Chen & Wang, 2017), b) self-powered sensors (Tasneem et al., 2022), c) wave energy harvesters (Liang et al., 2023), d) biomechanical energy harvesters acting as power sources for other electronic devices (Babu et al., 2022).

The rapid advancement and increasing popularity of portable and handheld chemical or biosensors in recent decades has posed a scientific issue for their sustained energizing. Therefore, mechanical energy harvesters have lately been investigated, either as detectors or threshers to retain charge in compact, long-lasting energy-storage devices to power the detectors (Khandelwal & Dahiya, 2022; Zheng et al., 2022). Examples of such harvesters include piezoelectric and triboelectric generators (TEGs). With such multifunctional actions, fewer instruments are required in a system, which allows to address the technical challenges; this is especially intriguing when it comes to the usage of energy harvesters as detectors. While evidence of the triboelectric effect dates to antiquity, the precise mechanism by which it works remains a matter of intense debate. Many different processes, including electron transfer, ion transfer, bond dissociation, chemical change, and material transfer, may be at play depending on the specific material and ambient conditions (Wang & Wang 2019; Wang, 2015). Triboelectric nanogenerators (TENGs) are electrical circuit-forming devices made from the coupling of layers with dissimilar properties by the use of complementary conductors (Zhu et al., 2015). Given their low cost and ease of manufacture, polymers can be found in almost every modern technological device. These structures are often used in triboelectric systems; however, they are readily distorted after prolonged usage. However, semiconductor thin films provide an alternative to polymers because of their extended service lives, resistance to harsh environments, and ability to be created with a surface roughness on the nanoscale, depending on the application (Yüzüak et al., 2022). While applied to the structure, mechanical deformation occurs when creating parallel but opposing loads on the surfaces. Depending on the instantaneous potential shift, the supplied electron flow facilitates the creation of power that is needed by tiny electronic devices. Nanogenerators are a promising new technology for addressing the growing challenge of meeting the world's ever-increasing energy needs. Increasing the surface charge density is important to boost the triboelectric effect's effectiveness (Wang & Wang, 2019). This may be achieved by adjusting the micro- and nanostructures as well as the effective contact surface area. For example, several research projects have sought to produce polymer surfaces as electrodes in TENGs. Although polymers are simple to be manufactured, they fall short in performance because of how quickly they distort under stress. The most crucial factor in improving TENG's efficiency is ensuring long-term performance and switching to electrode materials with a higher rate of electron loss compared to polymers. Compared to TiO_2 or ZnO , the n-type semiconductor SnO_2 is an attractive option because of its carrier mobility ($100\text{-}200\text{ cm}^2/\text{V}\cdot\text{s}$) (Breckenridge & Hosler, 1953) and broad band gap (3.62 eV), both of which point to a more rapid transit of photo-generated electrons and better long-term electron stability (Gao et al., 2014). In addition, when other materials, such as TiO_2 or ZnO , are used, a surface dipole layer is formed toward SnO_2 due to its low net charge and positive charge transfer boundary (G. Yang et al., 2012).

The research conducted by the reference (N. H. Lee et al., 2017) is one of the most impressive outcomes found for this semiconductor in the published paper. Based on the research presented in the paper, a semiconductor SnO_2 triboelectric layer may be created by placing an Al-coated electrode on a Pt substrate. After determining that this was not enough, the researchers attempted to cover the electrode's AlO_2 substrate to boost its efficiency. But there are difficulties in the manufacturing procedure. The electrodes made using ALD required an additional annealing step since the first heating and cooling cycles did not result in the expected crystallization. The result is a delay in the manufacturing process. Pt coating is an extra and very costly feature. When they realized there was a glitch in the experiment, they added Al_2O_3 beneath the SnO_2 to boost its conductivity. A similar Al electrode was utilized. The resulting thin films have a thickness of 5-25 nm. The results of this analysis reveal: a voltage of 125 V, a current density of $2.75\text{ A}/\text{cm}^2$, and a power density of $0.344\% \text{ mW}/\text{cm}^2$. Other research has shown that heating SnO_2 films to temperatures between 773 K and 1073 K results in a tetragonal structure (Terrier et al., 1997). It was found that the thin film with the substrate was heated to 473 K, and SnO_2 films developed in a tetragonal crystal structure (Wang, 2013). The tetragonal structure is known to have a greater charge density all around the density of state in the vicinity of Fermi energy.

In the present work, thin films with semiconductor features will be used as a triboelectric layer on the friction surface, with the expectation that this will improve efficiency. It is hypothesized that the created TENG will profit more from using a SnO₂ layer, as semiconductors have the property of delivering long-term performance and losing electrons quicker than polymers. For this aim,

- The Ag electrode and SnO₂ thin films generated on the Si(100) substrate using the magnetron sputtering technique and,
- The PMMA/ITO structure is what will be used to create the secondary electrode component

was used to form of the TENG. After doing characterizations to the friction layer, the potential changes in the electrical output power of the TENGs will be explored, by using a contact sensor in a commercial computer keyboard that generates its own energy and has been proven to have this efficiency.

2. MATERIAL AND METHOD

Conventional RF and DC magnetron co-sputtering were used to deposit SnO₂ and Ag layers onto Si(100) substrates. For the sputtering process, a SnO₂ target (99.999%) with dimensions of 2 inches in diameter and 0.250 inches in thickness was used in a high-vacuum chamber with a pressure of more than 2×10^{-6} Torr. Argon and oxygen inert gases (6N) were used at a working pressure of 5 mTorr. To keep the film consistent throughout its thickness, we rotated the substrate at 12 rpm as it was growing up. SnO₂ films' high-temperature crystal phase effect on Ag buffer via 673 K heat-treatment was investigated by scanning electron microscopy (SEM) with energy dispersive X-ray (EDX), atomic force microscopy (AFM), and electro-impedance spectroscopy measurements (EIS) for structural and electrical characterizations.

TENG is formed by combining these two different parts of electrodes with electrical connections (Figure 1a) and its working mechanism representation in contact separation mode (Figure 1b). The potential changes in the contact density of the semiconductor thin film and the electrical output power of TENG will be examined due to the different physical properties and different surface roughness of the SnO₂ thin films used in the produced TENGs. For better performance, the SnO₂ thin films are heat-treated at 673 K. For the purpose of applying consistent external forces, we used an analogue oscilloscope to coordinate the timing of the pushing motion and a force indicator to regulate the pushing forces themselves. As the second friction electrode, PMMA/ITO film was considered because of its strong negative force, simplicity of production, and basic approach. The effective surface area of TENGs was about 0.32 cm². No fluctuations were found, and; all readings were taken under constant circumstances. We used a four-channel digital storage oscilloscope and a DC 24 V, 10-100 rpm mechanic motor coupled to a linear gear to measure the resulting electrical output. As a result of connecting the oscilloscope's two terminals, the open circuit voltage (V_{OC}) was calculated over ITO and Ag electrodes. All measurements of electrical performance were carried out at room temperature with a relative humidity of 55% RH. The holding cell for EIS measurements was protected by a grounded shield.

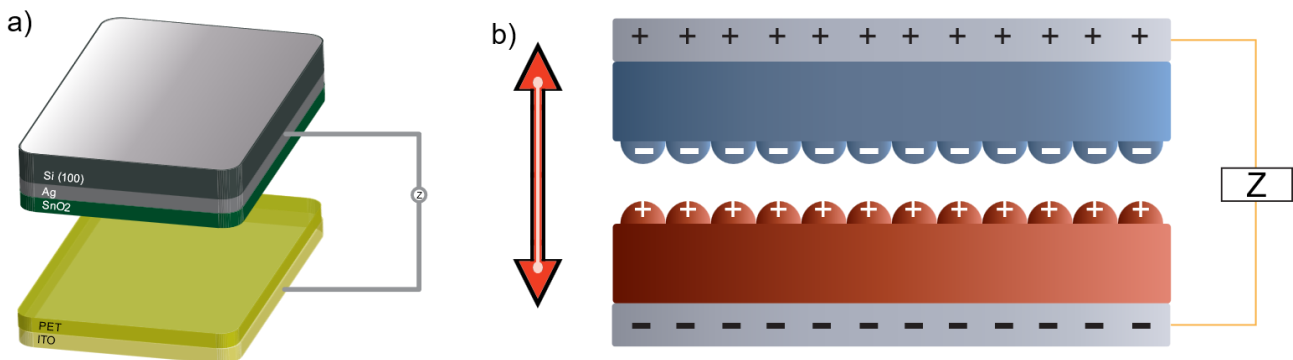


Figure 1. a) Layers in TENG in the present study and b) its working mechanism representation on contact separation mode

3. RESULTS AND DISCUSSION

SEM pictures of the surface morphology of the untreated and 673 K SnO₂ thin films are shown in Figures 2a and 2b in a systematic manner. Based on electron microscopy micrographs as seen in Figure 2a and 2b, it was found that heat treatment altered the surface morphology irreversibly. Tiny grains make up the unprocessed sample. There are agglomerates formed when grains are linked together. The surface morphology of SnO₂ film is unaltered by annealing to 673 K, and it has the same film-like appearance. From the result obtained, it is seen in Figure 2a that the untreated thin film produced at 50 Watt of sputtering power and 5 mTorr of sputtering pressure with a thickness of 200 nm is homogeneously deposited on the surface and has a spherical particle structure. A heat treatment at 673 K was found to have no effect on the particle size of the thin film compared to its pre-heat-treatment enlargement condition.

On the surface of the thin film, however, aggregation was shown to have risen. The SnO₂ films that were formed at high temperatures were discovered to have cracks as well as macroscopic flaws, as it was reported in the research that was published (Turan et al., 2022). It was observed to be free from macroscopic defects. Coating islands might originate from the unwinding of tensile stress on the film coat or from the removal and ignition of phase transition after continuous heat treatment (Zakaria et al., 2022). Using the EDX, we were able to determine the chemical content and purity of SnO₂ thin films that had been formed at room temperature. According to the EDX results, within the experimental error, the atomic percentage of elements Sn and O in the SnO₂ thin film formed was found to be in close agreement with the nominal stoichiometry.

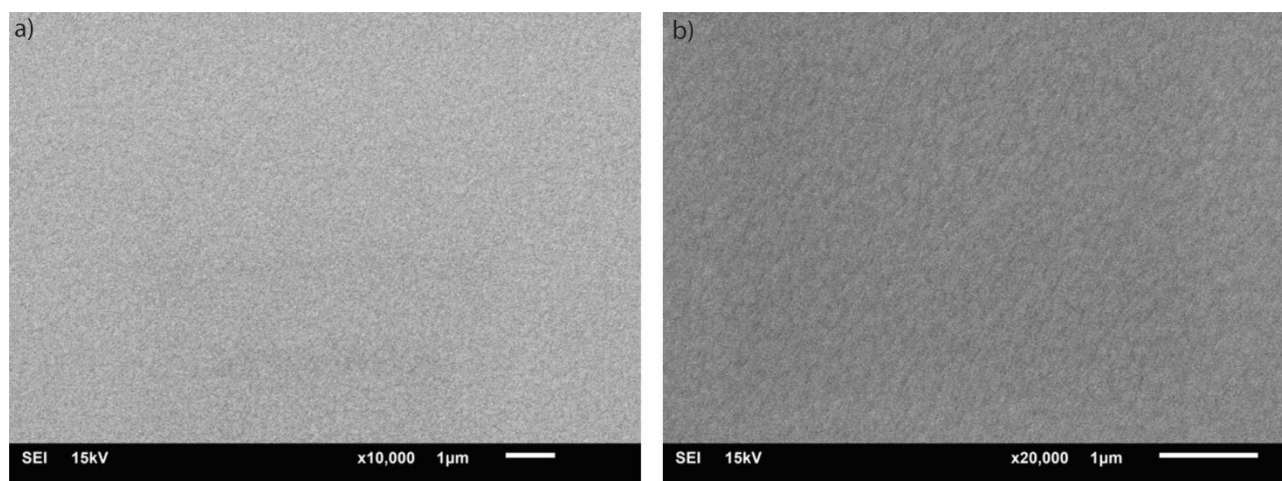


Figure 2. SEM micrographs of **a)** untreated and **b)** 673 K thin films

EIS was used to evaluate the electrochemical characteristics of thin films. Figures 3a and 3b depict, in the range of 1V–2.2V bias voltages, the frequency-dependent real (Z_1 , Z') and imaginary (Z_2 , Z'') impedance part plots (Nyquist plots) of the as-deposited SnO₂ and 673 K thin films. EIS spectrum analyzer was used to model the electrochemical impedance behavior by means of the corresponding electrical circuit (inset of Figure 3a) (Bondarenko & Ragoisha, 2005). The resistance of the solution and all its associated contacts made up "R_s" in the circuit, whereas "R_p" represented the charge transfer resistance. A material's electrical properties can be seen in the form of semicircular arcs. The illustration clearly depicts a single semicircle, but another study observed two semicircles in SnO₂ film (Chandra Bose et al., 2005). Understanding the mechanism and processes of electron transport can be aided by the EIS (Ouyang et al., 2014). Plots show that the hopping phenomenon in semiconductors causes the real part (Z') impedance to rise with decreasing frequency. Accumulated charge carriers at the grain boundaries have enough energy to hop the barrier at low frequencies, which is great for operating at the TENGs' intrinsically low oscillation frequency. This circumstance is reminiscent of one's seen in earlier research, and the dissipation rate of conductivity is measured in terms of its "hopping frequency" (Shen et al., 2018). The actual component of the complex impedance, as measured by comparing two plots, decreases with increasing frequency, a trend that correlates with the particles' grain boundaries. The whole thin film frequency changes upward as particle size grows.

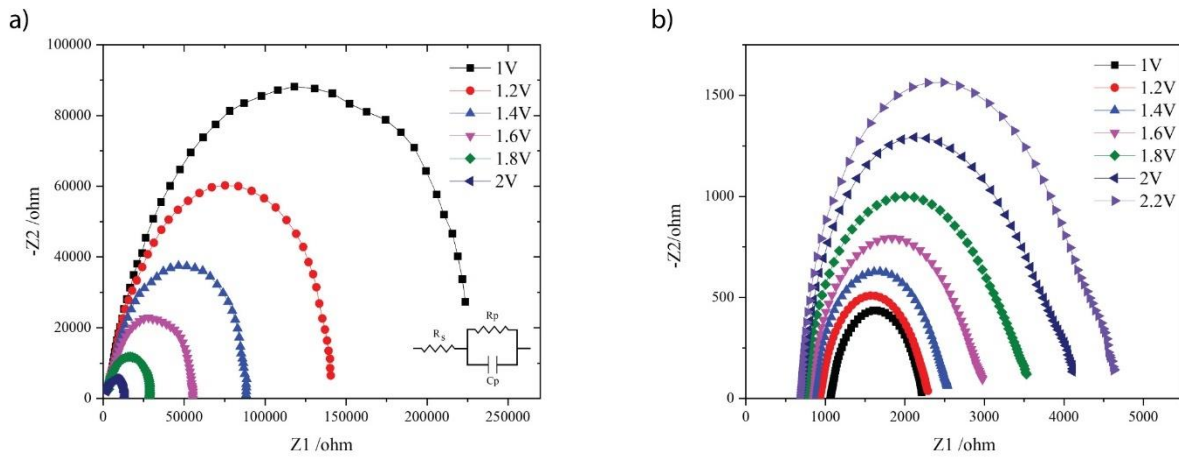


Figure 3. EIS measurements of **a)** untreated and **b)** 673 K thin films

Atomic force microscopy, used in non-contact mode, was employed to examine the SnO₂ film's surface topography. Here, the probe cantilever's frequency is oscillated very close to its natural resonance. Figures 4a, 4b, 4c and 4d, 4e, 4f reveal AFM images and line height analysis of untreated and 673 K treated thin films, respectively. AFM images (2D and 3D) were produced, which also bolstered the surface roughness investigations that were performed subsequently. These AFM images demonstrated that post-heat treatment surface roughness was much higher. The results are generally consistent with those of earlier investigations, with some small variations (Muthukrishnan et al., 2022). It is believed to be the result of microscopic and nanoscale flaws in the crystal structure produced between the semiconductor and conductive layers. The images clearly show that the surface morphology of the 100 nm thin film comprises spherical particles. This can be noticed when looking at the images. It can be noted that the findings obtained are consistent with those acquired using SEM.

The linear facial profile measurements acquired with the AFM were also very helpful. Figures 4b and 4e illustrate the results before and after heat treatment, respectively. It appears to have had a dramatic change in its development between before and after heat treatment, as measured by the depth of its surface, as shown by these numbers. According to this, the depths were shallow (-9 μm to 7 μm) before the heat treatment but grew significantly (-15 μm to 11 μm) thereafter. We can attribute this to the fact that Sn and O₂ ratios have levelled out on a regional scale (J. R. Lee et al., 2007). The surface roughness plots generated have about the value of 1.7 nm and 5.2 nm as its average value for untreated and 673 K, respectively. This result is consistent with the literature that we have reviewed, which supports our results (Y. Yang et al., 2022). The topographical image may be used to produce a 3D image, which can then be used to study the particles' distribution, which can be seen to be uniform.

In terms of applicability, we implemented TENG in a traditional keyboard designed for usage on desktop computers in the office. Using double-sided conductive silver tape, the SnO₂/Ag - PMMA/ITO film composite developed in this work was attached to the secured beneath the "Enter" key of a commercial keyboard. The findings for the scenario with the help of a digital oscilloscope are shown in Figure 5a. With the use of the enter key and a raised hand, we were able to get an output voltage of up to 2 V. The continuous pressing and releasing action, on the other hand, results in a maximum of 4 V but exhibits some discontinuity, as seen in Figure 5b. Pulses obtained at low frequencies were much more stable than those obtained by increasing the key press speed. This situation can be considered an output of triboelectric technology, which is both reactive and a function of frequency. The variance in force used to push the enter key is regarded as the primary cause of this break in continuity. So, it is safe to assume that the next generation of sensing and self-powered smart keycap technology will be ushered in by the logical processing of these electrical pulses.

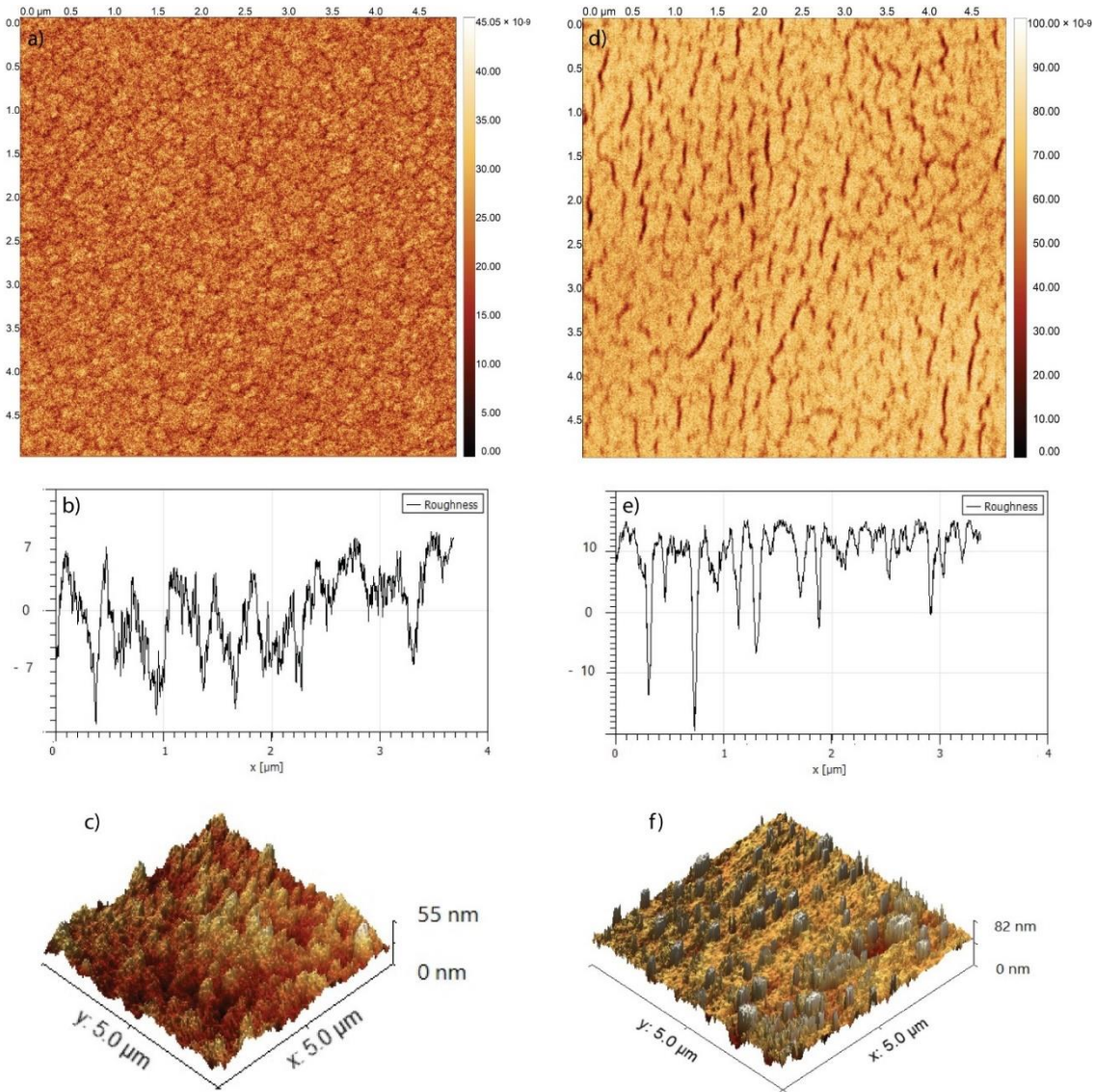


Figure 4. 2D, line profiles and 3D AFM measurements of a), b), c) untreated and d), e), f) 673 K thin films, respectively

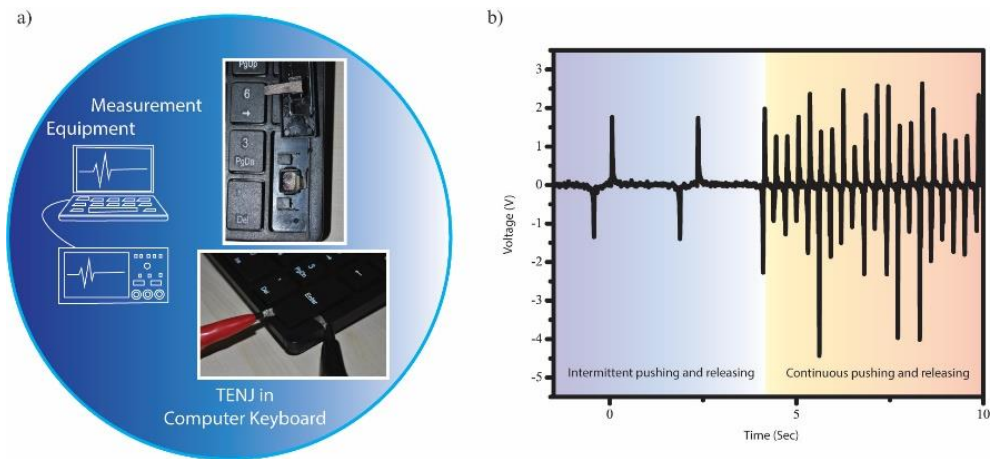


Figure 5. a) Triboelectric nanogenerator and measuring mechanism mounted on the mechanical keyboard, b) electrical voltage measurement graphs obtained with this mechanism in periods I (intermittent pressing and releasing) and II (continuous pressing and releasing)

4. CONCLUSION

Triboelectric systems are newly presented renewable and clean energy sources worldwide. The discovery of new systems with triboelectric properties and the use of these systems in electricity generation technology are of great importance, both technologically and in terms of existing science and literature. In this study, the improvement was achieved only by the deposition of SnO₂ thin films with an Ag buffer layer on the Si (100) substrate, without any sublayer or electrical poling. In order to make the work visible and applicable, the keyboard application was tried as a prototype of a physical application of this. It is apparent that the use of semiconductors in this kind of application area will lead to a rise in the number of places where they are put to be used. Therefore, the study presented here will provide a novel outlook on boosting triboelectric effect features.

ACKNOWLEDGEMENT

This work was supported by the Scientific and Technological Research Council of Turkey (TÜBİTAK) under the grant number of 119M972. The research for the present work was carried out by the Functional Materials Research Group (FMRG) at Recep Tayyip Erdogan University. Some parts of the study were presented at the 9th International Conference on Materials Science and Nanotechnology for Next Generation (MSNG-2022).

CONFLICT OF INTEREST

The authors declare no conflict of interest.

REFERENCES

- Babu, A., Rakesh, D. Supraja, P., Mishra, S., Kumar, K. U., Kumar, R. R., Haranath, D., Mamidala, E., & Nagapuri, R. (2022). Plant-based triboelectric nanogenerator for biomechanical energy harvesting. *Results in Surfaces and Interfaces*, 8, 100075. doi:[10.1016/j.rsurfi.2022.100075](https://doi.org/10.1016/j.rsurfi.2022.100075)
- Breckenridge, R. G., & Hosler, W. R. (1953). Electrical properties of titanium dioxide semiconductors. *Physical Review*, 91(4), 793-802. doi:[10.1103/PhysRev.91.793](https://doi.org/10.1103/PhysRev.91.793)
- Bondarenko, A. S., & Ragoisha, G. A. (2005). EIS Spectrum Analyser. In: Pomerantsev A. L. (Eds.), *Progress in Chemometrics Research* (pp. 89-102). Nova Science Publishers: New York. [URL](#)
- Chandra Bose, A., Thangadurai, P., Ramasamy, S., & Purniah, B. (2005). Impedance spectroscopy and DSC studies on nanostructured SnO₂. *Vacuum*, 77(3), 293-300. doi:[10.1016/j.vacuum.2004.10.007](https://doi.org/10.1016/j.vacuum.2004.10.007)
- Chen, J., & Wang, Z. L. (2017). Reviving Vibration Energy Harvesting and Self-Powered Sensing by a Triboelectric Nanogenerator. *Joule*, 1(3), 480-521. doi:[10.1016/j.joule.2017.09.004](https://doi.org/10.1016/j.joule.2017.09.004)
- Gao, C., Li, X., Zhu, X., Chen, L., Zhang, Z., Wang, Y., Zhang, Z., Duan, H., & Xie, E. (2014). Branched hierarchical photoanode of titanium dioxide nanoneedles on tin dioxide nanofiber network for high performance dye-sensitized solar cells. *Journal of Power Sources*, 264, 15-21. doi:[10.1016/j.jpowsour.2014.04.059](https://doi.org/10.1016/j.jpowsour.2014.04.059)
- Khandelwal, G., & Dahiya R. (2022). Self-powered active sensing based on triboelectric generator, *Advanced Materials*, 34(33), 2200724. doi:[10.1002/adma.202200724](https://doi.org/10.1002/adma.202200724)
- Lee, N. H., Yoon, S. Y., Kim, D. H., Kim, S. K., & Choi, B. J. (2017). Triboelectric Charge Generation by Semiconducting SnO₂ Film Grown by Atomic Layer Deposition. *Electronic Materials Letters*, 13(4), 318-323. doi:[10.1007/s13391-017-6289-0](https://doi.org/10.1007/s13391-017-6289-0)
- Lee, J. R., Kim, D. G., Lee, G. H., Park, Y. H., & Song, P. K. (2007). Characteristics of IZSO films deposited by a co-sputtering system. *Metals and Materials International*, 13(5), 399-402. doi:[10.1007/BF03027875](https://doi.org/10.1007/BF03027875)

- Liang, X., Liu, S., Yang, H., & Jiang, T. (2023). Triboelectric Nanogenerators for Ocean Wave Energy Harvesting: Unit Integration and Network Construction. *Electronics*, 12(1), 225. doi:[10.3390/electronics12010225](https://doi.org/10.3390/electronics12010225)
- Muthukrishnan, A. P., Lee, J., Kim, J., Kim, C. S., & Jo, S., (2022). Low-temperature solution-processed SnO₂ electron transport layer modified by oxygen plasma for planar perovskite solar cells. *RSC Advances*, 12(8), 4883-4890. doi:[10.1039/D1RA08946C](https://doi.org/10.1039/D1RA08946C)
- Shen, W., Ou, T., Wang, J., Qin, T., Zhang, G., Zhang, X., Han, Y., Ma, Y., & Gao, C. (2018). Effects of high pressure on the electrical resistivity and dielectric properties of nanocrystalline SnO₂. *Scientific Reports*, 8, 5086. doi:[10.1038/s41598-018-22965-8](https://doi.org/10.1038/s41598-018-22965-8)
- Tasneem, N. T., Biswas, D. K., Adhikari, P. R., Gunti, A., Patwary, A. B., Reid, R. C., & Mahbub, I. (2022). A self-powered wireless motion sensor based on a high-surface area reverse electrowetting-on-dielectric energy harvester. *Scientific Reports*, 12, 3782. doi:[10.1038/s41598-022-07631-4](https://doi.org/10.1038/s41598-022-07631-4)
- Terrier, C., Chatelon, J. P., & Roger, J. A. (1997). Electrical and optical properties of Sb:SnO₂ thin films obtained by the sol-gel method. *Thin Solid Films*, 295(1-2), 95-100. doi:[10.1016/S0040-6090\(96\)09324-8](https://doi.org/10.1016/S0040-6090(96)09324-8)
- Turan, E., Kul, M., & Akin, S. (2022). Structural and optical investigation of spray-deposited SnO₂ thin films. *Journal of Materials Science: Materials in Electronics*, 33(19), 15689-15703. doi:[10.1007/s10854-022-08472-7](https://doi.org/10.1007/s10854-022-08472-7)
- Ouyang, P., Zhang, H., Wang, Y., Chen, W., & Li, Z. (2014). Electrochemical & microstructural investigations of magnetron sputtered nanostructured ATO thin films for application in Li-ion battery. *Electrochimica Acta*, 130, 232-238. doi:[10.1016/j.electacta.2014.03.021](https://doi.org/10.1016/j.electacta.2014.03.021)
- Wang, Z. L. (2013). Triboelectric Nanogenerators as New Energy Technology for Self-Powered Systems and as Active Mechanical and Chemical Sensors. *ACS Nano*, 7(11), 9533-9557. doi:[10.1021/nn404614z](https://doi.org/10.1021/nn404614z)
- Wang, Z. L. (2015). Triboelectric nanogenerators as new energy technology and self-powered sensors-Principles, problems and perspectives. *Faraday Discussions*, 176, 447-458. doi:[10.1039/C4FD00159A](https://doi.org/10.1039/C4FD00159A)
- Wang, Z. L. (2020). On the first principle theory of nanogenerators from Maxwell's equations. *Nano Energy*, 68, 104272. doi:[10.1016/j.nanoen.2019.104272](https://doi.org/10.1016/j.nanoen.2019.104272)
- Wang, Z. L., & Wang, A. C. (2019). On the origin of contact-electrification. *Materials Today*, 30, 34-51. doi:[10.1016/j.mattod.2019.05.016](https://doi.org/10.1016/j.mattod.2019.05.016)
- Xia, X., Fu, J., & Zi, Y. (2019). A universal standardized method for output capability assessment of nanogenerators. *Nature Communications*, 10, 4428. doi:[10.1038/s41467-019-12465-2](https://doi.org/10.1038/s41467-019-12465-2)
- Yang, G., Yan, Z., & Xiao, T. (2012). Preparation and characterization of SnO₂/ZnO/TiO₂ composite semiconductor with enhanced photocatalytic activity. *Applied Surface Science*, 258(22), 8704-8712. doi:[10.1016/j.apsusc.2012.05.078](https://doi.org/10.1016/j.apsusc.2012.05.078)
- Yang, Y., Maeng, B., Jung, D. G., Lee, J., Kim, Y., Kwon, J., An, H. K., & Jung, D. (2022). Annealing Effects on SnO₂ Thin Film for H₂ Gas Sensing. *Nanomaterials*, 12(18), 3227. doi:[10.3390/nano12183227](https://doi.org/10.3390/nano12183227)
- Yüzüak, D. G., Karagöz, C., & Yüzüak, E. (2022). Exploring the Sputtering Conditions in ZnO Thin Film for Triboelectric Nanogenerator Electrode. *International Journal of Energy Research*, 46(14), 20494-20500. doi:[10.1002/er.7777](https://doi.org/10.1002/er.7777)
- Zakaria, Y., Aïssa, B., Fix, T., Ahzi, S., Samara, A., Mansour, S., & Slaoui, A. (2022). Study of wide bandgap SnOx thin films grown by a reactive magnetron sputtering via a two-step method. *Scientific Reports*, 12(1), 15294. doi:[10.1038/s41598-022-19270-w](https://doi.org/10.1038/s41598-022-19270-w)
- Zheng, Y., Liu, T., Wu, J., Xu, T., Wang, X., Han, X., Cui, H., Xu, X., Pan, C., & Li, X. (2022). Energy conversion analysis of multi-layered triboelectric nanogenerators for synergistic rain and solar energy harvesting. *Advanced Materials*, 34(28), 2202238. doi:[10.1002/adma.202202238](https://doi.org/10.1002/adma.202202238)
- Zhu, G., Peng, B., Chen, J., Jing, Q., & Wang, Z. L. (2015). Triboelectric nanogenerators as a new energy technology: From fundamentals, devices, to applications. *Nano Energy*, 14, 126-138. doi:[10.1016/j.nanoen.2014.11.050](https://doi.org/10.1016/j.nanoen.2014.11.050)



Gazi University

Journal of Science

PART A: ENGINEERING AND INNOVATION

<http://dergipark.org.tr/guj.1259370>

Investigation of Mechanical Properties of Aluminum 7075 Alloy via Surface Engineering

Gözde ALTUNTAŞ^{1*} Gamze YAZBAHAR² Bülent BOSTAN¹¹Gazi University, Faculty of Technology, Department of Metallurgical and Materials Engineering, Ankara, Türkiye²Gazi University, Institute of Science and Technology, Ankara, Türkiye

Keywords	Abstract
Micro Arc Oxidation (MAO)	In this study, MAO process, which is one of the surface coating methods, was applied to 7075-T6 Al alloy in a thin thickness and the relationship between its mechanical properties compared to its uncoated state was investigated. Surface microstructure images of the prepared samples, coating thickness from the cross section and eds analysis were measured by scanning electron microscope (SEM). With the XRD analysis, the peaks in the material on which the coating is made were determined and the difference was examined according to the uncoated state. How the coating affects the dislocation density was investigated. The microhardness value of the samples, which were coated with 2 µm MAO from the surface, was measured according to HV 0.5. The hardness value was thus increased by 50%. The weight loss of coated and uncoated materials was calculated. Despite such a thin coating, the wear resistance has increased approximately 8 times compared to the uncoated state.
7075 Al alloy	
Wear	
Dislocation Density	

Cite

Altuntaş, G., Yazbahar, G., & Bostan, B. (2023). Investigation of Mechanical Properties of Aluminum 7075 Alloy via Surface Engineering. *GU J Sci, Part A, 10(2)*, 157-165. doi:10.54287/guj.1259370

Author ID (ORCID Number)	Article Process
0000-0003-4504-0850	Submission Date 02.03.2023
0000-0002-4085-4786	Revision Date 27.03.2023
0000-0002-6114-875X	Accepted Date 03.04.2023
	Published Date 15.06.2023

1. INTRODUCTION

Aluminum alloys are widely used in areas such as aviation and space due to their high strength and low density properties (G. Altuntaş et al., 2021). It is also a material group that can compete with steels (O. Altuntaş & Güral, 2015). 7075, an aluminum alloy, is extensively used due to its high strength (O. Altuntaş, 2022). The naturally occurring aluminum oxide film on the surface of the aluminum alloy cannot protect the matrix for a long time (Li et al., 2019).

It is known that some coatings applied to aluminum alloy are effective in improving hardness, corrosion and wear. One of these methods, MAO, is an electrochemical plasma treatment that creates oxide ceramic coatings on light metals (Dean et al., 2015). The MAO process is also referred to by many names in the literature, such as spark anodic oxidation, micro plasma oxidation or plasma electrolytic oxidation. In this process, there is an electrolytic cell, the metal to be oxidized in the anode part, a metal such as stainless steel in the cathode part, a suitable solution that provides ion transport and oxidation, and a cooling system with a power source. The passive oxide layer is broken with the applied high voltage and a much thicker oxide layer is obtained at very high voltage values. For example, when aluminum is exposed to micro arc oxidation, oxides such as α and γ alumina can be formed. According to traditional anodic oxidation, MAO is more reliable and does not contain heavy metal elements (Baxi et al., 2008). Ceramic coatings produced with MAO coating exhibit good adhesion to the substrate, high wear resistance and corrosion resistance (Yilmaz et al., 2021). Characteristics of ceramic coatings are mainly affected by the factors with electrolyte composition and current density (Sundararajan & Krishna, 2003). It is also known that the microhardness of micro arc films decreases with increasing depth

*Corresponding Author, e-mail: gozdealtuntas@gazi.edu.tr

from the interface to the coating surface (Qi et al., 2022). The performance of micro arc coatings depends on their chemical structure, composition and porosity. To improve the properties of micro-arc coatings, the mechanism of micro-discharge formation during micro-arc operation should be known (Song & Shi, 2014). Various organic compounds and other special chemical additives are used during MAO coatings by modifying the electrolyte solution to impart the desired qualities, especially better corrosion resistance (Zhang et al., 2023). Considering the high performance of the MAO coating, this process still has great potential application and therefore many researchers are making significant efforts to reduce or close the micropores to further improve the corrosion resistance it offers. (Shen et al., 2023). In a study that applied MAO to 7075 aluminum alloy; All samples treated with MAO showed better corrosion and wear resistance compared to the substrate.

In this study, the effect of MAO on the mechanical properties of Al 7075-T6 alloy was investigated in a very thin thickness. With the thin coating, the cost was reduced and the hardness value increased by approximately 50%. The abrasion resistance of the coated sample was improved 8 times on average.

2. MATERIAL AND METHOD

In the experimental study; 7075 aluminum sheet material was purchased. The chemical composition of the material is given in Table 1. The uncoated material was designated S.

Table 1. Chemical composition of the material (% weight)

ELEMENTS (%)						
Mg	Zn	Cr	Cu	Fe	Si	Al
2,61	5,7	0,175	1,72	0,14	0,063	Balance

Prior to MAO treatment, 7075 Al/T6 alloy was sanded successively with 400#, 600#, 800# and 1200# SiC sandpapers to achieve average surface roughness. It was then ultrasonically cleaned with ethanol and deionized water for 5 minutes. Finally, it was dried with nitrogen. Before the coating process, the frequency, voltage and time parameters effective on the MAO process were determined as constant. In the MAO process, the frequency value was applied at 1000 Hz. The positive and negative voltages applied to the process were applied over 420V and 100V, respectively, and the positive duty cycle (Duty Cycle) was studied at 20% negative duty cycle 5%. In the experimental process, 7075-T6 aluminum alloy sample was chosen as the anode and the stainless steel bath wall as the cathode. During the process, the electrolyte was mixed and cooled with cooling water passed through the bath wall so that it does not rise to a temperature above 30°C. Then, the coated 7075-T6 aluminum alloy samples, which were treated with MAO, were washed with distilled water and alcohol and dried. This sample is coded as SM. Figure 1 shows the schematic of the hardware used in the MAO process.

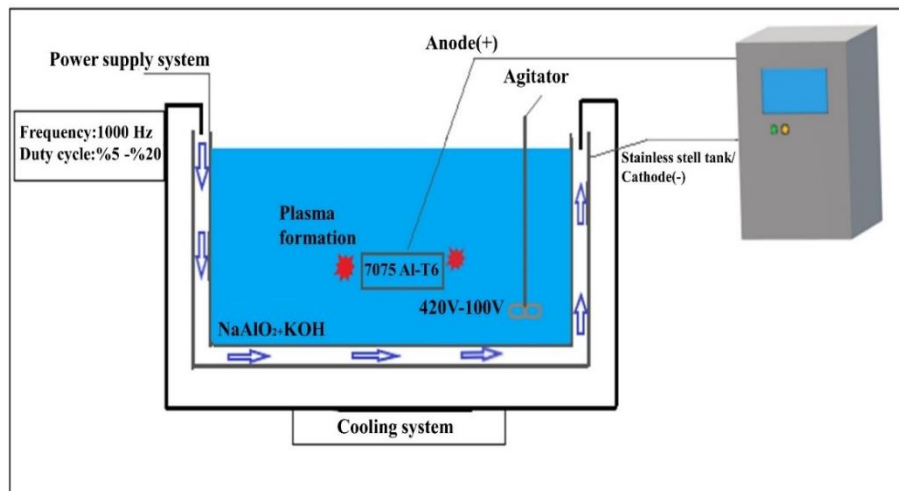


Figure 1. Schematic representation of the equipment used in the MAO process

Surface microstructure and element analysis of MAO coatings were examined using the JSM-6060LV scanning electron microscope (SEM). Coating thickness was measured from SEM cross-section images of MAO samples. In addition, ImageJ software was used to measure the porosity of the MAO coatings. The micro hardness of the samples was measured in QNESS Hardness device according to HV0.5. The friction and wear behavior of the samples were evaluated with a wear tester (Turkyus) under dry sliding condition. For the wear test, loads were selected as 5N, 10N, 15N respectively.

3. RESULTS AND DISCUSSION

The coating thickness and surface appearance of the sample coated with MAO are shown in Figure 2a. It is understood that the coating is carried out in a homogeneous way. It is seen that the coating thickness on the surface is about 2µm. In Figure 2b, the diameters of the porosities on the surface were measured with the Image J image software program (Schneider et al., 2020). Measurements at 5 points were measured as 1.4µm, 1.5µm, 1.3µm, 1.6µm and 1.6µm, respectively. Average porosities were calculated as 1.48µm. Increasing the voltage while coating increases the thickness of the coating and also increases the diameter of the porosities (Sobolev et al., 2020).

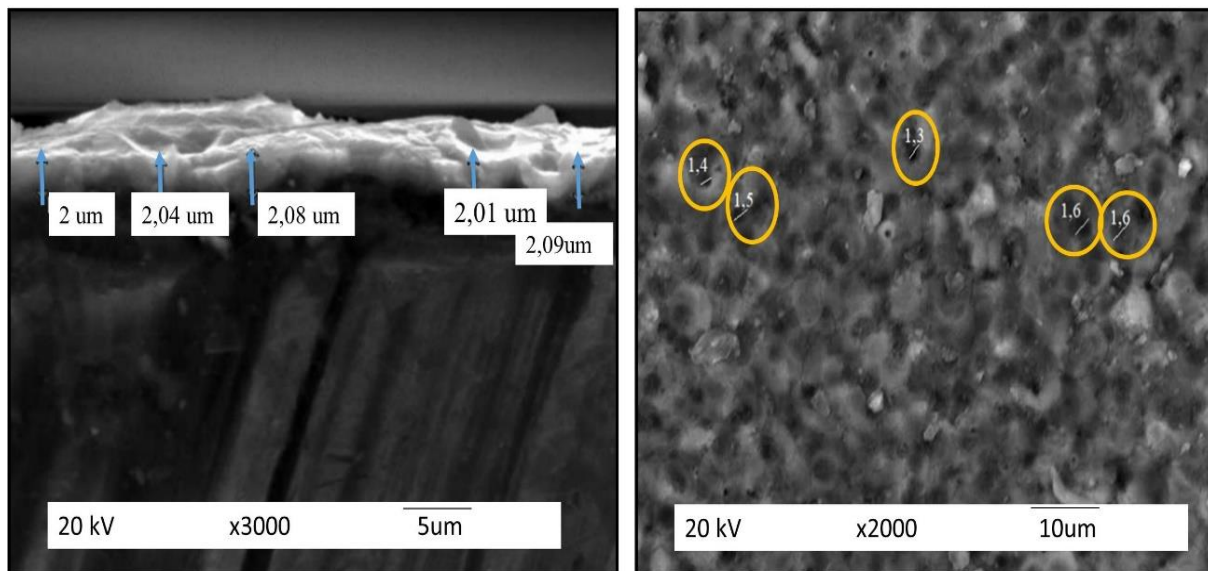


Figure 2. a) Cross-sectional SEM image of SM sample b) Surface SEM image of SM sample

Figure 3 shows the EDS analysis of the coating region. Type B discharge consists of regional high electric field density produced during the process. Type A discharges, on the other hand, occur as gas discharges within the micropores on the surface. A-type discharges, on the other hand, create small and large pores on the surface because they occur in micropores close to the surface and have lower energy than B-type discharges. As a result of the oxidation of the base metal in type B discharges, the metal's oxide grows inwards, while in type A discharges, oxides containing electrolyte components grow outward as the existing oxide and molten metal react with the electrolyte components (Hussein et al., 2013). With the rapid solidification of Al_2O_3 during the coating process, metastable $\gamma\text{-Al}_2\text{O}_3$ phase formation begins. As the coating surface comes into contact with the electrolyte, it cools quickly and $\gamma\text{-Al}_2\text{O}_3$ is formed in the outer surface layer. (Figure 3). However, due to the low thermal conductivity of alumina, the main layer of the coatings remains hot because the heat cannot be easily dissipated. Therefore, the outer surface layer changes from $\gamma\text{-Al}_2\text{O}_3$ to $\alpha\text{-Al}_2\text{O}_3$. Thus, the expected $\alpha\text{-Al}_2\text{O}_3$ continues to increase up to the coating-material interface (Xin et al., 2006).

Figure 4 shows the XRD analysis of 7075-T6 Al alloy (S) and MAO (SM) coating. In the S sample, the (111) plane showed the strongest XRD peak. This plane shows the strongest XRD peak in Al alloys. However, with the effect of the coating, it was observed that the most intense XRD peak was in the (200) plane. $\gamma\text{-Al}_2\text{O}_3$ on the coating surface intensely peaks at 39.4, 45.7, and 66.7 degrees. There is $\gamma\text{-Al}_2\text{O}_3$ at 39.4° (222), 45.7° (400) and 66.7° (440) plane. The existence of Al_2O_3 coating, which we observed with microstructures, was proved by XRD analysis.

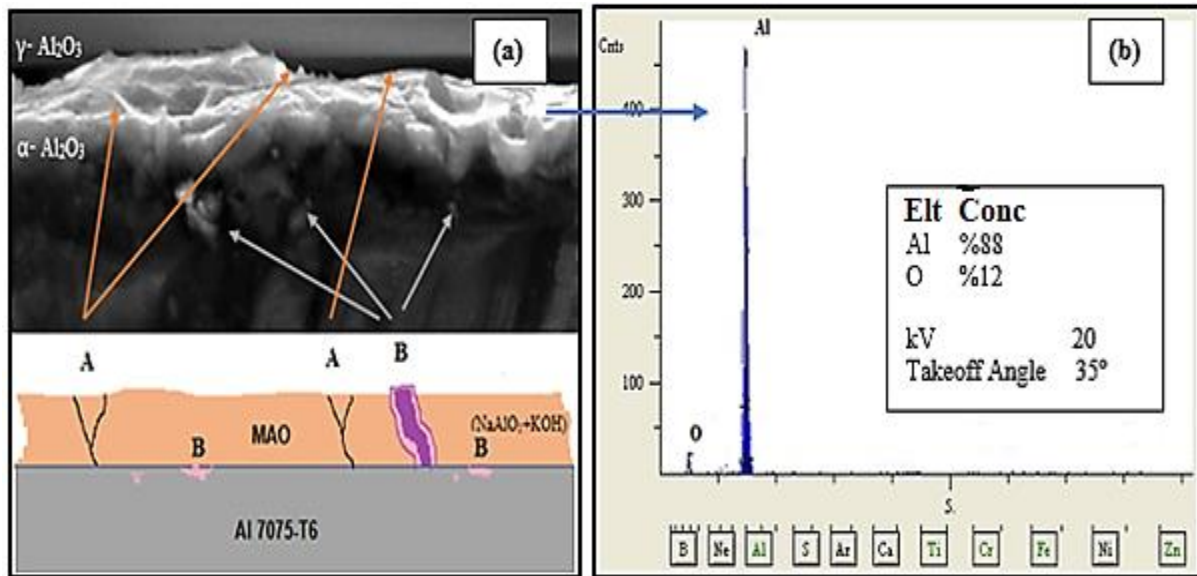


Figure 3. a) Schematic view of the discharge channels from the cross-section
b) EDS analysis of coating zone

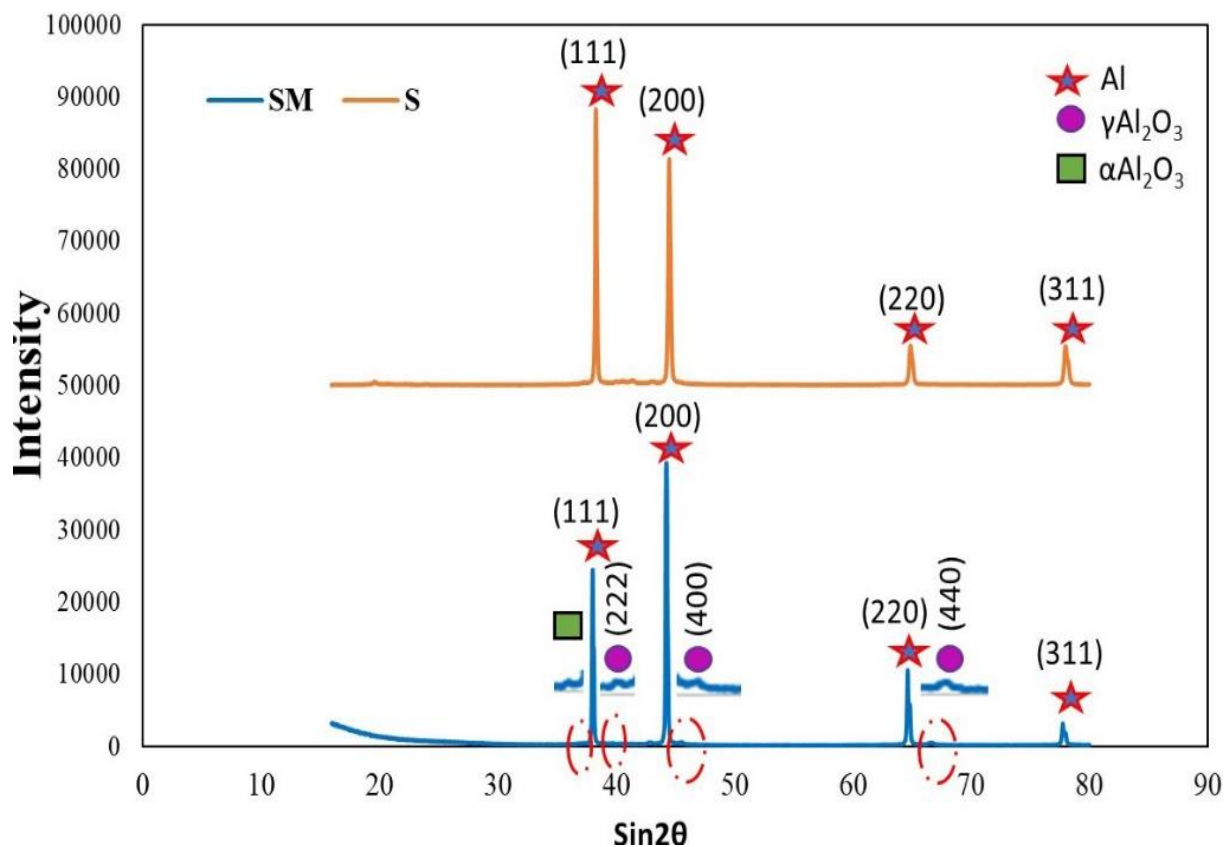


Figure 4. X-ray diffraction patterns of SM and S sample

The hardness values of the starting material Al 7075-T6 (S) and MAO coated samples (SM) are shown in Figure 5. The hardness of the (S) sample was measured as 180 HV0.5. The hardness of the micro arc coated sample (SM) was measured as 272 HV0.5.

It is known from the literature that the hardness of the coating will increase. However, although the 2µm coating was thin, the hardness value increased by about 50%. In order to examine the relationship between hardness value and dislocation density, dislocation densities were calculated by XRD analysis. In Figure 2, the

dislocation density values are given together with the hardness value. At the same time, crystallite size value was calculated while dislocation density calculations were made. The Crystallite size and dislocation density of the samples with the Debye Scherrer formula was calculated.

Debye Scherrer's equation;

$$Dp = k * \lambda / \beta * \cos \theta \quad (1)$$

The dislocation density (δ)

$$\delta = 1/Dp^2 \quad (2)$$

Crystallite sizes calculated with the FWHM value obtained by XRD analysis; It was found to be $611.8 \cdot 10^{-10}$ m in the S sample and $568.2 \cdot 10^{-10}$ m in the SM sample. The crystallite size of the coated sample decreased. It is thought that the grain form changes due to diffusion during coating. Therefore, Figure 2 shows that the dislocation density of the coated sample also increased. At the same time, while coating is being done, the atoms tend to move towards the surface during diffusion. Thus, crystal structure errors occur. It is thought that these faults lock the dislocations and increase the hardness.

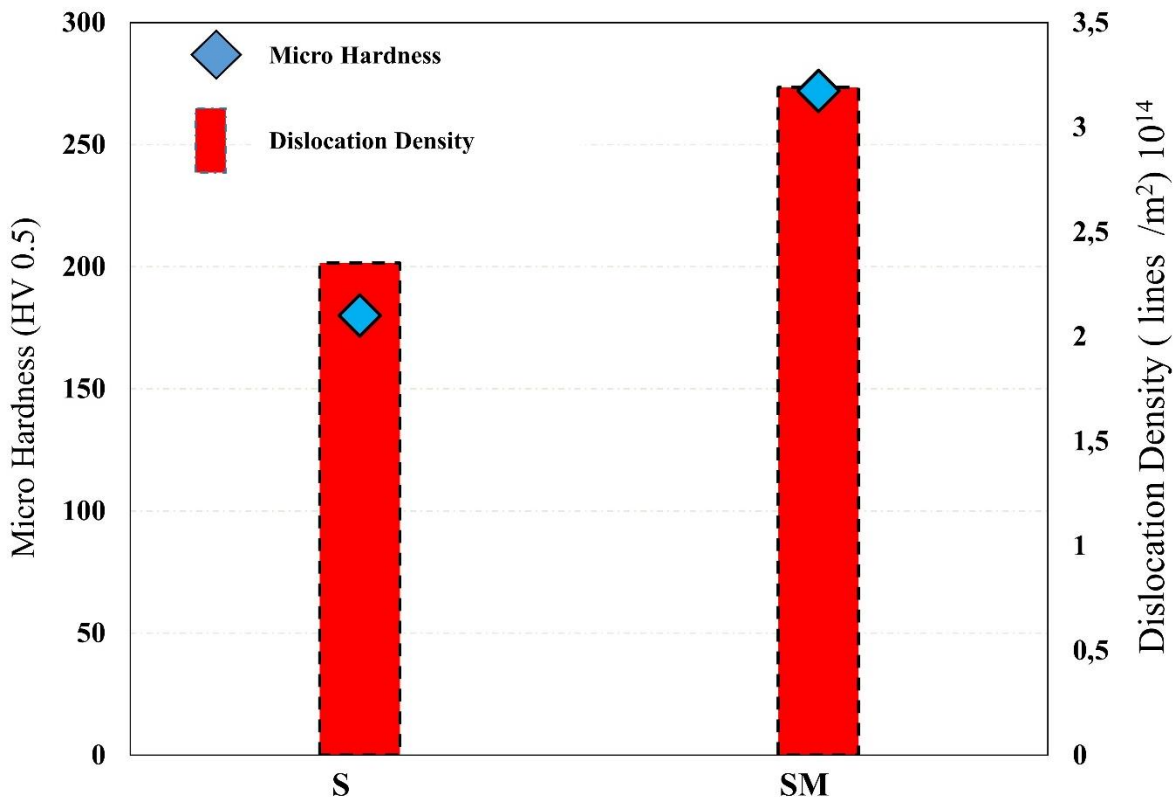


Figure 5. Microhardness results and dislocation densities of samples

Figure 6-7 and Table 2 show the wear test weight loss of the samples. In the experiments carried out to determine the wear performance, the test load and the total sliding distance were chosen as 5N, 10N, 15N and 500-1000-1500 m, respectively. When Table 2 is examined, it is possible to say that there is a relatively homogeneous weight loss depending on the unit distance. This homogeneity in weight losses is reflected as a linear increase in the slope of the graphs. We can say that the steepness of the slope is increased by the applied force. When the weight losses are examined, the fact that the weight loss of the sample with 2 μ m coating thickness applied 5N load is the least compared to the other coated samples can be attributed to the stronger interfacial bond strength. Based on this, other samples with micro arc coated 10N and 15N loads support this

result. The SEM image of the SM sample, as examined in Figure 6, supports the image of the weight loss caused by the applied 5N load. When the traces formed were examined, it was determined that the wear lines became more pronounced due to the increasing weight. In Figure 7, wear graphs of the S sample are shown. With the applied coating, the wear behavior of the material is directly affected by its mechanical and structural properties. The MAO coating showed significant wear resistance compared to its uncoated state. According to the wear test results, it was determined that the wear marks of the samples applied with 5N test load were less than the samples applied with 10N and 15N test loads. Based on this, according to the sample SEM results, the wear marks increased with the increase in the test load. The visible white coatings on the MAO 2 μ m 15N surface are thought to have been re-adhered to the surface of the broken pieces. It shows that the weight loss of the SM sample with increasing test loads is less compared to the S sample and thus its wear resistance is higher. Compared to the S sample, the abrasion resistance of the SM sample increased approximately 8 times at 5N load, 10 times at 10N and 7.5 times at 15N load.

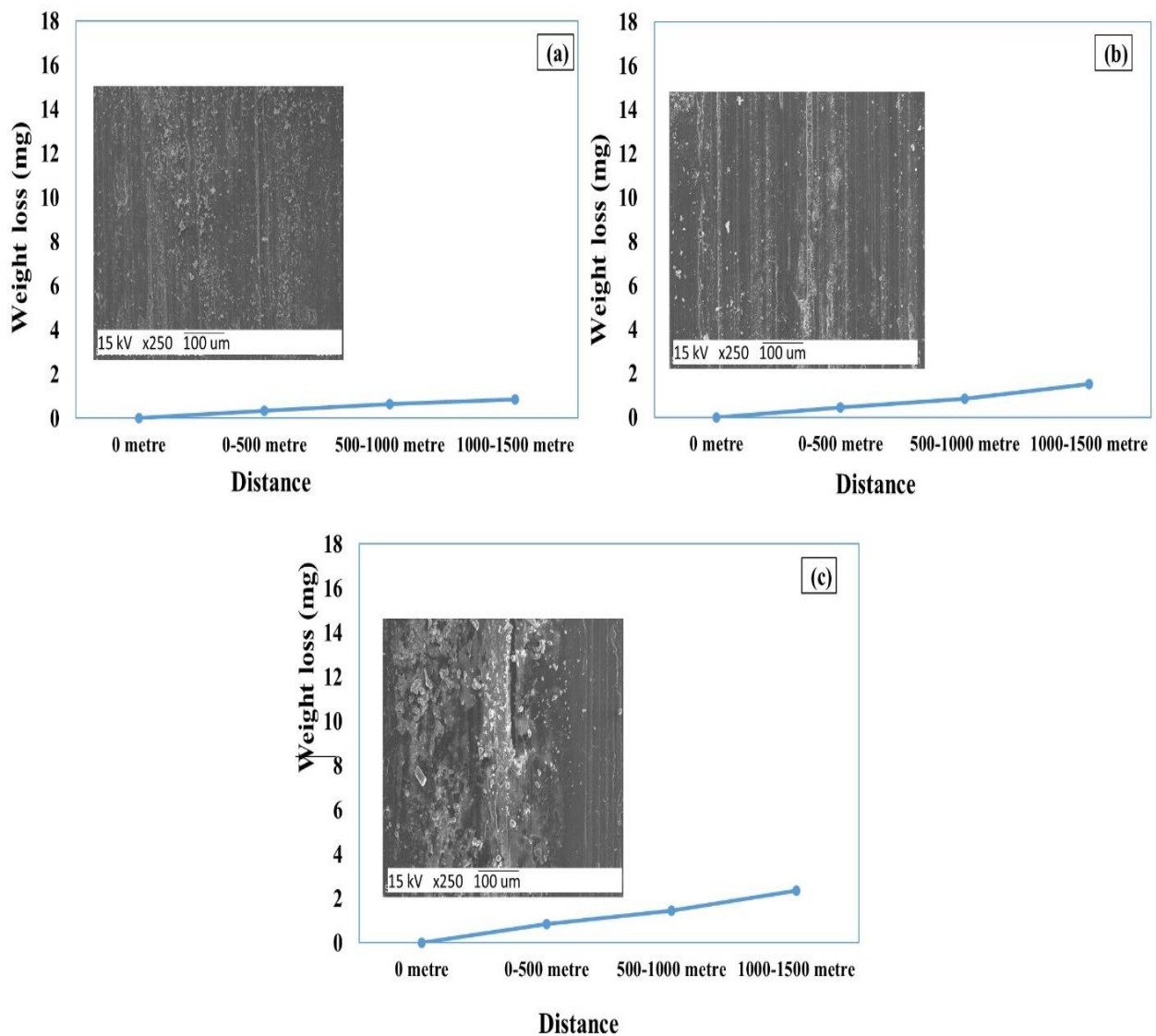


Figure 6. Abrasion test weight loss graphs of SM (7075-T6 Al+MAO) sample at a) 5N b) 10N c) 15N loads

Figure 8 shows the friction coefficient-distance graph of the samples. The friction coefficient of the SM sample was 0.2, and the friction coefficient of the S sample was 0.5. The fact that the SM sample has less friction coefficient indicates that the abrasion resistance is better.

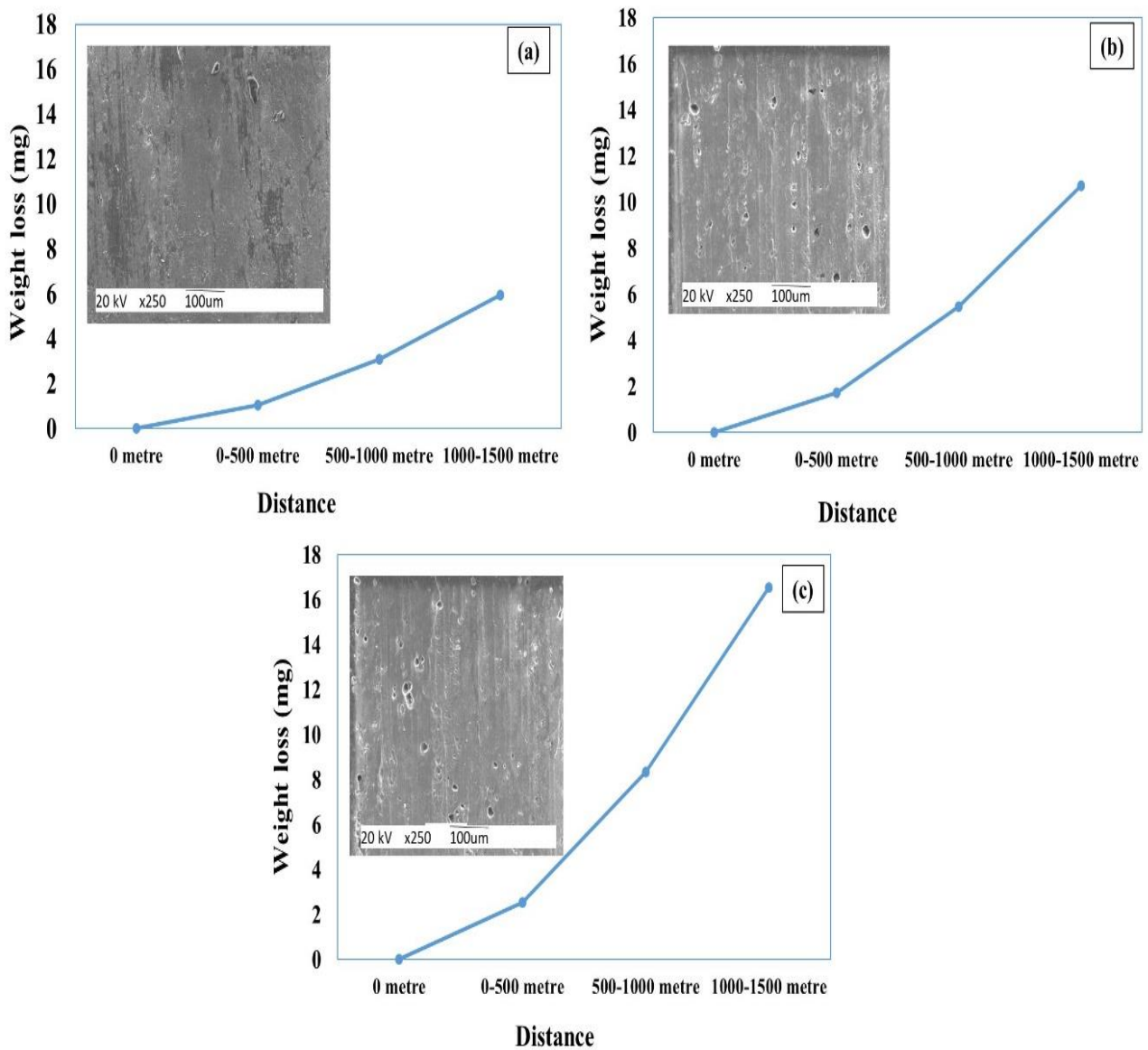


Figure 7. Abrasion test weight loss graphs of S (7075-T6 Al) sample a)5N b)10N c)15N loads

Table 2. Wear test weight loss results of SM and S samples

Material	Weight Loss			
	0-500 metre	500-1000 metre	1000-1500 metre	Total Weight
SM 2µm 5N	0,33 mg	0,31 mg	0,21 mg	0,85 mg
SM 2µm 10N	0,45 mg	0,38 mg	0,67 mg	1,50 mg
SM 2µm 15N	0,83 mg	0,61 mg	0,9 mg	2,34 mg
S 5N	1,04 mg	2,05 mg	2,85 mg	5,94 mg
S 10N	1,74 mg	3,71 mg	5,27 mg	10,72 mg
S 15N	2,52 mg	5,81 mg	8,22 mg	16,55 mg

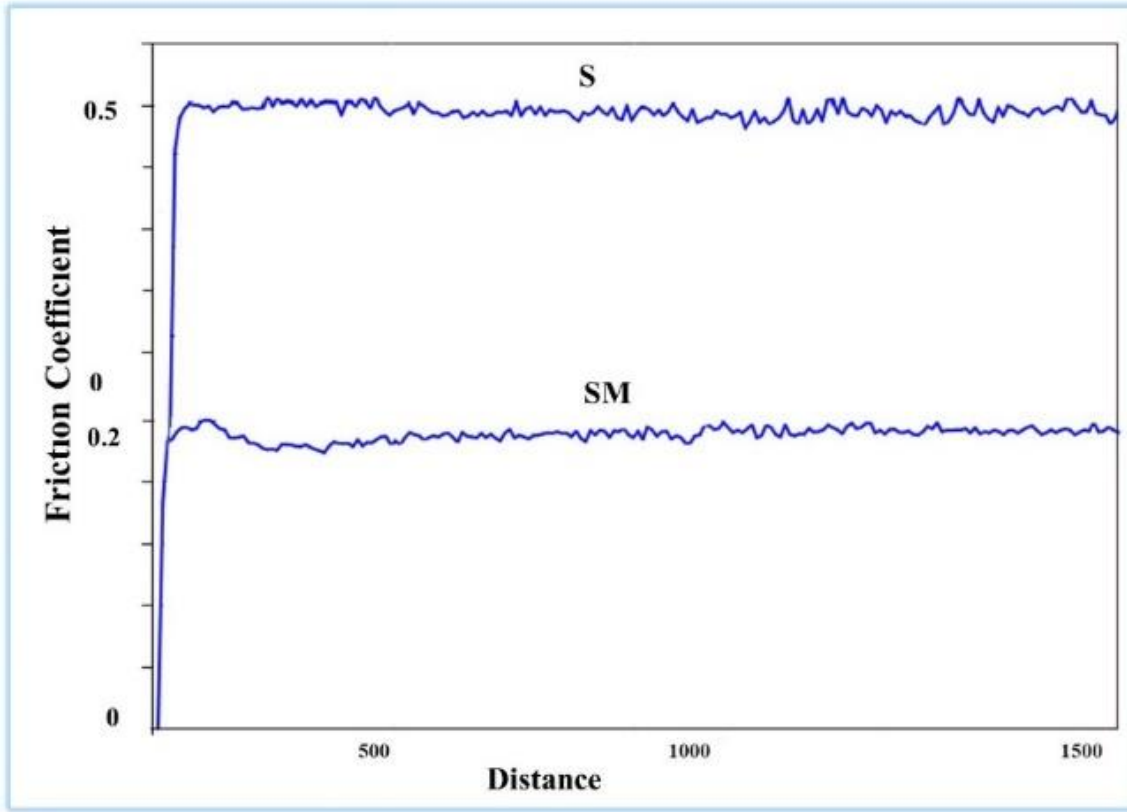


Figure 8. Friction coefficient values of SM and S samples

4. CONCLUSION

In this study, a very thin 2 micron MAO coating was applied to the Al 7075-T6 alloy to reduce the cost. The following results were obtained

- The hardness of the MAO-coated samples increased by 50% compared to the uncoated samples.
- Although the coating thickness of the sample that was coated on the aluminum 7075-T6 surface was so thin, the wear resistance increased 8 times compared to the uncoated sample.
- The friction coefficient of the sample coated with MAO is lower than the Al 7075-T6 sample.
- By coating the samples with MAO, the average pore diameters are 1.48 μm .

ACKNOWLEDGMENT

This research was supported by the Gazi University BAP unit with the project number FDK-2023-7620.

CONFLICT OF INTEREST

The authors declare no conflict of interest.

REFERENCES

Altuntaş, O. (2022). Enhancement of impact toughness properties of Al 7075 alloy via double aging heat treatment. *Gazi University Journal of Science Part C: Design and Technology*, 10(2), 194-202. doi:[10.29109/gujsc.1108116](https://doi.org/10.29109/gujsc.1108116)

Altuntaş, O., & Güral, A. (2015). Yüksek Karbonlu Sinterlenmiş Çeliklerin Darbe Tokluklarına Küreselleştirme Isıl İşlemlerinin Etkisinin İncelenmesi [Examining Effect of Speheroidization Heat Treatments on Impact Toughness of High Carbon Sintered Steel]. *Politeknik Dergisi*, 18(3), 107-112.

- Altuntaş, G., Altuntaş, O., & Bostan, B. (2021). Characterization of Al-7075/T651 Alloy by RRA Heat Treatment and Different Pre-deformation Effects. *Transactions of the Indian Institute of Metals*, 74(12), 3025-3033. doi:[10.1007/s12666-021-02369-5](https://doi.org/10.1007/s12666-021-02369-5)
- Baxi, J., Kar, P., Liang, H., Polat, A., Usta, M., & Uçışık, A. H. (2008) Tribological characterization of microarc oxidized alumina coatings for biological applications. *Vacuum*, 83(1), 217-222. doi:[10.1016/j.vacuum.2008.03.085](https://doi.org/10.1016/j.vacuum.2008.03.085)
- Dean, J., Gu, T., & Clyne, T. W. (2015). Evaluation of residual stress levels in plasma electrolytic oxidation coatings using a curvature method. *Surface and Coatings Technology*, 269, 47-53. doi:[10.1016/j.surfcoat.2014.11.006](https://doi.org/10.1016/j.surfcoat.2014.11.006)
- Hussein, R. O., Nie, X., & Northwood, D. O. (2013). An investigation of ceramic coating growth mechanisms in plasma electrolytic oxidation (PEO) processing. *Electrochimica Acta*, 112, 111-119. doi:[10.1016/j.electacta.2013.08.137](https://doi.org/10.1016/j.electacta.2013.08.137)
- Li, Z.-y., Cai, Z.-b., Cui, Y., Liu, J.-h., & Zhu, M.-h. (2019). Effect of oxidation time on the impact wear of micro-arc oxidation coating on aluminum alloy. *Wear*, 426-427(A) 285-295. doi:[10.1016/j.wear.2019.01.084](https://doi.org/10.1016/j.wear.2019.01.084)
- Qi, X., Song, R., Wang, C., & Jiang, B. (2022). Influence of Interfacial Stress Produced by MAO on Electrochemical Corrosion and Stress Corrosion Cracking Behavior in 7075 Aluminum Alloy, *Journal of The Electrochemical Society*, 169(2), 020559. doi:[10.1149/1945-7111/ac534b](https://doi.org/10.1149/1945-7111/ac534b)
- Schneider, C. A., Rasband, W. S., & Eliceiri, K. W. (2012). NIH Image to ImageJ: 25 years of image analysis. *Nature Methods*, 9(7) 671-675. doi:[10.1038/nmeth.2089](https://doi.org/10.1038/nmeth.2089)
- Shen, Z., Wu, Z., Wang, T., Jia, T., & Liu, C. (2023). Research on Technology of 7075 Aluminum Alloy Processed by Variable Polarity TIG Additive Manufacturing Utilizing Nanoparticle-Reinforced Welding Wire with TiB₂. *Crystals*, 13(3), 399. doi:[10.3390/cryst13030399](https://doi.org/10.3390/cryst13030399)
- Sobolev, A., Peretz, T., & Borodianskiy, K. (2020). Fabrication and characterization of ceramic coating on Al7075 Alloy by plasma electrolytic oxidation in molten salt. *Coatings*, 10(10), 993. doi:[10.3390/coatings10100993](https://doi.org/10.3390/coatings10100993)
- Song, G.-L., & Shi, Z. (2014). Corrosion mechanism and evaluation of anodized magnesium alloys. *Corrosion Science*, 85, 126-140. doi:[10.1016/j.corsci.2014.04.008](https://doi.org/10.1016/j.corsci.2014.04.008)
- Sundararajan, G., & Krishna, L. R. (2003). Mechanisms underlying the formation of thick alumina coatings through the MAO coating technology. *Surface and Coatings Technology*, 167(2-3), 269-277. doi:[10.1016/S0257-8972\(02\)00918-0](https://doi.org/10.1016/S0257-8972(02)00918-0)
- Xin, S.-G., Song, L.-X., Zhao, R.-G., & Hu, X.-F. (2006). Composition and thermal properties of the coating containing mullite and alumina. *Materials Chemistry and Physics*, 97(1), 132-136. doi:[10.1016/j.matchemphys.2005.07.073](https://doi.org/10.1016/j.matchemphys.2005.07.073)
- Yılmaz, M. S., Özer, G., Şahin, O., & Karaaslan, A. (2021). Investigation of the Effects of Different Retrogression and Re-Aging Parameters Applied to the 7075 Alloy on the Micro-Arc Oxidation Process. *Surface Review and Letters*, 28(09), 2150078. doi:[10.1142/S0218625X21500785](https://doi.org/10.1142/S0218625X21500785)
- Zhang, J., Dai, W., Wang, X., Wang, Y., Yue, H., Li, Q., Yang, X., Guo, C., & Li, C. (2023). Micro-arc oxidation of Al alloys: Mechanism, microstructure, surface properties, and fatigue damage behavior. *Journal of Materials Research and Technology*, 23, 4307-4333. doi:[10.1016/j.jmrt.2023.02.028](https://doi.org/10.1016/j.jmrt.2023.02.028)



Asphaltite Pyrolysis in Fluidized Bed Reactor

Samad MOGHANIRAHIMI^{1*} Hüseyin TOPAL¹

¹Gazi University, Faculty of Engineering, Ankara, Türkiye

Keywords	Abstract
Asphaltite Pyrolysis Fluid Bed Liquid Fuel	In this study, the pyrolysis properties of asphaltite samples taken from Şırnak and Hakkari regions in a fluidized bed reactor under catalyst and non-catalyst conditions were determined by rapid and batch pyrolysis. Basic analysis, FTIR and XRF analyses were performed for the raw material. GC-MS analysis methods were used for liquid pyrolysis products and FTIR were used for solids. In order to acquire the condition of the highest liquid product yield in pyrolysis, several effective variables such as particle diameter, vacuum, nitrogen flow rate, temperature, raw material feed rate, catalyst type, raw material type and duration were experimented and the results were evaluated. In general, the vacuum effect has led to an increase in liquid product yield and a decrease in gas product yield. Liquid product yield increased at 700°C pyrolysis temperature in continuous feed system and 550 - 650°C in batch system. In the pyrolysis studies carried out, a maximum liquid product yield of 16.5% was achieved in the continuous fed reactor at 700°C temperature, 400 mmHg vacuum, 2 g/min feed rate and 500 µm particle size.

Cite

Moghanirahimi, S., & Topal, H. (2023). Asphaltite Pyrolysis in Fluidized Bed Reactor. *GU J Sci, Part A, 10(2)*, 166-175. doi:10.54287/guj.1256330

Author ID (ORCID Number)	Article Process
0000-0002-3737-1345	Submission Date 25.02.2023
0000-0001-7406-4398	Revision Date 03.04.2023
	Accepted Date 04.04.2023
	Published Date 15.06.2023

1. INTRODUCTION

Gao et al. (2022) investigated bed agglomeration in pyrolysis of biofat-derived fuels in fluid bed. Biocoal, methanol, biooil, methanol fuels, whose yield was found to be lower than bio-oil, were used as inputs. The agglomeration yield due to the resulting tar yield and formation showed a positive linear correlation. Li et al. (2023) investigated the contribution of the joint delivery of oxygen and nitrogen to the system in two frit fluid bed reactors in pine sawdust oxidative rapid pyrolysis, the effect on the yield, formation and distribution of bio-oil, as well as its light and heavy components. Bilgin (2021) the effects of reagents by flotation enrichment process of asphaltite coal were examined. In the results of the experiments, it was determined by adding 100 g / t fuel oil reagent to reduce the sulfur rate. The sulfur content was reduced from 6.46% to 5.71%.

Kosan et al. (2021) have studied ammonia adsorption on asphaltite ash and thermodynamic approach on issues such as physical and chemical adsorption capacities, decrease in ΔH and ΔS , decrease in endothermic chemical adsorption, progression of increased exothermic physical adsorption reaction. Hameed et al. (2023) developed and simulated a CFD (Computational Fluid Dynamics) model to study cellulose pyrolysis using two different kinetic schemes in a fluidized bed reactor and to combine reaction kinetics with hydrodynamics. It was determined that the frequency factor and activation energies affected the yield of pyrolysis product. The yield of coal and tar increased, the fraction of gases decreased at high activation energy. Sezer et al. (2008) in the experiments in flash pyrolysis system, the content of the liquid product was thinned and classified by GC-MS analysis and the highest yield of the liquid product was tried to be reached under different test conditions. The solid residue was also analyzed as FT-IR, showing that the constant percentage of carbon and ash increases

*Corresponding Author, e-mail: s.mughanli@gmail.com

with temperature. In the pyrolysis study conducted by Sert et al. (2011) raw and demineralized Şırnak asphaltite was examined in terms of liquid product yield and determination of the amount of volatile matter at different temperatures. Hamamci et al. (1997) Turkey has reserves of approximately 77.5 million tons of asphaltite. In their experimental studies, Şırnak and Hazro tried to remove the sulfur of asphalt with the "Meyer Method".

Taskesen, et al. (2022) An investigation was conducted to obtain natural humic acid from the content of asphaltite samples taken from the reserve of asphaltites commonly found in Şırnak-Uludere Region. Demirci et al. (2019) Comprehensive information such as the formation of asphaltite resources in 13 regions of Turkey, the fact that it is known as an important resource due to valuable elements such as molybdenum, nickel and vanadium in it, its use in a 405 MW fluid bed thermal power plant, its inconvenient domestic use, its high caloric value, and the elimination of environmental risks due to its sulfur content are given.

One of the original aspects of this research is the study of thermal and catalytic pyrolysis of asphaltite in a fluidized bed reactor. One of the main objectives of the study is to obtain maximum liquid products and to contribute to growth of the country's economy in the future because of their hydrocarbon content. Another aim is to ensure that the by-products (gas, solids, etc.) obtained in the pyrolysis process can be recovered in the future by using environment friendly technologies. In addition, the main purpose of the liquid pyrolysis products to be obtained is to produce liquid products that do not create environmental pollution and will be possible to burn with high efficiency in classical combustion systems. In this way, a significant contribution will be made to the use of domestic resources, which are important for the country, in the energy field. Therefore, it is important for the environment and economy that asphaltites, which have large reserves in our country and have rich hydrocarbon content, are brought back to the Turkish industry by using combined technological methods such as pyrolysis, catalytic hydrocracking, hydrodealkylation, etc. in the future.

2. MATERIAL AND METHOD

In this study, the pyrolysis properties of asphaltite in a fluidized bed reactor under laboratory conditions were examined thermally and by use of catalysts in continuous feed and batch systems, accompanied by fluidizing nitrogen gas. By using three different asphaltite samples as raw materials in the pyrolysis process, various temperature, vacuum pressure, particle size, nitrogen flow rate, feed rate and catalyst effect were experimentally investigated. The average temperature distribution of the reactor was determined by thermocouple in nitrogen environment, nitrogen-free, vacuum and non-vacuum conditions and the suitability status was clarified before the experiments. The laboratory experimental system diagram is shown in Figure 1.

The rapid pyrolysis test system consists of DC motor, reductor, hopper and auger, tubular stainless steel reactor with a length of 30 cm and a diameter of 3.8 cm, a 1200 watt heater furnace, condenser, separator, digital gas meter, vacuum pump and automatic control system. In the discrete system, the DC motor, reducer, hopper and auger are removed from the system. In order to examine the physical-chemical properties and to be used in experimental studies, asphaltite samples were reduced to four different particle sizes (100, 200,... micrometer) with the help of sample crushing, grinding machine and sieve. The raw material supply speed was realized with the help of DC motor and reducer. Nitrogen gas is supplied to the system from under the reactor with a perforated metal plate distributor in order to prevent the stuttering of the asphaltite and to fluidize it. The minimum fluidization rate of nitrogen was calculated from Ergün's equation as 0.01001 m/s and the flow rate as 0.75 Lt/min.

3. EXPERIMENTAL STUDIES: CONCLUSIONS AND INTERPRETATIONS

Raw material and product analyzes, test conditions and analysis results and interpretation were made.

3.1. Investigation of Asphaltite Samples

Samples were simplified, FTIR and XRF (X-ray fluorescence), samples were obtained from those regions through Hakkari and Şırnak Universities.

3.1.1. Brief Analysis

The results of moisture, ash, volatile matter and constant carbon analysis of asphaltite samples are presented in Table 1. The sulfur content in the samples was determined in the XRF analysis.

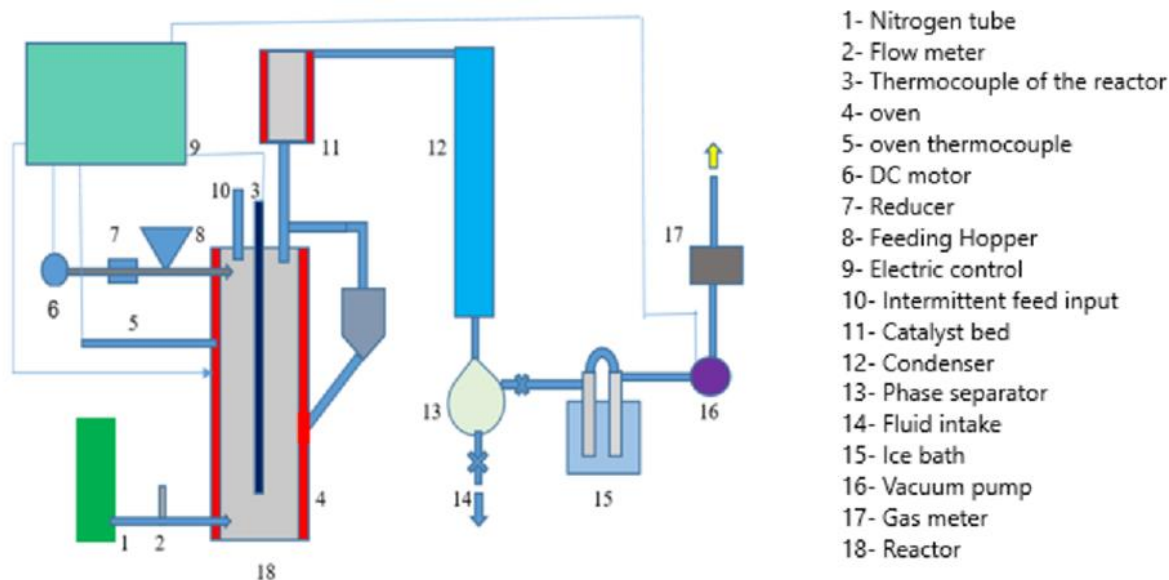


Figure 1. Laboratory pyrolysis test system

Table 1. Brief Analysis of Samples

	Humidity %	Ash %	Volatile matter %	Fixed carbon %
Hakkari-1 sample	2,60	35,28	45,42	16,7
Hakkari-2 sample	1,59	35,42	35,70	30,29
Şırnak sample	3,11	31	34,04	31,85

3.1.2. FTIR Analysis

The molecular structures of the Hakkari-1, 2 and Şırnak samples were examined by the FTIR method, and since the results were similar, only the IR spectrum of the Hakkari-1 sample was presented in Figure 2. As can be seen from the results, the IR spectra of all three asphaltite samples are close to each other, based on either to their peak levels or their frequencies. In addition, the most effective peak frequency in all three spectra is approximately in the range of 3000-2900 cm^{-1} . The frequency of the less effective peak next to it is 2900-2800 cm^{-1} . Both peak frequencies are generally thought to belong to carbon and hydrogen bonds (C-H), i.e. alkanes (Paraffins). Less effective peaks in the IR spectra of raw material quantities 1, 2 and 3 and frequencies from 1600-1400 cm^{-1} are considered to levels belong to C = C bonds, that is, mainly to aromatic hydrocarbons. Thus, although there are certain differences in the efficiency of the peaks in the IR spectra of the samples, the frequency ranges of all three asphaltites are very close. Therefore it is possible to accept that all three asphaltite samples are mainly composed of various alkanes and aromatic hydrocarbons.

3.1.3. XRF Analysis

XRF analysis results of asphaltite samples are given in Figure 3-6. From the results obtained, it was determined that the asphaltite samples contained metals such as Ca, Si, Al, Fe, V, Ti, Ni, Mo as well as C, O, S.

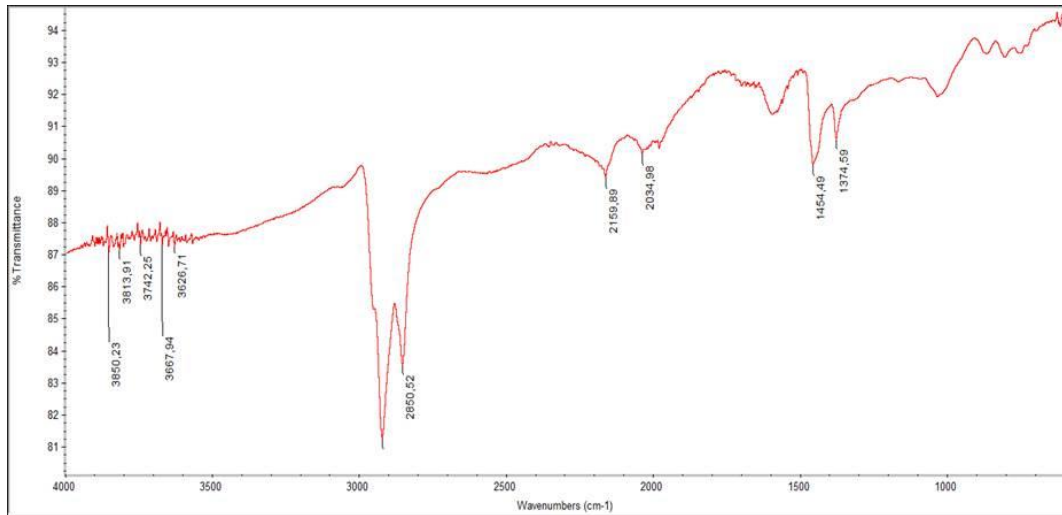


Figure 2. FTIR analysis of Hakkari-1 sample

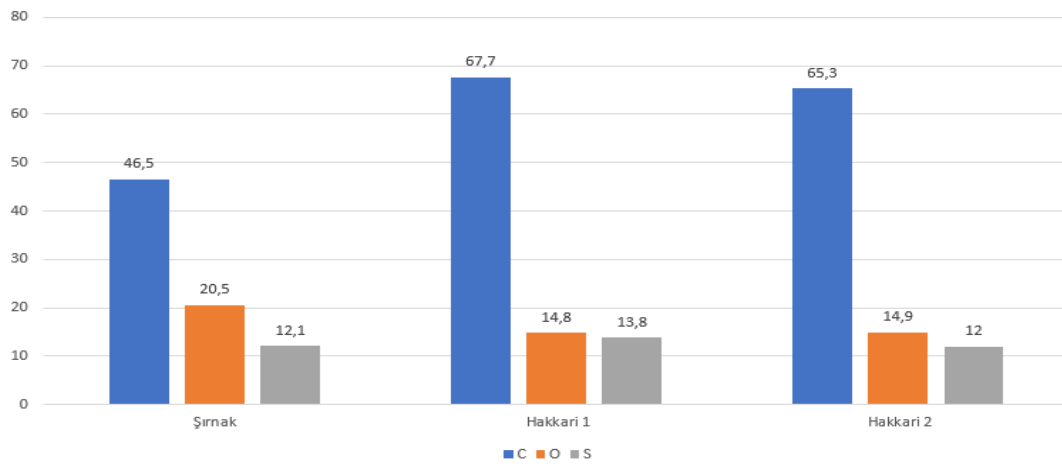


Figure 3. XRF analysis results of Hakkari-1, 2 and Şırnak asphaltite samples (c, o, s)

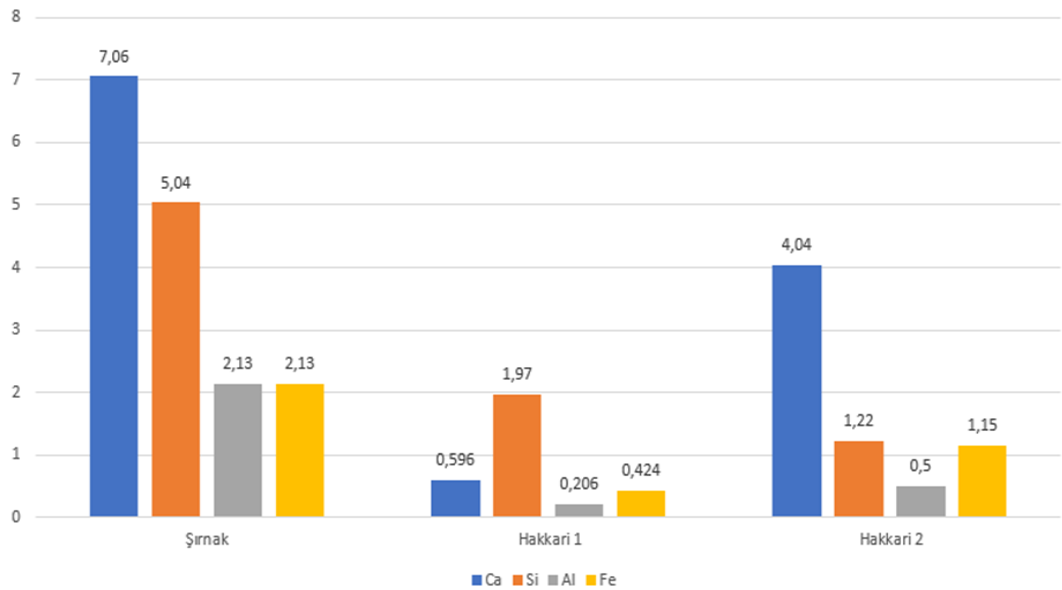


Figure 4. XRF analysis results of Hakkari-1, 2 and Şırnak asphaltite samples (Ca, Si, Al, Fe)

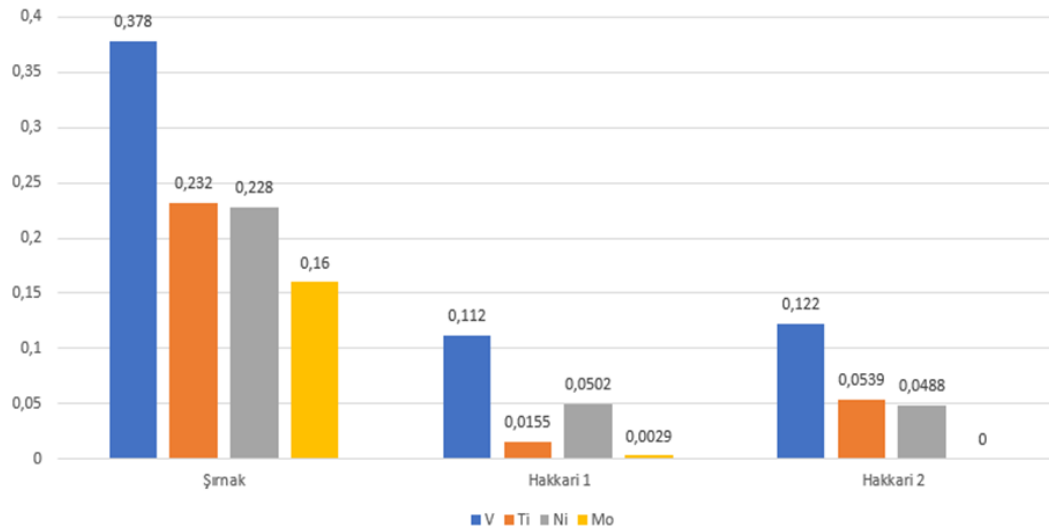


Figure 5. XRF analysis results of Hakkari-1, 2 and Şırnak asphaltite samples (V, Ti, Ni, Mo)

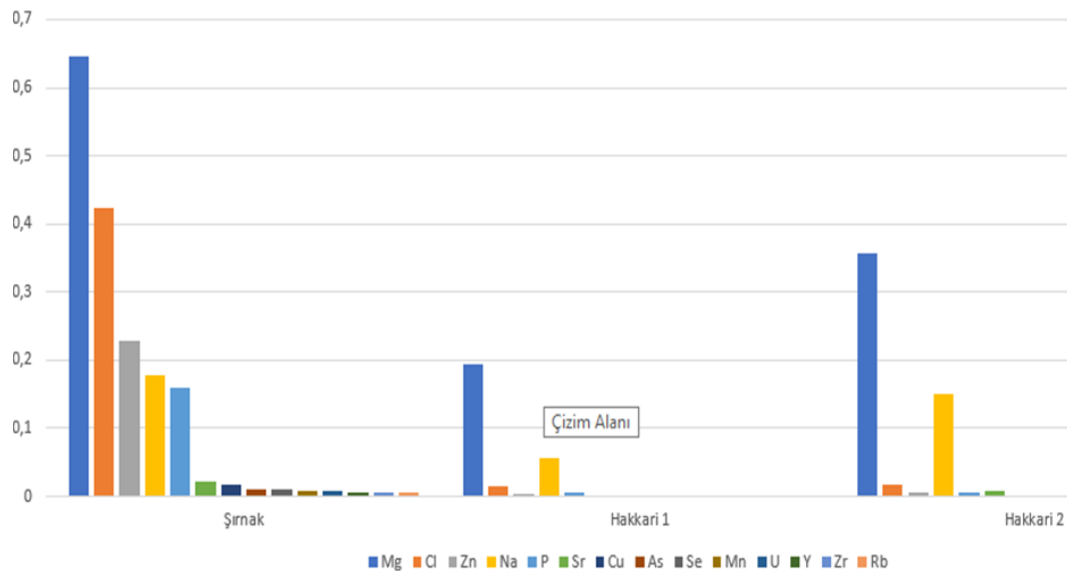


Figure 6. XRF analysis results of Hakkari-1, 2 and Şırnak asphaltite samples (other content)

According to the results of XRF analysis, the carbon ratios in Hakkari-1 and Hakkari-2 asphaltite samples (67.7% and 65.3%, respectively) are significantly higher than Şırnak asphaltite (46.5%) and the oxygen content is low. The high carbon content of Hakkari asphalt will allow the production of valuable liquid products with various hydrocarbon content (gasoline, diesel fuel, etc.) with higher efficiency under pyrolysis process conditions. In addition, under pyrolysis conditions, thermodynamically significant proportions of gas products such as H_2 and C_1-C_4 can be obtained. Whether liquid or gaseous products formed under pyrolysis conditions may contain unsaturated hydrocarbons as well as saturated hydrocarbons. If the process of pyrolysis of asphaltites is applied throughout the industry, the hydrocarbon products to be produced, especially the liquid products, must be purified from unsaturated hydrocarbons and sulfurous compounds by catalytic hydrogenation method. Although Şırnak asphaltite has a relatively low carbon ratio, it has a much higher metal ratio and metal diversity than Hakkari asphaltite.

This situation is thought to bring precious metals such as Al, Fe, K, V, Zn to the economy as well as other hydrocarbon products from Şırnak asphaltite throughout the industry. In addition, in the results of the analysis, it was concluded that both Şırnak and Hakkari asphaltites contain sulfurous compounds in high rates (approximately 12-14%). These sulfurous compounds are thought to be composed mainly of different thiophenes and mercaptans. Under pyrolysis conditions, these sulfurous compounds can deteriorate and turn

into hydrogen sulfide and sulfur oxides, and elemental sulfur, which is widely used in different industrial areas, can be produced on their basis. As a result of the pyrolysis of asphaltites, heavy products that may consist mainly of polycyclic aromatic hydrocarbons (naphthalene, terphenyls, etc.) will be able to be used in bitumen and asphalt production and other industrial areas. The fact that Hakkari asphaltite has a higher carbon content, it is possible to acquire from Şırnak asphaltite more valuable liquid and gas products as fuels, chemicals, etc.

3.2. Pyrolysis Results of Asphaltite Samples

The pyrolysis of Hakkari and Şırnak asphaltite samples was investigated in nitrogen gas environment and without nitrogen using various temperature (350-700°C) and vacuum pressure (100-600 mmHg) and various asphaltite particle sizes (100-500 µm). In addition, the effect of different raw material feeding methods and commercial Al-Ni-Co catalyst on pyrolysis results was also examined in the experiments. One of the main goals targeted in the pyrolysis process was to determine the conditions under which high liquid product yield could be achieved.

GC-MS analysis methods were used for liquid product analysis obtained as a result of pyrolysis and FTIR analysis methods were used for solids. According to the experimental pyrolysis results obtained, it was observed that the increase in vacuum pressure and the decrease in asphaltite grain sizes increased the yield of the liquid product obtained. In addition, the realization of pyrolysis in nitrogen gas environment causes an increase in liquid and gas product yield. The use of catalyst and different raw material feeding methods in the process has less effect on product efficiency.

Process temperature has the most effect on the efficiency of liquid and gaseous products obtained in pyrolysis supply in asphaltite raw material. In Figure 7 below, the effect of pyrolysis temperature in the Hakkari-1 asphaltite sample is given to the yield of liquid, gas and solid products. Liquid product yield from Hakkari 2 and Şırnak samples is about 12 and 13 percent. It has been determined that under the continuous feeding conditions of the raw material, the liquid product yield increases significantly with the temperature increasing up to 700°C and in the batch system up to 550-650°C. In addition, the highest 16.5% liquid product yield was achieved at 700°C temperature, 400 mmHg vacuum pressure, 2g/min raw material feed rate and 500 µm particle size in continuous feeding conditions. The content of GC-MS analysis of the liquid product obtained under these conditions is given in Table 2 and its chromatogram in Figure 8.

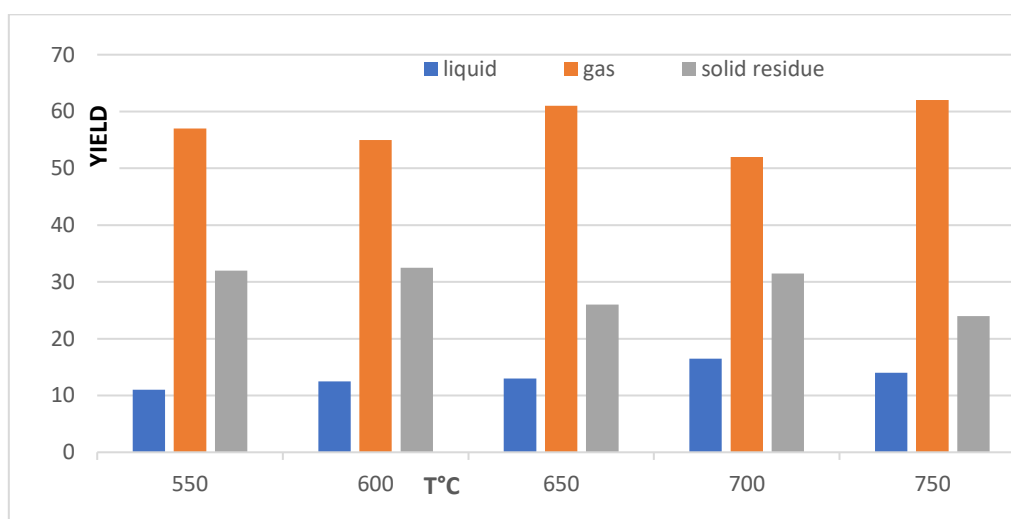


Figure 7. The effect of pyrolysis temperature of Hakkari-1 asphaltite on liquid, gas and solid product yields

As can be seen from Table 2 the liquid product mostly contains aliphatic hydrocarbons and their homologues. The carbon number of aliphatic hydrocarbons varies mainly in the C_8 (1-octane) and C_{20} (2,6,10,14-hexadecane) ranges. The aromatic compounds in the liquid are mainly composed of monocyclic (single-ring) and polycyclic (multi-ring) hydrocarbons. Single-ring aromatics mostly contain di-methyl benzenes (i.e. precious xylenes). Multi-cyclic aromatic hydrocarbons are mainly composed of naphthalene, biphenyl and their homologues. In addition, the liquid product contains a small amount of anthracene.

Table 2. Components and percentages of liquid product GC-MS from the first experiment

Detention time	component name	percent	Type	Detention time	component name	percent	Type
2,316	1-OCTENE	0,772	Alkene	12,395	Naphthalene, 2-methyl-	3,59	Polycyclic aromatic
2,725	1,3-Dimethyl-1-cyclohexen	0,126	Cycloalkene	12,607	Tridecane	0,982	Alkane
2,838	Cyclohexane, ethyl-	0,246	Alkane	14,263	Hexadecane, 2,6,10,14-tetramethyl	0,321	Alkane
3,237	Benzene, 1,3-dimethyl-	3,802	Aromatic	14,423	Benzo[b]thiophene, 3,5-dimethyl-	1,203	Sulphurous aromatic
3,362	p-Xylene	10,061	Aromatic	14,553	Naphthalene, 1-ethyl-	0,885	Polycyclic aromatic
3,487	Thiophene, 3,4-dimethyl-	0,302	Sulphurous aromatic	15,079	Naphthalene, 1,6-dimethyl-	1,016	Polycyclic aromatic
3,839	Nonane	0,835	Alkane	15,143	Naphthalene, 2,3-dimethyl-	0,679	Polycyclic aromatic
4,292	Benzene, (1-methylethyl)-	0,365	Aromatic	15,476	Naphthalene, 2,3-dimethyl-	0,379	Polycyclic aromatic
4,453	Octane, 2,6-dimethyl-	0,2	Alkane	15,661	Biphenylen	0,393	Polycyclic aromatic
4,846	Benzene, propyl-	1,03	Aromatic	15,793	Naphthalene, 1,4-dimethyl-	0,652	Polycyclic aromatic
5,009	Benzene, 1-ethyl-2-methyl-	4,771	Aromatic	16,819	Pentadecane	1,871	Alkane
5,143	Benzene, 1,2,3-trimethyl-	8,97	Aromatic	16,913	Benzo[b]thiophene, 2-ethyl-7-methyl-	0,566	Sulphurous aromatic
5,804	Decane	0,825	Alkane	17,336	Naphthalene, 1,4,5-trimethyl-	0,468	Polycyclic aromatic
6,557	Indane	0,515	Aromatic	17,649	Naphthalene, 1,6,7-trimethyl-	0,394	Polycyclic aromatic
6,746	Indene	0,916	Aromatic	17,965	Naphthalene, 1,4,6-trimethyl-	0,858	Polycyclic aromatic
6,925	Benzene, 1-methyl-3-propyl-	0,755	Aromatic	18,431	Naphthalene, 1,4,5-trimethyl-	0,466	Polycyclic aromatic
7,016	p-Mentha-1,5,8-triene	0,388	Cycloalkene	18,72	Hexadecane	1,259	Alkane
7,089	Benzene, 1-ethyl-2,4-dimethyl-	2,782	Aromatic	20,614	Heptadecane	1,41	Alkane
7,851	1-Undecene	0,471	Alkene	21,408	Dibenzothiophene	0,675	Sulphurous aromatic
8,049	Undecane	0,766	Alkane	21,879	Anthracene	0,683	Polycyclic aromatic
8,342	Benzene, 1,2,3,5-tetramethyl-	0,432	Aromatic	22,83	Octadecane	0,798	Alkane
8,478	Benzene, 1,2,4,5-tetramethyl	0,699	Aromatic	22,533	Hexadecane, 2,6,10,14-tetramethyl-	0,545	Alkane
8,899	1H-Indene, 2,3-dihydro-5-methyl-	0,284	Aromatic	23,142	Dibenzothiophene, 4-methyl-	1,246	Sulphurous aromatic
9,131	Benzene, (1-methyl-2-cyclopropen-1-yl)-	0,973	Aromatic	23,857	1-Methyldibenzothiophene	0,489	Sulphurous aromatic
9,207	Benzene, 1,2,3,4-tetramethyl-	0,624	Aromatic	23,927	Phenanthrene, 1-methyl-	0,348	Polycyclic aromatic
9,257	2-Methylindene	0,909	Aromatic	24,062	Nonadecane	0,678	Alkane
9,901	Naphthalene	1,511	Polycyclic aromatic	24,806	3,7-Dimethyldibenzothiophene	1,811	Sulphurous aromatic
10,099	Benzo[b]thiophene	0,296	Sulphurous aromatic	25,155	3,7-Dimethyldibenzothiophene	0,749	Sulphurous aromatic
10,16	1-Dodecene	0,391	Alkene	25,665	Eicosane	0,745	Alkane
10,354	Dodecane	0,723	Alkane	27,209	Heneicosane	1,15	Alkane

Based on the GC-MS results, the total proportion of hydrocarbons detected in the liquid product of asphaltite pyrolysis was 73% and 27% was not detected by GC-MS method. The classification of hydrocarbons according to the results of the analysis is as follows. In each hydrocarbon group, the percentage of the total proportion belonging to that class is given. Alkane 13.35 %, Alkene 1.63 %, Cycloalkene 0.51 %, Aromatic 37.8 %, Polycyclic aromatic 12.32 %, Sulphurous aromatic 7.33 % As can be seen from the above results, approximately 50% of the hydrocarbons detected in liquid products are monocyclic aromatic compounds, that is, they consist of benzol and mainly precious alkyl benzols. Therefore, it is economically important to extract and evaluate these valuable hydrocarbons from the liquid products obtained from the asphaltite pyrolysis method by the extraction method.

In order to recover the hydrocarbons remaining after the extraction of aromatic hydrocarbons, they all need to be subjected to the combined catalytic hydrocleaning method. As a result of this method, the double bonds of all unsaturated hydrocarbons are saturated with hydrogen, and sulfurous compounds will be converted into hydrocarbons and hydrogen sulfide as hydrocracking. The resulting 15% alkanes and cycloalkanes can be used as fuel. Naphthalene and alkylnaphthalenes can be used as valuable chemicals in the petrochemical industry and other industrial areas. From the hydrogen sulfide formed, elemental sulfur and hydrogen can be obtained by certain methods in industry.

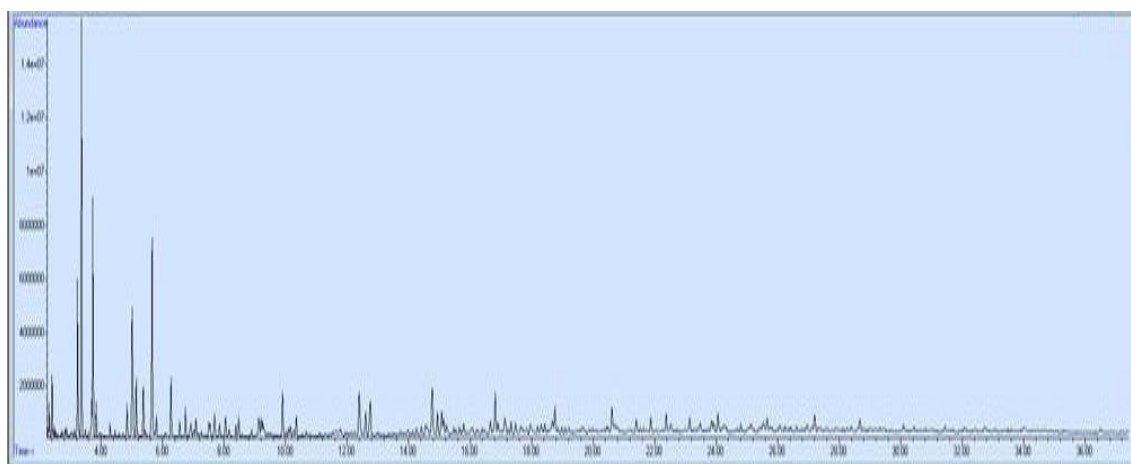


Figure 8. GC-MS chromatogram of the first plant

It is evident from the GC-MS analysis results of liquid products obtained at different pyrolysis temperatures that the change in pyrolysis temperature in the range of 500-700°C affects their concentration more than the hydrocarbon content of the obtained liquid products. The liquid product obtained in pyrolysis of Şırnak asphaltite with the use of Al-Ni-Co catalyst contains alkanes and aromatic hydrocarbons, as well as various cyclic alkanes (naphthens) such as cyclo-pentane, cyclo-hexane etc. in a significant amount. Sulfurous compounds in liquid products are mostly composed of thiofene homologs (benzo-thiophene, etc.).

4. CONCLUSION

Based on the experimental data obtained and the results of various physical and chemical analyzes, it can be said that asphaltides, which have large reserves in our country, have a very rich and diverse hydrocarbon content (mainly saturated aliphatic and aromatic hydrocarbons) as a petroleum-based material. In addition, as research shows, asphaltites also contain high amounts of organic sulfurous compounds, mostly thiophene-based. Therefore, with the use of effective technological and environmentalist methods, it is important both economically and strategically to transform asphaltites into valuable products to contribute to our country's industry. Taking these into account, different technological methods and recommendations that can be applied in industry for the effective evaluation of asphaltites, as well as thermal pyrolysis:

1. Catalytic Hydrocracking

Asphaltalates can be subjected to Catalytic Hydrocracking process with a high pressure of 200-250 bar hydrogen pressure and low temperature 300-350°C. In this process, all heavy hydrocarbons, aromatics and

sulfurous compounds are broken down by exposure to hydrocracking reactions, resulting in sulfur-free gasoline, diesel fuel C₁-C₄ (Methane, ethane, propane, butane) and Hydrogen sulfide (H₂S). In addition, from the formed hydrogen sulfide, elemental sulfur, which is widely used in industry, can be produced. Industrial catalysts can be used in the process.

2. Extraction

Fractions containing monocyclic aromatic hydrocarbons (benzol and alkylbenzols) and cyclic aromatic hydrocarbons (naphthalene and alkylnaphthalenes) contained in asphaltites are separated under vacuum and precious pure aromatic hydrocarbons can be obtained from them by extraction (removing valuable aromatics with a solvent by distillation method). The solvent is constantly circulating in the system. The rest of the asphaltite can be subjected to Catalytic Hydrocracking to obtain liquid products such as gasoline, diesel fuel and C₁-C₄ gas products that can be used as fuel.

3. Hydrodealkylation-hydrocracking

The only difference of this method from method 2 is that the aromatic fractions separated from the asphaltite are subjected to the high-temperature and low-pressure hydrodealkylation-hydrocracking process instead of extraction, and finally pure benzol and naphthalene can be obtained. In this process, alkyl benzons are subjected to the dealkylation reaction and turn into a very important hydrocarbon such as benzol in the petrochemical industry. The remaining non-aromatic ones also turn into gases as hydrocracking. Thus, as a result of the high-temperature hydrodealkylation-hydrocracking process, high-purity benzol (99,99%) and the gas products C₁-C₄ are obtained. The hydrodealkylation-hydrocarbon process is carried out catalytically at a hydroreal pressure of 625°C and 55-60 bar and thermally at a hydrogen pressure of 700-725°C and 25-30 bar. Each of these proposed methods has its advantages and flaws. Therefore, of course, in order to determine an optimal production method, it is necessary to make a preliminary feasibility of their economic and technological indicators. It is also important that the selected technology is tested on a pilot scale before its industrial application.

ACKNOWLEDGEMENT

We would like to thank Gazi University BAP unit for its support in the research project FDK-2022-7294 throughout this study.

CONFLICT OF INTEREST

The authors declare no conflict of interest.

REFERENCES

- Bilgin, O. (2021). Investigation of the cleanability of asphaltite by flotation. *Chemical Physics Letters*, 776, 138710. doi:[10.1016/j.cplett.2021.138710](https://doi.org/10.1016/j.cplett.2021.138710)
- Demirci, S., Sivrikaya, O., & Vapur, H. (2019). Enerji Kaynağı Olarak Asfaltit: Oluşumu, İçeriği, Türkiye Rezervleri, Temizlenmesi [Asphaltite as Energy Source; Formation, Content, Turkey Reserves, Cleaning]. *Niğde Ömer Halisdemir Üniversitesi Mühendislik Bilimleri Dergisi*, 8(1), 312-325. doi:[10.28948/ngumuh.517131](https://doi.org/10.28948/ngumuh.517131)
- Gao, W., Zhang, M., & Wu, H. (2022). Bed agglomeration during fast pyrolysis of bio-oil derived fuels in a fluidized-bed reactor. *Fuel*, 328, 125359. doi:[10.1016/j.fuel.2022.125359](https://doi.org/10.1016/j.fuel.2022.125359)
- Hamamci, C., Kahraman, F., & Düz, M. Z. (1997). Desulfurization of southeastern Anatolian asphaltites by the Meyers method. *Fuel Processing Technology*, 50(2-3), 171-177. doi:[10.1016/s0378-3820\(96\)01077-6](https://doi.org/10.1016/s0378-3820(96)01077-6)
- Hameed, S., Sharma, A., & Pareek, V. (2023). A Distributed Activation Energy Model for Cellulose Pyrolysis in a Fluidized Bed Reactor. *Chemical Engineering Research and Design*, 191, 414-425. doi:[10.1016/j.cherd.2023.01.048](https://doi.org/10.1016/j.cherd.2023.01.048)

- Kosan, İ., Ustunisik, G., Önal, M., Sarıkaya, Y., & Bozkurt, P. A. (2021). Irreversible ammonia adsorption on asphaltite bottom ash: A thermodynamic approach. *Colloids and Surfaces A: Physicochemical and Engineering Aspects*, 626, 126933. doi:[10.1016/j.colsurfa.2021.126933](https://doi.org/10.1016/j.colsurfa.2021.126933)
- Li, B., Song, M., Xie, X., Wei, J., Xu, D., Ding, K., Huang, Y., Zhang, S., Hu, X., Zhang, S., & Liu, D. (2023). Oxidative fast pyrolysis of biomass in a quartz tube fluidized bed reactor: Effect of oxygen equivalence ratio. *Energy*, 270, 126987. doi:[10.1016/j.energy.2023.126987](https://doi.org/10.1016/j.energy.2023.126987)
- Sert, M., Ballice, L., Yüksel, M., & Sağlam, M. (2011). Effect of mineral matter on the isothermal pyrolysis product of Şırnak asphaltite (Turkey). *Fuel*, 90(8), 2767-2772. doi:[10.1016/j.fuel.2011.04.007](https://doi.org/10.1016/j.fuel.2011.04.007)
- Sezer, M., Bilgesü, A. Y., & Karaduman, A. (2008). Flash pyrolysis of Silopi asphaltite in a free-fall reactor under vacuum. *Journal of Analytical and Applied Pyrolysis*, 82(1), 89-95. doi:[10.1016/j.jaap.2008.01.003](https://doi.org/10.1016/j.jaap.2008.01.003)
- Taskesen, E., Acar, Ş., Arlı, F., Dumrul, H., Ertuğrul, G., Bülbül, Ş., & Özcan, E. (2022). Şırnak-Uludere Bölgesinde Yaygın Olarak Bulunan Asfaltitlerden Doğal Hüyük Asit Elde Edilebilirliğinin İncelenmesi [Investigation of the ability to obtain natural humic acid from asphaltites widely found in Şırnak-Uludere region]. *Politeknik Dergisi*, 25(2), 691-697. doi:[10.2339/politeknik.766461](https://doi.org/10.2339/politeknik.766461)



Gazi University

Journal of Science

PART A: ENGINEERING AND INNOVATION

<http://dergipark.org.tr/guj.1276486>

Comparison of the Number of Particle History for Monte Carlo Codes in Gamma-Ray Spectroscopy

Esra UYAR^{1*} Zeynep AybÜke GÜNEKBAY¹ ¹Gazi University, Faculty of Sciences, Department of Physics, Ankara, Türkiye

Keywords	Abstract
HPGe detector	Monte Carlo is a numerical computation algorithm that is widely used in many fields of science and is used to obtain numerical results with a large number of repeated random samplings. Radiation transport with Monte Carlo simulation continues to increase its popularity in the fields of radiation measurement. The high accuracy and precision measurement of radionuclide activity amounts in gamma-ray spectrometry depends on the efficiency calibration of the detector. Efficiency calibration is carried out in two ways, using certified reference materials, by experimental method or Monte Carlo simulation method. The experimental method is expensive, procedurally complex and time-consuming due to the supply of reference material. The use of the Monte Carlo technique in a reliable way without the need for a standard radioactive source in determining the detector efficiency is becoming common. The most critical step for accurate and precise results in getting the response of a detector with the Monte Carlo method is modeling the detector with its realistic dimensions. Another parameter as important as detector modeling is the number of histories in the simulation code examined in this study. The effect of the number of histories on efficiency was examined in detail using PHITS, GESPECOR and DETEFF Monte Carlo simulation codes. Since there is no definite number about this effect, which is important for obtaining meaningful and realistic results, the change in the efficiency value was examined by increasing the number of stories from 105 to 108. The results obtained in this work showed that at least 107 particle numbers should be used in all three programs where the uncertainty is below 1%. If the existing facilities are sufficient, it can be increased to 108s in case of having a more equipped and fast computer. However, going higher than this value does not make any sense as seen from the study.
Monte Carlo	
History Number	
Particle Number	
Number of Runs	
PHITS	

Cite

Uyar, E., & Günekbay, Z. A. (2023). Comparison of the Number of Particle History for Monte Carlo Codes in Gamma-Ray Spectroscopy. *GU J Sci, Part A, 10(2)*, 176-183. doi:10.54287/guj.1276486

Author ID (ORCID Number)	Article Process
0000-0001-7585-9635	Submission Date 03.04.2023
0009-0000-4049-1391	Revision Date 22.05.2023
	Accepted Date 12.06.2023
	Published Date 20.06.2023

1. INTRODUCTION

Monte Carlo (MC) simulation is a statistical technique for directly simulating a physical process. The basis of the MC method is a random number generator consisting of random numbers in the range (0, 1). Since such numbers are generated by deterministic algorithms, they are untruly random. However, such pseudo-random numbers are statistically indistinguishable from real random numbers that are evenly distributed in the range (0, 1) and are independent of each other (Kroese & Rubinstein, 2012). Simulating particle transport in MC codes is widely used in a wide variety of fields such as radiotherapy, radiation shielding, detector modeling, medical physics, nuclear technology, accelerator design, astrophysics applications (Iwamoto et al., 2017; Lépy et al., 2019). The MC simulation technique is increasingly used in gamma-ray spectrometry due to advances in technology and a variety of simulation codes (Cebastien Joel et al., 2018; Ordóñez et al., 2019). Accurate modeling of the detection chain via the MC method is crucial for obtaining quality data from detectors and for the design of experiments. MC modeling of radiation detectors is a widely accepted numerical method for detector characterization. For example, MC programs are an excellent guide for the characterization of the

*Corresponding Author, e-mail: esrauyar@gazi.edu.tr

detectors by determining the dead layer thickness, which is a time-varying parameter in HPGe detectors (Uyar & Bölükdemir, 2022). In gamma-ray spectrometric studies, the MC method is mostly used to obtain the detector efficiency (Sima, 2012; Mrdja et al., 2018; Ordóñez et al., 2019). In addition to the efficiency, MC simulation programs are used to acquire the true coincidence summing correction factor, which is an important correction factor (Vidmar et al., 2011; Yoon et al., 2020). Since this method is a statistical process in which random numbers are used, keeping the number of histories as high as possible allows us to obtain more meaningful results.

The principle of the Monte Carlo method consists in simulating the history of a certain number of photons passing through the HPGe crystal. Therefore, these photons should interact with the Ge crystal in an appropriate number for the photoelectric effect, Compton scattering and pair production mechanisms at energies greater than 1022 keV to take place. The number of these photons is called the history number in Monte Carlo simulations. But there is no exact value regarding the number of histories. For example, Ordóñez et al. in order to obtain a statistical error of less than 1.5%, they set the number of histories in each simulation at 20 million (Ordóñez et al., 2019). Azli & Chaoui (2015) used 100 million particles to achieve a relative error of less than 1% in the calculated efficiency. Subercaze et al. (2022) used 3 million and Miroslav et al. used 1 million particles in their study (Jeřkovský et al., 2019). Therefore, as can be seen from the literature, a number of histories ranging from 1 million to 100 million were used. Here, the performance and features of the computer used in the calculation are very important.

In this study, the effect of history number on efficiency calculation with the MC method was investigated using three different MC programs. For this purpose, the effect of history number was examined in a wide energy range using 59.5 keV, 383.9 keV, 661.7 keV, 1173.2 keV and 1332.5 keV gamma energies. 10^5 , 10^6 , 10^7 and 10^8 were chosen as history numbers.

2. MATERIAL AND METHOD

MC codes used in HPGe detector response fall into two categories: specialized codes in gamma-ray spectrometry, mostly written specifically for efficiency calculations, and multi-purpose MC codes for a wide variety of applications. The PHITS used in this study is a multi-purpose code for all kinds of applications; GESPECOR and DETEFF are specialized purpose MC codes.

2.1. PHITS Monte Carlo simulation code

PHITS is a multi-purpose MC simulation code for particle transport that was created in cooperation between JAEA, KEK, RIST, and numerous other institutions. With the use of several nuclear reaction models and nuclear data libraries, it can be interested in the transport of all particles over various energies (Sato et al., 2018). The parameters for the history number in PHITS are maxcas and maxbch (Figure 1). The total number of histories is equal to the product of maxcas, the number of particles per batch, and maxbch, the number of batches. It is recommended to set the maxbch value greater than or equal to 10 to obtain reliable results. A larger maxbch provides more reliable statistical uncertainties, but may require a longer computation time.

```
[ Parameters ]
icntl   =          0    # (D=0) 3:ECH 5:NOR 6:SRC 7,8:GSH 11:DSH 12:DUMP
maxcas  = 1000000    # (D=10) number of particles per one batch
maxbch  =          10  # (D=10) number of batches
```

Figure 1. Defining the number of histories in the PHITS MC code

2.2. GESPECOR

GESPECOR is a special-purpose Monte Carlo-based code used for calculating true coincidence summing and self-absorption effects, especially full energy peak efficiency in gamma-ray spectrometry. In GESPECOR, variance reduction techniques are applied to improve the statistical accuracy of the computation versus the computation time. The number of histories is determined by the number of runs entered in the window that opens automatically in the system before starting the simulation (Figure 2). This window opens for each quantity desired to be calculated by defining the detector, material, geometry, and prompts the user to enter a random number and a history number.

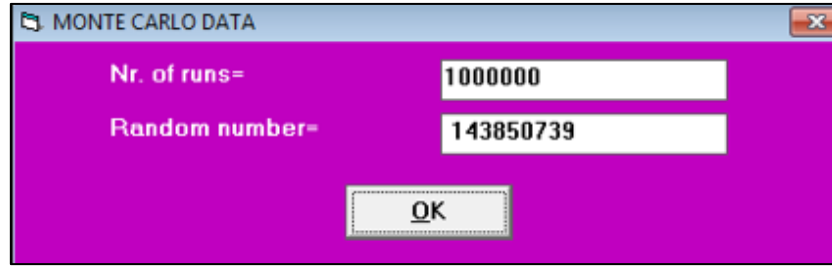


Figure 2. Defining the number of histories in the GESPECOR MC code

2.3. DETEFF

DETEFF; it is a user friendly MC program for calculating the full energy peak efficiency in gamma-ray detectors such as NaI, CsI, Ge(Li), HPGGe and Si(Li) (DÍaz & Vargas, 2010). In DETEFF, the parameters for the number of histories are experiments and number of photons in the Statistics tab (Figure 3). The total number of histories is equal to the value in the experiments multiplied by the number of photons.

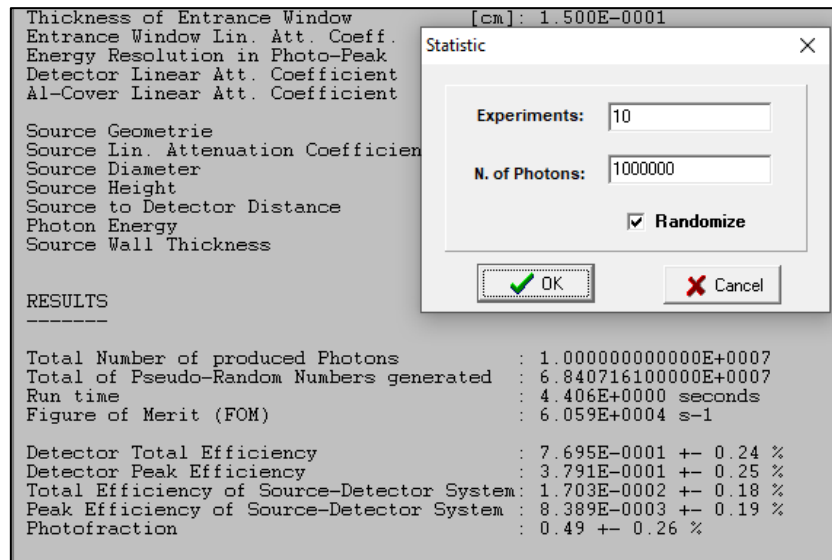


Figure 3. Defining the number of histories in the DETEFF MC code

3. RESULTS AND DISCUSSION

Measurements were taken at 10^5 , 10^6 , 10^7 , 10^8 using PHITS, GESPECOR and DETEFF MC codes and ^{241}Am (59.54 keV), ^{133}Ba (383.85 keV), ^{137}Cs (661.66 keV) and ^{60}Co (1173.23 keV and 1332.49 keV) peaks. The efficiency values taken at different particle numbers, with their uncertainties, are given in Table 1.

As shown in the Table 1, the increase in the number of history does not cause a linear change in the efficiency. While the increase in the number of histories decreases the efficiency in some energies, the efficiency increases in some energies. However, the percentage uncertainty values decrease as the number of history increases in all MC codes, that is, they improve. According to Table 2, where the relationship between the history numbers is examined, the percentage difference decreases as the number of particles increases in all MC codes. The percentage difference values between the history numbers (n) were calculated according to the Equation 1.

$$\frac{|10^n + 10^{n+1}|}{10^n} \times 100 \quad (1)$$

For example, when the percentage difference value according to the efficiency values obtained with 10^5 and 10^6 history numbers with an energy value of 59.54 keV is calculated according to Equation 1; $\frac{|0.00455 - 0.00475|}{0.00455} \times 100 = 4.37$ is obtained.

Table 1. Efficiency values obtained with PHITS, GESPECOR and DETEFF for different particle numbers

Particle Number	Nuclide	Energy (keV)	PHITS (Uncertainty %)	GESPECOR (Uncertainty %)	DETEFF (Uncertainty %)
10 ⁵	²⁴¹ Am	59.54	0.00455 (0.047)	0.00539 (0.057)	0.00529 (0.840)
	¹³³ Ba	383.85	0.01095 (0.030)	0.01086 (0.270)	0.01150 (1.770)
	¹³⁷ Cs	661.66	0.00766 (0.036)	0.00803 (0.360)	0.00855 (2.440)
	⁶⁰ Co	1173.23	0.00568 (0.042)	0.00592 (0.510)	0.00628 (3.780)
	⁶⁰ Co	1332.49	0.00517 (0.044)	0.00552 (0.370)	0.00611 (3.410)
10 ⁶	²⁴¹ Am	59.54	0.00475 (0.015)	0.00539 (0.012)	0.00534 (0.440)
	¹³³ Ba	383.85	0.01082 (0.010)	0.01089 (0.110)	0.01115 (0.830)
	¹³⁷ Cs	661.66	0.00796 (0.011)	0.00807 (0.160)	0.00848 (0.420)
	⁶⁰ Co	1173.23	0.00589 (0.013)	0.00594 (0.140)	0.00616 (1.000)
	⁶⁰ Co	1332.49	0.00543 (0.014)	0.00550 (0.120)	0.00577 (0.910)
10 ⁷	²⁴¹ Am	59.54	0.00483 (0.005)	0.00539 (0.006)	0.00530 (0.130)
	¹³³ Ba	383.85	0.01090 (0.003)	0.01089 (0.024)	0.01126 (0.270)
	¹³⁷ Cs	661.66	0.00815 (0.004)	0.00807 (0.042)	0.00842 (0.210)
	⁶⁰ Co	1173.23	0.00599 (0.004)	0.00593 (0.068)	0.00615 (0.250)
	⁶⁰ Co	1332.49	0.00557 (0.006)	0.00551 (0.042)	0.00571 (0.150)
10 ⁸	²⁴¹ Am	59.54	0.00483 (0.001)	0.00539 (0.004)	0.00530 (0.050)
	¹³³ Ba	383.85	0.01091 (0.001)	0.01088 (0.012)	0.01125 (0.070)
	¹³⁷ Cs	661.66	0.00815 (0.001)	0.00807 (0.011)	0.00838 (0.060)
	⁶⁰ Co	1173.23	0.00600 (0.001)	0.00592 (0.015)	0.00616 (0.100)
	⁶⁰ Co	1332.49	0.00559 (0.001)	0.00551 (0.011)	0.00571 (0.100)

Table 2. Percentage difference values between history numbers from PHITS, GESPECOR and DETEFF

History Number	Nuclide	Energy (keV)	PHITS	GESPECOR	DETEFF
n:5	²⁴¹ Am	59.54	4.37	0.02	0.98
	¹³³ Ba	383.85	1.21	0.25	3.04
	¹³⁷ Cs	661.66	3.90	0.53	0.78
	⁶⁰ Co	1173.23	3.84	0.30	1.85
	⁶⁰ Co	1332.49	5.11	0.36	5.57
n:6	²⁴¹ Am	59.54	1.75	0.01	0.64
	¹³³ Ba	383.85	0.79	0.04	0.99
	¹³⁷ Cs	661.66	2.34	0.05	0.70
	⁶⁰ Co	1173.23	1.50	0.25	0.19
	⁶⁰ Co	1332.49	2.59	0.15	1.04
n:7	²⁴¹ Am	59.54	0.05	0.01	0.08
	¹³³ Ba	383.85	0.25	0.06	0.09
	¹³⁷ Cs	661.66	0.25	0.04	0.32
	⁶⁰ Co	1173.23	0.37	0.04	0.16
	⁶⁰ Co	1332.49	0.42	0.03	0.14

The biggest difference in the PHITS MC code occurred at n:5, that is, between 10^5 and 10^6 history numbers (up to 5.1%). When 10^6 and 10^7 data are examined, it is seen that the difference values are smaller and close to each other (Figure 4).

When the percent difference values between the particle numbers calculated according to the Equation (1) were examined for GESPECOR, an uncertainty of less than 1% was obtained in all particle numbers. The lowest uncertainty was obtained between 10^7 and 10^8 , as expected (Figure 5).

The biggest difference in the DETEFF MC code occurred at n:5, that is, between the historical numbers 10^5 and 10^6 (up to 5.6%). When the 10^7 and 10^8 data are examined, it is seen that the difference values are less than 1% (Figure 6).

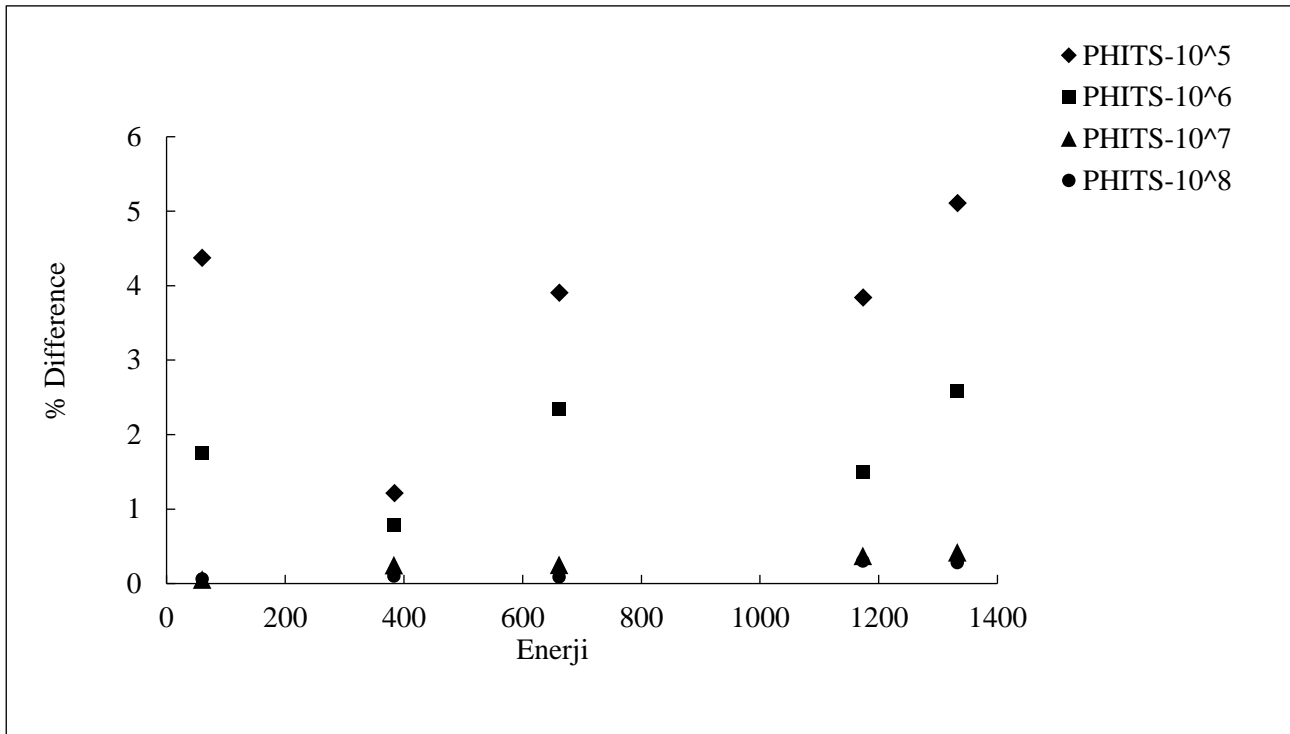


Figure 4. Variation of percent difference values between particle numbers obtained with PHITS according to energy

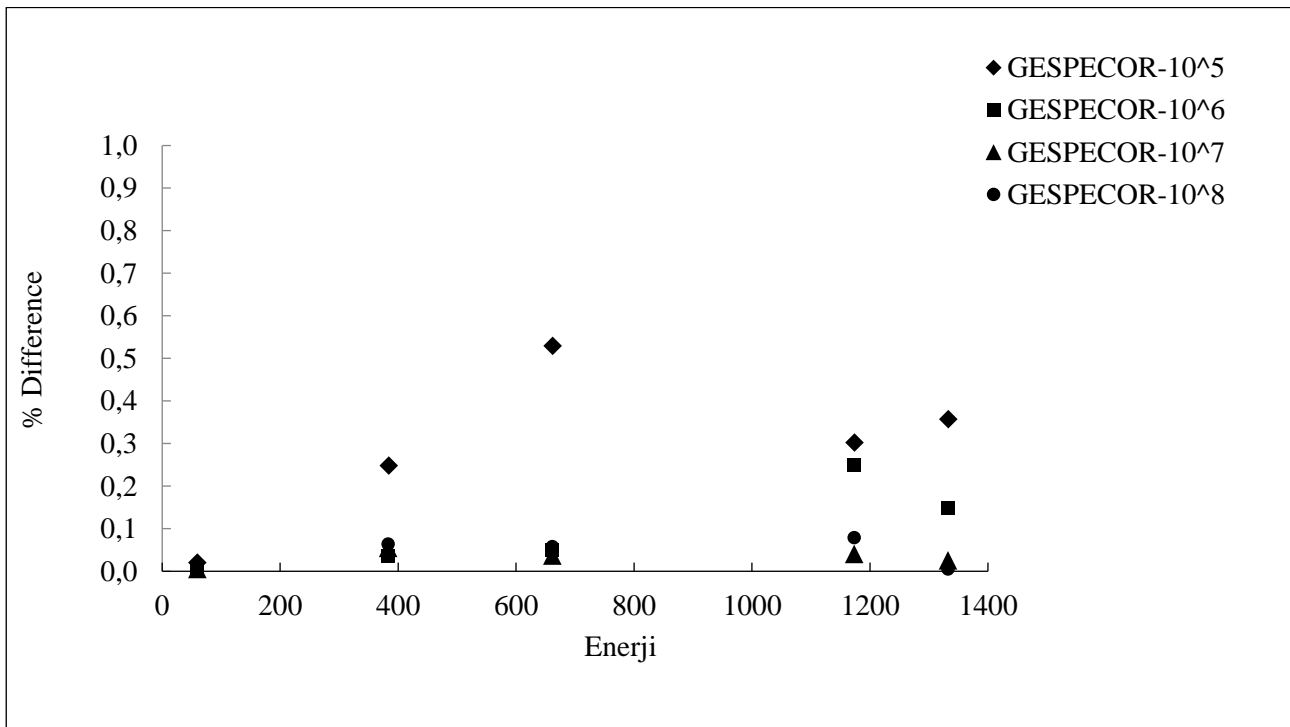


Figure 5. Variation of percent difference values between particle numbers obtained with GESPECOR according to energy

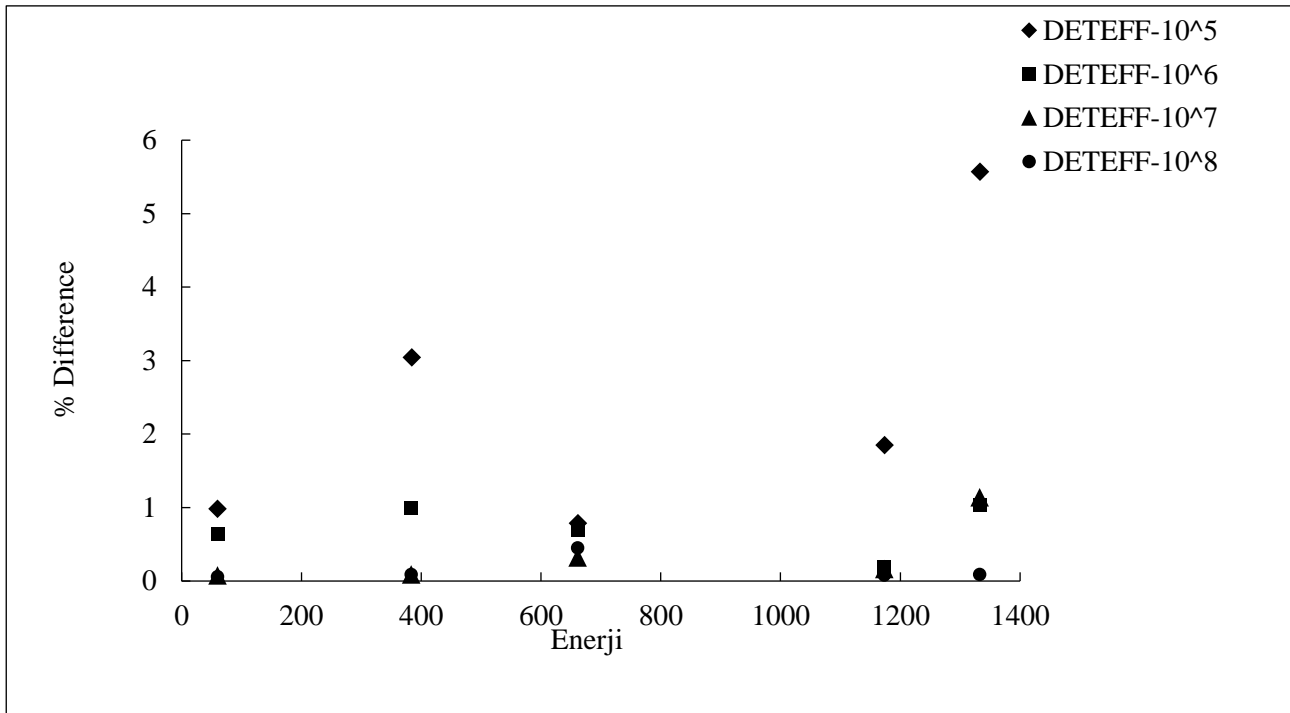


Figure 6. Variation of percent difference values between particle numbers obtained with DETEFF according to energy

4. CONCLUSION

In this study, the effect of the number of histories on the efficiency was investigated with different Monte Carlo codes. Efficiency values were obtained at energies in the range of 59.5-1332.5 keV by using 10^5 , 10^6 , 10^7 and 10^8 particle numbers. Efficiency values were obtained for each code at the same particle count and the same energy at varying times ranging from a few seconds to several hours. Therefore, it is seen that the execution times of each code is different from each other. It has been observed that the dedicated packages GESPECOR and DETEFF give much faster results on average than general-purpose MC code PHITS. In MC programs, faster results are obtained by applying reduction techniques to the variance value, which is the mean of the square of the differences from the mean, also known as the standard deviation. MC programs such as GESPECOR and DETEFF, which are specially developed for gamma-ray spectrometric studies, cause faster results due to the algorithms developed by applying these techniques. General-purpose packages like PHITS are at a disadvantage in terms of speed to get results due to their more complex physics and particle tracking. In DETEFF and GESPECOR the percentage difference between particle counts is less, but repeatability is low. In other words, different values were obtained in each repeated simulation.

When the efficiency values in all MC programs are examined according to Table 1, it is seen that the efficiency value in low history numbers is determined with a difference of up to 8% from what it should be. Therefore, while uncertainty contributes to the efficiency value from many factors, we should avoid increasing the uncertainty by keeping the number of histories low. In conclusion, it was determined that at least 10^7 particle numbers should be adjusted to obtain good statistics in simulations where gamma-ray spectrometric calculations are made.

CONFLICT OF INTEREST

The authors declare no conflict of interest.

REFERENCES

- Azli, T., & Chaoui, Z. E.-A. (2015). Performance reevaluation of a N-type coaxial HPGe detector with front edges crystal using MCNPX. *Applied Radiation and Isotopes*, 97, 106-112. doi:[10.1016/j.apradiso.2014.12.027](https://doi.org/10.1016/j.apradiso.2014.12.027)
- Cebastien Joel, G. S., Maurice, N. M., Eric Jilbert, N. M., Ousmanou, M., & David, S. (2018). Monte Carlo method for gamma spectrometry based on GEANT4 toolkit: Efficiency calibration of BE6530 detector. *Journal of Environmental Radioactivity*, 189, 109-119. doi:[10.1016/j.jenvrad.2018.03.015](https://doi.org/10.1016/j.jenvrad.2018.03.015)
- Díaz, N. C., & Vargas, M. J. (2010). Improving the trade-off between simulation time and accuracy in efficiency calibrations with the code DETEFF. *Applied Radiation and Isotopes*, 68(7-8), 1413-1417. doi:[10.1016/j.apradiso.2009.11.021](https://doi.org/10.1016/j.apradiso.2009.11.021)
- Iwamoto, Y., Sato, T., Hashimoto, S., Ogawa, T., Furuta, T., Abe, S., Kai, T., Matsuda, N., Hosoyamada, R., Niita, K. (2017). Benchmark study of the recent version of the PHITS code. *Journal of Nuclear Science and Technology*, 54(5), 617-635. doi:[10.1080/00223131.2017.1297742](https://doi.org/10.1080/00223131.2017.1297742)
- Ješkovský, M., Javorník, A., Breier, R., Slučiak, J., & Povinec, P. P. (2019). Experimental and Monte Carlo determination of HPGe detector efficiency. *Journal of Radioanalytical and Nuclear Chemistry*, 322(3), 1863-1869. doi:[10.1007/s10967-019-06856-4](https://doi.org/10.1007/s10967-019-06856-4)
- Kroese, D. P., & Rubinstein, R. Y. (2012). Monte Carlo methods. *Wiley Interdisciplinary Reviews: Computational Statistics*, 4(1), 48-58. doi:[10.1002/wics.194](https://doi.org/10.1002/wics.194)
- Lépy, M. C., Thiam, C., Anagnostakis, M., Galea, R., Gurau, D., Hurtado, S., Karfopoulos, K., Liang, J., Liu, H., Luca, A., Mitsios, I., Potiriadis, C., Savva, M. I., Thanh, T. T., Thomas, V., Townson, R. W., Vasilopoulou, T., & Zhang, M. (2019). A benchmark for Monte Carlo simulation in gamma-ray spectrometry. *Applied Radiation and Isotopes*, 154, 108850. doi:[10.1016/j.apradiso.2019.108850](https://doi.org/10.1016/j.apradiso.2019.108850)
- Mrdja, D., Bikit, K., Forkapic, S., Bikit, I., Slivka, J., & Hansman, J. (2018). Improvement of in-situ gamma spectrometry methods by Monte-Carlo simulations. *Journal of Environmental Radioactivity*, 188, 23-29. doi:[10.1016/j.jenvrad.2017.11.005](https://doi.org/10.1016/j.jenvrad.2017.11.005)
- Ordóñez, J., Gallardo, S., Ortiz, J., Sáez-Muñoz, M., & Martorell, S. (2019). Intercomparison of full energy peak efficiency curves for an HPGe detector using MCNP6 and GEANT4. *Radiation Physics and Chemistry*, 155, 248-251. doi:[10.1016/j.radphyschem.2018.06.049](https://doi.org/10.1016/j.radphyschem.2018.06.049)
- Sato, T., Iwamoto, Y., Hashimoto, S., Ogawa, T., Furuta, T., Abe, S., Kai, T., Tsai, P.-E., Matsuda, N., Iwase, H., Shigyo, N., Sihver, L., & Niita, K. (2018). Features of Particle and Heavy Ion Transport code System (PHITS) version 3.02. *Journal of Nuclear Science and Technology*, 55(6), 684-690. doi:[10.1080/00223131.2017.1419890](https://doi.org/10.1080/00223131.2017.1419890)
- Sima, O. (2012). Efficiency Calculation of Gamma Detectors by Monte Carlo Methods. *Encyclopedia of Analytical Chemistry*. doi:[10.1002/9780470027318.a9142](https://doi.org/10.1002/9780470027318.a9142)
- Subercaze, A., Sauzedde, T., Domergue, C., Destouches, C., Philibert, H., Fausser, C., Thiollay, N., Gregoire, G., & Zoia, A. (2022). Effect of the geometrical parameters of an HPGe detector on efficiency calculations using Monte Carlo methods. *Nuclear Instruments and Methods in Physics Research Section A: Accelerators, Spectrometers, Detectors and Associated Equipment*, 1039, 167096. doi:[10.1016/j.nima.2022.167096](https://doi.org/10.1016/j.nima.2022.167096)
- Uyar, E., & Bölükdemir, M. H. (2022). Characterisation of two p-type HPGe detectors by measurements and Monte Carlo simulations. *Measurement*, 204, 112092. doi:[10.1016/j.measurement.2022.112092](https://doi.org/10.1016/j.measurement.2022.112092)
- Vidmar, T., Kanisch, G., & Vidmar, G. (2011). Calculation of true coincidence summing corrections for extended sources with EFFTRAN. *Applied Radiation and Isotopes*, 69(6), 908-911. doi:[10.1016/j.apradiso.2011.02.042](https://doi.org/10.1016/j.apradiso.2011.02.042)
- Yoon, E. T., Kang, M. Y., Kim, I. J., Sun, G. M., & Choi, H.-D. (2020). Coincidence summing correction for a voluminous ¹⁵²Eu source. *Nuclear Engineering and Technology*, 52(6), 1266-1270. doi:[10.1016/j.net.2019.11.015](https://doi.org/10.1016/j.net.2019.11.015)



Gazi University

Journal of Science

PART A: ENGINEERING AND INNOVATION

<http://dergipark.org.tr/guj.1264848>

Evaluation of Range Estimation Performance of FLIR with Field Requirements Criteria

Buket AKIN^{1*} ¹Gazi University, Faculty of Science, Department of Physics, Ankara, Türkiye

Keywords	Abstract
Forward-Looking Infrared Thermal Imaging Infrared System Performance	Thermal imaging performance depends on many variables, ranging from the properties of the imaged object to atmospheric transmittance and system parameters. After clarification of the functional needs in system design or procurement, system parameters of the design that can meet these needs should be determined. Diagnosis/recognition from a distance is one of the foremost of these needs. The following briefly introduces the Forward Looking Infrared (FLIR) systems, followed by explanations for calculating the theoretical diagnostic range. After the theoretical information, sample systems are given, and high-performance FLIR systems are presented. To accurately analyze, measure and predict the performance of FLIR systems, a model should calculate summary performance measures of the system in the form of Minimum Resolvable Temperature (MRT) and Modulation Transfer Function (MTF) between a target and its background and estimate range for a given scenario electro-optical required for the performance evaluation of the system. The accuracy of these calculations will ultimately determine the accuracy of the model by which the performance of the FLIR system is evaluated.

Cite

Akin, B. (2023). Evaluation of Range Estimation Performance of FLIR with Field Requirements Criteria. *GU J Sci, Part A, 10(2)*, 184-195. doi:10.54287/guj.1264848

Author ID (ORCID Number)	Article Process
0000-0002-9748-4886 Buket AKIN	Submission Date 14.03.2023 Revision Date 27.03.2023 Accepted Date 18.04.2023 Published Date 21.06.2023

1. INTRODUCTION

Long-range electro-optical surveillance systems (Javidi, 2006) have been widely used in industrial applications. FLIR, one of these applications, was used for mapping purposes by the US Air Force in the 1960s in the infrared systems looking toward the earth from aircraft. When these systems were modified to develop new systems for imaging purposes, the Forward Looking Infrared (FLIR) was used to distinguish it from downward-facing systems. FLIR can be perceived as a camera that displays in the infrared band. The primary purpose is to perform the function of seeing in the dark by perceiving and processing the natural dispersion created by the objects, and Planck's law explains this spread.

Thermal imagers are intended to utilize the atmospheric transmission window to gather target radiation in the infrared region of the spectrum. Due to variations in IR signature and atmospheric transmission in the scene, the range is impacted by the choice of spectral sensitivity band. The atmosphere is not equally permeable at all wavelengths. The ranges with high permeability are between 3-5 μ m and 8-14 μ m. The 3-5 μ m band is called medium wavelength infrared (MWIR), and the 8-14 μ m band is called long wavelength infrared (LWIR). The transmittance in these ranges also makes FLIR systems different from other night vision systems. Other night vision systems provide images by amplifying visible light in the environment that is so dim that human eye cannot perceive. FLIR systems, on the other hand, can provide images in complete darkness, even from behind a curtain of fog and smoke. Every user is interested in knowing the range of these imagers, which is a crucial parameter. The range parameters for these systems can be determined by computer simulations, field testing,

*Corresponding Author, e-mail: bktkn90@gmail.com

or laboratory measurements. Calculating range parameters in computer simulations requires the a priori knowledge of the exact characteristics of the optical system, detector array, signal processing, and imaging modules of a particular thermal imager.

Thermal cameras' detection, recognition, and identification ranges can be determined using many methods. The oldest and most famous of these methods is the Johnson criterion, published in 1958 (Johnson, 1958). It allows an observing device's detection, recognition, and identification ranges (assuming a 50% target discrimination probability) to be determined based on the measured spatial resolution characteristics. Its calculation method is based on how many pixels are adequate to detect, recognize and identify (DRI) an object with 50% probability. For instance, the number of pixels to resolve a human are 3.5x1, 11x3 and 23x6 for DRI, respectively. The minimum resolvable temperature difference (MRTD) or minimum resolvable temperature (MRT) characteristics must be measured to determine thermal camera's detection, diagnosis, and recognition ranges. MRT links Johnson's concept of target critical size resolvable rods and thermal imaging system performance. MRT is the fundamental measurement parameter for evaluating the overall imaging performance of FLIR systems. The value of MRT measurement is determined by incorporating sensitivity (temporal and spatial), resolution, system performance and observer effects. The MRT measurement creates an association between the performance of the thermal imager and the thermal imaging model to deliver the anticipated range value with good precision and reproducibility in real-world settings.

MRT is often the primary imaging requirement specified for a FLIR system, as it is the basis for range estimates. The NATO standards (NATO Standardization Agency, 1995) define the MRT measurement process and the determination of range parameters, and the parameter N50 specifies the number of pairs per target size. Although Johnson's criteria contribute to predicting the range parameters of thermal cameras, they do not provide reliable results in today's systems. The Johnson criteria do not consider image noise levels, electronic circuits used for high-frequency amplification, digital filtering, or interpolation, which impact range performance in such systems. Therefore, the latest, complete and reliable Targeting Mission Performance Metric (TTP) model has been developed by the US Army Night Vision and Electronic Sensors Directorate since 2000 (Schmieder & Weathersby, 1983; Driggers et al., 2000; Vollmerhausen & Driggers, 2000; NATO Research and Technology Organisation, 2003; Moyer et al., 2004; 2006; Vollmerhausen & Jacobs, 2004; Krapels et al., 2006; 2008; Teaney et al., 2007; Vollmerhausen et al., 2010) and the NVThermIP software (U.S. Army Night Vision and Electronic Sensors Directorate, 2001) is based on this model. Based on the 2.7*N50, it was defined as V50 (Krapels et al., 2008). The TTP model is highly sophisticated since it takes the detector, platform, environment, and target specified in the image into account. (Vollmerhausen & Jacobs, 2004; Hou et al., 2022).

Most range estimation models deal with parameter definitions of the imaging system, depending on the scenario, and the range of the image. These models make thermal image analysis and synthesis convenient, which are used to define the best system design. To verify the utility of these models, the results are expanded to range estimation of the images using various techniques, such as visual information detection modeling, target IR signature, and atmospheric route-dependent image distortion (Figure 1). Currently, efforts to use automatic objective target resolution criteria are ongoing. However, current applications have not yet reached the required level of accuracy as it involves developing complex image-processing techniques (Perić et al., 2019; Sagan et al., 2019).

The estimation models of range parameters of thermal imagers are based on the modulation transfer function (MTF). MTF is a fundamental parameter that determines the imaging resolution of the sensor and is utilized in system design and analysis. The diffraction-limited optical system MTF function can be reasonably calculated in terms of the limits defining the resolution of the system and the highest attainable spatial frequency because the MTF function has a known square detector shape (Perić & Livada, 2019; Vollmer, 2021). This parameter is often shown down to the cutoff frequencies and is accurate for all spatial frequencies. The detector array's spatial Nyquist frequency (ξ_{Ny}) must be considered to avoid aliasing effects. Although the detector MTF is the electro-optical system's limiting component, it is typically the mixture of optical and electronic responses that provides the total system MTF because $\xi_{Ny} \ll \xi_{cutoff}$ in general. The MTF function of a thermal imaging system may be tested in a lab setting, and the MTF function of each subsystem can be

modeled. The system MTF is appropriate for evaluating the effectiveness of system design. In addition, MTF analysis can help identify the root cause of deficiencies in case a system is not performing as expected.

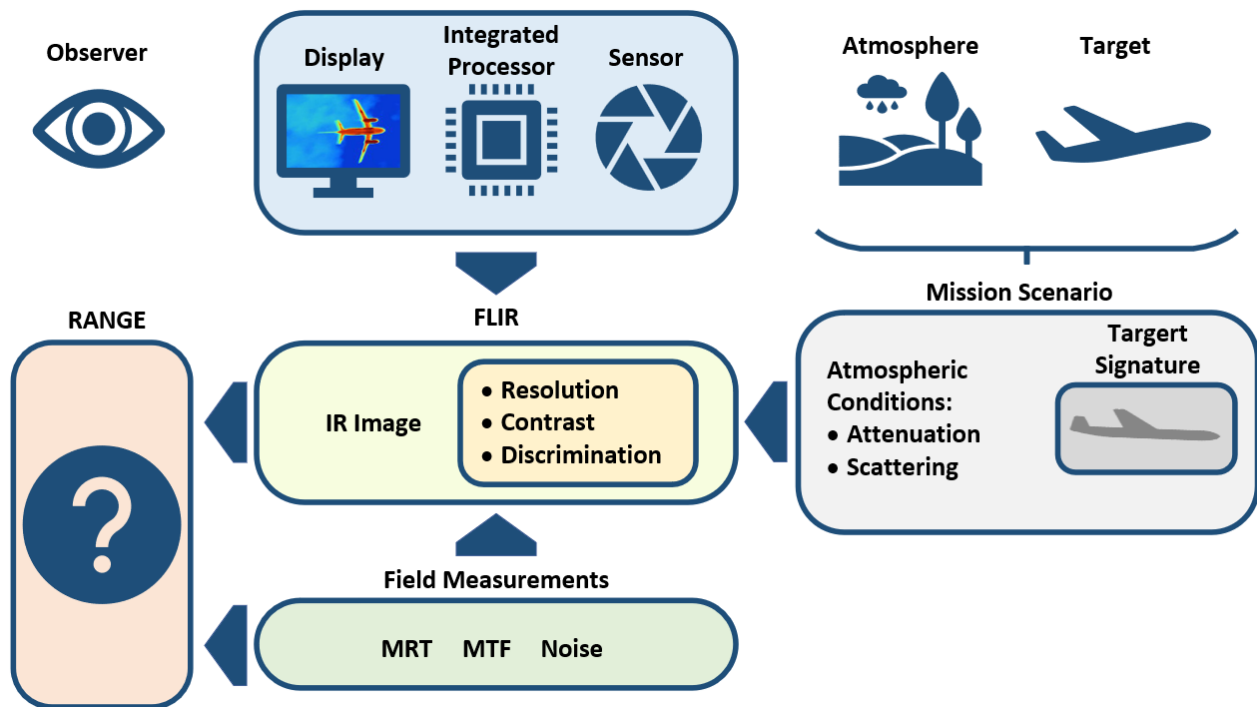


Figure 1. FLIR Range Estimation Data Sources and Targeting

To be able to detect and track with the system designed, traditionally, images of a target from different angles are collected, using other cameras with the same wavelength as the system in such a way that the maximum number of pixels falls on the target but, there are specific difficulties in determining thermal imager performance in two stages, moving target detection and target recognition. The first phase involves detecting moving targets in the entire frame using background subtraction from clutter. Background subtraction might not always be possible due to detecting isolated pixels. Therefore, connected components smaller than the object size should be eliminated by clutter rejection.

The second step is processing the image using morphological transformations and fusion to extract the region of interest containing the detected target in the thermal image. The target recognition phase consists of feature extraction and target classification. A CNN-based (convolutional neural network) deep neural network model can be used for target classification. Target classification is training a classifier with extracted features to create a classification model to classify new data. But unlike visual datasets, thermal datasets are limited, and CNNs often do not fare well with test data. To overcome this challenge, the researchers propose using transfer learning, in which deep networks trained on large datasets for a different application or detection method are adapted for another task or data.

This study is to determine the basic electro-optical parameters related to IR thermal imager range estimations and to define how these parameters can be used for range estimation by describing them under field conditions. It is crucial to determine the system parameters correctly before starting the design and to limit the design for cost and time. To make the design fit for the purpose, the fundamental optical parameters such as optical aperture, F/#, focal length, Noise equivalent temperature (NET), and Field of view (FOV) are determined. Performance analyses are performed using MATLAB according to the specified parameters. These parameters may vary according to system requirements. This article presents the range performance analysis of FLIR, which is more compact, lighter, serves more missions, and can identify a target at a distance of 2.4 km.

2. FUNDAMENTALS OF THERMAL IMAGING METHOD

All objects with a temperature above "absolute zero" emit electromagnetic radiation. Calculating this emission with the following formula (1), depending on the temperature and wavelength, is possible.

$$M_e(\lambda, T) = \left(\frac{2\pi hc^2}{\lambda^5} \right) \left[\exp\left(\frac{hc}{\lambda kT} \right) - 1 \right]^{-1} [Wm^{-3}] \quad (1)$$

where c is the speed of light in vacuum= $2.997 \times 10^8 \text{ms}^{-1}$, h is Planck constant= $6.626 \times 10^{-34} \text{J.s}$, k is Boltzman constant= $1.381 \times 10^{-23} \text{J.K}^{-1}$, T is the absolute temperature in Kelvin, and λ refers to wavelength in meter.

The formula (1) is "Planck's black body radiation law". When it is desired to calculate the actual emission from an object, it is used together with the emission value, which depends on the wavelength of the object (Wolfe & Zissis, 1985).

$$[M_e(\lambda, T)]_{real} = E(\lambda, T)M_e(\lambda, T) \quad (2)$$

Since it is the amount of energy per photon ($E=hc/\lambda$), Planck's law can be written regarding photon flux as follows:

$$M_q(\lambda, T) = \frac{\lambda}{hc} M_e(\lambda, T) [photon.s^{-1}.m^{-3}] \quad (3)$$

The total energy emitted from an object is obtained by integrating equation (1) at all wavelengths.

$$M_e(T) = \sigma T^4 [W.m^{-2}] \quad (4)$$

where σ is Stefan-Boltzmann constant= $5.67 \times 10^{-8} \text{W.m}^{-2}.\text{K}^{-4}$.

According to (4), a total power of 460W is emitted from an object with a temperature of 300 K and a surface area of 1m^2 .

The variation of the radiated energy concerning the temperature is obtained by taking the derivative of (4) concerning the temperature.

$$\frac{\partial M_e}{\partial T} = 4\sigma T^3 [W.m^{-2}K^{-1}] \quad (5)$$

Therefore, a 1-degree change in the temperature of a 1m^2 object at 300 K leads to a change of approximately 6 Watts compared to (5); however, this is the sum across all wavelengths. The 8-14 μm range carries about a third of the total energy, accounting for an energy difference of approximately 2 Watts. In summary, if an object with a temperature of 300 Kelvin is observed in the 8-14 μm band, the parts with a temperature difference of 1 degree between them will radiate with a total energy difference of about 2 Watts. The detector can detect a significant, tiny portion of this energy difference. This perceived difference will create a visual contrast depending on the temperature difference, and an image will be made this way.

2.1. FLIR Types

FLIR systems are divided into "staring" and "scanning" (scanning). Staring-type FLIR systems use detectors in the form of a focal plane array. On the other hand, scanning systems can be evaluated in two groups "series" and "parallel."

In parallel scanning, each detector in the FLIR scans a line of the image to be acquired. Since the detectors are arrayed one after the other, the whole image is obtained when a "forward scan" is performed as a whole scan

Figure 2. Since the lines between the detectors will not be scanned due to the physical gaps between the detectors, the detectors are shifted by the length of the detector while returning from the end of the line, and a "back-scan" is performed. Thus, there is no unscanned area in the area. When scanning is performed at a frequency so high that the human eye cannot detect (e.g., > 20 Hz), the resulting image will appear as a still image.

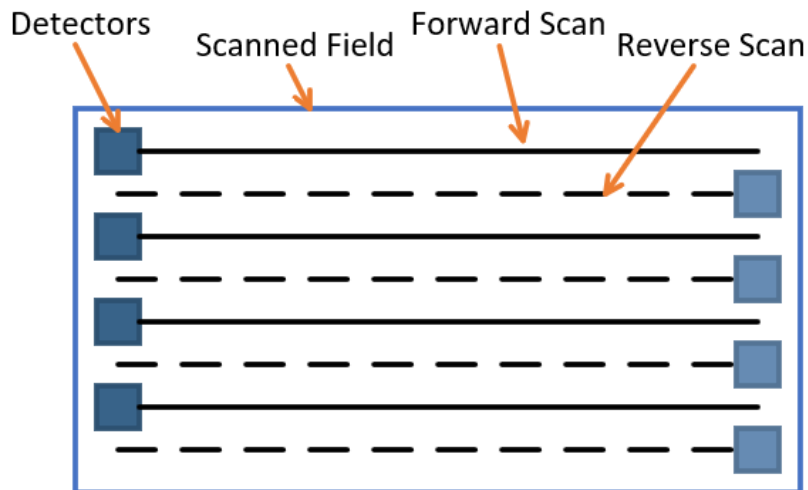


Figure 2. Detector Scanning Model

In a serial scan, the detectors in the FLIR are stacked in a row, so they scan the entire image, not just a line, as in parallel scanning. Since the detectors are in a row, the image of the position of the 1st detector at time t will be obtained again when the second detector comes to that position at time $t+1$. The images obtained by all these cascading detectors are integrated with a process called "time delay integration TDI" Figure 3.

Fixed surveillance, on the other hand, is a type of design that can be realized by integrating many detectors into a series. This design is called Focal Plane Array (FPA). In this design, scanning is unnecessary as the arrays cover entirely the image area.

The main detector types used in FLIR devices are Platinum Silicide (PtSi), Mercury Cadmium Telluride (HgCdTe), Indium Antimonide (InSb), and Gallium Arsenide (GaAs). PtSi Schottky-barrier detectors are the most suitable material for large arrays of 3-5 μm , as they provide high resolution when used as a surveillance array. The cost of these detectors is also low, as their production is based on already advanced silicon technology. Although the quantum efficiency is low due to the large number of detectors in the array, the sensitivity of the device is high.

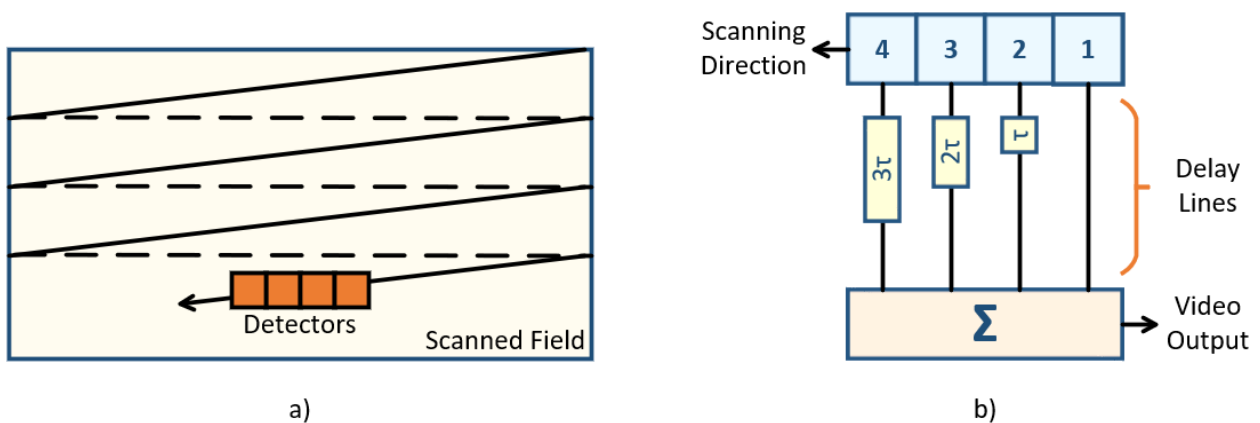


Figure 3. a) The method of Staring FLIR, b) Delay Lines

3. SYSTEM REQUIREMENTS RESULT ANALYSIS

System requirements can be grouped under three main categories. The first is related to image quality, the second is related to field performance, and the third is the category of requirements related to resource cost (size, weight, power requirement, etc.). Most of these requests require different engineering solutions to design an electro-optical thermal camera system. The design trade-off to meet the criteria determines the system's success. In this study, especially, evaluations related to field performance requirements will be included.

3.1. Field Performance Requirements

One of the most basic requirements for the user is to see sufficient detail at a certain distance. This requirement is provided by meeting objects' detection, diagnosis, and recognition functions. However, different levels of detail are required depending on the application area. For example, while it is sufficient for a security camera system to detect only human presence from a few hundred meters, it may be necessary to obtain an image in detail to be identified from a distance of 10 kilometers in a weapon system.

Spatial resolution is an essential parameter for the level of detail. However, since this parameter is related to the number of pixels of the detector, resolution/price is evaluated regarding availability (Biberman, 1975).

Considering the temperature differences, atmospheric permeability, and noise on the surfaces of the objects to be imaged, it is seen that the image contrast is as important a parameter as the resolution. The parameter used to measure the image contrast is the MRT value. This value is measured by a 7-line pattern formed by four hot sticks with three equal spaces between them. This pattern is called an MRT-type target. The calculations for detecting the MRT target at ΔT temperature at a specific atmospheric transmittance at a distance R are examined below to evaluate the field performance.

3.2. Field Performance Calculations

When the atmospheric permeability is represented with the propagation constant β , the temperature to be perceived by the system, ΔT_A , can be found by the following equation.

$$\Delta T_A = \Delta T e^{-\beta R} \quad [K] \quad (6)$$

On an MRT-type target, a line (1/7th of the total pattern) is angularly denoted by $\Delta\Phi$.

$$\Delta\Phi = \frac{S}{7 \cdot R} \quad [mrad] \quad (7)$$

where S indicates the total width of the 7-line MRT target (m), and R refers to the distance of the target (km).

Using (7), the target frequency can be determined as follows.

$$f = \frac{1}{2\Delta\Phi} = \left(\frac{3.5}{S}\right) R \quad [cycles.mrad^{-1}] \quad (8)$$

R_0 is given as

$$R_0 = \frac{S}{7 \cdot \Delta\theta} \quad [km] \quad (9)$$

The following equation (10) gives the system reference frequency f_0 .

$$\frac{f}{f_0} = \frac{\Delta\theta}{\Delta\Phi} = \frac{R}{R_0} \quad (10)$$

(11) is valid since the temperature required to detect the target with sufficient resolution is MRT at the target frequency.

$$\Delta T \cdot e^{-\beta R} = MRT \left(\frac{R}{R_0} \right) [K] \tag{11}$$

(11) is the fundamental equation for determining the sensing distance of a system. Both sides of the equation are plotted as a function of range, R, and propagation constant, β , and the intersection point gives the range at which detection can be made (Figure 4).

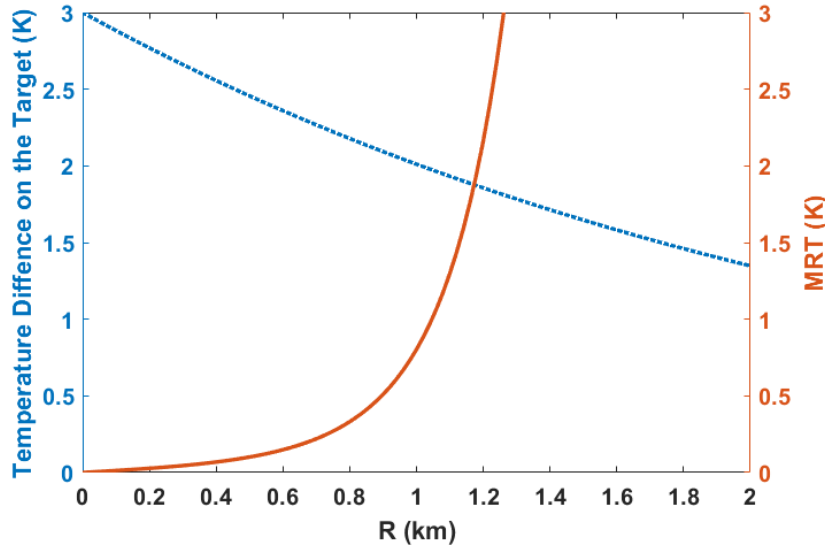


Figure 4. The Aperture of the System is $A_R=0.7$, the System Output Noise Equivalent Temperature is $NET^*=0.14^\circ C$, and the Atmospheric Reduction Coefficient is $\beta=0.4 km^{-1}$

However, range calculations using (11) can be useful for systems with specified parameters. To be able to analyze, it is necessary to use functions that depend on parameters. By this way, it is possible to investigate what parameter impacts the range in which way. The starting point for this is the following equation.

$$MRT \left(\frac{R}{R_0} \right) \cong 0.7 NET^* \left(\frac{R}{R_0} \right) \exp \left[\alpha \left(\frac{R}{R_0} \right)^2 \right] \tag{12}$$

To combine equations (11) and (12), we can define:

$$\alpha = -\ln MTF_S(1) \quad \text{and} \quad \gamma = \frac{\Delta T}{0.7 NET^*} \tag{13}$$

So, (11) and (12) can be written as:

$$\ln \gamma - \beta R = \ln \left(\frac{R}{R_0} \right) + \alpha \left(\frac{R}{R_0} \right)^2 \tag{14}$$

R/R_0 logarithm can be expanded approximately as follows:

$$\ln \left(\frac{R}{R_0} \right) \cong \left(\frac{R}{R_0} - 1 \right) - \frac{1}{2} \left(\frac{R}{R_0} - 1 \right)^2 \tag{15}$$

When equation (15) is substituted into (14):

$$\left(\alpha - \frac{1}{2} \right) \left(\frac{R}{R_0} \right)^2 + 2 \left(\frac{R}{R_0} \right) - \left(\frac{3}{2} + \ln \gamma - \beta R \right) = 0 \tag{16}$$

Then, R/R_0 can be found as:

$$\frac{R}{R_0} = \frac{\left[1 + \left(\alpha - \frac{1}{2} \right) \left(\frac{3}{2} + \ln \gamma - \beta R \right) \right]^{\frac{1}{2}}}{\left(\alpha - \frac{1}{2} \right)} \tag{17}$$

The relation between the system relative aperture A_R and the aperture D_0 of the optical part is defined as

$$A_R = D_0 \Delta\theta \quad (18)$$

The equation between R_0 and D_0 is given in (19).

$$R_0 = \frac{S}{7\Delta\theta} = \left(\frac{S}{7A_R}\right) D_0 \quad (19)$$

Substituting equation (19) in (17), the following formula for the optical aperture is obtained.

$$D_0 = \left\{ \frac{7\left(\alpha - \frac{1}{2}\right)\left(\frac{A_R}{S}\right)}{\left[1 + \left(\alpha - \frac{1}{2}\right)\left(\frac{3}{2} + \ln \gamma - \beta R\right)\right]^{\frac{1}{2}} - 1} \right\} R \quad (20)$$

When the target's temperature, height, atmospheric transmittance coefficient, and system parameters are known as A_R , NET^* , and MTF_S , the optical aperture value should be used to detect the target from a certain distance can be obtained by using (20). The system parameters A_R , NET^* , and MTF_S depend on each other.

$$NET^* = (\eta_S^{1/2} A_R)^{-1} NET_0 \quad (21)$$

where η_S is the efficiency of the FLIR system (proportional to the square root of the number of detector pixels in the system).

$$MTF_S(1) = 0.64 \left(\frac{4A_R - 1}{4A_R}\right) MTF_D(1) \quad (22)$$

(20), (21), and (22) are sufficient for many analyses.

3.3. Field Performance Sample Calculation

In this chapter, the calculations for a linear detector array with 120 elements positioned vertically and scanning horizontally are given. The index is used as "2:1 interlace" to output in 240x380 format. The values used in the calculations are given in Table 1. The system parameters obtained using the values in Table 1 are given in Table 2.

Table 1. Optic and Detector Parameters

Parameters	Symbol	Value
IR optic aperture	D_0	4 in
IR optic focal length	f_l	11.4 in
IR transmission	τ_o	0.70
IR optic design haze	σ_o	0.058mrad
Scanning efficiency	ε_s	0.70
Cold-shield efficiency	η_{cs}	0.42
Detector elements	N	120
Detector element size	$\omega_x \omega_x$	2.0x2.0mils ²
Detector efficiency	η_D	0.10
Spectral range	λ_1, λ_2	8.0-10.0 μ m

Table 2. The System Parameters Calculated Using the Values in Table 1

Parameters	Equations	Values
$\Delta\theta$	ω/f_i	0.175 (mrad)
f_o	$1/2 \Delta\theta$	2.86 (cycles.mrad ⁻¹)
$(FOV)_y$	$240 \Delta\theta$	42.0 (mrad)
$(FOV)_x$	$320 \Delta\theta$	56.0 (mrad)
A_R	$D_o \Delta\theta$	0.70
η_{cov}	$N \Delta\theta^2 / ((FOV)_x (FOV)_y)$	1.56×10^{-3}
η_s	$\tau_o \varepsilon_s^{1/2} \eta_{cov}^{1/2} \eta_{cs}^{1/2} \eta_D^{1/2}$	4.76×10^{-3}
NET_o	$\left(\frac{7.87 M_q^{1/2}}{M'_q \tau_F^{1/2}} \right)$	4.58×10^{-4} (°C)
G_o	$(\eta_s D_o)^2 NET_o^2$	5.79×10^{-5} (°C ² mrad ²)
NET^*	$G_o^{1/2} \Delta\theta$	0.14 (°C)

$$MTF_{diff} \left(\frac{f}{f_0} \right) = 1 - \left(\frac{1}{4A_R} \right) \left(\frac{f}{f_0} \right) = 1 - 0.36 \left(\frac{f}{f_0} \right) \tag{23}$$

$$MTF_{det} \left(\frac{f}{f_0} \right) = \exp[-\pi(f_\infty)^2] = \exp \left[-0.086 \left(\frac{f}{f_0} \right)^2 \right] \tag{24}$$

$$MTF_{det} \left(\frac{f}{f_0} \right) = \text{sinc} \left[(\pi/2) \left(\frac{f}{f_0} \right) \right] \tag{25}$$

The multiplication of (23), (24), and (25) equations are shown as the "IR detector" in Figure 5.

The electronic display part can be considered a Gaussian curve with a value of 0.90 at f_0 .

$$MTF_{\frac{elektronik}{display}} \left(\frac{f}{f_0} \right) = \exp \left[-0.10 \left(\frac{f}{f_0} \right)^2 \right] \tag{26}$$

The modulus of the optical transfer function (contrast) vs. f/f_0 is depicted as an MTF curve in Figure 5. (resolution) using (26). MTF of the detector is 0.51 at 0.8 f/f_0 . However, since it is 0.94 for the electronic display/signal processing unit, by multiplying those, the total system MTF is achieved to be 0.48 at 0.8 f/f_0 .

The MRT value can also be found with the following equation.

$$MRT = 0.7 \left(\frac{f}{f_0} \right) \left[\frac{NET^*}{MTF_s(f/f_0)} \right] = 0.098 \left[\frac{f/f_0}{MTF_s(f/f_0)} \right] \tag{27}$$

The relationship between the MRT and f/f_0 for a typical FLIR system is seen in Figure 6 by using (27). The maximum range for classification or recognition is the range where the target/background ΔT matches MRT at the spatial frequency specified by the relevant criterion, as MRT is a function of spatial frequency.

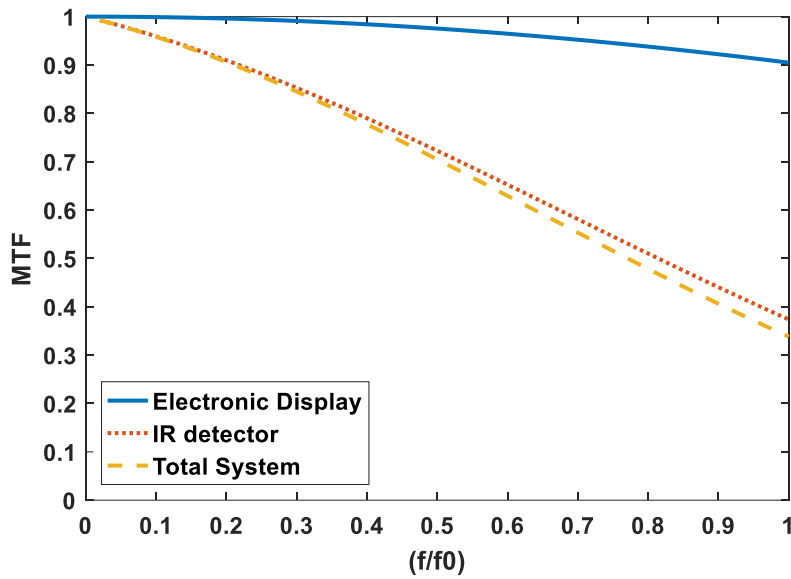


Figure 5. MTF Analysis for the Designed Thermal Camera System

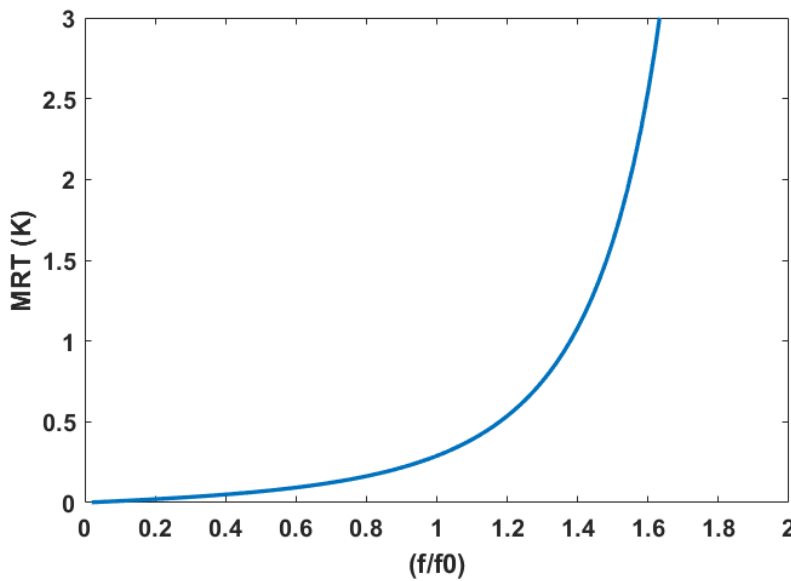


Figure 6. MRT Analysis for the Designed Thermal Camera System

Using the equations and Figure 6, the range at which an object with a width of 2 m and a temperature of 3°C above the ambient temperature can be detected is calculated where the atmospheric permeability is 0.4 km⁻¹.

$$\alpha = -\ln MTF_S(1) = -\ln 0.339 = 1.0 \tag{28}$$

$$\gamma = \frac{\Delta T}{0.7NET^*} = \frac{3}{0.098} = 30.6 \tag{29}$$

The values obtained by (28) and (29) are substituted in equation (20) and solved for R, the range is found to be 2.4 km.

$$R \cong 2.4km \tag{30}$$

4. CONCLUSION

Based on MRT characteristics, Johnson criteria enable the determination of the thermal camera range parameters. Since all the information pertinent to the scenario is unknown, it is difficult and sometimes impossible to provide simple answers regarding the range of a thermal imaging device. The solutions can be highly inaccurate even if all the data are known. Despite all the drawbacks, Johnson's criteria still apply for estimating the range of an IR thermal imager. Although IR thermal imaging system model improvements offer beneficial tools for analysis and synthesis that may be used during development for design optimization, imager range estimates in real-world settings are not significantly improved. Based on Johnson's criterion, IR thermal imaging systems produce MRT measurements, measurement results that also serve as a quality control tool to assess how well the image is made, and data that can be used to calculate the predefined target and distance of the imager. In this study, we calculated the field range performance of the system by defining the optical and detector parameters to obtain the fundamental parameters of the thermal camera system that we designed briefly. The range value (R) obtained from these calculations confirmed that range performance could also vary significantly in a thermal imaging system design depending on target dimensions, ambient temperature, and atmospheric transmittance.

CONFLICT OF INTEREST

The author declares no conflict of interest.

REFERENCES

- Biberman, L. M. (1975). Displays and Perception of Displayed Information Seminar Series, University of Tel Aviv, 1–10 September 1974. *Applied Optics*, 14(4), 800. doi:[10.1364/ao.14.000800](https://doi.org/10.1364/ao.14.000800)
- Driggers, R. G., Vollmerhausen, R. H., & Krapels, K. A. (2000). Target identification performance as a function of low spatial frequency image content. *Optical Engineering*, 39(9), 2458-2462. doi:[10.1117/1.1288362](https://doi.org/10.1117/1.1288362)
- Hou, F., Zhang, Y., Zhou, Y., Zhang, M., Lv, B., & Wu, J. (2022). Review on infrared imaging technology. *Sustainability*, 14(18), 11161. doi:[10.3390/su141811161](https://doi.org/10.3390/su141811161)
- Javidi, B. (Ed.) (2006). *Optical Imaging Sensors and Systems for Homeland Security Applications*. New York: Springer. doi:[10.1007/b137387](https://doi.org/10.1007/b137387)
- Johnson, J. (1958, October 6-7). *Analysis of imaging forming systems*. In: Proceedings of the Image Intensifier Symposium (pp. 249-273). Ford Belvoir, VA.
- Krapels, K., Driggers, R. G., Larson, P., Garcia, J., Walden, B., Agheera, S., Deaver, D., Hixson, J., & Boettcher, E. (2008, March 16-20). *Small craft ID criteria (N_{50}/V_{50}) for short wave infrared sensors in maritime security*. In: G. C. Holst (Eds.), Proceedings of the Infrared Imaging Systems: Design, Analysis, Modeling, and Testing XIX, 694108, Orlando, Florida, United States. SPIE. doi:[10.1117/12.778062](https://doi.org/10.1117/12.778062)
- Krapels, K., Deaver, D., & Driggers, R. (2006, September 11-14). *Small craft identification discrimination criteria N_{50} and V_{50} for visible and infrared sensors in maritime security*. In: R. G. Driggers & D. A. Huckridge (Eds.), Proceedings of the Electro-Optical and Infrared Systems: Technology and Applications III, 63950T, Stockholm, Sweden. SPIE. doi:[10.1117/12.689140](https://doi.org/10.1117/12.689140)
- Moyer, S. K., Hixson, J. G., Edwards, T. C., & Krapels, K. A. (2006). Probability of identification of small hand-held objects for electro-optic forward-looking infrared systems. *Optical Engineering*, 45(6), 063201. doi:[10.1117/1.2213997](https://doi.org/10.1117/1.2213997)
- Moyer, S. K., Flug, E., Edwards, T. C., Krapels, K. A., & Scarbrough, J. (2004, April 12-16). *Identification of handheld objects for electro-optic/FLIR applications*. In: G. C. Holst (Eds.), Proceedings of the Infrared Imaging Systems: Design, Analysis, Modeling, and Testing XV, Orlando, Florida, United States. SPIE. doi:[10.1117/12.542066](https://doi.org/10.1117/12.542066)
- NATO Standardization Agency. (1995). Measurement of the Minimum Resolvable Temperature Difference (MRTD) of Thermal Cameras (NATO STANAG 4349).

- NATO Research and Technology Organisation. (2003). Experimental Assessment Parameters and Procedures for Characterization of Advanced Thermal Imagers. No: RTO-TR-075(II). (Accessed: 01/03/2023) [PDF](#)
- Perić, D., & Livada, B. (2019, June 3-6). *MRTD Measurements Role in Thermal Imager Quality Assessment*. In: S. Vukosavić, & B. Lončar (Eds.), Proceedings of 6th International Conference on Electrical, Electronic and Computing Engineering ((Ic)ETRAN 2019) in conjunction with 63rd National Conference on Electrical, Electronic and Computing Engineering (ETRAN), (pp. 336-340), Silver Lake, Serbia.
- Perić, D., Livada, B., Perić, M., & Vujić, S. (2019). Thermal imager range: Predictions, expectations, and reality. *Sensors*, 19(15), 3313. doi:[10.3390/s19153313](https://doi.org/10.3390/s19153313)
- Sagan, V., Maimaitijiang, M., Sidike, P., Eblimit, K., Peterson, K. T., Hartling, S., Esposito, F., Khanal, K., Newcomb, M., Pauli, D., Ward, R., Fritschi, F., Shakoor, N., & Mockler, T. (2019). UAV-based high resolution thermal imaging for vegetation monitoring, and plant phenotyping using ICI 8640 P, FLIR Vue Pro R 640, and thermoMap cameras. *Remote Sensing*, 11(3), 330. doi:[10.3390/rs11030330](https://doi.org/10.3390/rs11030330)
- Schmieder, D. E., & Weathersby, M. R. (1983). Detection performance in clutter with variable resolution. *IEEE Transactions on Aerospace and Electronic Systems*, AES-19(4), 622-630. doi:[10.1109/taes.1983.309351](https://doi.org/10.1109/taes.1983.309351)
- Teaney, B. P., Reynolds, J. P., & O'Connor, J. (2007, April 9-13). *Guidance on methods and parameters for Army target acquisition models*. In: G. C. Holst (Eds.), Proceedings of the Infrared Imaging Systems: Design, Analysis, Modeling, and Testing XVIII, 65430L, Orlando, Florida, United States. SPIE. doi:[10.1117/12.734511](https://doi.org/10.1117/12.734511)
- U.S Army Night Vision and Electronic Sensors Directorate. (2001). Night Vision Thermal Imaging Systems Performance Model: User's Manual & Reference Guide. Fort Belvoir, VA.
- Vollmer, M. (2021). Infrared Thermal Imaging. In: K. Ikeuchi (Eds.), *Computer Vision*, (pp. 666-670). Springer International Publishing. doi:[10.1007/978-3-030-63416-2_844](https://doi.org/10.1007/978-3-030-63416-2_844)
- Vollmerhausen, R. H., & Driggers, R. G. (2000). *Analysis of Sampled Imaging Systems*. SPIE Press, Bellingham, Washington USA. doi:[10.1117/3.353257](https://doi.org/10.1117/3.353257)
- Vollmerhausen, R. H., Reago Jr., D. A., & Driggers, R. G. (2010). *Analysis and Evaluation of Sampled Imaging Systems*. SPIE Press, Bellingham, Washington USA. doi:[10.1117/3.853462](https://doi.org/10.1117/3.853462)
- Vollmerhausen, R. H., & Jacobs, E. (2004). The Targeting Task Performance (TTP) Metric A New Model for Predicting Target Acquisition Performance. Defense Technical Information Center Technical Report, No: ADA422493.
- Wolfe, W. L., & Zissis, G. J. (1985). *The Infrared Handbook*, Revised Edition. SPIE Press.



Gazi University

Journal of Science

PART A: ENGINEERING AND INNOVATION

<http://dergipark.org.tr/guj.1282992>

Convergence Properties of a Kantorovich Type of Szász Operators Involving Negative Order Genocchi Polynomials

Erkan AGYUZ^{1*} ¹Gaziantep University, Naci Topçuoğlu Vocational School, Gaziantep, Türkiye

Keywords	Abstract
Generating Function	The goal of this research is to construct a generalization of a Kantorovich type of Szász operators involving negative-order Genocchi polynomials. With the aid of Korovkin's theorem, modulus of continuity, Lipschitz class, and Peetre's K-functional the approximation properties and convergence rate of these operators are established. To illustrate how operators converge to a certain function, we present some examples.
Korovkin Type Approximation	
Modulus of Continuity	
Genocchi Polynomials	

Cite

Agyuz, E. (2023). Convergence Properties of a Kantorovich Type of Szász Operators Involving Negative Order Genocchi Polynomials. *GU J Sci, Part A, 10(2)*, 196-205. doi:[10.54287/guj.1282992](https://doi.org/10.54287/guj.1282992)

Author ID (ORCID Number)	Article Process
0000-0003-1110-7578 Erkan AGYUZ	Submission Date 14.04.2023
	Revision Date 22.05.2023
	Accepted Date 12.06.2023
	Published Date 22.06.2023

1. INTRODUCTION

In analytic number theory, the generating functions method has an important place because this method provides to construct many useful and significant results, identities, and theorems for special polynomials and numbers (Simsek, 2008; 2012; 2013; 2017; 2018; Kucukoglu et al., 2019; Kucukoglu, 2022; Kilar & Simsek, 2020). The following is a definition of the Genocchi polynomials' generating function:

$$\left(\frac{2t}{e^t + 1}\right) e^{xt} = \sum_{n=0}^{\infty} G_n(x) \frac{t^n}{n!}, |t| < \pi, \quad (1)$$

Horadam (1992) defined negative-order Genocchi polynomials and studied on their properties such as summation formula and complementary arguments. The generating functions of negative-order Genocchi polynomials are defined to be

$$\sum_{n=0}^{\infty} G_n^{-k}(x) \frac{t^n}{n!} = \left(\frac{1 + e^t}{2t}\right)^k e^{tx}, \quad (2)$$

where $k \in \mathbb{N} = \{1, 2, 3, \dots\}$ (Horadam, 1992).

Some Genocchi polynomials, $G_n^{-1}(x)$, were given by A. F. Horadam as follows:

$$\begin{aligned}
 G_0^{-1}(x) &= x + \frac{1}{2}, \\
 G_1^{-1}(x) &= \frac{1}{2} \left(x^2 + x + \frac{1}{2} \right), \\
 G_2^{-1}(x) &= \frac{1}{3} \left(x + \frac{1}{2} \right) (x^2 + x + 1), \\
 G_3^{-1}(x) &= \frac{1}{4} \left(x^4 + 2x^3 + 3x^2 + 2x + \frac{1}{2} \right),
 \end{aligned}$$

where $x \in [0, \infty)$. For more information on Genocchi polynomials and their applications, follow these references (Cangul et al., 2009; Kilar & Simsek, 2021; Srivastava & Choi, 2001; Srivastava et al., 2012)

An example of the applied disciplines of generating functions of unique polynomials is approximation theory (Jakimovski & Leviatan, 1969; Davis, 1975; Lupas, 1995 Gupta & Rassias, 2019). Varma et al. (2012) provided a new generalization of the Szász type operators that are described using Brenke-type polynomials. Through the use of Korovkin's theorem, continuity's second modulus, and Peetre's K -functional, they could able to determine the approximation properties of their operators as well as the order of convergence (Varma et al., 2012). İçöz et al. (2016) presented the definition and proof of a new sort of approximation theorem for a series of type operators that includes generalized Appell polynomials. Menekşe Yılmaz (2022) provided an operator form that makes use of the generating function of order α Apostol-Genocchi type polynomials. and reached the approximation of the operator by applying the Korovkin's theorem and using moments and central moments. Many techniques, including the K -functional, continuity's modulus, and continuity's second modulus, were used to calculate the operator's rate of convergence (Menekşe Yılmaz, 2022). Mursaleen et al. (2018) constructed a generalize Chlodowsky type Szász type operators involving Boas-Buck type polynomials and studied their some approximation properties such as Korovkin type theorem. Atakut and Büyükyazıcı (2016) presented some approximation properties of a generalization Kantorovich- Szász type operator including Brenke-type polynomials. Agyuz (2021a; 2021b; 2022; 2023) defined positive linear operators of Szász type and Kantorovich-Szász type by using generator functions of various family of special polynomials and examined the approximation these operators' characteristics.

By the inspired above studies, we offer a generalization Kantorovich type of Szász operators involving negative-order Genocchi type polynomials by way of their generating functions of when $k = 1$ because negative-order Genocchi polynomials are positive for $k = 1$. The operator is defined in the following definition:

Definition 1.1. For all $x \in [0, \infty)$, we have

$$\mathcal{H}_n^*(f, x) = \frac{2}{e+1} n e^{-nx} \sum_{k=0}^{\infty} \frac{G_k^{-1}(nx)}{k!} \int_{\frac{k}{n}}^{\frac{k+1}{n}} f(t) dt. \quad (3)$$

In this study, we explore the convergence properties of $\mathcal{H}_n^*(f, x)$. First, we construct the Korovkin's theorem by using moment functions for $\mathcal{H}_n^*(f, x)$. Second, we calculate the rate of convergence applying Peetre's K -functional, the local Lipschitz class's constituents, and the continuity's modulus. Finally, we use the Maple to provide numerical examples to prove error estimate of our operator.

2. MAIN RESULTS

In this part, we examine the convergence properties of $\mathcal{H}_n^*(f, x)$ using approximation methods such as modulus of continuity, Korovkin's theorem, Peetre's K -functional and local Lipschitz class. To demonstrate these properties, first the moment and central moment functions are given for the operator $\mathcal{H}_n^*(f, x)$.

Consider the following definition of the class E :

$$E: = \left\{ f: x \in [0, \infty), \frac{f(x)}{1+x^2} \text{ is convergent as } x \rightarrow \infty \right\}.$$

The moment functions of $\mathcal{H}_n^*(f, x)$ are given at the subsequent lemma:

Lemma 2.1. Let $\forall x \in [0, \infty)$, the $\mathcal{H}_n^*(f, x)$ yields at the following equations:

$$\mathcal{H}_n^*(1, x) = 1, \quad (4)$$

$$\mathcal{H}_n^*(s, x) = x + \frac{5e + 3}{2n(e + 1)}, \quad (5)$$

$$\mathcal{H}_n^*(s^2, x) = x^2 + \frac{6e + 4}{n(e + 1)}x + \frac{6e + 2}{n^2(e + 1)}. \quad (6)$$

Proof: Let $t = 1$ and $x \rightarrow nx$. If we take $f = 1$ at Eq. (3), we give

$$\mathcal{H}_n^*(1, x) = \frac{2}{e + 1} ne^{-nx} \sum_{k=0}^{\infty} \frac{G_k^{-1}(nx)}{k!} \int_{\frac{k}{n}}^{\frac{k+1}{n}} dt. \quad (7)$$

By taking an integral and applying the Eq. (2) at Eq. (7), we obtain

$$\mathcal{H}_n^*(1, x) = \frac{2}{e + 1} ne^{-nx} \left(\left(\frac{1 + e}{2} \right) e^{nx} \right) \left(\frac{k + 1}{n} - \frac{k}{n} \right) = 1. \quad (8)$$

Let $f = s$. The $\mathcal{H}_n^*(s, x)$ is described to be

$$\mathcal{H}_n^*(s, x) = \frac{2}{e + 1} ne^{-nx} \sum_{k=0}^{\infty} \frac{G_k^{-1}(nx)}{k!} \int_{\frac{k}{n}}^{\frac{k+1}{n}} t dt. \quad (9)$$

By taking an integral and applying the Eq. (2) at Eq. (9), we obtain

$$\begin{aligned} \mathcal{H}_n^*(s, x) &= \frac{2}{e + 1} ne^{-nx} \sum_{k=0}^{\infty} \frac{G_k^{-1}(nx)}{k!} \left(\frac{\left(\frac{k + 1}{n} \right)^2}{2} - \frac{\left(\frac{k}{n} \right)^2}{2} \right) \\ &= \frac{2}{e + 1} ne^{-nx} \sum_{k=0}^{\infty} \frac{G_k^{-1}(nx)}{k!} \left(\frac{2k + 1}{2n^2} \right), \\ &= \frac{2}{e + 1} ne^{-nx} \frac{1}{2n^2} \left(\sum_{k=0}^{\infty} \frac{2k G_k^{-1}(nx)}{k!} + \sum_{k=0}^{\infty} \frac{G_k^{-1}(nx)}{k!} \right) \\ &= x + \frac{5e + 3}{2n(e + 1)}, \end{aligned} \quad (10)$$

where $\sum_{k=0}^{\infty} \frac{k G_k^{-1}(nx)}{k!}$ is the first derivative of -1 order Genocchi polynomials in terms of their generating function for $t = 1$ and $x \rightarrow nx$ and is defined to be

$$\sum_{k=0}^{\infty} \frac{k G_k^{-1}(nx)}{k!} = \frac{1}{2} e^{nx} (nx + e(nx + 2) + 1).$$

Let $f = s^2$. The $\mathcal{H}_n^*(s^2, x)$ is defined to be

$$\mathcal{H}_n^*(s^2, x) = \frac{2}{e+1} n e^{-nx} \sum_{k=0}^{\infty} \frac{G_k^{-1}(nx)}{k!} \int_{\frac{k}{n}}^{\frac{k+1}{n}} t^2 dt. \quad (11)$$

By taking an integral and applying the Eq. (2) at Eq. (11), we obtain

$$\begin{aligned} \mathcal{H}_n^*(s^2, x) &= \frac{2}{e+1} n e^{-nx} \sum_{k=0}^{\infty} \frac{G_k^{-1}(nx)}{k!} \left(\frac{\left(\frac{k+1}{n}\right)^3}{3} - \frac{\left(\frac{k}{n}\right)^3}{3} \right) \\ &= \frac{2}{e+1} n e^{-nx} \sum_{k=0}^{\infty} \frac{G_k^{-1}(nx)}{k!} \left(\frac{3k^2 + 3k + 1}{3n^3} \right), \\ &= \frac{2}{e+1} n e^{-nx} \frac{1}{3n^3} \left(\sum_{k=0}^{\infty} \frac{3k^2 G_k^{-1}(nx)}{k!} + \sum_{k=0}^{\infty} \frac{3k G_k^{-1}(nx)}{k!} \right. \\ &\quad \left. + \sum_{k=0}^{\infty} \frac{G_k^{-1}(nx)}{k!} \right) \\ &= x^2 + \frac{6e+4}{n(e+1)} x + \frac{6e+2}{n^2(e+1)}, \end{aligned} \quad (12)$$

where $\sum_{k=0}^{\infty} \frac{k^2 G_k^{-1}(nx)}{k!}$ is part of the second derivative of -1 order Genocchi polynomials in terms of their generating function for $t = 1$ and $x \rightarrow nx$ is defined to be

$$\sum_{k=0}^{\infty} \frac{k^2 G_k^{-1}(nx)}{k!} = \frac{1}{2} e^{nx} (nx(nx+2) + e^{nx}(nx+1)(nx+3)) + \frac{1}{2} e^{nx} (nx + e(nx+2) + 1).$$

Therefore, the desired results are obtained.

We need central moments to estimate for our operator's rate of convergence. The central moments of $\mathcal{H}_n^*(f, x)$ are given at the subsequent lemma:

Lemma 2.2. For all $x \in [0, \infty)$, the $\mathcal{H}_n^*(f, x)$ provides at the following equations:

$$\mathcal{H}_n^*((s-x), x) = \frac{5e+3}{2n(e+1)}, \quad (13)$$

$$\mathcal{H}_n^*((s-x)^2, x) = \frac{x}{n} + \frac{6e+2}{n^2(e+1)}. \quad (14)$$

Proof: Via the use of linearity property of $\mathcal{H}_n^*(f, x)$, we discover

$$\mathcal{H}_n^*((s-x), x) = \mathcal{H}_n^*(s, x) - x \mathcal{H}_n^*(1, x) = \frac{5e+3}{2n(e+1)}, \quad (15)$$

and

$$\begin{aligned}\mathcal{H}_n^*((s-x)^2, x) &= \mathcal{H}_n^*(s^2, x) - 2x\mathcal{H}_n^*(s, x) + x^2\mathcal{H}_n^*(1, x) \\ &= \frac{x}{n} + \frac{6e+2}{n^2(e+1)}.\end{aligned}\tag{16}$$

In view of the above equations, we obtain the desired results.

Korovkin-type theorems offer elementary and effective methods for assessing whether an accepted series of positive linear operators acting on a function space is functioning approximatively or, alternatively, if it greatly converges to the identity operator. In general, these theorems offer a variety of test subsets of functions that, if they are true, warranty that the approximation (or convergence) feature is true across the board.

The phrase "Theorems of the Korovkin kind" alludes to P. P. Korovkin, who showed in 1953 that the functions $1, x,$ and x^2 have such a property in the collection of all continuous functions on the real interval $[0,1]$ known as $C([0,1])$. (Korovkin, 1953; 1960; Altomare, 2010).

Now, we give a theorem to show uniformly convergence of $\mathcal{H}_n^*(f, x)$ as below:

Theorem 2.3. Let $f \in C[0, \infty) \cap E$. We give,

$$\lim_{n \rightarrow \infty} \mathcal{H}_n^*(f, x) = f(x),\tag{17}$$

uniformly on all of the compact subsets of $[0, \infty)$.

Proof: We know for a fact that

$$\begin{aligned}\lim_{n \rightarrow \infty} \mathcal{H}_n^*(1, x) &= \lim_{n \rightarrow \infty} 1 = 1 \\ \lim_{n \rightarrow \infty} \mathcal{H}_n^*(s, x) &= \lim_{n \rightarrow \infty} \left(x + \frac{5e+3}{2n(e+1)} \right) = x \\ \lim_{n \rightarrow \infty} \mathcal{H}_n^*(s^2, x) &= \lim_{n \rightarrow \infty} \left(x^2 + \frac{6e+4}{n(e+1)}x + \frac{6e+2}{n^2(e+1)} \right) = x^2\end{aligned}$$

The Korovkin's theorem can be used to obtain the desired result.

As stated in its definition, continuity's modulus is shown by

$$\omega(f, \delta) := \sup_{\substack{x, y \in [0, \infty) \\ |x-y| \leq \delta}} |f(x) - f(y)|,\tag{18}$$

where f is a function that is continuous throughout $[0, \infty)$, and that $\delta > 0$. A property of the modulus of continuity is given at the subsequent inequality:

$$|f(x) - f(y)| \leq \omega(f, \delta) \left(\frac{|x-y|}{\delta} + 1 \right).\tag{19}$$

By using the definition and property of the continuity's modulus, we have a theorem for $\mathcal{H}_n^*(f, x)$ as follows:

Theorem 2.4. Let $f \in C_B[0, \infty) \cap E$, then

$$|\mathcal{H}_n^*(f, x) - f(x)| \leq 2\omega(f, \delta_n),\tag{20}$$

where $\delta_n(x) = \sqrt{\mathcal{H}_n^*((s-x)^2, x)}$.

Proof Lemma 2.1 and the monotonicity property of $\mathcal{H}_n^*(f, x)$ lead to this conclusion

$$|\mathcal{H}_n^*(f, x) - f(x)| \leq \mathcal{H}_n^*(|f(x) - f(y)|; x). \quad (21)$$

By using Eq. (19), what Eq. (21) reveals to us is as follows:

$$|\mathcal{H}_n^*(f, x) - f(x)| \leq \omega(f, \delta_n) \left(1 + \frac{1}{\delta} \mathcal{H}_n^*(|x - y|, x) \right). \quad (22)$$

When we consider Eq. (22)'s right side and apply the Cauchy-Schwarz inequality, we obtain

$$|\mathcal{H}_n^*(f, x) - f(x)| \leq \omega(f, \delta_n) \left(1 + \frac{1}{\delta} \sqrt{\mathcal{H}_n^*((x - y)^2, x)} \right). \quad (23)$$

The evidence is concluded if the answer is $\delta := \delta_n(x) = \sqrt{\mathcal{H}_n^*((s - x)^2, x)}$ in Eq. (23).

An estimate of the approximation error of \mathcal{H}_n^* operators to f , similarly the modulus of continuity, is given by the Lipschitz class, which is defined below:

$$\text{Lip}_M(\alpha) := \{f \in C_B[0, \infty) : |f(t) - f(x)| \leq M|t - x|^\alpha; t, x \in [0, \infty)\},$$

where $C_B[0, \infty)$ is the set of spaces of continuous and bound functions, $M > 0$, and $\alpha \in (0, 1]$.

The subsequent theorem satisfies a prediction for the error of the operator \mathcal{H}_n^* to a function f belonging to the Lipschitz class of order α by above equation.

Theorem 2.5. We suppose that $f \in C_B[0, \infty)$. For $x \geq 0$, we give

$$|\mathcal{H}_n^*(f, x) - f(x)| \leq M\delta_n^\alpha(x), \quad (24)$$

where $\delta_n(x) = \sqrt{\mathcal{H}_n^*((s - x)^2, x)}$.

Proof: According to the monotonicity characteristics of the operators \mathcal{H}_n^* , we obtain

$$|\mathcal{H}_n^*(f, x) - f(x)| \leq M\mathcal{H}_n^*(|s - x|^\alpha; x). \quad (25)$$

The following can be written using the Hölder inequality and from (25),

$$|\mathcal{H}_n^*(f, x) - f(x)| \leq M \left(\mathcal{H}_n^*((s - x)^2, x) \right)^{\frac{\alpha}{2}}.$$

Consequently, the theorem's proof is complete.

In approximation theory, the Peetre's K -functional proved to be a highly useful tool for calculating the error. The Peetre's K functional is given to be as follows:

$$\mathcal{K}(f, \delta) = \inf \left\{ \|f - h\|_{C_B[0, \infty)} + \delta \|h\|_{C_B^2[0, \infty)} \right\},$$

where $\delta > 0$, $f \in C_B[0, \infty)$ and $C_B^2[0, \infty) := \{h \in C_B[0, \infty) : h', h'' \in C_B[0, \infty)\}$, here the norm is defined to be as

$$\|h\|_{C_B^2[0, \infty)} := \|h\|_{C_B[0, \infty)} + \|h'\|_{C_B[0, \infty)} + \|h''\|_{C_B[0, \infty)} \quad (\text{ DeVore \& Lorentz, 1993}).$$

We will use the definition of Peetre's K -functional at the subsequent theorem to assess the degree of approximation for this purpose.

Theorem 2.6. Let $f \in C_B[0, \infty)$ and $x \in [0, \infty)$. The inequality that follows is true

$$|\mathcal{H}_n^*(f, x) - f(x)| \leq 2\mathcal{K}(f, \varphi_u(x)), \quad (26)$$

where $\varphi_u(x) = \frac{1}{4n}x + \frac{2e[(2n+1)(e+1)+(e-1)]}{8n^2(e+1)^2}$.

Proof: Suppose that $h \in C_B^2[0, \infty)$. Using the linearity property of \mathcal{H}_n^* operators and Taylor's expansion, we bring

$$\mathcal{H}_n^*(h, x) - h(x) = h'(x)\mathcal{H}_n^*(s - x, x) + \frac{h''(\tau)}{2}\mathcal{H}_n^*((s - x)^2, x), \tau \in (x, s).$$

The aforementioned equality allows for the writing

$$|\mathcal{H}_n^*(f, x) - f(x)| \leq \left(\frac{1}{4n}x + \frac{2e[(2n+1)(e+1)+(e-1)]}{8n^2(e+1)^2} \right) \|h\|_{C_B^2[0, \infty)} \quad (27)$$

As opposed to that, applying Lemma (2.1) and expression (27), we obtain

$$\begin{aligned} |\mathcal{H}_n^*(f, x) - f(x)| &\leq |\mathcal{H}_n^*(f - h, x)| + |\mathcal{H}_n^*(h, x) - h(x)| + |f(x) - h(x)| \\ &\leq 2\|f - h\|_{C_B[0, \infty)} + |\mathcal{H}_n^*(h, x) - h(x)| \\ &\leq 2\left(\|f - h\|_{C_B[0, \infty)} + \varphi_u(x)\|h\|_{C_B^2[0, \infty)}\right) \end{aligned} \quad (28)$$

Catching the upper limit to the right of Eq. (28) over all $h \in C_B^2[0, \infty)$, we obtain the subsequent inequality.

$$|\mathcal{H}_n^*(f, x) - f(x)| \leq 2\mathcal{K}(f, \varphi_u(x)).$$

Therefore, the proof is completed.

Now, we provide a few examples to help we obtain a higher limit for the error $f(x) - \mathcal{H}_n^*(f, x)$ by means of the continuity modulus. Maple2023TM was used to complete the computations for this paper.

Example 2.7. The approximation of $\mathcal{H}_n^*(f, x)$ to $f(x) = \sin(\pi x)$ depends on $[0, \infty)$ is illustrated in the Table 1.

Table 1. Modulus of continuity-based error estimate for function $f(x) = \sin(\pi x)$

n	$\sin(\pi x) - \mathcal{H}_n^*(f, x)$
10	0.9037367966
10^2	0.06591390272
10^3	0.006314114694
10^4	0.0006286279188
10^5	0.00006283494702
10^6	0.000006283216246
10^7	0.0000006283188400

Example 2.8. The approximation of $\mathcal{H}_n^*(f, x)$ to $f(x) = \frac{x}{\sqrt{x^2+1}}$ depends on $[0, \infty)$ is illustrated in the Table 2.

Table 2. Modulus of continuity-based error estimate for function $f(x) = \frac{x}{\sqrt{x^2+1}}$

n	$\frac{x}{\sqrt{x^2+1}} - \mathcal{H}_n^*(f, x)$
10	0.2952150886
10^2	0.02098369184
10^3	0.002009847454
10^4	0.0002000984836
10^5	0.00002000098484
10^6	0.000002000009848
10^7	0.0000002000000984

In these two examples, we use continuity's modulu to numerically determine the approximations of $\mathcal{H}_n^*(f, x)$ to the functions, respectively, $f(x) = \sin(\pi x)$ and $f(x) = \frac{x}{\sqrt{x^2+1}}$. We found that a tiny quantity of inaccuracy was produced when using ω . According to Table 1 and Table 2, we observe that the amount of error when using ω gets smaller as n increases.

3. CONCLUSION

Many mathematicians, physicists, engineers, and other experts have extensively studied the generating functions method. Particularly, the generating functions of Genocchi type polynomials have found widespread application in a wide range of fields. Due to this, we have constructed a generalization of Kantorovich type of Szász linear positive operator, $\mathcal{H}_n^*(f, x)$, using generating functions of -1 order Genocchi polynomials.

We investigated convergence properties of $\mathcal{H}_n^*(f, x)$. Firstly, we obtained moment and central moment functions of our operator. Secondly, we gave Korovkin's theorem for $\mathcal{H}_n^*(f, x)$ by using moment functions. By the help of this theorem, we satisfied uniformly convergence property of our operator. And then, we investigated to estimate rate of convergence of $\mathcal{H}_n^*(f, x)$ by using some well-known approximation devices such as modulus of continuity, Lipshitz class, and Peetre's K -functional. Finally, by means of the modulus of continuity, we have discovered a higher limit for the error $f(x) - \mathcal{H}_n^*(f, x)$ for particular functions.

The study's methods were all employed to look at the created operator's characteristics, including convergence rate and uniform convergence. These methods have demonstrated that our operator smoothly converges to all functions under favorable conditions, and the approximation speed is adequate.

In this work, we describe a generalization of positive linear operators involving -1 -order Genocchi polynomials that have important applications, particularly in analytical number theory. This study can be shown as an important example of defining the special polynomial families with the help of generator functions and forming linear positive operators. As a result, numerous fields, including operator theory, mathematics, and engineering, may benefit from this study's findings.

The original results obtained in this study may inspire the use of special polynomial families defined in q - and (p, q) -analysis to construct positive linear operators in approximation theory.

ACKNOWLEDGEMENT

A portion of this study has been presented at "The 5th Mediterranean International Conference of Pure & Applied Mathematics and Related Areas (MICOPAM 2022)" held in Antalya, Turkey on October 27- 30, 2022.

CONFLICT OF INTEREST

The author declares no conflict of interest.

REFERENCES

- Agyuz, E. (2021a). On The Convergence Properties of Kantorovich-Szász Type Operators Involving Tangent Polynomials. *Adiyaman University Journal of Science*, 11(2), 244-252. doi:[10.37094/adyujsci.905311](https://doi.org/10.37094/adyujsci.905311)
- Agyuz, E. (2021b, November 11-12). *Convergence by Szász type operators based on Euler type polynomials*. In: The 3rd & 4th Mediterranean International Conference of Pure & Applied Mathematics and Related Areas (MICOPAM 2020-2021). Antalya, Türkiye.
- Agyuz, E. (2022). A Study on Kantorovich Type Operator Involving Adjoint Euler Polynomials. *Conference Proceedings of Science and Technology*, 5(1), 178-181.
- Agyuz, E. (2023). A Generalization of Szász Type Operators Involving Generating Function of Negative Order Genocchi Polynomials. In: A. Akpınar (Eds.), *Research on Mathematics and Science*, (pp. 15-26). doi:[10.58830/ozgur.pub81](https://doi.org/10.58830/ozgur.pub81)
- Altomare, F. (2010). Korovkin-type theorems and approximation by positive linear operators. *Survey Approx. Theory*, 5, 92-164.
- Atakut, Ç., & Büyükyazıcı, İ. (2016). Approximation by Kantorovich-Szász type operators based on Brenke type polynomials. *Numerical Functional Analysis and Optimization*, 37(12), 1488-1502. doi:[10.1080/01630563.2016.1216447](https://doi.org/10.1080/01630563.2016.1216447)
- Cangul, İ. N., Ozden, H., & Simsek, Y. (2009) A new approach to q-Genocchi numbers and their interpolation functions. *Nonlinear Analysis: Theory, Methods & Applications*, 71(12), e793-e799. doi:[10.1016/j.na.2008.11.040](https://doi.org/10.1016/j.na.2008.11.040)
- Davis, P. J. (1975). *Interpolation and approximation*. Courier Corporation.
- DeVore, R. A., & Lorentz, G. G. (1993). *Constructive approximation (Vol. 303)*. Springer, Berlin.
- Gupta, V., & Rassias, M. T. (2019). *Moments of linear positive operators and approximation*. Switzerland: Springer International Publishing. doi:[10.1007/978-3-030-19455-0](https://doi.org/10.1007/978-3-030-19455-0)
- Horadam, A. F. (1992). Negative order Genocchi polynomials. *Fibonacci Q*, 30, 21-34.
- İçöz, G., Varma, S., & Sucu, S. (2016). Approximation by operators including generalized Appell polynomials. *Filomat*, 30(2), 429-440. doi:[10.2298/FIL1602429I](https://doi.org/10.2298/FIL1602429I)
- Jakimovski, A., & Leviatan, D. (1969). Generalized Szász operators for the approximation in the infinite interval. *Mathematica (Cluj)*, 11(34), 97-103.
- Kılar, N., & Simsek, Y. (2020). Formulas involving sums of powers, special numbers and polynomials arising from p-adic integrals, trigonometric and generating functions. *Publications de l'Institut Mathématique*, 108(122), 103-120. doi:[10.2298/PIM2022103K](https://doi.org/10.2298/PIM2022103K)
- Kılar, N., & Simsek, Y. (2021). Formulas and Relations of Special Numbers and Polynomials arising from Functional Equations of Generating Functions. *Montes Taurus Journal of Pure and Applied Mathematics*, 3(1), 106-123.
- Korovkin, P. P. (1953). Convergence of linear positive operators in the spaces of continuous functions (Russian). *Doklady Akad. Nauk. SSSR (N.S.)*, 90, 961-964.
- Korovkin, P. P. (1960). *Linear Operators and Approximation Theory*. Translated from the Russian ed. (1959), *Russian Monographs and Texts on Advances Mathematics and Physics, Vol. III*. Gordon and Breach Publishers, Inc. New York, Hindustan Publ. Corp. (India), Delhi.
- Kucukoglu, I., Simsek, B., & Simsek, Y. (2019). An approach to negative hypergeometric distribution by generating function for special numbers and polynomials. *Turkish Journal of Mathematics*, 43(5), 2337-2353. doi:[10.3906/mat-1906-6](https://doi.org/10.3906/mat-1906-6)

- Kucukoglu, I. (2022). Computational and implementational analysis of generating functions for higher order combinatorial numbers and polynomials attached to Dirichlet characters. *Mathematical Methods in the Applied Sciences*, 45(9), 5043-5066. doi:[10.1002/mma.8092](https://doi.org/10.1002/mma.8092)
- Lupas, A. (1995, March 13-17). *The approximation by some positive linear operators*. In: M. W. Müller, M. Felten, D. H. Mache. (Eds.), Proceedings of the International Dortmund Meeting on Approximation Theory (pp. 201-229). Witten, Germany.
- Menekşe Yılmaz, M. (2022). Approximation by Szasz Type Operators Involving Apostol-Genocchi Polynomials. *CMES-Computer Modeling in Engineering & Sciences*, 130(1), 287-297. doi:[10.32604/cmcs.2022.017385](https://doi.org/10.32604/cmcs.2022.017385)
- Mursaleen, M., Al-Abied, A. A. H., & ACU, A. M. (2018). Approximation by Chlodowsky type of Szasz operators based on Boas--Buck-type polynomials. *Turkish Journal of Mathematics*, 42(5), 2243-2259. doi:[10.3906/mat-1803-62](https://doi.org/10.3906/mat-1803-62)
- Simsek, Y. (2008). Generating functions of the twisted Bernoulli numbers and polynomials associated with their interpolation functions. *Advanced Studies in Contemporary Mathematics*, 16(2), 251-278.
- Simsek, Y. (2012). Generating functions for q-Apostol type Frobenius-Euler numbers and polynomials. *Axioms*, 1(3), 395-403. doi:[10.3390/axioms1030395](https://doi.org/10.3390/axioms1030395)
- Simsek, Y. (2013). Generating functions for generalized Stirling type numbers, array type polynomials, Eulerian type polynomials and their applications. *Fixed Point Theory and Applications*, 2013(1), 87. doi:[10.1186/1687-1812-2013-87](https://doi.org/10.1186/1687-1812-2013-87)
- Simsek, Y. (2017). Computation methods for combinatorial sums and Euler-type numbers related to new families of numbers. *Mathematical Methods in the Applied Sciences*, 40(7), 2347-2361. doi:[10.1002/mma.4143](https://doi.org/10.1002/mma.4143)
- Simsek, Y. (2018). New families of special numbers for computing negative order Euler numbers and related numbers and polynomials. *Applicable Analysis and Discrete Mathematics*, 12(1), 1-35. doi:[10.2298/AADM1801001S](https://doi.org/10.2298/AADM1801001S)
- Srivastava, H. M., & Choi, J. (2001). *Series Associated with the Zeta and Related Functions*. Kluwer Academic Publishers, Dordrecht, Boston and London.
- Srivastava, H. M., Kurt, B., & Simsek, Y. (2012). Some families of Genocchi type polynomials and their interpolation functions. *Integral Transforms and Special Functions*, 23(12), 919-938. doi:[10.1080/10652469.2011.643627](https://doi.org/10.1080/10652469.2011.643627)
- Varma, S., Sucu, S., & İçöz, G. (2012). Generalization of Szász operators involving Brenke type polynomials. *Computers & Mathematics with Applications*, 64(2), 121-127. doi:[10.1016/j.camwa.2012.01.025](https://doi.org/10.1016/j.camwa.2012.01.025)



Gazi University

Journal of Science

PART A: ENGINEERING AND INNOVATION

<http://dergipark.org.tr/guj.1303347>

A Control Scheme for a Quasi-Z Source Three-Phase Inverter

Zafer ORTATEPE^{1*} Sadık ÖZDEMİR²

¹Pamukkale University, Department of Automotive Engineering, Denizli, Türkiye

²Pamukkale University, Department of Mechatronics Engineering, Denizli, Türkiye

Keywords	Abstract
DC-AC Inverter Modulation Scheme Quasi-z Source Inverter	This paper presents a novel control scheme for a three-phase quasi-z source inverter (qZSI) using a capacitor voltage and input current-based sinusoidal pulse width modulation (SPWM) technique. The proposed scheme combines the advantages of both qZSI and SPWM techniques to achieve improved performance. The SPWM technique utilizes a sinusoidal modulation signal, which is compared with a high-frequency triangular carrier wave and two shoot-through (ST) references to determine the switching states for the three-phase qZSI. The positive and negative ST references are obtained from the capacitor voltages and input current, allowing for control of the DC bus voltage and ST states of the inverter. Additionally, the proposed control scheme generates the three-phase modulation signal through decoupling control in the dq reference frame. The detailed analysis of the control scheme includes its operating principle, transient state, steady-state responses, and the effects of parameter variations. Simulation studies are conducted using MATLAB/Simulink to assess the performance of the three-phase qZSI under the proposed control scheme. The simulation results demonstrate the effectiveness of the control scheme in terms of output voltage quality, DC bus voltage control, and robustness against reference variations. Overall, the proposed capacitor voltage and input current-based SPWM control scheme for the three-phase qZSI shows promising performance improvements and robustness, as confirmed through comprehensive simulation studies.

Cite

Ortatepe, Z., & Özdemir, S. (2023). A Control Scheme for a Quasi-Z Source Three-Phase Inverter. *GU J Sci, Part A, 10(2)*, 206-221. doi:10.54287/guj.1303347

Author ID (ORCID Number)	Article Process
0000-0001-7771-1677	Submission Date 27.05.2023
0000-0001-7676-7484	Revision Date 19.06.2023
	Accepted Date 21.06.2023
	Published Date 23.06.2023

1. INTRODUCTION

Three-phase voltage source inverters (VSIs) have found extensive application in the field of power electronics. However, despite their widespread use, they are not without limitations. Specifically, VSIs can generate harmonic distortions in the output waveform and have constraints in achieving higher output voltages beyond the input DC voltage.

Z-source inverter (ZSI) has been proposed as a solution to overcome the disadvantages associated with conventional VSIs (Peng, 2002; 2003; Peng et al., 2003). The ZSI is designed with a unique impedance network in its DC input circuit. Some of the advantages of ZSIs include the ability to provide voltage boost capability, which is useful in applications that require higher output voltage levels than the input source voltage can provide. Additionally, ZSIs offer inherent short-circuit protection (Parla & Özdemir, 2022). However, ZSIs also have some limitations, including discontinuous input current.

To overcome these drawbacks, a new qZSI topology is proposed as a modified version of ZSI to achieve similar functionalities with lower-rated passive components (Anderson & Peng, 2008a; 2008b; Cao & Peng, 2009). The qZSI topology features a continuous input current and enables operation at a wide range of input

*Corresponding Author, e-mail: zortatepe@pau.edu.tr

voltages, making it suitable for diverse applications (Hong & Cha, 2021; Li et al., 2022; Elmorshedy et al., 2023). Additionally, the topology has two operation modes: non-shoot-through (NST) state and shoot-through (ST) state (Paikray et al., 2022). The diode network and LC connected to qZSI change the operation of the topology to allow an ST state. In the ST state, the inverter voltage shoots through the impedance source network like a short circuit, allowing the qZSI to act as a voltage buck/boost without the need for an additional DC/DC converter (Liu et al., 2019; Poorali & Adib, 2020). However, the ST state is undesirable, as it can result in high current flow, and potentially cause damage to the inverter (Sun et al., 2013; Padmavathi & Natarajan, 2020).

Proper control and modulation techniques have been employed to ensure the safe and reliable operation of the qZSI (Endiz & Akkaya, 2022). Various PWM modulation methods have been studied to achieve less device stress, less switching/commutation, and simple applicability over a wide modulation range in three-phase qZSI applications (Devaraj et al., 2019; Mohammadi et al., 2020; Nguyen & Choi, 2021). Although many modulation techniques have been studied in the literature, SPWM is the primary modulation technique employed in three-phase qZSI circuits. SPWM modulation has been applied to the qZSI with four basic ST methods, including maximum constant boost control, maximum boost control, simple boost control, and third-harmonic injection. Each method has its own advantages and disadvantages.

In this paper, the ST state references are identified from the capacitor voltages and input current to control the DC bus and ST states of qZSI. Besides, three-phase reference modulation signals are generated using the decoupling control method in a dq reference frame. A high-frequency triangular carrier wave, three-phase sinusoidal modulation signals, and two positive and negative ST references obtained from the input capacitor voltages and input current of the qZS network are used to determine ST and NST switching states of the qZSI.

Following the introduction, the paper is organized as follows: Section 2 presents the three-phase qZSI mathematical model. Then, Section 3 introduces the decoupling control in a dq reference frame and SPWM control methods, followed by a discussion of the results. Finally, the article concludes with a conclusion and recommendations section.

2. MATHEMATICAL MODEL OF THREE-PHASE QZSI

Figure 1 illustrates the equivalent circuit of a three-phase qZSI. The qZS network comprises two capacitors (C_1, C_2), two inductors (L_1, L_2), and one diode (D). V_{in} represents the DC input voltage of the qZS network, while V_{PN} represents the connection point between the qZS network and the conventional three-phase VSI and serves as the DC input voltage of the conventional three-phase inverter. For the mathematical analysis conducted in this paper, the inductances and capacitors of the qZS network are assumed to be equivalent as indicated by Equations (1) and (2).

$$L_1 = L_2 = L \quad (1)$$

$$C_1 = C_2 = C \quad (2)$$

2.1. Non-Shoot-Through State

Figure 2 illustrates the equivalent circuit of the active (non-shoot-through) state of the three-phase qZSI. During the NST state operation, the three-phase VSI is treated as a current source. In this state, the energy stored during the ST state is transferred to the load. The instantaneous load current (i_{load}) is equal to the inverter input current (i_{inv}) as indicated by Equation (3).

$$i_{inv} = i_{load} \quad (3)$$

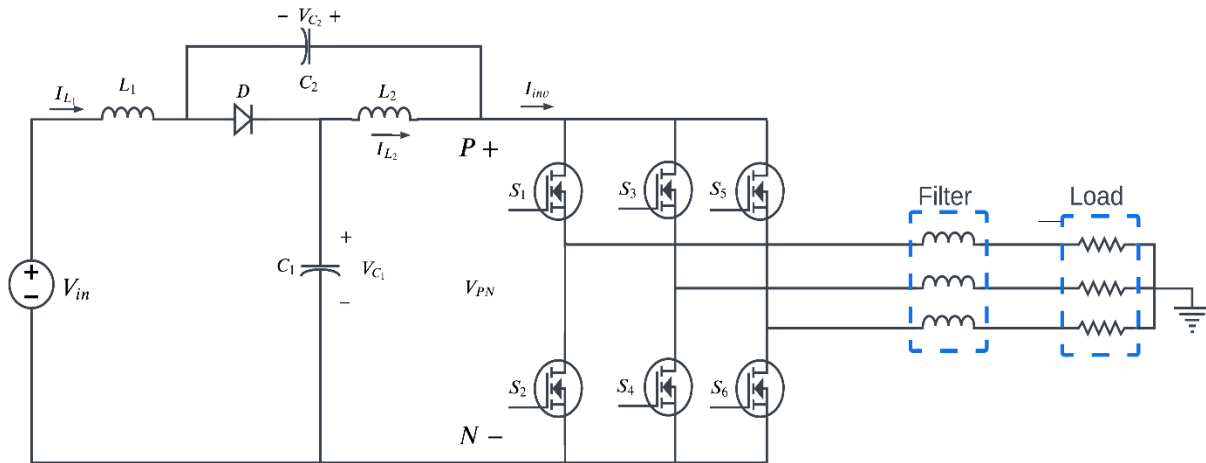


Figure 1. Three-phase qZSI equivalent circuit

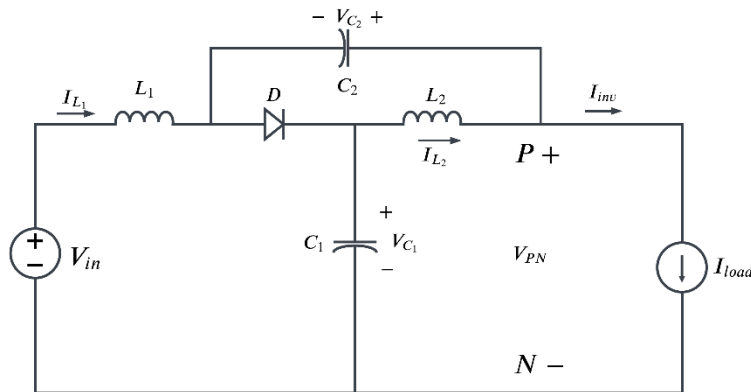


Figure 2. NST state operation of the qZSI

The inductance current (i_{L1}) can be derived from the equivalent circuit for the NST state as shown in Equation (4):

$$L \frac{di_{L1}}{dt} = V_{in} - v_{C1} \tag{4}$$

The C_1 capacitor voltage (v_{C1}) can also be derived using the equivalent circuit depicted in Figure 2. The equation that describes the derivation of C_1 capacitor voltage is given by Equation (5).

$$C \frac{dv_{C1}}{dt} = i_{L1} - i_{inv} \tag{5}$$

In Equation (6), the variables (S_a, S_b, S_c) represent integer values that can take the numbers 0 and 1. A value of 0 indicates that the corresponding switch is in the off state, while a value of 1 indicates that the switch is in the on state. On the other hand, (i_a, i_b, i_c) represent the three-phase load currents.

$$i_{inv} = S_a i_a + S_b i_b + S_c i_c \tag{6}$$

2.2. Null State

Figure 3 presents the equivalent circuit of the null state of a three-phase qZSI. In the null state operation, all the switches of the VSI are in the off state, meaning that no current flows through the VSI.

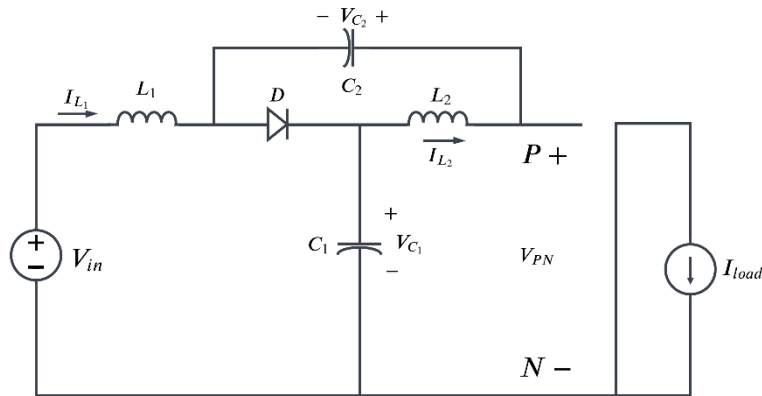


Figure 3. Null state operation of the qZSI

From Figure 3, the expression for the inductance current (i_{L1}) of the L_1 inductance and the equation for the capacitor voltage (v_{C1}) of the C_1 capacitor can be derived. These equations are represented as Equations (7) and (8), respectively.

$$L \frac{di_{L1}}{dt} = V_{in} - v_{C1} \quad (7)$$

$$C \frac{dv_{C1}}{dt} = i_{L1} \quad (8)$$

2.3. Shoot-Through State

Figure 4 illustrates the equivalent circuit of the ST state in a three-phase qZSI. Unlike a conventional VSI, during the ST state, the lower and upper switches of each phase in the three-phase qZSI are short-circuited. This configuration allows the qZS network to store energy from the DC bus, leading to voltage boosting. The voltage boosted during the ST operation can then be transferred to the load during the NST state. It's important to note that during the ST state, the diode of the qZS network is off. This is because the polarity of the capacitors C_1 and C_2 blocks the diode D from conducting.

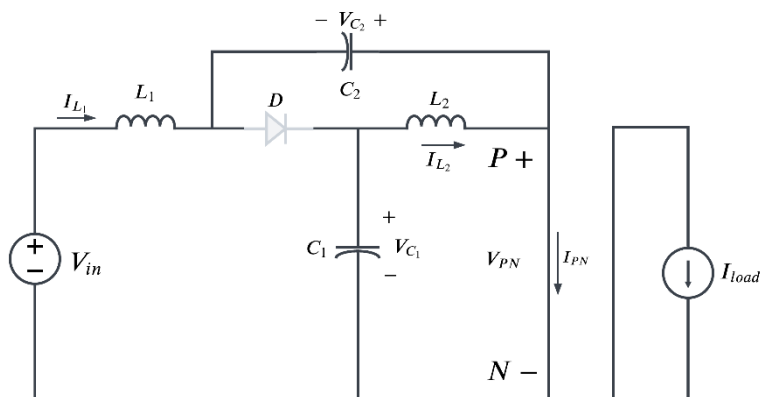


Figure 4. ST state operation of the qZSI

The L_1 inductance current (i_{L1}) and the capacitor C_1 voltage (v_{C1}) equations can be obtained from Figure. 4 as given in Equations (9) and (10), respectively.

$$L \frac{di_{L1}}{dt} = V_{in} + v_{C2} \quad (9)$$

$$C \frac{dv_{C1}}{dt} = -i_{L2} \quad (10)$$

According to Kirchoff's voltage law, the relationship between the input voltage and capacitor voltages is expressed in Equation (11), and as shown in Figure 4, inductance currents are equal to Equation (12).

$$v_{C1} - v_{C2} = v_{in} \quad (11)$$

$$i_{L1} = i_{L2} \quad (12)$$

2.4. Decoupling Control in dq Reference Frame

Equations (13) to (15) provide the representation of the virtual three-phase output voltages. In the equations, V_{max} represents the maximum voltage and ω the angular frequency.

$$v_a = V_{max} \sin(\omega t) \quad (13)$$

$$v_b = V_{max} \sin(\omega t - 2\pi/3) \quad (14)$$

$$v_c = V_{max} \sin(\omega t + 2\pi/3) \quad (15)$$

The equations giving the relationship between the three-phase load and inverter are shown in Equation (16). This equation is defined in (abc) stationary reference frame.

$$\begin{bmatrix} di_a \\ di_b \\ di_c \end{bmatrix} = \begin{bmatrix} -\frac{R}{L} & 0 & 0 \\ 0 & -\frac{R}{L} & 0 \\ 0 & 0 & -\frac{R}{L} \end{bmatrix} \begin{bmatrix} i_a \\ i_b \\ i_c \end{bmatrix} + \frac{1}{L} \begin{bmatrix} u_a - v_a \\ u_b - v_b \\ u_c - v_c \end{bmatrix} \quad (16)$$

By performing the park transformation, the equation given above (16) in the stationary reference frame can be converted to the synchronously rotating reference frame as given in Equation (17). In this equation, i_d and i_q are d-axis and q-axis output currents, v_d and v_q are d-axis and q-axis load voltages and u_d and u_q are d-axis and q-axis inverter voltages, respectively.

$$\begin{bmatrix} \frac{di_d}{dt} \\ \frac{di_q}{dt} \end{bmatrix} = \frac{1}{L} \begin{bmatrix} -R & \omega L \\ \omega L & -R \end{bmatrix} \begin{bmatrix} i_d \\ i_q \end{bmatrix} - \frac{1}{L} \begin{bmatrix} v_d \\ v_q \end{bmatrix} + \frac{1}{L} \begin{bmatrix} u_d \\ u_q \end{bmatrix} \quad (17)$$

Equations (18) and (19) give the decoupling dq-axis inverter voltages in the synchronously rotating reference frame. In these equations, inverter voltage is formulated as the sum of load voltage and other coupling parameters.

$$u_d = L \frac{di_d}{dt} + Ri_d - \omega Li_q + v_d \quad (18)$$

$$u_q = L \frac{di_q}{dt} + Ri_q - \omega Li_d + v_q \quad (19)$$

The reference and measured dq-axis load voltages are compared, and its PI controller output gives dq-axis reference currents as given in Equations (20) and (21). This reference dq-axis currents and the measured and transformed dq-axis output currents are compared with the PI controller to make the closed-loop controller stable in the decoupling control. Its formulation is given in Equations (22) and (23).

$$i_{dref} = \left(K_{p1} + \frac{K_{i1}}{s} \right) (V_{dref} - V_d) \quad (20)$$

$$i_{qref} = \left(K_{p2} + \frac{K_{i2}}{s} \right) (V_{qref} - V_q) \quad (21)$$

$$u_d = \left(K_{p3} + \frac{K_{i3}}{s} \right) (i_{dref} - i_d) - \omega Li_q + V_d \quad (22)$$

$$u_q = \left(K_{p4} + \frac{K_{i4}}{s} \right) (i_{dref} - i_q) - \omega Li_d + V_q \quad (23)$$

The decoupling control of three-phase qZSI is shown in Figure 5.

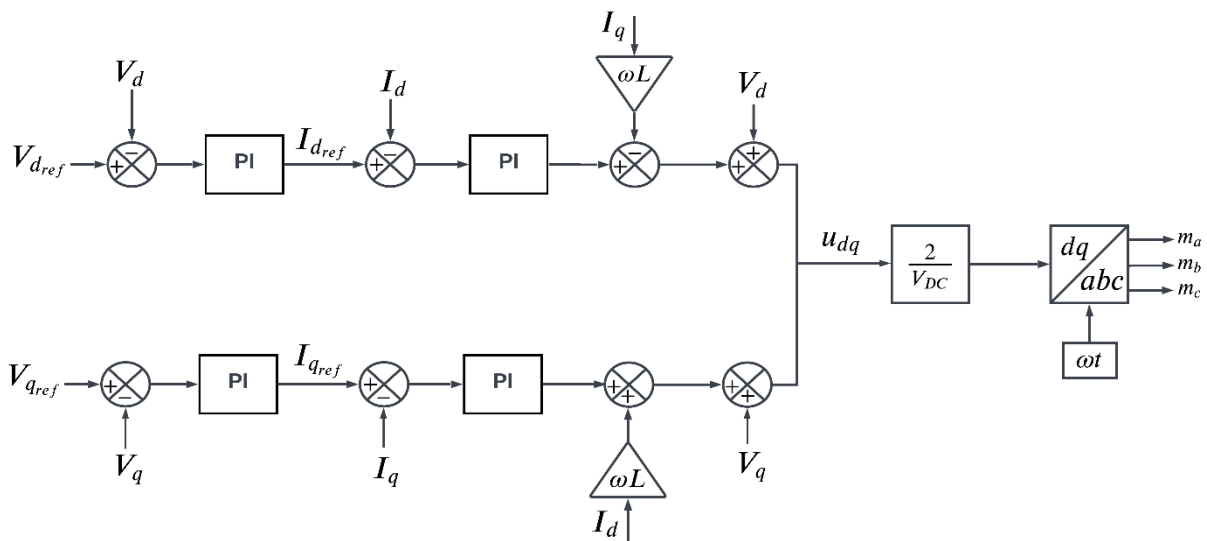


Figure 5. Modulation control strategy in dq reference frame

2.5. Sinusoidal PWM (SPWM) Control Strategy

The fundamental concept behind SPWM is to utilize a sine wave to modulate the duty cycle of a square wave. In SPWM, the output signal takes on a waveform resembling a sine wave, and its fundamental frequency matches the frequency of the modulating sine wave. A waveform with variable amplitude and frequency is produced when the square wave's duty cycle varies proportionally to the sine wave's amplitude. Simple boost control, maximum boost control, maximum constant boost control, and third-harmonic injection are the main SPWM modulation techniques (Sabeur et al., 2018; Zhao et al., 2019; Garcia-Vazquez et al., 2020; Xu et al., 2020).

In this paper, ST state references are identified from the capacitor voltages and input current to control DC bus voltage and ST states of qZSI. The positive and negative ST state (+D and -D) generation control block diagram is given in Figure 6. Reference ($V_{C_{ref}}$) and the sum of actual capacitor voltages ($V_{C_1} + V_{C_2}$) are compared, and its output gives reference input current as given in Equation (24). This reference and the measured input currents are compared in the PI controller to obtain the ST state of the qZSI as given in Equation (25).

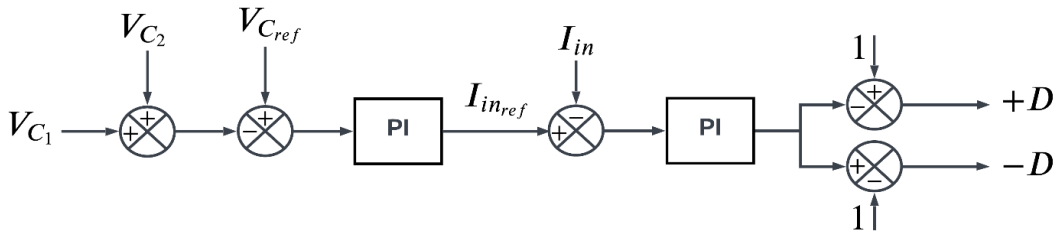


Figure 6. Positive and negative ST state (+D and -D) generation control block diagram

$$I_{in_{ref}} = \left(K_{p_5} + \frac{K_{i_5}}{s} \right) \left(V_{C_{ref}} - (V_{C_1} + V_{C_2}) \right) \quad (24)$$

$$1 - D = \left(K_{p_6} + \frac{K_{i_6}}{s} \right) \left(I_{in_{ref}} - I_{in} \right) \quad (25)$$

Figure 7 shows the generation of switching signals of a three-phase qZSI by decoupling control and ST state control methods. To generate the +D and -D references, the sum of capacitor voltages ($V_{C_1} + V_{C_2}$) of the qZS network is compared with reference capacitor voltage ($V_{C_{ref}}$). Error is employed to PI controlled to generate qZS network input current reference. +D and -D references are generated by adding ± 1 output obtained by comparing the measured input current with the PI controller respectively.

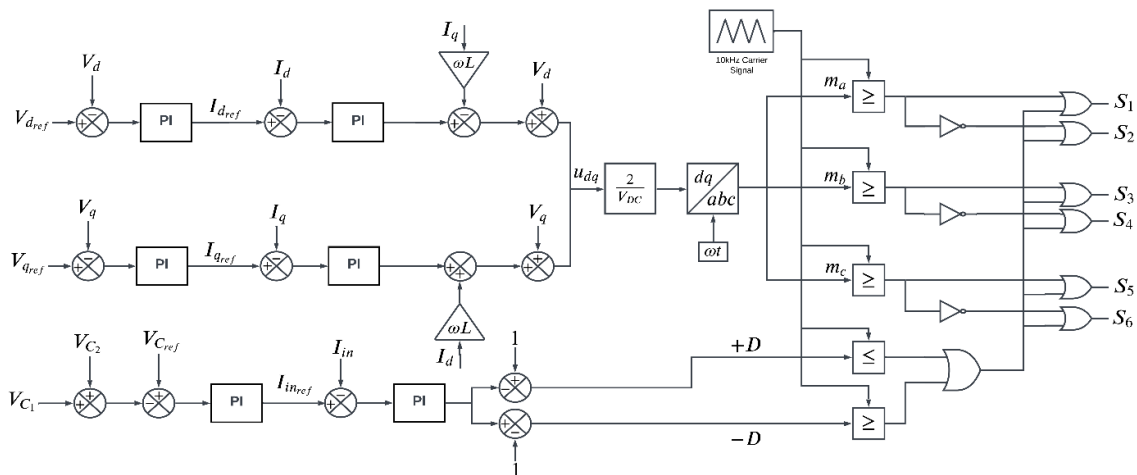


Figure 7. Modulation and ST state control with SPWM controller

The control layout of three-phase qZSI is given in Figure 8. Output voltages and currents measured at the load are converted to the synchronously rotating reference frame. The resulting dq-axis output currents are used to generate inverter reference voltages in the current controller. The generated reference inverter voltages and the measured output voltages converted to the dq axis are used to generate the reference dq axis output voltages using the decoupling control equations. The calculated dq-axis output reference voltages are transformed to a stationary abc-axis reference frame and (m_a, m_b, m_c) voltage references are obtained.

The sum of the capacitor voltages V_{C1} and V_{C2} of the qZS network is compared with the reference capacitor voltage. This reference capacitor voltage also equals the maximum DC bus voltage. Reference input current is generated by passing the error through PI control. The obtained input reference current is compared with the actual/measured input current and the difference is subjected to PI control. The PI controller output is used to have +D and -D references.

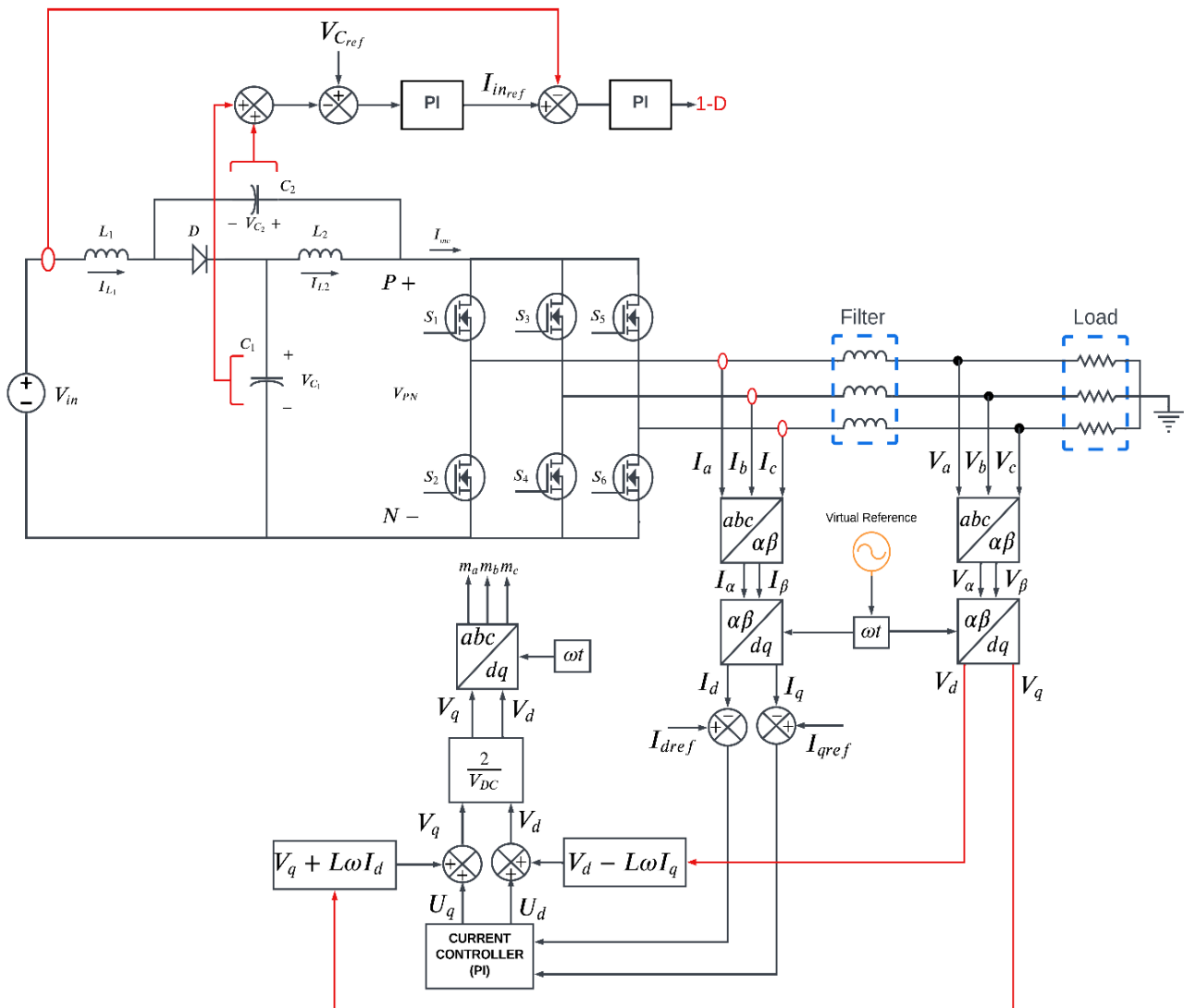


Figure 8. The control layout of the three-phase qZSI

3. SIMULATION RESULTS

Simulation studies have been performed with Matlab/Simulink program to evaluate the performance of three-phase qZSI. Moreover, the whole control scheme of the qZSI is designed in Matlab/Simulink. Therefore, the parameters used in the paper are presented in Table 1.

Table 1. Simulation parameters are used in this paper.

Parameters	Symbols	Values
Input voltage	V_{in}	100 [V _{dc}]
Output load	R_L	40 [Ω]
Filter inductance	L_f	10 [mH]
Switching frequency	f_s	10 [kHz]
DC bus voltage	V_{PN}	800 [V _{dc}]
qZSI Inductances	L_1, L_2	500 [μ H]
qZSI Capacitors	C_1, C_2	300 [μ F]

Also, the layout of the whole control system of qZSI is depicted in Figure 9. Decoupling control and ST state control scheme are given on the upper side, and three-phase qZSI is given on the lower side. DC bus voltage is determined as 800 V_{dc}. All inductance and capacitor values are selected as 500 μ H and 300 μ F, respectively. Besides, the switching frequency is selected as 10kHz. Finally, the output filter and resistive load parameters are determined as 10 mH and 40 Ω , respectively.

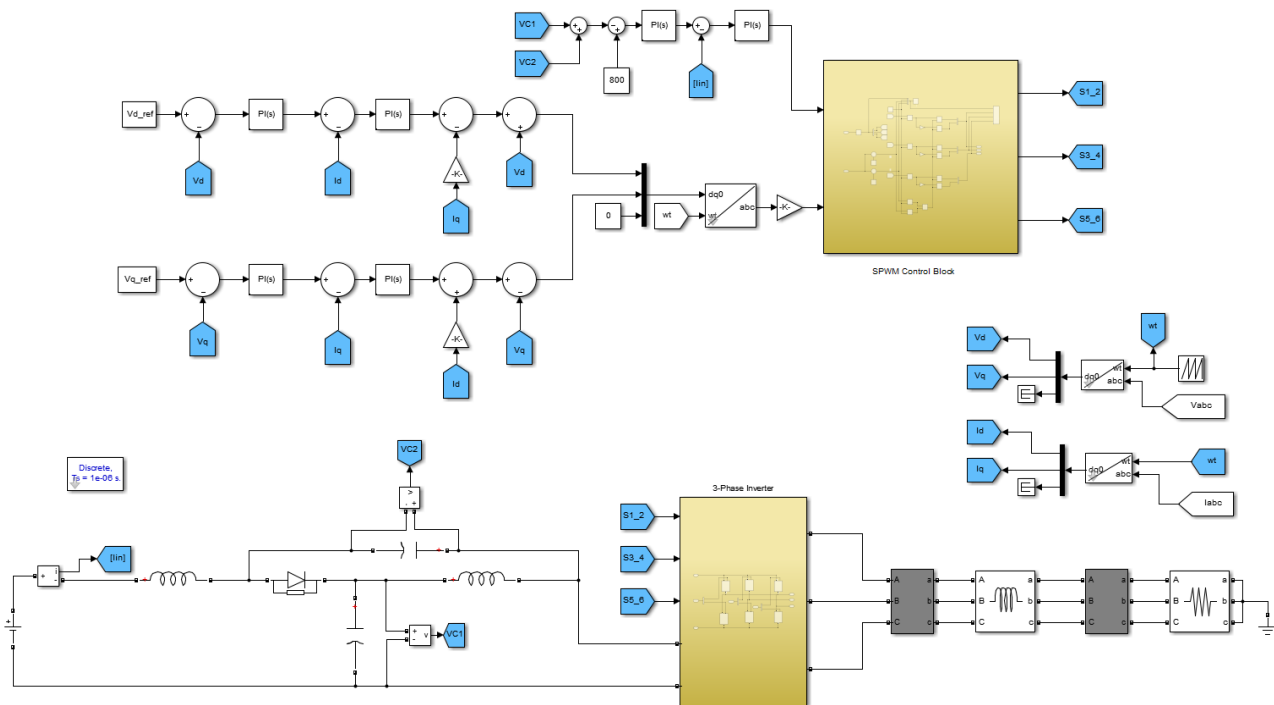


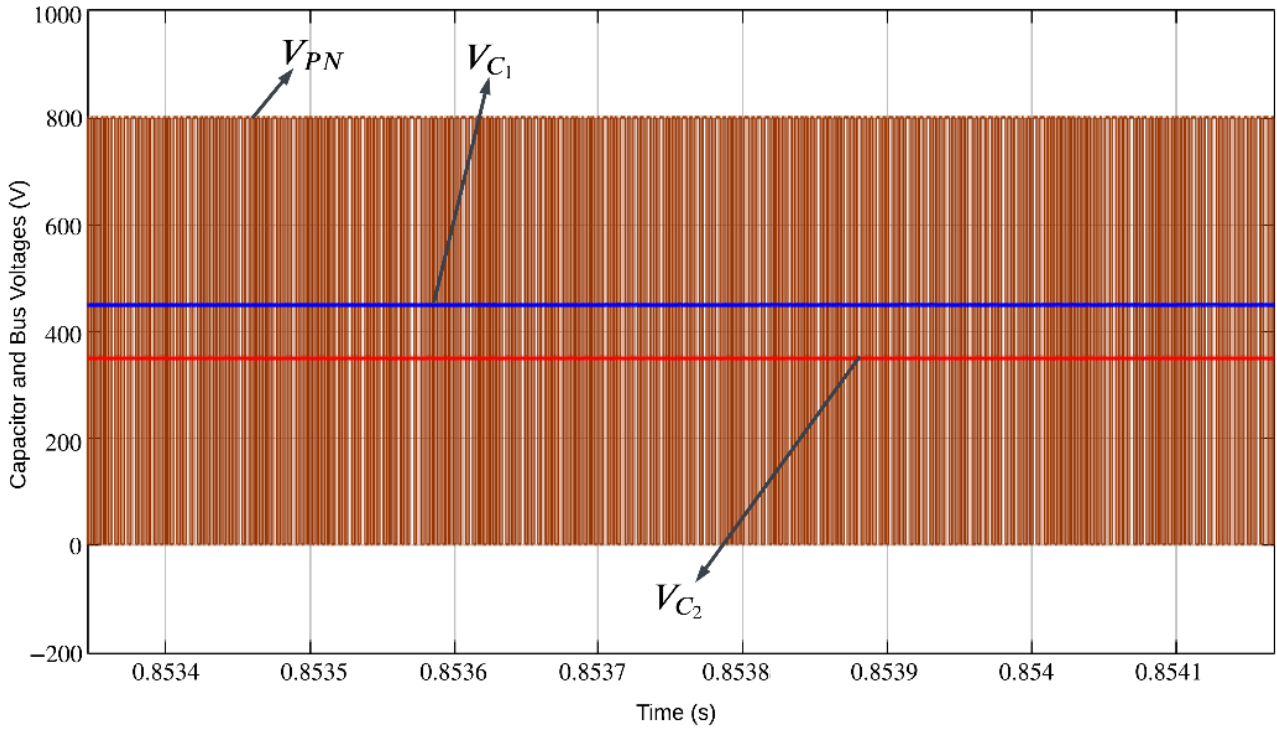
Figure 9. The layout of the whole control system of the qZSI

Besides, the six PI controller parameters used in the simulation are also shown in Table 2. PI_1 and PI_2 controllers are responsible for generating the I_{dref} and I_{qref} , respectively. PI_3 and PI_4 controllers are responsible for generating the u_d and u_q , respectively. Finally, PI_5 and PI_6 controllers are responsible for generating the ST state as $1 - D$.

Table 2. PI parameters used in the qZSI controller.

Parameters	Symbols	Values
PI_1	K_{P_1}, K_{I_1}	0.001, 0.2
PI_2	K_{P_2}, K_{I_2}	0.001, 0.2
PI_3	K_{P_3}, K_{I_3}	5, 5000
PI_4	K_{P_4}, K_{I_4}	5, 5000
PI_5	K_{P_5}, K_{I_5}	0.06, 5
PI_6	K_{P_6}, K_{I_6}	1.5, 0.01

The proposed control scheme and qZSI are analyzed in transient, steady state, and some parameter variations. Figure 10 depicts the steady-state capacitor and bus voltages of the SPWM-based three-phase qZSI. In typical operating conditions, the bus voltage is equal to the sum of V_{C_1} and V_{C_2} . However, when the system is in the ST state, the output voltage is zero. Furthermore, it can be deduced that the input voltage, V_{in_1} , is equal to the difference between V_{C_1} and V_{C_2} .

**Figure 10.** Capacitor (V_{C_1}, V_{C_2}) and bus voltage (V_{PN}) waveforms of the SPWM-based qZSI

Transient state output voltage (V_d, V_q) and output current (I_d, I_q) waveforms of the SPWM-based three-phase qZSI in a dq reference frame are illustrated in Figure 11. To observe the transient response of the circuit, $V_{d_{ref}} = 311V$ and $V_{q_{ref}} = 0V$ are applied to the input as reference voltages and the output current $I_d \cong 4A$ and $I_q \cong -2.15A$ are obtained. It has been observed that all current and voltage values are set to a 2% reference band at approximately 300 ms.

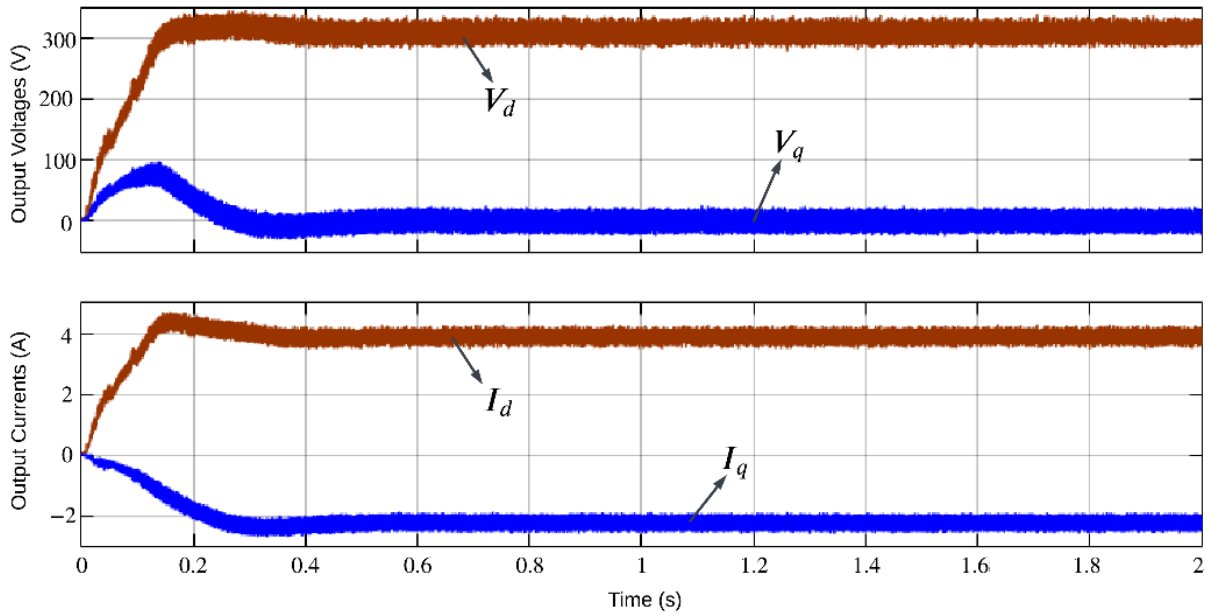


Figure 11. Output voltage (V_d, V_q) and output current (I_d, I_q) waveforms of the SPWM-based qZSI in a dq reference frame.

Steady-state phase-neutral output voltages (V_{an}, V_{bn}, V_{cn}) and filtered output current ($I_{o_a}, I_{o_b}, I_{o_c}$) waveforms of the SPWM-based three-phase qZSI are given in Figure 12, respectively. $V_{d_{ref}} = 311V$ and $V_{q_{ref}} = 0V$ are applied to the input as reference voltages to examine the steady response of the circuit and the maximum value of the balanced output current $I_{o_a} \cong I_{o_b} \cong I_{o_c} \cong 4.9A$ are obtained. The filtered output current has a sinusoidal form while the input voltage has three-level square waveform. Moreover, the THD value of the output current is measured as 3.9 % and it can be concluded that the THD value of the input current is acceptable limits for IEC61000-3-2.

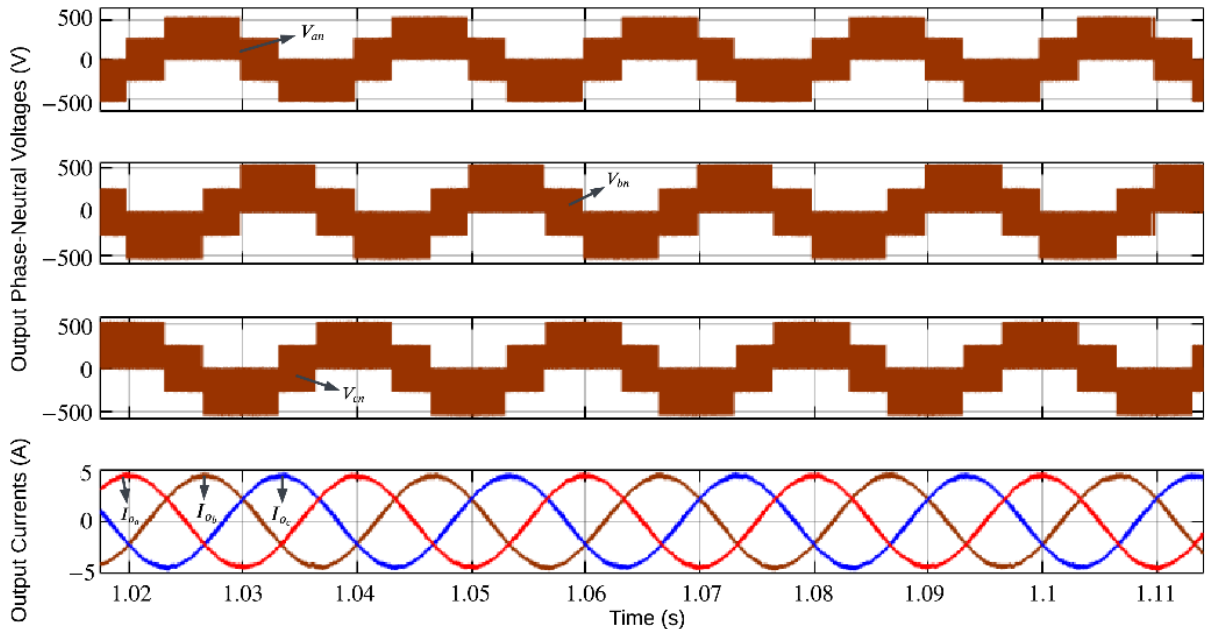


Figure 12. Output phase-neutral voltages (V_{an}, V_{bn}, V_{cn}) and filtered output current ($I_{o_a}, I_{o_b}, I_{o_c}$) waveforms of the SPWM-based qZSI

Steady-state filtered output phase-phase voltages (V_{ab}, V_{bc}, V_{ca}) and output current ($I_{o_a}, I_{o_b}, I_{o_c}$) waveforms of the SPWM-based three-phase qZSI are shown in Figure 13, respectively. It can be inferred that all filtered current and voltage waveforms of qZSI are sinusoidal in a steady state.

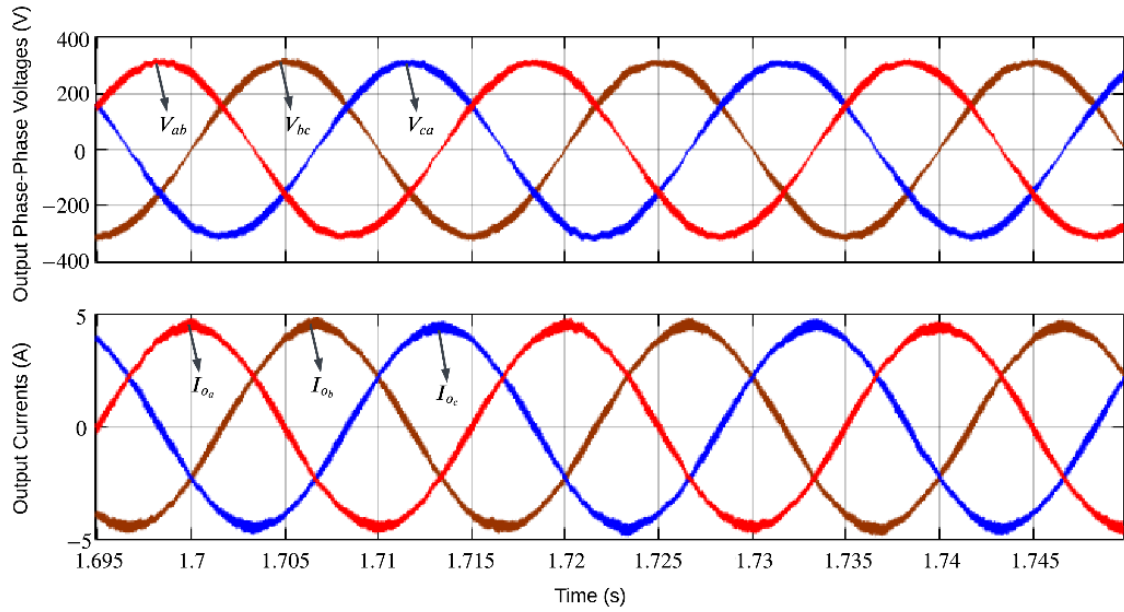


Figure 13. Filtered output phase-phase voltages (V_{ab}, V_{bc}, V_{ca}) and output current ($I_{o_a}, I_{o_b}, I_{o_c}$) waveforms of the SPWM-based qZSI

Step responses of the output voltage (V_d, V_q), output current (I_d, I_q), phase-phase output voltage (V_{ab}, V_{bc}, V_{ca}), and output current ($I_{o_a}, I_{o_b}, I_{o_c}$) waveforms of the SPWM-based three-phase qZSI are depicted in Figure 14, respectively. To study the step response of the circuit, $V_{d_{ref}} = 311V$ and $V_{q_{ref}} = 0V$ are applied to the input as reference voltages. After 0.7 seconds, $V_{d_{ref}} = 200V$ and $V_{q_{ref}} = 0V$ are applied as a reference, and after 1.4 seconds, $V_{d_{ref}} = 200V$ and $V_{q_{ref}} = -150V$ are applied, respectively. In all cases, the system settles to the 2% reference band at a maximum of 200 ms.

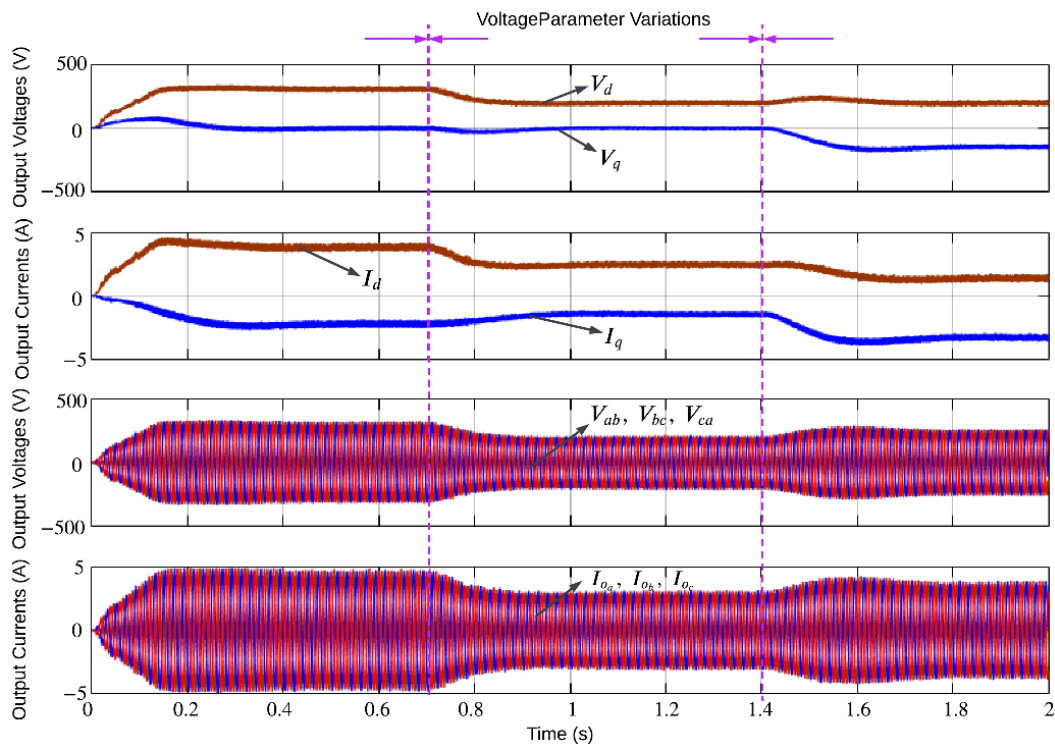


Figure 14. Output voltage (V_d, V_q), output current (I_d, I_q), phase-phase output voltage (V_{ab}, V_{bc}, V_{ca}), and output current ($I_{o_a}, I_{o_b}, I_{o_c}$) waveforms of the SPWM-based qZSI

Step responses of the capacitor voltages (V_{C_1}, V_{C_2}) and input current (I_{in}) waveforms of the SPWM-based three-phase qZSI are illustrated in Figure 15, respectively. To analyze the step response of the circuit, $V_{d_{ref}} = 311V$ and $V_{q_{ref}} = 0V$ are applied to the input as reference voltages. After 0.7 seconds, $V_{d_{ref}} = 200V$ and $V_{q_{ref}} = 0V$ are applied as a reference, and after 1.35 seconds, $V_{d_{ref}} = 200V$ and $V_{q_{ref}} = -150V$ are applied, respectively. In a transient state, maximum voltage ripples of the capacitor voltages V_{C_1} and V_{C_2} are obtained as 2%. Moreover, it has been observed that the capacitor voltages do not change in the steady state even if the reference voltage variations and settle to the reference after a few hundred milliseconds.

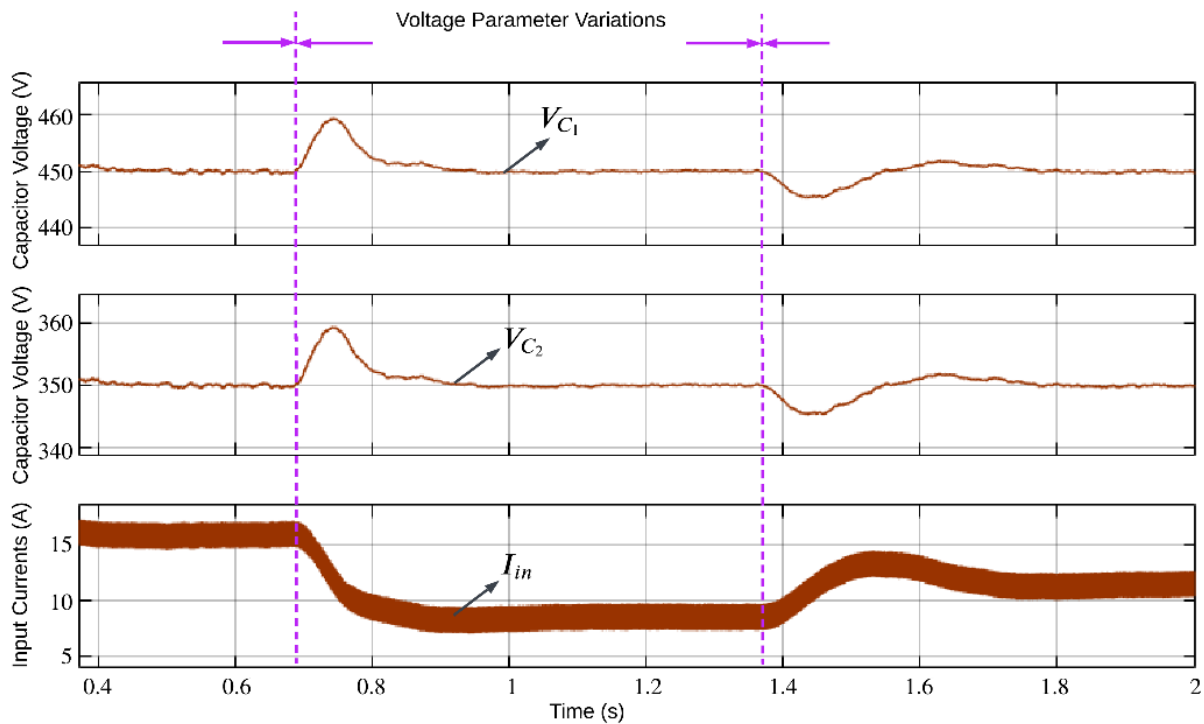


Figure 15. Capacitor voltages (V_{C_1}, V_{C_2}) and input current (I_{in}) waveforms of the SPWM based qZSI

Step responses of the output voltage (V_d, V_q), output current (I_d, I_q), phase-phase output voltage (V_{ab}, V_{bc}, V_{ca}), and output current ($I_{o_a}, I_{o_b}, I_{o_c}$) waveforms of the SPWM-based three-phase qZSI are depicted in Figure 16, respectively. To study the step response of the circuit, $I_{d_{ref}} = 3A$ and $I_{q_{ref}} = 0A$ are applied to the input as reference currents. After 0.7 seconds, $I_{d_{ref}} = 1A$ and $I_{q_{ref}} = 0A$ are applied as a reference, and after 1.35 seconds, $I_{d_{ref}} = 1A$ and $I_{q_{ref}} = -3A$ are applied, respectively. In all cases, the system settles to the 2% reference band at a maximum of 100 ms. In this case, it can be deduced that the response of the system to the current reference is about two times faster than the response to the voltage reference.

Current harmonic limits of the SPWM based three-phase qZSI under full load and half load conditions are shown in Figure 17a and 17b, respectively. According to the figure, IEC61000-3-2 Class C harmonic limits are met for both conditions, and the THD value of the output current is measured as 3.9% for the full load condition and 4.5% for the half load condition.

Figure 18 shows the PF values for different load conditions for the SPWM-based three-phase qZSI output current. As can be seen from the figure that the power factor increases from half load to full load. Moreover, it can be deduced from the figure that the PF is about 99% under all load conditions after half load.

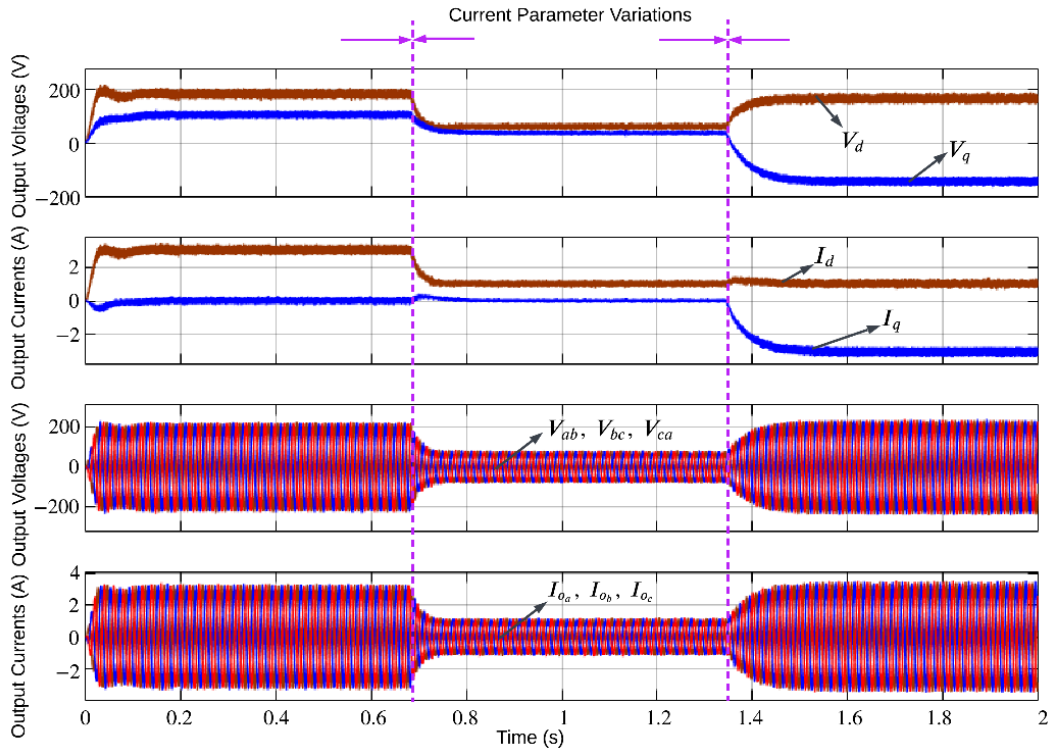


Figure 16. Output voltage (V_d, V_q), output current (I_d, I_q), phase-phase output voltage (V_{ab}, V_{bc}, V_{ca}), and output current (I_{oa}, I_{ob}, I_{oc}) waveforms of the SPWM-based qZSI

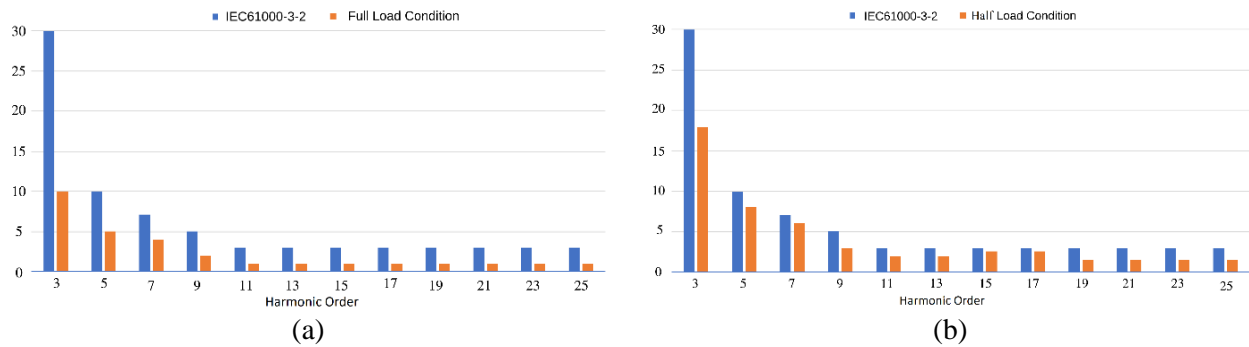


Figure 17. Current harmonic limits of qZSI a) full load condition b) half load condition

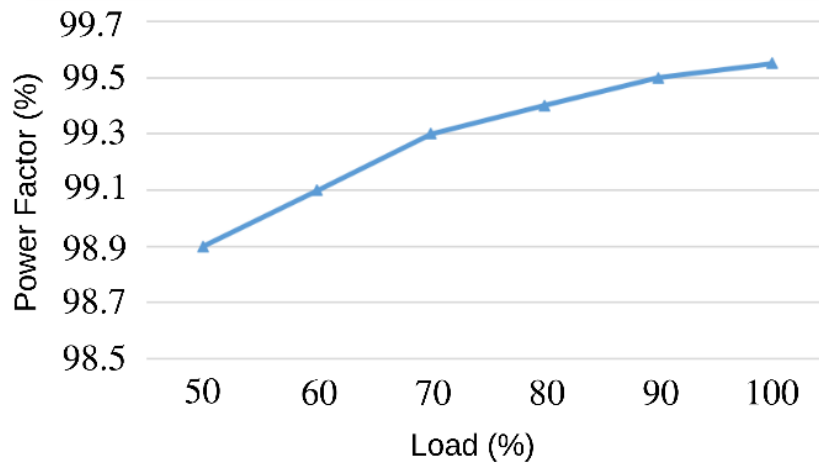


Figure 18. Power factor (PF) measurement of the output current under different load conditions

4. CONCLUSION

In this paper, a capacitor voltage and input current-based SPWM control scheme for a three-phase qZSI has been extensively tested and analyzed under various conditions. The circuit underwent thorough testing in transient, steady-state, and parameter change scenarios, and consistently exhibited excellent performance.

Furthermore, the inverter was subjected to separate tests for both current and voltage references, and it demonstrated precise tracking of all the references. This indicates that the circuit is capable of accurately controlling both the current and voltage, making it a reliable power source suitable for a wide range of applications.

The current THD value was consistently found to be below 5 % under different parameter and load change conditions. This outcome highlights the inverter's ability to generate high-quality output current while complying with the current harmonic limits specified by the IEC61000-3-2 Class C standard.

Overall, the proposed control scheme presents a promising solution for power conversion, as it effectively reduces harmonic distortion and enables accurate control of current and voltage. The scheme's performance has been thoroughly tested and analyzed, showcasing its potential for diverse applications.

CONFLICT OF INTEREST

The authors declare no conflict of interest.

REFERENCES

- Anderson, J., & Peng, F. Z. (2008a, October 5-9). A Class of Quasi-Z-Source Inverters. In: Proceedings of the IEEE Industry Applications Society Annual Meeting (IAS), Edmonton, Canada. doi:[10.1109/08IAS.2008.301](https://doi.org/10.1109/08IAS.2008.301)
- Anderson, J., & Peng, F. Z. (2008b, June 15-19). Four quasi-Z-Source inverters. In: Proceedings of the 39th IEEE Annual Power Electronics Specialists Conference (PESC), (pp. 2743-2749), Rhodes, Greece. doi:[10.1109/PESC.2008.4592360](https://doi.org/10.1109/PESC.2008.4592360)
- Cao, D., & Peng, F. Z. (2009, February 15-19). A family of Z-source and Quasi-Z-source DC-DC converters. In: Proceedings of the Twenty-Fourth Annual IEEE Applied Power Electronics Conference and Exposition (APEC), (pp. 1097-1101), Washington, USA. doi:[10.1109/APEC.2009.4802800](https://doi.org/10.1109/APEC.2009.4802800)
- Devaraj, U., Ramalingam, S., & Sambasivam, D. (2019). Evaluation of Modulation Strategies for Single-Phase Quasi-Z-Source Inverter. *Journal of The Institution of Engineers (India): Series B*, 100(4), 333-341. doi:[10.1007/s40031-019-00378-z](https://doi.org/10.1007/s40031-019-00378-z)
- Elmorshedy, M. F., Essawy, I. J. A., Rashad, E. M., Islam, M. R., & Dabour, S. M. (2023). A Grid-Connected PV System Based on Quasi-Z-source Inverter with Maximum Power Extraction. *IEEE Transactions on Industry Applications*, 1-11. doi:[10.1109/TIA.2023.3275557](https://doi.org/10.1109/TIA.2023.3275557)
- Endiz, M. S., Akkaya, R. (2022). Performance Analysis of Z-Source Inverter Control Techniques. *El-Cezeri Journal of Science and Engineering*, 9(2), 625-633. doi:[10.31202/ecjse.990144](https://doi.org/10.31202/ecjse.990144)
- Garcia-Vazquez, C. A., Sanchez-Sainz, H., Gonzalez-Rivera, E., Llorens-Iborra, F., & Fernandez-Ramirez, L. M. (2020, June 9-12). Decoupled Maximum Constant Boost Control for Quasi-Z-Source Inverter. In: Proceedings of the IEEE International Conference on Environment and Electrical Engineering and IEEE Industrial and Commercial Power Systems Europe (EEEIC / I & CPS Europe), Madrid, Spain. doi:[10.1109/EEEIC/ICPSEUROPE49358.2020.9160623](https://doi.org/10.1109/EEEIC/ICPSEUROPE49358.2020.9160623)
- Hong, D., & Cha, H. (2021). LED Current Balancing Scheme Using Current-Fed Quasi-Z-Source Converter. *IEEE Transactions on Power Electronics*, 36(12), 14187-14194. doi:[10.1109/TPEL.2021.3083842](https://doi.org/10.1109/TPEL.2021.3083842)
- Li, J., Chen, D., & Jiang, J. (2022). Single-Phase ZVS Quasi-Z-Source Inverter with High Voltage Gain. *IEEE Transactions on Power Electronics*, 37(4), 4346-4357. doi:[10.1109/TPEL.2021.3121712](https://doi.org/10.1109/TPEL.2021.3121712)

- Liu, J., Wu, J., Qiu, J., & Zeng, J. (2019). Switched Z-Source/Quasi-Z-Source DC-DC converters with reduced passive components for photovoltaic systems. *IEEE Access*, 7, 40893-40903. doi:[10.1109/ACCESS.2019.2907300](https://doi.org/10.1109/ACCESS.2019.2907300)
- Mohammadi, M., Mirzaee, A., Magnone, P., Moghani, J., & Mattavelli, P. (2020). Performance improvement of pulse width-amplitude modulation-based quasi-Z-source inverters: Analysis and implementation. *International Journal of Circuit Theory and Applications*, 48(10), 1786-1799. doi:[10.1002/CTA.2808](https://doi.org/10.1002/CTA.2808)
- Nguyen, M.-K., Choi, Y.-O. (2021). Modulation Technique for Modified Active Quasi-Z-Source Inverter with Common-Mode Voltage Reduction. *Electronics*, 10(23), 2968. doi:[10.3390/ELECTRONICS10232968](https://doi.org/10.3390/ELECTRONICS10232968)
- Padmavathi, P., & Natarajan, S. (2020). Single switch quasi Z-source based high voltage gain DC-DC converter. *International Transactions on Electrical Energy Systems*, 30(7), e12399. doi:[10.1002/2050-7038.12399](https://doi.org/10.1002/2050-7038.12399)
- Paikray, A., Prudhvi, S., & Nayak, S. K. (2022, December 14-17). Improved Enhanced-Boost Quasi-Z-Source Inverter. In: Proceedings of the 10th IEEE International Conference on Power Electronics, Drives and Energy Systems (PEDES-2022), Jaipur, India. doi:[10.1109/PEDES56012.2022.10080512](https://doi.org/10.1109/PEDES56012.2022.10080512)
- Parla, G., & Özdemir, M. (2022). Design of a Three Phase Z-Source Inverter for Photovoltaic Systems. *Dicle University Journal of Engineering*, 13(2), 253-261. doi:[10.24012/dumf.1100464](https://doi.org/10.24012/dumf.1100464)
- Peng, F. Z. (2002, October 13-18). Z-source inverter. In: Proceedings of the Conference Record of the 2002 IEEE Industry Applications Conference, 37th IAS Annual Meeting, vol. 2, (pp. 775-781), Pittsburgh, USA. doi:[10.1109/IAS.2002.1042647](https://doi.org/10.1109/IAS.2002.1042647)
- Peng, F. Z. (2003). Z-source inverter. *IEEE Transactions on Industry Applications*, 39(2), 504-510. doi:[10.1109/TIA.2003.808920](https://doi.org/10.1109/TIA.2003.808920)
- Peng, F. Z., Yuan, X., Fang, X., & Qian, Z. (2003). Z-source inverter for adjustable speed drives. *IEEE Power Electronics Letters*, 1(2), 33-35. doi:[10.1109/LPEL.2003.820935](https://doi.org/10.1109/LPEL.2003.820935)
- Poorali, B., & Adib, E. (2020). Soft-Switched High Step-Up Quasi-Z-Source DC-DC Converter. *IEEE Transactions on Industrial Electronics*, 67(6), 4547-4555. doi:[10.1109/TIE.2019.2922948](https://doi.org/10.1109/TIE.2019.2922948)
- Sabeur, N., Mekhilef, S., & Masaoud, A. (2018). A Simplified Time-Domain Modulation Scheme-Based Maximum Boost Control for Three-Phase Quasi-Z Source Inverters. *IEEE Journal of Emerging and Selected Topics in Power Electronics*, 6(2), 760-769. doi:[10.1109/JESTPE.2017.2763974](https://doi.org/10.1109/JESTPE.2017.2763974)
- Sun, D., Ge, B., Bi, D., & Peng, F. Z. (2013). Analysis and control of quasi-Z source inverter with battery for grid-connected PV system. *International Journal of Electrical Power & Energy Systems*, 46, 234-240. doi:[10.1016/J.IJEPES.2012.10.008](https://doi.org/10.1016/J.IJEPES.2012.10.008)
- Xu, G., Chen, D., & Qu, A. (2020, October 19-21). Simple Boost Modified Space Vector Modulation Strategy for Three-Phase Quasi-Z-Source Inverter. In: Proceedings of the 46th Annual Conference of the IEEE Industrial Electronics Society, (pp. 5365-5370), Singapore. doi:[10.1109/IECON43393.2020.9255384](https://doi.org/10.1109/IECON43393.2020.9255384)
- Zhao, Z., Elgendy, M. A., Armstrong, M., & Muhammad, M. (2019, September 3-5). Constant boost control with third harmonic injection for quasi-Z source inverter used in PV grid-connected system. In: Proceedings of the 21st European Conference on Power Electronics and Applications (EPE'19 ECCE Europe), Genova, Italy. doi:[10.23919/EPE.2019.8915379](https://doi.org/10.23919/EPE.2019.8915379)



Gazi University

Journal of Science

PART A: ENGINEERING AND INNOVATION

<http://dergipark.org.tr/guj.1302064>

The Investigation of CO₂ Gas Sensing Performance of ZnO Nanorods Growth on RF Sputtered Seed Layer

Fatih BULUT^{1*} Özgür ÖZTÜRK² Selim ACAR³ ¹Sinop University, Scientific and Technological Research Application and Research Center, Sinop, Türkiye²Kastamonu University, Department of Electrical and Electronics Engineering, Kastamonu, Türkiye³Gazi University, Faculty of Science, Department of Physics, Science Faculty, Ankara, Türkiye

Keywords	Abstract
Zinc Oxide	In this study, one-dimensional ZnO nanorod structures with different ratios of nickel doping were produced using the hydrothermal method. The presence of nickel doping in different ratios caused variations in the fundamental characteristics of the nanorods that grew on the RF sputtered seed layer, such as crystallinity quality, morphology, diameter of the nanorods, band gap energy, resistance of the sample, and CO ₂ gas sensing. Produced samples were found to form like hexagonal rods and crystallize in a wurtzite structure, and the ratio of nickel doping improved the crystallin quality and the morphology of sample surface. This study showed that the 5% nickel doped sample provided the most effective results in sensing CO ₂ gas at different concentrations. Overall, the study provided valuable insights into the relationship between doping system and the basic characteristics of wurtzite-type hexagonal ZnO.
Nanorod	
Hydrothermal	
CO ₂ Gas Sensor	
Nickel Doping	

Cite

Bulut, F., Öztürk, Ö., & Acar, S. (2023). The Investigation of CO₂ Gas Sensing Performance of ZnO Nanorods Growth on RF Sputtered Seed Layer. *GU J Sci, Part A, 10(2)*, 222-231. doi:10.54287/guj.1302064

Author ID (ORCID Number)	Article Process
0000-0001-5335-2307	Fatih BULUT
0000-0002-0391-5551	Özgür ÖZTÜRK
0000-0003-4014-7800	Selim ACAR
	Submission Date 24.05.2023
	Revision Date 10.06.2023
	Accepted Date 16.06.2023
	Published Date 23.06.2023

1. INTRODUCTION

Sensors have greatly improved our lives and made things easier by providing information to machines and processors in response to changes in the environment. They come in various types and serve different purposes, like regulating temperature in our homes or determining fuel levels in our vehicles (Jagdale et al., 2018). Sensors can convert chemical or physical quantities into electrical signals using different stimuli, such as heat, light, pressure, force, electricity, and distance. The investigating and developing of air quality and gas sensors has become increasingly essential in addressing global warming and air pollution (K. Xu et al., 2018). Carbon dioxide (CO₂) gas sensing is particularly relevant due to its role in the greenhouse gas effect. ZnO-based semiconductor sensors are commonly used in this field due to their low cost, non-toxicity, and modifiable selectivity and sensing properties through dopant elements (Mirzaei et al., 2016). However, these sensors have drawbacks including insufficient stability, inadequate response, and high operating temperature, which researchers address through doping or changes in production techniques (Cai et al., 2023). Researchers have explored various ZnO-based nanomaterial structures, such as nanorods, nanowires, and nanoparticles, to improve gas sensing properties. One-dimensional (1D) orientation and surface morphology are preferable for enhancing gas sensing properties, as they increase the surface area (Zhang et al., 2018). Additionally, the electronic performance of one-dimensional zinc oxide nanostructures is critical in electronic applications, and element doping is another means of improving sensing properties (Saini et al., 2022; Wan et al., 2022). Kamble et al. (2021) has reported in 2021 that 2% Ni-doped ZnO sensor responded at its maximum level of 356% to NO₂ gas at a concentration of 100 ppm at operating temperature of 200°C.

*Corresponding Author, e-mail: fatihbulut@sinop.edu.tr

M. Xu et al. (2014) state that nickel doped zinc oxide nanorods were created using quick microwave hydrothermal synthesis, and their enhanced gas-sensing performance was demonstrated in the work. The sensitivity of the produced samples based on nickel doped zinc oxide NRs was up to 313 at 500 ppm ethanol environment. (M. Xu et al., 2014). Abdel All et al. (2021) reported that nickel doped zinc oxide nanoparticles were used as the functional material for CO₂ gas sensors. The data collected at 350°C showed an improvement in the sensor's sensitivity to CO₂.

In the current study, zinc oxide nanorods doped with nickel were produced on an RF-sputtered seed layer by hydrothermal method in 1D orientation. In addition to their structural, morphological, and optical properties, 1D oriented nanorods exhibit CO₂ gas sensing capabilities were investigated.

2. MATERIAL AND METHOD

RF sputtering at 150°C temperature and 10mTorr chamber pressure were applied for coating ZnO seed layer on glass substrate. RF sputtering power set to 75W, and substrate rotated by 10 rpm during sputtering, and sputtered glass substrates were annealed at 600°C for half hour. Doped and undoped ZnO nanorods were produced by hydrothermally on seed layer at 90°C for 3 hours. In 50 mL DI water, we mixed 0.1 M Zn Acetate dehydrate and hexamethylenetetramine (HMTA, C₆H₁₂N₄) to prepare hydrothermal solutions. For the doping process, they added the required amount of doping elements (1, 3 and 5%wt) to the same solution. These solutions were then used in a hydrothermal process to grow nanorods on seed layer-coated substrates, which were placed in a Teflon autoclave. After production processes at 90°C for 3 hours, samples were rinsed using DI water and dried at 50°C (Bulut et al., 2022).

Bruker D8 Advance powder X-ray diffractometer, FEI Quanta FEG 250 SEM, Shimadzu 2600 UV-Spectrometer are used to measure phase purities, surface morphology, optical properties of produced samples. Gas sensing properties of produced samples investigated by homemade gas sensing system which has MKS series mass flow controllers, LakeShore 325 temperature controller and Keithley 2400 DC sourcemeter.

3. RESULTS AND DISCUSSION

XRD results of undoped, and nickel doped samples have given in Figure 1. All samples have single (002) peak which is responsible for c axis growing (Galioglu et al., 2018; Bura et al., 2022). The peak in Figure 1 supports that crystals have grown in c axis and resulted as nanorod. In the diffraction patterns, no contaminants or secondary phases like Ni or NiO were seen. The effective insertion of Ni ions into the Zn sites in the crystal structure is responsible for the absence of any secondary phases. By using Warren-Sheerer equation c lattice parameter of all samples have been calculated and listed in Table1 (Galioglu et al., 2018; Bulut et al., 2022). By increasing of the Ni doping ratio in the ZnO system, c lattice parameters tended to decrease while the crystal size increased. The incorporation of dopant particles into ZnO materials affects their lattice cell parameters by creating unique strain fields within the crystal structure. These interactions also produce variations in energy levels, leading to significant changes in the c lattice cell parameter (Bulut et al., 2022).

SEM images of the sample were taken at 1µm scaled and given in Figure 2. SEM images are important to see the surface of the produced material, grain boundaries, measuring grain size and also having information about the surface morphology of the samples. Nanorods grown on an RF-sputtered seed layer exhibit perfect hexagonal symmetry and the nanorods were perpendicular to the substrate, as demonstrated via Figure 2. Calculated NR average diameter values are given in Table 1 as nm and it is clear that Ni doping ratio effected the NR average diameter. Minimum NR average diameter measured for 1Ni sample as 61.21nm. It is to be mentioned here that generally the doping ratio increases the nanorod diameter. In addition, the varying ionic radii (IoRad) of dopant elements ($IoRad_{Zn^{+2}} = 0.72\text{Å}$, $IoRad_{Ni^{+2}} = 0.69\text{Å}$) may be depend on the diameters changes.

Basically, the band gap which can be calculated via the transmittance–wavelength graph taken from UV-Spectrophotometer, is the parameter to having knowledge of the conductivity of the samples produced. The band gap values of the samples given in Table1 and represented in Figure 3. enhancing of the doping ratio

caused the decreasing of E_g values which may attributed to having closer atomic radios of Zn^{+2} (0.72\AA) and Ni^{+2} (0.69\AA) (Singh et al., 2017). According to the table, the highest E_g of the pure sample is calculated as 3.26 eV, is consistent with ZnO nanorod values in the literature. In addition, Table 1 demonstrates that the band gap energy decreases monotonically with increasing dopant concentration. This is due to the band-shrinkage effect brought about by the increase in concentration of the carriers. In addition, the inhomogeneity of the interfacial charges, the different diameters of the nanorods grown, the composition and thickness of the ZnO oxide layer all play key role in the reduction of the E_g values.

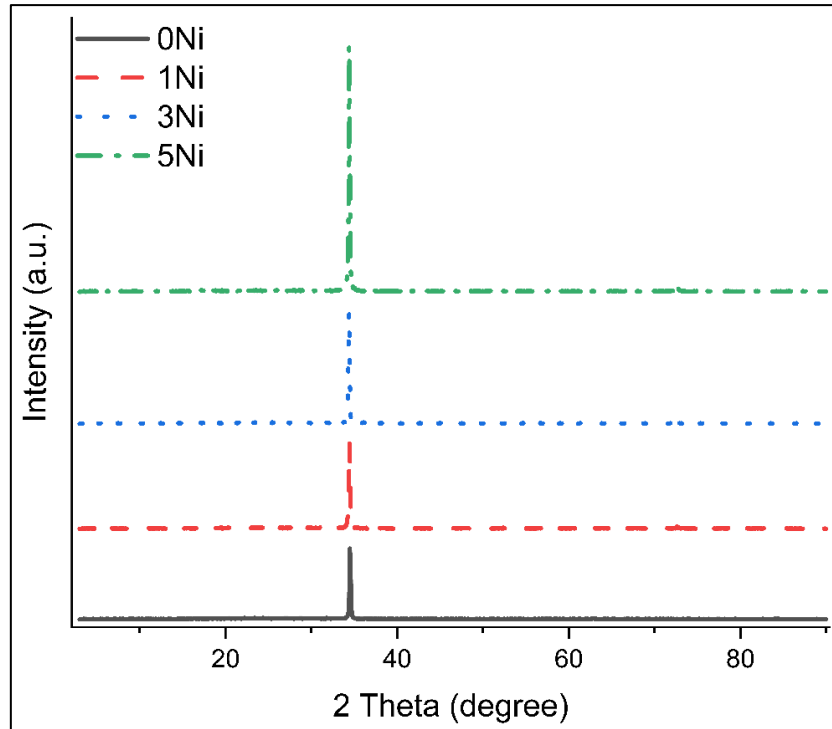


Figure 1. XRD results of produced samples

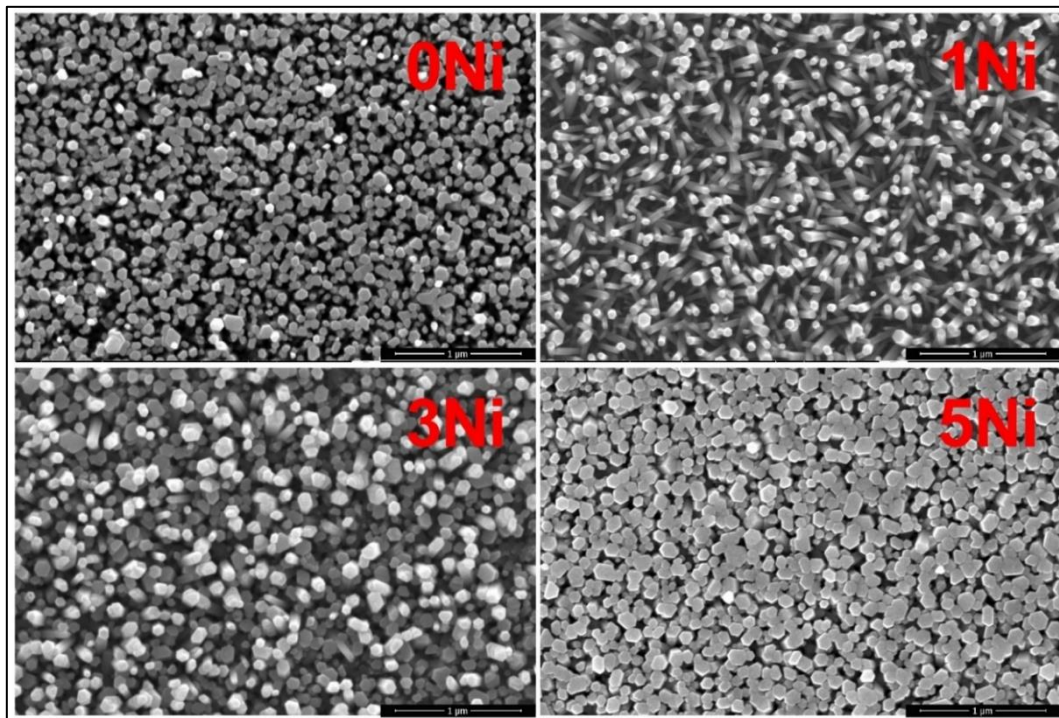


Figure 2. SEM images of produced samples

Table 1. The parameters such as crystallite size (*D*), *c* lattice parameter, average diameter and band gap calculated from XRD, SEM and optical analysis

Sample Name	D (nm)	c (Å)	Average Diameter of NRs (nm)	E _g (eV)
0Ni	36.49	5.209	72.91	3.23
1Ni	41.27	5.205	61.21	3.19
3Ni	45.72	5.202	73.84	3.11
5Ni	49.13	5.197	77.36	3.08

Metal oxide materials offer a technique for gas detection based on the chemical reactions that happen between the gas molecules and the surface of the MO. Due to its ability to grab an electron in the metal oxide's conductivity band (CB) and stick to the surface, oxygen's chemical absorption plays a major part in sensing process.

Sensor materials use a surface-controlled method for sensing, with adsorption/desorption process of the O₂ on the outside layer of sensor. At low temperatures, on the sensor's surface, O₂ molecules are adsorbed, which traps valence band electrons. At higher temperatures, O₂ molecules separate into active species that are negatively charged. CO₂ gas combines with the oxygen species that adsorbed by surface, lowering the resistance. When CO₂ gas was introduced to the ZnO sensor, the deposited O ions reacted with the gas to remove the electrons from the CB of n-type zinc oxide sensor (Eqs.1 & 2). As a result, there were less electrons present on sensor's surface, and the sensor resistance increased (Anderson et al., 2009; Kannan et al., 2014).

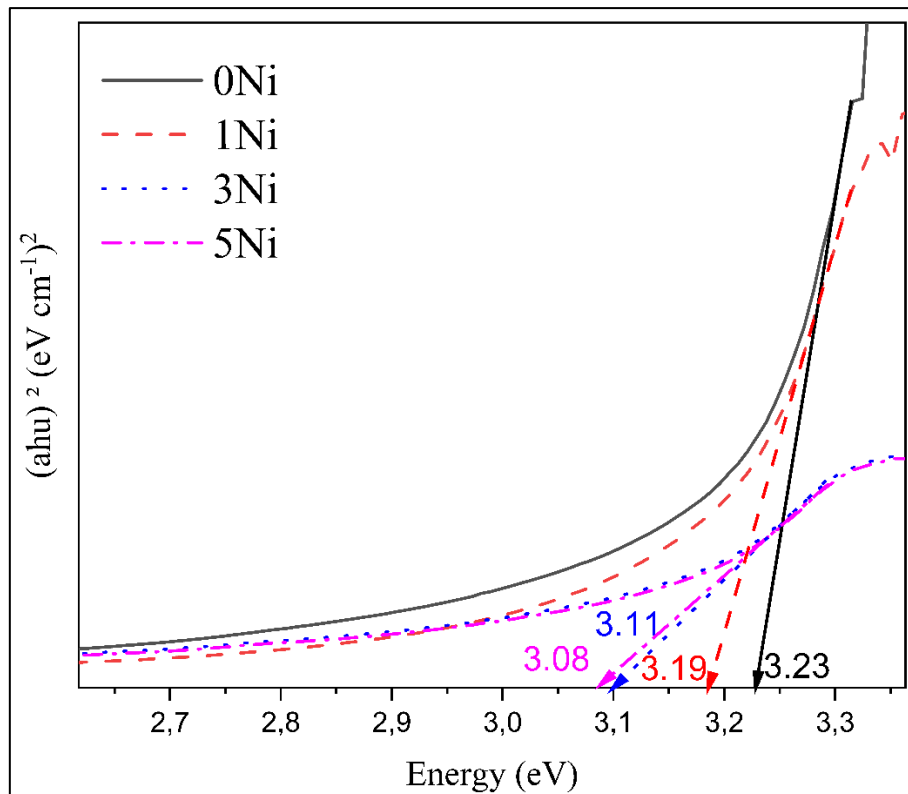
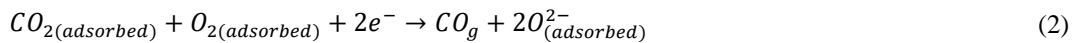


Figure 3. Band gap graph of produced samples

Sensing response (S) is one of the important parameters for the gas sensors like response end recovery times (Barin et al., 2022). For the chemiresistive gas sensors, calculating sensing response is depending on the resistance measurement under air and target gas atmosphere. To identify the optimum operating/sensing temperature, resistance measurement of the sensors performed for 50ppm CO₂ gas. Because of the oxidizing nature of CO₂ gas, the interaction with sensors returns as increasing resistance. This circumstance is explained by the restricted mobility of the charge carrier. In addition, it should be mentioned, nickel doped ZnO sensors have significantly higher sensor resistance value. That situation attributed to the properties of the optical band gap and the crystal structure (Saxena et al., 2020; Ocak et al., 2021). Sensing response values were calculated using the Eq.3 given below,

$$S = \frac{\Delta R}{R_a} = \frac{|R_a - R_g|}{R_a} \quad (3)$$

In Eq3, while S is the sensing response, Ra–Rg represents the resistance values of the sensor under air–gas atmosphere, respectively. Calculated S values are represented in the Figure 4. Increasing of the sensing response values under CO₂ gas atmosphere were clearly visible from the Figure 4 and that is the characteristic behavior of the semiconductor which are categorized as n type sensor under oxidizing gas (Wisitorsaat et al., 2009). The increasing of the sensing temperature also enhanced the sensing responses of produced sensors. The optimum temperature was determined as 420K of the sensors except for the 5Ni sample and, for 5Ni, the working temperature is 400K. While 1Ni has the highest sensing response at 420K, 5Ni has the lowest.

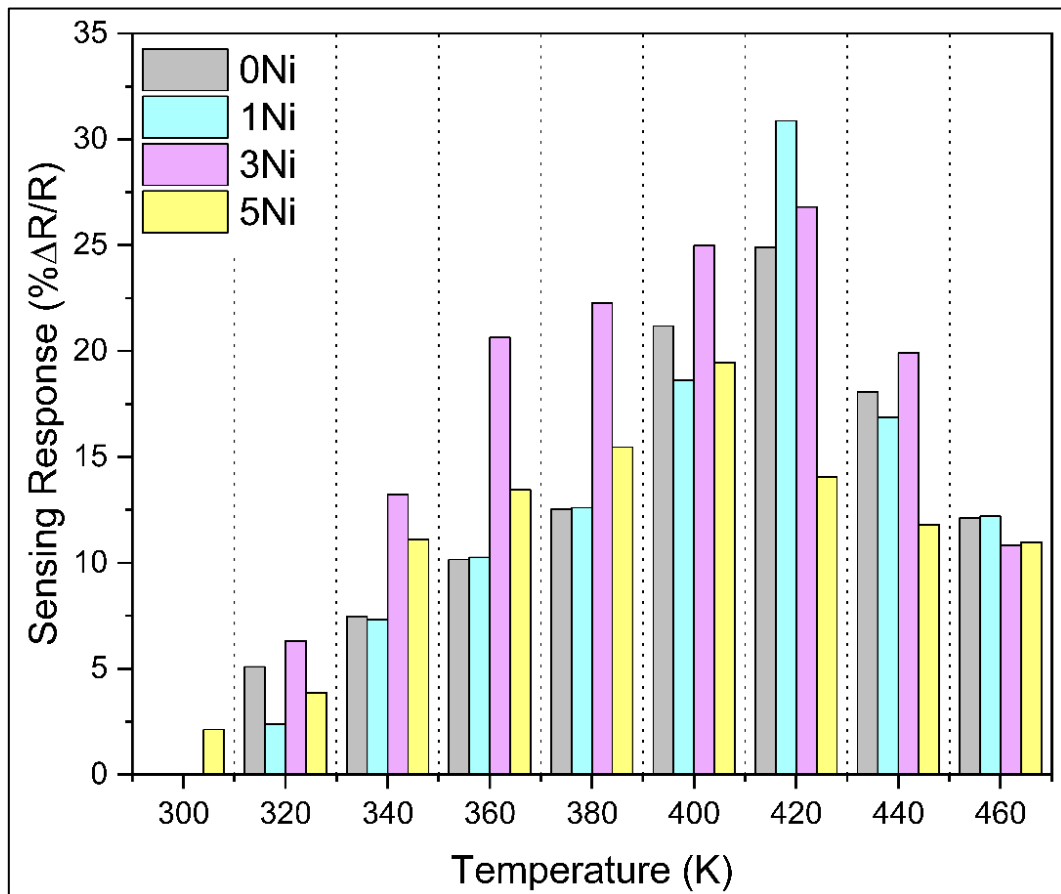


Figure 4. Calculated response of the sensors at different temperatures

After determining the working temperatures, the sensors are exposed to different concentrations of gas at these temperatures (Figure 5). In this way, the selectivity of the sensors for a CO₂ is examined, and the result are given in Figure 6. By enhancing of the gas concentration exposure of the gas sensor, resistance of the produced sensors was increased. Nickel doped ZnO sensors' resistance levels under gas atmosphere are

shown to grow progressively with increasing CO₂ content, according to experimental data. It is evident that the doping ratio influences sensor behavior. While 5Ni sensor has given the lowest value at 50ppm CO₂ in different temperatures, it represented the highest CO₂ sensing response at 100ppm CO₂. With sufficient spacing between the rods, more surface-target gas interaction is provided for the 1Ni sample. The CO₂ gas may not be able to reach every spot because of the 5Ni sensor restricted surface and bigger nanorod diameters. While 1Ni shows the best CO₂ detection performance at different concentrations, the 3Ni sample comes in second in this field. However, when the surface morphologies are investigated, it is understood that the 3Ni sensor's surface is less stable than 1Ni. Although it has hexagonal nanorods on the surface, the 3Ni sensor does not have standardized NRs like the 1Ni sample. Deterioration of NRs on the surface of the 3Ni sensor with 3% Ni doping may have caused a diminish in the CO₂ sensing performance.

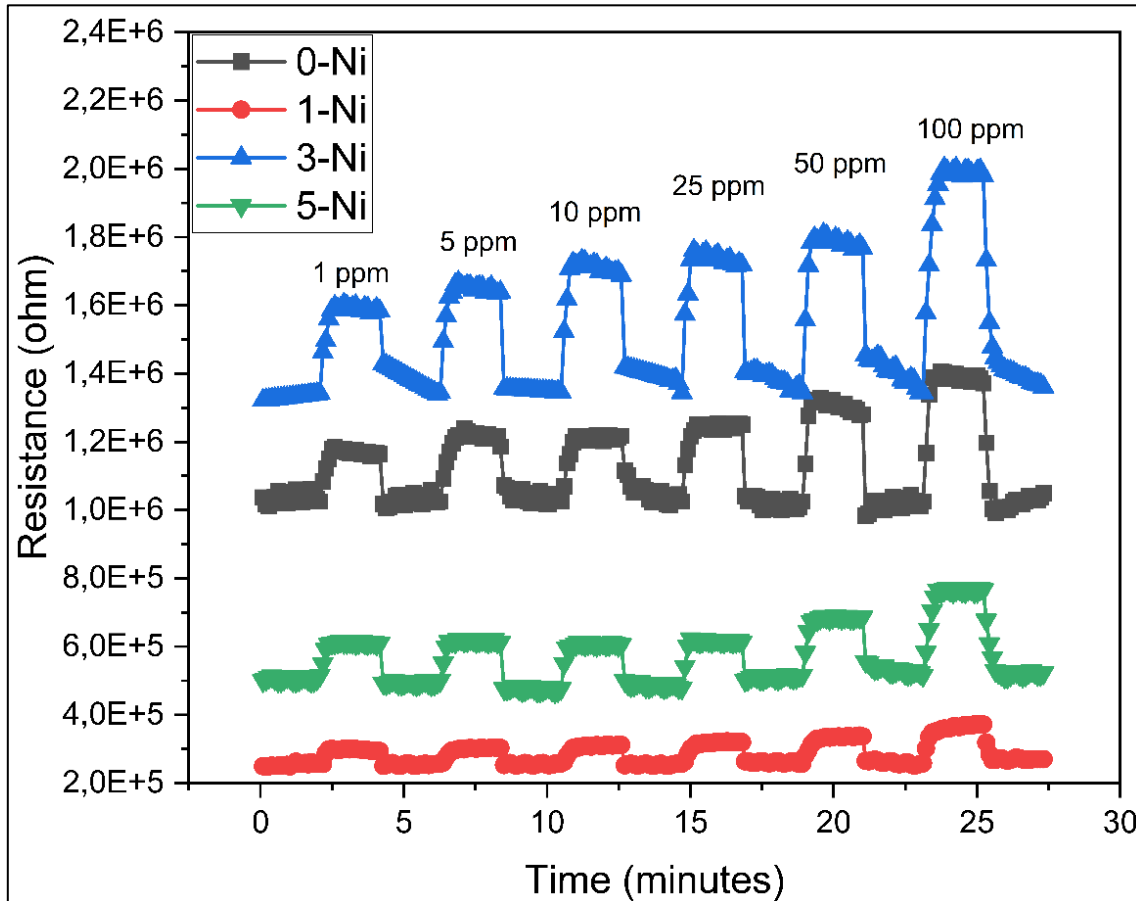


Figure 5. Resistance vs Time graph of the sensors at different concentrations

Another key parameter for gas sensors are the response time and the recovery time. Figure 7a and 7b represents the response and recovery times of the sensor produced in this study. Response times of the sensors shows that 1Ni sensor has lower response time among all sensors while has nearly faster recovery time. 5N sensor gives the highest recovery time. Surface morphology of the sensors given in the Figure 2 may support the recovery times of the sensors. It is seen from the SEM images of the 5Ni sensor that the surface density is high. This causes a decrease in the gap between the NRs. If the gap between the NRs is small, it is seen that the recovery time value is high. This interpretation is supported when Figure 2 and Figure 7 are evaluated together. Accordingly, the recovery time values of the 1Ni sensor, where NRs are rare, are quite low compared to the 5Ni sensor.

In the wurtzite crystal structure, local p-n junctions form when nickel ions aren't replaced by zinc ions, according to experimental observations published in the scientific literature (Cho et al., 2015). As a result, as mentioned in the literature (Kar & Kamilla, 2021), instead of Schottky barriers, p-n junctions could control the sensor's response. The data obtained in this study are compared with the literature in Table 2, where the ZnO structures produced for gas sensing. As known the sensor's response is influenced by the surface area,

and 1Ni has more NRs that are perpendicular to the surface. Comparing the reactions of Ni-doped sensors at 500K and 50 ppm CO₂, it is evident that 1Ni exhibits greater sensitivity than the other due to its larger surface area.

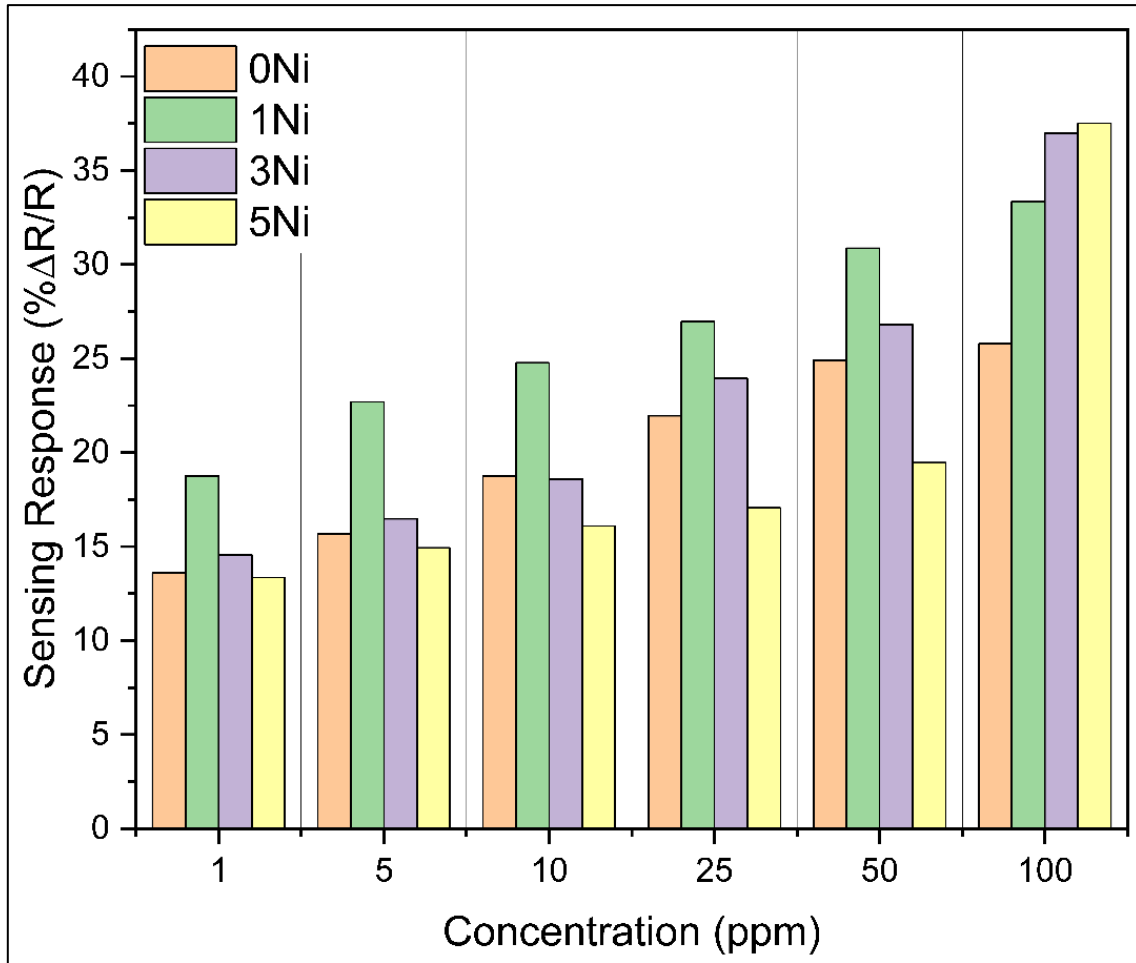


Figure 6. Calculated response of the sensors at different CO₂ gas concentrations

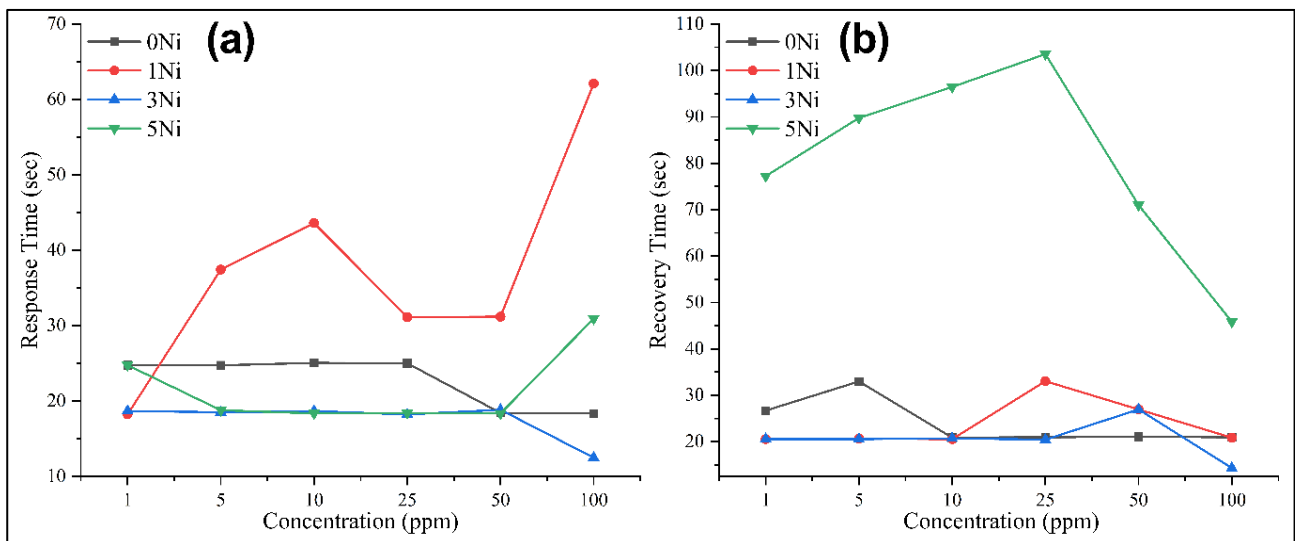


Figure 7. Calculated; a) response and b) recovery times of produced sensors

Table 2. Summarized results for CO₂ gas sensing properties

Doping and Host Material	Method/Production	Working Temperature (Kelvin)	Target Gas Concentration (ppm)	% Sensing Response
Ni-doped ZnO nanorods (M. Xu et al., 2014)	Fast microwave hydrothermal	643	500	313
ZnO Nanoflowers (Kanaparthi & Singh, 2019)	Precipitation (Simple method)	520	200	23
ZnO Nanoparticles, Al doped (Dhahri et al., 2017)	Sol-Gel thin film	520	10000	100
ZnO loaded %50La (Jeong et al., 2016)	Hydrothermal	670	5000	65
5Ni (this study)	Hydrothermal	500	100	37.5

4. CONCLUSION

By doping Ni at different ratios, ZnO nanorods were hydrothermally produced on the RF sputtered ZnO seed layers. The growth of ZnO nanorods doped with Ni in various ratios was accomplished using RF sputtered ZnO seed layers. A single (002) peak was found when the structural properties were examined using XRD analysis. The sample's computed crystalline sizes revealed an increase in crystalline size with higher doping ratios. The surface morphology and typical nanorod properties were examined using SEM. A UV spectrophotometer was used to illuminate the doping effect on band gap values and show how doping causes a drop in the band gap value. The 0Ni, 1Ni, and 3Ni samples all showed higher reaction rates at 420K, while the 5Ni sample showed a response rate at 400K. After figuring out the operating temperatures, the sensing performance of the samples at various CO₂ concentrations was evaluated. For the 1Ni sensor, higher response rates at various concentrations were seen. The sensors' response and recovery times were calculated. For various concentrations, the sensors with smaller nanorod diameters displayed faster response times. In contrast to other sensors, the 1Ni sensor featured a sparse structure and a smaller average nanorod diameter. The gas detection capabilities of the zinc oxide NR structure grown on the seed layer made using the RF sputtering method were shown to be enhanced by doping nickel at various concentrations.

CONFLICT OF INTEREST

The authors declare no conflict of interest.

REFERENCES

- Abdel All, N., El Ghouli, J., & Khouqueer, G. (2021). Synthesis and Characterization of Ni-Doped ZnO Nanoparticles for CO₂ Gas Sensing. *Journal of Nanoelectronics and Optoelectronics*, 16(11), 1762-1768. doi:[10.1166/jno.2021.3121](https://doi.org/10.1166/jno.2021.3121)
- Anderson, T., Ren, F., Pearton, S., Kang, B. S., Wang, H.-T., Chang, C.-Y., & Lin, J. (2009). Advances in Hydrogen, Carbon Dioxide, and Hydrocarbon Gas Sensor Technology Using GaN and ZnO-Based Devices. *Sensors*, 9(6), 4669-4694. doi:[10.3390/s90604669](https://doi.org/10.3390/s90604669)
- Barin, Ö., Ajjaj, A., Çağırtekin, A. O., Karaduman Er, I., Yıldırım, M. A., Ateş, A., & Acar, S. (2022). Pivotal role of nucleation layers in the hydrothermally-assisted growth of ZnO and its H₂ gas sensing performance. *Sensors and Actuators B: Chemical*, 371, 132499. doi:[10.1016/j.snb.2022.132499](https://doi.org/10.1016/j.snb.2022.132499)
- Bulut, F., Ozturk, Ö., Acar, S., & Yildirim, G. (2022). Effect of Ni and Al doping on structural, optical, and CO₂ gas sensing properties of 1D ZnO nanorods produced by hydrothermal method. *Microscopy Research and Technique*, 85(4), 1502-1517. doi:[10.1002/jemt.24013](https://doi.org/10.1002/jemt.24013)
- Bura, M., Singh, G., Gupta, D., Malik, N., Salim, A., Kumar, A., Singhal, R., Kumar, S., & Aggarwal, S. (2022). Transition in the preferred orientation of RF sputtered ZnO/Si thin films by thermal annealing:

Structural, morphological, and optical characteristics. *Optical Materials*, 133, 113024. doi:[10.1016/j.optmat.2022.113024](https://doi.org/10.1016/j.optmat.2022.113024)

Cai, Z., Park, J., & Park, S. (2023). Synergistic effect of Pd and Fe₂O₃ nanoparticles embedded in porous NiO nanofibers on hydrogen gas detection: Fabrication, characterization, and sensing mechanism exploration. *Sensors and Actuators B: Chemical*, 388, 133836. doi:[10.1016/j.snb.2023.133836](https://doi.org/10.1016/j.snb.2023.133836)

Cho, Y. H., Liang, X., Kang, Y. C., & Lee, J.-H. (2015). Ultrasensitive detection of trimethylamine using Rh-doped SnO₂ hollow spheres prepared by ultrasonic spray pyrolysis. *Sensors and Actuators, B: Chemical*, 207(Part A), 330-337. doi:[10.1016/j.snb.2014.10.001](https://doi.org/10.1016/j.snb.2014.10.001)

Dhahri, R., Leonardi, S. G., Hjjiri, M., Mir, L. E., Bonavita, A., Donato, N., Iannazzo, D., & Neri, G. (2017). Enhanced performance of novel calcium/aluminum co-doped zinc oxide for CO₂ sensors. *Sensors and Actuators B: Chemical*, 239, 36-44. doi:[10.1016/j.snb.2016.07.155](https://doi.org/10.1016/j.snb.2016.07.155)

Galioglu, S., Karaduman, I., Çorlu, T., Akata, B., Yıldırım, M. A., Ateş, A., & Acar, S. (2018). Zeolite A coated Zn_{1-x}Cu_xO MOS sensors for NO gas detection. *Journal of Materials Science: Materials in Electronics*, 29(2), 1356-1368. doi:[10.1007/s10854-017-8042-8](https://doi.org/10.1007/s10854-017-8042-8)

Jagadale, S. B., Patil, V. L., Vanalakar, S. A., Patil, P. S., & Deshmukh, H. P. (2018). Preparation, characterization of 1D ZnO nanorods and their gas sensing properties. *Ceramics International*, 44(3), 3333-3340. doi:[10.1016/j.ceramint.2017.11.116](https://doi.org/10.1016/j.ceramint.2017.11.116)

Jeong, Y.-J., Balamurugan, C., & Lee, D.-W. (2016). Enhanced CO₂ gas-sensing performance of ZnO nanopowder by La loaded during simple hydrothermal method. *Sensors and Actuators B: Chemical*, 229, 288-296. doi:[10.1016/j.snb.2015.11.093](https://doi.org/10.1016/j.snb.2015.11.093)

Kamble, V. S., Navale, Y. H., Patil, V. B., Desai, N. K., & Salunkhe, S. T. (2021). Enhanced NO₂ gas sensing performance of Ni-doped ZnO nanostructures. *Journal of Materials Science: Materials in Electronics*, 32(2), 2219-2233. doi:[10.1007/s10854-020-04987-z](https://doi.org/10.1007/s10854-020-04987-z)

Kanaparthy, S., & Singh, S. G. (2019). Chemiresistive Sensor Based on Zinc Oxide Nanoflakes for CO₂ Detection. *ACS Applied Nano Materials*, 2(2), 700-706. doi:[10.1021/acsanm.8b01763](https://doi.org/10.1021/acsanm.8b01763)

Kannan, P. K., Saraswathi, R., & Rayappan, J. B. B. (2014). CO₂ gas sensing properties of DC reactive magnetron sputtered ZnO thin film. *Ceramics International*, 40(8, Part B), 13115-13122. doi:[10.1016/j.ceramint.2014.05.011](https://doi.org/10.1016/j.ceramint.2014.05.011)

Kar, N., & Kamilla, S. K. (2021, October 8-10). Performance of Ni-doped ZnO nanoparticles towards CH₃-CO-CH₃ sensing. In: N. Nayak, T. Parida, T. P. Dash, L. M. Satpathy, M. Mishra, M. Sahani, D. A. Gadnayak, & S. Coudhury (Eds.), Proceedings of the International Conference in Advances in Power, Signal, and Information Technology (APSIT), Bhubaneswar, India. doi:[10.1109/APSIT52773.2021.9641451](https://doi.org/10.1109/APSIT52773.2021.9641451)

Mirzaei, A., Park, S., Kheel, H., Sun, G.-J., Lee, S., & Lee, C. (2016). ZnO-capped nanorod gas sensors. *Ceramics International*, 42(5), 6187-6197. doi:[10.1016/j.ceramint.2015.12.179](https://doi.org/10.1016/j.ceramint.2015.12.179)

Ocak, Y. S., Zeggar, M. L., Genişel, M. F., Uzun, N. U., & Aida, M. S. (2021). CO₂ sensing behavior of vertically aligned Si Nanowire/ZnO structures. *Materials Science in Semiconductor Processing*, 134, 106028. doi:[10.1016/j.mssp.2021.106028](https://doi.org/10.1016/j.mssp.2021.106028)

Saini, S., Kumar, A., Ranwa, S., & Tyagi, A. K. (2022). Highly sensitive NO₂ gas sensor based on Ag decorated ZnO nanorods. *Applied Physics A*, 128(5), 454. doi:[10.1007/s00339-022-05606-w](https://doi.org/10.1007/s00339-022-05606-w)

Saxena, N., Manzhi, P., Choudhary, R. J., Upadhyay, S., Ojha, S., Umopathy, G. R., Chawla, V., Sinha, O. P., & Krishna, R. (2020). Performance optimization of transparent and conductive Zn_{1-x}Al_xO thin films for opto-electronic devices: An experimental & first-principles investigation. *Vacuum*, 177. doi:[10.1016/j.vacuum.2020.109369](https://doi.org/10.1016/j.vacuum.2020.109369)

Singh, S., Kumar, Y., Kumar, H., Vyas, S., Periasamy, C., Chakrabarti, P., Jit, S., & Park, S.-H. (2017). A study of hydrothermally grown ZnO nanorod-based metal-semiconductor-metal UV detectors on glass substrates. *Nanomaterials and Nanotechnology*, 7. doi:[10.1177/1847980417702144](https://doi.org/10.1177/1847980417702144)

Wan, M., Shi, C., Qian, X., Qin, Y., Jing, J., Che, H., Ren, F., Li, J., & Yu, B. (2022). Interface assembly of flower-like Ni-MOF functional MXene towards the fire safety of thermoplastic polyurethanes. *Composites Part A: Applied Science and Manufacturing*, *163*, 107187. doi:[10.1016/j.compositesa.2022.107187](https://doi.org/10.1016/j.compositesa.2022.107187)

Wisitsoraat, A., Tuantranont, A., Comini, E., Sberveglieri, G., & Wlodarski, W. (2009). Characterization of n-type and p-type semiconductor gas sensors based on NiO_x doped TiO₂ thin films. *Thin Solid Films*, *517*(8), 2775-2780. doi:[10.1016/j.tsf.2008.10.090](https://doi.org/10.1016/j.tsf.2008.10.090)

Xu, K., Fu, C., Gao, Z., Wei, F., Ying, Y., Xu, C., & Fu, G. (2018). Nanomaterial-based gas sensors: A review. *Instrumentation Science & Technology*, *46*(2), 115-145. doi:[10.1080/10739149.2017.1340896](https://doi.org/10.1080/10739149.2017.1340896)

Xu, M., Li, Q., Ma, Y., & Fan, H. (2014). Ni-doped ZnO nanorods gas sensor: Enhanced gas-sensing properties, AC and DC electrical behaviors. *Sensors and Actuators B: Chemical*, *199*, 403-409. doi:[10.1016/j.snb.2014.03.108](https://doi.org/10.1016/j.snb.2014.03.108)

Zhang, Y., Liu, Y., Zhou, L., Liu, D., Liu, F., Liu, F., Liang, X., Yan, X., Gao, Y., & Lu, G. (2018). The role of Ce doping in enhancing sensing performance of ZnO-based gas sensor by adjusting the proportion of oxygen species. *Sensors and Actuators, B: Chemical*, *273*, 991-998. doi:[10.1016/j.snb.2018.05.167](https://doi.org/10.1016/j.snb.2018.05.167)



Gazi University

Journal of Science

PART A: ENGINEERING AND INNOVATION

<http://dergipark.org.tr/guj.1280707>

Identities for a Special Finite Sum Related to the Dedekind Sums and Fibonacci Numbers

Elif CETIN^{1*} ¹Manisa Celal Bayar University, Faculty of Arts and Science, Department of Mathematics, Manisa TR-45140, Türkiye

Keywords	Abstract
Hardy Sums	The origin of this article is to achieve original equations related to the special finite sum $C(\mu, \beta; 1)$, which is connected with Dedekind, Hardy, Simsek, and many other finite sums. By using the analytic properties of this sum, many useful identities are established between the $C(\mu, \beta; 1)$ sum and other well-known finite sums. Through the use of these identities, the reciprocity law of this sum is obtained. Furthermore, another reciprocity law of the sum $C(\mu, \beta; 1)$ is presented for μ and β are particular Fibonacci numbers. This remarkable result establishes a connection between number theory and analysis.
Dedekind Sums	
Simsek Sums	
Fibonacci Numbers	

Cite

Cetin, E. (2023). Identities for a Special Finite Sum Related to the Dedekind Sums and Fibonacci Numbers. *GU J Sci, Part A, 10(2)*, 232-240. doi:10.54287/guj.1280707

Author ID (ORCID Number)	Article Process
0000-0002-8565-5393 Elif CETIN	Submission Date 10.04.2023
	Revision Date 15.05.2023
	Accepted Date 17.05.2023
	Published Date 26.06.2023

1. INTRODUCTION

The special finite sums have been widely studied by mathematicians due to their extensive applications in many other scientific fields. Lately, scientific developments have shown the importance of interdisciplinary studies. Therefore, the purpose of this research is to get beneficial connections for special finite sums. Cetin et al. (2014) introduced the sum $C(\mu, \beta; 1)$, and by using the relationships between this particular sum and other familiar sums, new identities are obtained. At the end, a formula expressing the reciprocal relationship of the sum $C(\mu, \beta; 1)$ has been provided, when μ and β are special Fibonacci numbers. This significant finding enables a fresh perspective for establishing new connections of analysis and number theory.

Definitions and notations concerning special finite sums are given below:

Let $\mathbb{N} = \{1, 2, 3, \dots\}$, and $\mathbb{Z} = \mathbb{N} \cup \{0, -1, -2, -3, \dots\}$. In this paper, we consider finite sums fundamentally involving the sawtooth function. This function is defined by

$$((y)) = \begin{cases} y - [y] - \frac{1}{2}, & \text{if } y \notin \mathbb{Z}, \\ 0, & \text{otherwise,} \end{cases}$$

where $[y]$ denotes the largest integer $\leq y$ (Apostol, 1976; Berndt & Dieter, 1982). In the 19th century, Richard Dedekind made significant contributions to the fields of number theory and algebra. Based on the sawtooth function, he defined the Dedekind sums as follows:

$$s(\mu, \beta) = \sum_{\gamma=1}^{\beta-1} \left(\left(\frac{\mu\gamma}{\beta} \right) \right) \left(\left(\frac{\gamma}{\beta} \right) \right), \quad (1)$$

assuming $\mu \in \mathbb{Z}$, and $\beta \in \mathbb{N}$ (Dedekind, 1892). The Dedekind sums have studied by many mathematicians and have invaluable properties (Rademacher & Grosswald, 1972; Goldberg, 1981; Sitaramachandrarao, 1987; Meyer, 2005; Simsek, 1993). However, this paper will provide limited information about the Dedekind sums according to the needs of the main results of this study. The next reciprocity law is a highly regarded property of Dedekind sums, and is widely studied:

$$s(\mu, \beta) + s(\beta, \mu) = -\frac{1}{4} + \frac{1}{12} \left(\frac{\mu}{\beta} + \frac{\beta}{\mu} + \frac{1}{\mu\beta} \right),$$

where μ and β are coprime positive integers (Dedekind, 1892). Although the first proof of the reciprocity law was provided by Richard Dedekind, many mathematicians subsequently proved it using different methods. One of the original proofs was given by the famous mathematician Hardy, who used contour integration (Hardy, 1905). In the same work, he also defined some new arithmetical sums, called the Hardy sums. These sums have many significant properties and are closely linked to the Dedekind sums and other famous special finite sums. Recently, Simsek (2003; 2006; 2009a) gave p -adic q -Hardy sums, and also generating functions for these sums. The Hardy sums are also deeply related to the finite $C(\mu, \beta; 1)$ sum. Therefore, it is now time to introduce some of the Hardy sums and their essential properties that will be needed in the following sections. The Hardy sums $S(\mu, \beta)$ and $s_5(\mu, \beta)$ are expressed by

$$S(\mu, \beta) = \sum_{\gamma \bmod \beta} (-1)^{\gamma+1+\lfloor \frac{\mu\gamma}{\beta} \rfloor}, \quad (2)$$

$$s_5(\mu, \beta) = \sum_{\gamma \bmod \beta} (-1)^{\gamma+\lfloor \frac{\mu\gamma}{\beta} \rfloor} \left(\left(\frac{\gamma}{\beta} \right) \right), \quad (3)$$

where $\mu \in \mathbb{Z}$ and $\beta \in \mathbb{N}$ (Hardy, 1905).

The sum $s_5(\mu, \beta)$ is also given by

$$s_5(\mu, \beta) = \frac{1}{\beta} \sum_{\gamma=1}^{\beta-1} \gamma (-1)^{\gamma+\lfloor \frac{\mu\gamma}{\beta} \rfloor}, \quad (4)$$

when μ and β are odd integers (Berndt & Goldberg, 1984). Hardy (1905) proposed the following theorem of reciprocity for the $s_5(\mu, \beta)$ sum:

Theorem 1.1. Let $(\mu, \beta) = 1$, and $\mu, \beta \in \mathbb{N}$. Assuming μ and β are both odd numbers, then

$$s_5(\mu, \beta) + s_5(\beta, \mu) = \frac{1}{2} - \frac{1}{2\mu\beta} \quad (5)$$

and if $\mu + \beta$ is odd then

$$s_5(\mu, \beta) = s_5(\beta, \mu) = 0. \quad (6)$$

The following theorem shows the relations between Dedekind sum and the $s_5(\mu, \beta)$ sum (Pettet & Sitaramachandrarao, 1987).

Theorem 1.2. For $(\mu, \beta) = 1$, the following equalities hold true:

$$s_5(\mu, \beta) = -10s(\mu, \beta) + 4s(2\mu, \beta) + 4s(\mu, 2\beta), \quad \text{if } \mu + \beta \text{ is even,} \quad (7)$$

$$s_5(\mu, \beta) = 0, \quad \text{if } \mu + \beta \text{ is odd.}$$

For the sum $S(\mu, \beta)$, the reciprocity law was proved by Hardy (1905) as given below:

Theorem 1.3. Let $(\mu, \beta) = 1$, and $\mu, \beta \in \mathbb{N}$. Then

$$S(\mu, \beta) + S(\beta, \mu) = 1 \quad \text{if } \mu + \beta \text{ is odd.} \quad (8)$$

In consideration of (8), Apostol and Vu (1982) derived the next theorem.

Theorem 1.4. Let μ, β are odd simultaneously, and $(\mu, \beta) = 1$, then

$$S(\mu, \beta) = S(\beta, \mu) = 0. \quad (9)$$

The upcoming theorems establish a connection between the $s(\mu, \beta)$ sums and the $S(\mu, \beta)$ sums.

Theorem 1.5. Let $(\mu, \beta) = 1$. Then

$$S(\mu, \beta) = 8s(\mu, 2\beta) + 8s(2\mu, \beta) - 20s(\mu, \beta), \quad \text{if } \mu + \beta \text{ is odd,} \quad (10)$$

$$S(\mu, \beta) = 0, \quad \text{if } \mu + \beta \text{ is even}$$

(Pettet & Sitaramachandrarao, 1987).

Theorem 1.6. Let $(\mu, \beta) = 1$. Then

$$S(\mu, \beta) = 4s(\mu, \beta) - 8s(\mu + \beta, 2\beta), \quad (11)$$

if $\mu + \beta$ is odd and $\beta \in \mathbb{N}$ (Sitaramachandrarao, 1987).

The Simsek sum $Y(\mu, \beta)$ is defined by

$$Y(\mu, \beta) = 4\beta \sum_{\gamma \bmod \beta} (-1)^{\gamma + \lfloor \frac{\mu\gamma}{\beta} \rfloor} \left(\frac{\gamma}{\beta} \right) \quad (12)$$

(Simsek, 2009b).

An equation that connecting the sum $Y(\mu, \beta)$ and the sum $s_5(\mu, \beta)$ was provided as follows:

$$Y(\mu, \beta) = 4\beta s_5(\mu, \beta) \quad (13)$$

(Simsek, 2009b).

The reciprocal relationship associated with the Simsek sum can be stated as follows:

$$\mu Y(\mu, \beta) + \beta Y(\beta, \mu) = 2\mu\beta - 2. \quad (14)$$

Main motivation of this study is to give several identities containing connections between the Fibonacci numbers and the certain family of the Finite sums. Therefore, we need the following properties of these numbers. Lately, Simsek (2023) described the following common expression

$$\frac{\sum_{v=0}^k q_v(y_v)t^v}{\sum_{v=1}^j p_v(y_v)t^v + 1} = \sum_{m=0}^{\infty} S_m(p_1(y_1), \dots, p_j(y_j); q_0(y_0), q_1(y_1), \dots, q_k(y_k))t^m. \quad (15)$$

where $p_1(y_1), \dots, p_j(y_j), q_0(y_0), q_1(y_1), \dots, q_k(y_k)$ are any polynomials. For $j = 2$, setting $P_1(y_1) = P_2(y_2) = -1$ in Equation (15), we have the Fibonacci numbers. That is

$$F_m = S_m(-1, -1, 0, \dots, 0; 0, 1, 0, \dots, 0) = S_m(-1, -1; 0, 1)$$

see for detail Simsek (2023). For the properties of the Fibonacci numbers see also Koshy (2001). As a result, the following open question may arise:

Is it also possible to find and investigate new relationships among these new classes special of polynomials, numbers, and certain family finite sums including the $s(\mu, \beta)$ sums, the $S(\mu, \beta)$ sums, and the $Y(\mu, \beta)$ sums?

In 2005, Meyer showed that if $s(\mu, \beta) = s(\beta, \mu)$ then the pairs of integers $\{\mu, \beta\}$ is symmetric. He also gave many results for the Dedekind sums with the aid of this symmetric pair. The substitution of μ with F_{2m+1} and β with F_{2m+3} satisfies the symmetric pair property. In here F_k represents the k -th Fibonacci number. Thus, these type Fibonacci numbers satisfied this property.

In order to give our new results involving the symmetric pair, we need the next identity, which was given by Meyer (2005):

Theorem 1.7. Let $\mu, \beta \in \mathbb{Z}$ with $(\mu, \beta) = 1$. If μ and β form a symmetric pair, then we have

$$s(\mu, \beta) = 0. \quad (16)$$

The author (Cetin, 2016a) gave the following formula involving a relation between the Simsek sum $Y(\mu, \beta)$ and the Fibonacci numbers:

$$F_{2m+1}Y(F_{2m+1}, F_{2m+3}) + F_{2m+3}Y(F_{2m+3}, F_{2m+1}) = 2(F_{2m+1})^2 + 2(F_{2m+3})^2 - 4F_{2m+1}F_{2m+3}. \quad (17)$$

The finite sum $C_1(\mu, \beta)$ is defined by

$$C_1(\mu, \beta) = \sum_{\gamma=1}^{\beta-1} (-1)^{r+\lceil \frac{\mu\gamma}{\beta} \rceil} \left(\left(\frac{\mu\gamma}{\beta} \right) \right) \quad (18)$$

where $\mu, \beta \in \mathbb{N}$ with $(\mu, \beta) = 1$ (Cetin et al., 2014).

This has many relations with other well known finite sums. Cetin (2016a; 2016b) gave some useful properties for this sum.

The finite sum $B_1(\mu, \beta)$ defined by

$$B_1(\mu, \beta) = \sum_{\gamma=1}^{\beta-1} (-1)^{\gamma+\left[\frac{\mu\gamma}{\beta}\right]} \left[\frac{\mu\gamma}{\beta}\right] \quad (19)$$

(Cetin et al., 2014).

The author gave many properties of the sum $B_1(\mu, \beta)$.

Relation among $B_1(\mu, \beta)$, $s_5(\mu, \beta)$, and $C_1(\mu, \beta)$ is given by the following theorem, which was proved by the author (Cetin, 2016a):

Theorem 1.8. If μ and β are relatively prime odd numbers and β is a positive integer, then

$$B_1(\mu, \beta) = \mu s_5(\mu, \beta) - C_1(\mu, \beta). \quad (20)$$

Many mathematicians investigated two and three term polynomial relations by reason of they are connected to the $s(\mu, \beta)$ sums, the $S(\mu, \beta)$ sums, and several other special finite sums (Berndt & Dieter, 1982; Pettet & Sitaramachandrarao, 1987; Simşek, 1998). Cetin et al. (2014) defined new polynomials with the help of the n variable Carlitz polynomial. By taking partial derivative with respect to all variables, they gave some new equations involving some certain family of finite sums with open questions. They profoundly studied about equations and relations. Using them, they gave some original demonstration of the reciprocity laws for these sums.

In this paper, two term polynomial relation will be used for the next section. Therefore, it will be reminded as a corollary in below:

Corollary 1.9. Let $(\varphi, \rho) = 1$, then

$$(t-1) \sum_{x=1}^{\varphi-1} t^{x-1} n^{\left[\frac{\rho x}{\varphi}\right]} + (n-1) \sum_{y=1}^{\rho-1} n^{y-1} t^{\left[\frac{\varphi y}{\rho}\right]} = t^{\varphi-1} n^{\rho-1} - 1. \quad (21)$$

(21) is given by Berndt and Dieter (1982).

Cetin et al. (2014) introduced the sum $C(\mu, \beta; 1)$ with the equation below:

Let $(\mu, \beta) = 1$ and $\beta > 0$, then

$$C(\mu, \beta; 1) = \sum_{\gamma=1}^{\beta-1} \gamma (-1)^{\gamma+\left[\frac{\mu\gamma}{\beta}\right]}. \quad (22)$$

The relation between the sum $C(\mu, \beta; 1)$ and the Hardy sum $S(\mu, \beta)$ is described by the following equality:

Let $\mu + \beta$ is odd, $\beta > 0$, and $(\mu, \beta) = 1$ (Cetin, 2018), then

$$C(\mu, \beta; 1) = -\frac{\beta}{2} S(\mu, \beta). \quad (23)$$

One can express the connections the sum $C(\mu, \beta; 1)$ with the Hardy sums $s_5(\mu, \beta)$ and $S(\mu, \beta)$ as follows (Cetin, 2023):

Let μ and β be integers with $(\mu, \beta) = 1$. Then one can get the following identity:

$$C(\mu, \beta; 1) = \beta s_5(\mu, \beta) - \frac{\beta}{2} S(\mu, \beta).$$

Let μ and β are positive odd integers. Then,

$$C(\mu, \beta; 1) = \beta s_5(\mu, \beta). \quad (24)$$

2. RECIPROCITY LAWS FOR THE SUM $C(\mu, \beta; 1)$

For the sum $C(\mu, \beta; 1)$, a reciprocity law, and relations with other special sums are presented in this section. For this, we will use the Dedekind and the Hardy sums properties. With the aid of two term polynomial relation's partial derivatives, a different reciprocity law for the sum $C(\mu, \beta; 1)$ is also obtained. And finally when μ and β are special Fibonacci numbers, a new reciprocity identity will be given for this sum.

The reciprocity laws for the sum $C(\mu, \beta; 1)$ are given by the identities below.

Theorem 2.1. If $\mu + \beta$ is odd, $\beta > 0$, and $(\mu, \beta) = 1$, then

$$\mu C(\mu, \beta; 1) + \beta C(\beta, \mu; 1) = -\frac{\mu\beta}{2}$$

Proof. By combining (8) with (23), one can have,

$$-\frac{2}{\beta} C(\mu, \beta; 1) - \frac{2}{\mu} C(\beta, \mu; 1) = 1.$$

If the last equation multiplied by $\mu\beta$, and divided by -2 , then the required outcome is obtained.

Theorem 2.2. Let μ and β be positive and odd integers. Then the below equation holds true:

$$\mu C(\mu, \beta; 1) + \beta C(\beta, \mu; 1) = \frac{\mu\beta - 1}{2}$$

Proof. To prove the theorem, the two term polynomial relation will be used. If the partial derivative of (21) is taken with regard to t , we get

$$\begin{aligned} \sum_{x=1}^{\mu-1} t^{x-1} n^{\lfloor \frac{\beta x}{\mu} \rfloor} + (t-1) \sum_{x=1}^{\mu-1} (x-1) t^{x-2} n^{\lfloor \frac{\beta x}{\mu} \rfloor} + (n-1) \sum_{y=1}^{\beta-1} \left\lfloor \frac{\mu y}{\beta} \right\rfloor n^{y-1} t^{\lfloor \frac{\mu y}{\beta} \rfloor - 1} \\ = (\mu-1) t^{\mu-2} n^{\beta-1}. \end{aligned}$$

Substitute $t = n = -1$, into the above equation, we have

$$S(\beta, \mu) + 2C(\beta, \mu; 1) + 2B_1(\mu, \beta) = (\mu-1)(-1)^{\mu+\beta}. \quad (25)$$

Taking partial derivative of (21) with regard to n , we also get

$$\begin{aligned} (t-1) \sum_{x=1}^{\mu-1} \left\lfloor \frac{\beta x}{\mu} \right\rfloor t^{x-1} n^{\lfloor \frac{\beta x}{\mu} \rfloor - 1} + (n-1) \sum_{y=1}^{\beta-1} (y-1) n^{y-2} t^{\lfloor \frac{\mu y}{\beta} \rfloor} + \sum_{y=1}^{\beta-1} n^{y-1} t^{\lfloor \frac{\mu y}{\beta} \rfloor} \\ = (\beta-1) t^{\mu-1} n^{\beta-2}. \end{aligned}$$

Putting $t = n = -1$ in the above equation, we obtain

$$S(\mu, \beta) + 2C(\mu, \beta; 1) + 2B_1(\beta, \mu) = (\beta-1)(-1)^{\mu+\beta} \quad (26)$$

is found. If the Equation (25) is multiplied by β , we get

$$\beta S(\beta, \mu) + 2\beta C(\beta, \mu; 1) + 2\beta B_1(\mu, \beta) = \beta(\mu-1)(-1)^{\mu+\beta}. \quad (27)$$

Equation (26) is multiplied by μ , we obtain

$$\mu S(\mu, \beta) + 2\mu C(\mu, \beta; 1) + 2\mu B_1(\beta, \mu) = \mu(\beta - 1)(-1)^{\mu+\beta}. \quad (28)$$

Combining (27) and (28), allows us to assert the theorem.

Theorem 2.3. Let $\mu, \beta \in \mathbb{Z}$ with $\mu, \beta > 0$, and $\{\mu, \beta\}$ is a symmetric pair. If $(\mu, \beta) = 1$, $\mu = F_{6m-1}$ and $\beta = F_{6m+1}$ with $m \in \mathbb{N}$, where F_k is the k -th Fibonacci number then,

$$\begin{aligned} & F_{6m-1}C(F_{6m-1}, F_{6m+1}; 1) + F_{6m+1}C(F_{6m+1}, F_{6m-1}; 1) \\ &= \frac{(F_{6m-1})^2 + (F_{6m+1})^2}{2} - F_{6m-1}F_{6m+1} \end{aligned}$$

Proof. If we combine equation (13) with equation (24), then we have

$$4C(\mu, \beta; 1) = Y(\mu, \beta).$$

If we use this last equation with equation (17), then we have the desired result.

3. IDENTITIES FOR THE SUM $C(\mu, \beta; 1)$, THE SIMSEK SUM $Y(\mu, \beta)$, THE SUM $B_1(\mu, \beta)$, AND THE DEDEKIND SUMS

We now give relations among the sum $C(\mu, \beta; 1)$, the Simsek sum $Y(\mu, \beta)$, the sum $B_1(\mu, \beta)$, and the Dedekind sums by the next theorems.

Theorem 3.1. If $\mu + \beta$ is odd, $\beta > 0$, and $(\mu, \beta) = 1$, then

$$C(\mu, \beta; 1) = -4\beta s(\mu, 2\beta) - 4\beta s(2\mu, \beta) + 10\beta s(\mu, \beta)$$

Proof. By combining (10) with (23) the proof is completed.

Theorem 3.2. If $\mu + \beta$ is odd, $\beta > 0$, and $(\mu, \beta) = 1$, then

$$C(\mu, \beta; 1) = -2\beta s(\mu, \beta) + 4\beta s(\mu + \beta, 2\beta)$$

Proof. By combining (11) with (23) the intended outcome is achieved.

Theorem 3.3. Let $\mu, \beta \in \mathbb{N}$ be odd integers. Then

$$C(\mu, \beta; 1) = -10\beta s(\mu, \beta) + 4\beta s(2\mu, \beta) + 4\beta s(\mu, 2\beta)$$

Proof. By combining (7) with (23) the given equation is satisfied.

Theorem 3.4. Let $\mu, \beta \in \mathbb{N}$ be odd integers. Then the following result is derived:

$$C(\mu, \beta; 1) = \frac{\beta}{\mu} B_1(\mu, \beta) + \frac{\beta}{2\mu} - \frac{1}{2\mu}$$

Proof. If the Equation (20) is multiplied by β , then combining final equation with (24) and

$$C_1(\mu, \beta) = \frac{1}{2} - \frac{1}{2\beta}$$

(see Cetin (2016a)-Theorem 2.2.), we achieve the intended outcome.

4. CONCLUSION

In light of the above, this article has presented new identities related to Dedekind sums and Fibonacci numbers, and explored its connections with other well-known sums. Through this paper, a reciprocity law for the sum $C(\mu, \beta; 1)$ was discovered when μ and β are special Fibonacci numbers, adding a new dimension to the study of these special sums. This reciprocity law has the potential to deepen our understanding of the behavior of these sums.

In future studies, different proof of this law is investigated in diverse branches of mathematics, such as algebraic geometry and modular forms, as a results far-reaching implications maybe obtain.

Due to many important applications of the certain classes of finite sums in many branches of mathematics, our future goal is to derive new reciprocity laws for more general cases of certain finite sums with their proofs methods. To achieve this, our primary focus will be on solving the open questions posed by Cetin et al. (2014). Solving these questions would make a significant contribution to the theory of the certain finite sums. In addition, Simsek (2022) has also identified valuable open questions in his recent article, and addressing these questions would yield a substantial contribution to the theory of certain finite sums, complementing our primary objective of deriving new reciprocity laws for more common scenarios. Furthermore, attempts will be made to find new connections with the trigonometric representations provided by Simsek (2010), and Milovanović and Simsek (2020).

CONFLICT OF INTEREST

The author declares no conflict of interest.

REFERENCES

- Apostol, T. M. (1976). *Modular functions and Dirichlet Series in Number Theory*. Springer-Verlag.
- Apostol, T. M., & Vu, T. H. (1982). Elementary proofs of Berndt's reciprocity laws. *Pacific Journal of Mathematics*, 98(1), 17-23. doi:[10.2140/pjm.1982.98.17](https://doi.org/10.2140/pjm.1982.98.17)
- Berndt, B. C., & Dieter, U. (1982). Sums involving the greatest integer function and Riemann Stieltjes integration. *Journal für die Reine und Angewandte Mathematik*, 337, 208-220. doi:[10.1515/crll.1982.337.208](https://doi.org/10.1515/crll.1982.337.208)
- Berndt, B. C., & Goldberg, L. A. (1984). Analytic properties of arithmetic sums arising in the theory of the classical theta-functions. *SIAM Journal on Mathematical Analysis*, 15(1), 143-150. doi:[10.1137/0515011](https://doi.org/10.1137/0515011)
- Cetin, E., Simsek, Y., & Cangul, İ. N. (2014). Some Special Finite Sums Related to the Three-Term Polynomial Relations and Their Applications. *Advances in Difference Equations*, 2014, 283. doi:[10.1186/1687-1847-2014-283](https://doi.org/10.1186/1687-1847-2014-283)
- Cetin, E. (2016a). A Note on Hardy Type Sums and Dedekind Sums. *Filomat*, 30(4), 977-983. doi:[10.2298/FIL1604977C](https://doi.org/10.2298/FIL1604977C)
- Cetin, E. (2016b). Analytic Properties of the Sum $B_1(h, k)$. *Mathematical and Computational Applications*, 21(3), 31. doi:[10.3390/mca21030031](https://doi.org/10.3390/mca21030031)
- Cetin, E. (2018, October 26-29). *Remarks on Special Sums Associated with Hardy Sums*. In: Proceedings of the Mediterranean International Conference of Pure & Applied Mathematics and Related Areas (MICOPAM 2018), (pp. 153-156). Antalya.
- Cetin, E. (2023, March 11-13). *A Note on Trigonometric Identities of the Special Finite Sums*. In: Proceedings of the 13th Symposium on Generating Functions of Special Numbers and Polynomials and their Applications (GFSNP 2023), which is dedicated to Professor Yilmaz Simsek on the Occasion of his 60th Anniversary, (pp. 1-7). Antalya.
- Dedekind, R. (1892). *Erläuterungen zu zwei Fragmenten von Riemann-Riemann's Gesammelte Math. Werke*.
- Goldberg, L. A. (1981) *Transformation of Theta-functions and analogues of Dedekind sums*. MSc Thesis, University of Illinois.

- Hardy, G. H. (1905). On certain series of discontinues functions connected with the modular functions, *Quart. J. Math.*, 36, 93-123.
- Koshy, T. (2001). *Fibonacci and Lucas Numbers with Applications*. John Wiley and Sons, New York, USA.
- Meyer, J. L. (2005). Symmetric Arguments in the Dedekind Sum. *Fibonacci Quarterly*, 43(2), 122.
- Milovanović, G. V., & Simsek, Y. (2020). Dedekind and Hardy Type Sums and Trigonometric Sums Induced by Quadrature Formulas. In: A. Raigorodskii, M. Rassias (Eds.), *Trigonometric Sums and Their Applications* (pp. 183-228). Springer, Cham. doi:[10.1007/978-3-030-37904-9_10](https://doi.org/10.1007/978-3-030-37904-9_10)
- Pettet, M. R., & Sitaramachandrarao, R. (1987). Three-term relations for Hardy sums. *Journal of Number Theory*, 25(3), 328-339. doi:[10.1016/0022-314X\(87\)90036-9](https://doi.org/10.1016/0022-314X(87)90036-9)
- Rademacher, H., & Grosswald, E. (1972). *Dedekind sums*. Carus Mathematical Monographs, The Mathematical Association of America.
- Sitaramachandrarao, R. (1987). Dedekind and Hardy sums. *Acta Arithmetica*, 48(4), 325-340. doi:[10.4064/aa-48-4-325-340](https://doi.org/10.4064/aa-48-4-325-340)
- Simsek, Y. (1993). A note on Dedekind sums. *Bull. Calcutta Math. Soc.*, 85(6), 567-572.
- Simsek, Y. (1998). Theorems on Three-Term Relations for Hardy Sum. *Turkish Journal of Mathematics*, 22(2), 153-162.
- Simsek, Y. (2003). Relation between theta-function Hardy sums Eisenstein and Lambert series in the transformation formula of $\log \eta_{g,h}(z)$. *Journal of Number Theory*, 99(2) 338-360. doi:[10.1016/s0022-314x\(02\)00072-0](https://doi.org/10.1016/s0022-314x(02)00072-0)
- Simsek, Y. (2004). On generalized Hardy sums $s_5(h, k)$. *Ukrainian Mathematical Journal*, 56(10), 1712-1719. doi:[10.1007/s11253-005-0146-2](https://doi.org/10.1007/s11253-005-0146-2)
- Simsek, Y. (2006). p -adic q -higher-order hardy-type sums. *Journal of the Korean Mathematical Society*, 43(1), 111-131.
- Simsek, Y. (2009a). q -Hardy-Berndt type sums associated with q -Genocchi type zeta and q - l -functions. *Nonlinear Analysis*, 71(12), e377-e395. doi:[10.1016/j.na.2008.11.014](https://doi.org/10.1016/j.na.2008.11.014)
- Simsek, Y. (2009b). On analytic properties and character analogs of Hardy sums. *Taiwanese Journal of Mathematics*, 13(1), 253-268. doi:[10.11650/twjmath/1500405282](https://doi.org/10.11650/twjmath/1500405282)
- Simsek, Y. (2010). Special functions related to Dedekind-type DC-sums and their applications. *Russian Journal of Mathematical Physics*, 17(4), 495-508. doi:[10.1134/S1061920810040114](https://doi.org/10.1134/S1061920810040114)
- Simsek, Y. (2022). Some classes of finite sums related to the generalized Harmonic functions and special numbers and polynomials. *Montes Taurus Journal of Pure and Applied Mathematics*, 4(3), 61-79.
- Simsek, Y. (2023). Construction of general forms of ordinary generating functions for more families of numbers and multiple variables polynomials. *Revista de la Real Academia de Ciencias Exactas, Físicas y Naturales. Serie A. Matemáticas*, 117(3), 130. doi:[10.1007/s13398-023-01464-0](https://doi.org/10.1007/s13398-023-01464-0)



Gazi University

Journal of Science

PART A: ENGINEERING AND INNOVATION

<http://dergipark.org.tr/guj.1255461>

Process Improvement Between Company Departments with the Integration of ERP and CRM Software Programs

Miyase ULUSOY YILMAZ^{1*}  Bahar ÖZYÖRÜK²  Sema BİLGE OCAK¹ 

¹Gazi University, Graduate School of Natural and Applied Sciences, Department of Advanced Technologies, Ankara, Türkiye

²Gazi University, Faculty of Engineering and Architecture, Industrial Engineering, Ankara, Türkiye

Keywords	Abstract
ERP-CRM Integration	This study aims to examine the processes of a company that uses Enterprise Resource Planning (ERP) and Customer Relationship Management (CRM) systems, which are known as integrated systems, and improve these processes in an enterprise that produces decorative acoustic suspended building products. The company started to use Netsis software as an ERP system years ago. Then, it purchased the LogoCRM software, which could work integrated into Netsis software, to ensure information flow between these systems easily. Since it is known that the company still experiences information flow issues between the departments although the ERP and CRM systems of the company are integrated, the study tried to minimize these deficiencies in the information flow between the production and sales & marketing departments. The problems experienced between the departments of the company that we work with were determined by the interviews with the ERP and CRM system users in the company, and the ERP-CRM software was customized to be suitable for the use of the company. A user-friendly interface has been designed in the CRM software, and by providing integration between the software, it is possible to see the stock balance information instantly in the CRM software. In addition, in the CRM software that will work integrated with ERP, a smart coding algorithm was developed to minimize errors by considering the possibility of the sales team misreading the product cards, and it was aimed to reduce user errors by minimizing the screen interventions of the users. In the study, ModelEditor was used for the improvements made in the SQL-based CRM software. With this study, communication problems between sales-marketing and production departments were reduced by providing ERP-CRM integration. As a result of the improvements made, a common language was developed between the departments, reducing the amount of faulty production, and time savings were achieved by reinforcing the cooperation between departments.
CRM Software System	
ERP Software System	
Information Technologies	
Integrated Software Systems	
Coding	

Cite
Yilmaz, M. U., Özyörük, B., & Ocak, S. B. (2023). Process Improvement Between Company Departments with the Integration of ERP and Crm Software Programs. <i>GU J Sci, Part A, 10(2)</i> , 241-261. doi:10.54287/guj.1255461

Author ID (ORCID Number)	Article Process
0000-0003-1175-7239	Miyase ULUSOY YILMAZ
0000-0001-5434-6697	Bahar ÖZYÖRÜK
0000-0002-0590-7555	Sema BİLGE OCAK
	Submission Date 23.02.2023
	Revision Date 28.03.2023
	Accepted Date 24.04.2023
	Published Date 26.06.2023

1. INTRODUCTION

In line with the developments in the globalizing world, all concepts have been affected. The concept of Enterprise Resource Planning (ERP) has entered our lives with the start of performing the production, accounting, inventory, and warehouse control processes of enterprises in computer-based systems. Optionally, ERP modules can be implemented and integrated into logistics, marketing, social media data and other external data sources supplemented by various additional concepts such as Business Intelligence (BI) Methods, Supply Chain Management (SCM), and Customer Relationship Management (CRM) (Laverty, 2022)

Today, where the product-oriented marketing approach has been abandoned, enterprises have tended to follow the customer-oriented marketing approach. On the other hand, customers prefer enterprises that show individual relationship rather than traditional sales methods. Customer relationship management aims to

*Corresponding Author, e-mail: miyaseulusoy@gmail.com

identify profitable customers for the company and to increase the loyalty of these customers by managing the relationship between customers and the enterprise.

Based on the operational problems, Tacer realizes that they need a system that can integrate every part of the organization (Rinaldy & Juarna, 2022). According to the results of the assessments made by considering factors such as using Netsis software as an ERP system, price-performance efficiency, and the suitability of the software to the requirements, LogoCRM application was purchased as a CRM system to ensure the ERP-CRM integration.

LogoCRM, which has been purchased by the company, is a CRM software package of Logo, which has achieved to become a leading company in the Turkish software industry in a short time. After entering the ERP market with its accounting software package, Logo developed itself over time and introduced Tiger 3, Tiger 3 Enterprise, Tiger Wings, J-guar 3, Netsis 3 Enterprise products in the field of ERP (Tacer, 2023). Then, it increased its product range and activities in the industry and developed several products such as LogoCRM, which is used as a customer relationship management software, LogoHRM, where we can transfer human resources processes to the digital environment, LogoWMS, which is used as a warehouse management system, LogoFlow, which is used as workflow management software, and LogoISG, which enables to manage Occupational Health and Safety processes in accordance with legal regulations.

With LogoCRM, the company wanted to create its own customer portfolio by gathering its customers in a single database. Moreover, with the use of the LogoCRM system, sales representatives can transfer their quotes to the ERP system as an order through the software as soon as the quote they receive turns into a sale. This will facilitate the control of orders and reduce the workload by ensuring the production-sales integration quickly. Another expectation of the company from LogoCRM software is that sales representatives are now enabled to check the warehouse and provide accurate information to the customer.

In this context, the relationships between the production and sales & marketing departments in these systems were addressed. Then, the stages of customizing the LogoCRM software for the Tacer company, which has been studied as an example, in accordance with the needs of the company, are explained in detail, and an example road map has been created for other companies to eliminate the internal functioning problems.

2. INTRODUCTION RELATIONSHIP BETWEEN PRODUCTION AND MARKETING DEPARTMENTS

The Oxford Learner's Dictionaries define the term 'business' as follows: the activity of making, buying, selling, or supplying goods or services for money (Oxford Learner's Dictionary, 2023). Based on this definition, enterprises can be described as organizations founded by entrepreneurs by using their labor and capital to gain profit (Demirkapı, 2013). In order for enterprises to survive today, they need to be able to adapt to today's marketing methods. Therefore, the idea of relationship marketing, which emerged in the 1980s, caused traditional marketing systems to change. The concept of relationship marketing was first used by Leonard Berry in 1983 to mean service marketing (Savasci & Ventura, 2001). With the concept of relationship marketing, which entered our lives thanks to Berry, it has been understood that the concept of traditional sales and marketing, where only production exists, has not been enough for enterprises to continue their operations, and that the main thing has been trust-based relationships with customers (Morgan & Hunt, 1994).

Enterprises should constantly aim to improve themselves to adapt to today's marketing techniques and to survive in this competitive environment. Therefore, keeping the internal dynamics active within the enterprise has almost become a prerequisite for them. Of course, all departments should work synchronously to achieve it. In general, the concept of relationship marketing has focused on the relationships between company employees and customers, so the relationships between the departments in the enterprise have been neglected.

Perceptions and problems of marketing and production departments in the enterprise differ from each other. However, these departments need to achieve these goals in cooperation by setting goals that will serve the same mission together. In this part, production and sales & marketing departments and their functions will be defined to achieve this cooperation.

2.1. Production Systems

In its most general definition, it is the creation of goods and services with economic value. In the end, production is not only the physical creation of a product, but also all of the activities done to add or increase the value of a product. (Başkak & Tanyaş, 2006) As can be understood from its definition, the most significant point of the concept of production is the emergence of a product that creates benefits as a result of the activities carried out. With globalization and technological developments, manufacturing enterprises have started to change their production structures (Bagdat & Can, 2023). With the change in the production structures, the definition of production has started to evolve and change.

Production systems vary widely according to the type, quantity, or characteristics of the products. Thus, production methods vary taking into account this and many other features (Saadet, 2012). Although there are several different ideas in the literature on this subject, in general, we can list according to the amount or flow of production four types of production systems as follows:

- Continuous (Mass) Production Systems
- Batch Production Systems
- Mixed Production Systems
- Project-Type Production Systems (Kurgan, 2023)

Continuous (mass) production systems are used in productions where the demand is high and the variety of products is low. In batch production systems, the variety of products is high, that is, small quantities of various products are produced. In batch production systems, production is performed taking into account the customized orders of the customer, or the customer's continuous demand from certain product groups are produced. Mixed production systems can be considered as a combination of these two production systems. The company uses a mixed production system when manufacturing both customized orders for the customers and performing mass production to meet their continuous demands. In project-type productions, the level of technical specialization is high, and there is a special and unique product. Therefore, project-type production systems are the most costly production type.

Although the concept of production was first defined as the manufacturing of a product that creates benefits, since the manufacturing enterprises do it to make a profit and the resources are not unlimited, the production aims to use resources efficiently and to create the highest level of consumer satisfaction. Especially considering the competitive environment in today's world, the severity of the process should be understood. With the continuous development of technology and the growing of enterprises, we can no longer rely solely on manual data statistics and management (Liu et al., 2020).

Therefore, with the introduction of computer systems in our lives in recent years, production systems have also been tried to be integrated into computerized structures. With the developments in computer technologies, companies have begun to widely use computers in areas such as production and planning as well as management processes (Demirel & Karaagaç, 2014). Therefore, many concepts, such as computer-aided manufacturing (CAM), computer-aided design (CAD), computer-integrated manufacturing (CIM), and computer-integrated manufacturing (CIM), have emerged over time.

On the other hand, ERP systems have been designed as “integrated systems” due to the designs of applications that support the operations of companies (Sevim & Bulbul, 2016). ERP systems are fully integrated business management systems that plan all the resources of a company and meet all information needs. It combines the software processes of all departments into a single database (Kecek & Yıldırım, 2009). However, these systems may cause an increase in the number of inappropriate automation islets, and if this happens, the company experiences challenges in using all of its technology and equipment potential, resulting in a lack of integration and coordination (Sağlam, 2008). In other words, if the production and order systems of the company are not synchronized, this will cause a decrease in production efficiency as well as customer dissatisfaction.

2.2. Sales & Marketing Systems

People did not need sales and marketing in the periods when they consumed what they produced themselves. However, after the transition to settled life, people began to consume less than what they produced, and they exchanged the rest of their products with other products they needed. The exchange activities that started between people and small groups developed with the transformation of these groups into societies and turned into large commercial activities. With the change and development of commercial activities over time, the importance of marketing activities has increased. It is known that even in ancient times, specialization was made in terms of products, and these products were marketed (Doğan & Başgelen, 2008).

In the marketing literature, there are many definitions. Based on these definitions, we can follow the evolution and change of marketing over the years. For example, the definitions of marketing made by the American Marketing Association (AMA) over the years are as follows:

“Marketing is the performance of business activities that direct the flow of goods and services from producers to consumers.”

This definition was the first definition of marketing published by the American Marketing Association in 1935 (Kaya, 2023). Although various definitions were made over the years, the definition made in 2017 is as follows:

“Marketing is the activity, set of institutions, and processes for creating, communicating, delivering, and exchanging offerings that have value for customers, clients, partners, and society at large.”

As can be understood from the change between the two definitions, marketing has changed much over the years in terms of understanding and perspective. Especially with the emergence of the concept of relationship marketing in recent years, traditional marketing strategies have been abandoned. According to traditional marketing strategies, the goal is achieved with the sale of the product or service. On the other hand, in relationship marketing, the goal is to establish long-term customer relations with the customer after the sale of the product. Since customer satisfaction is so important, processes in relationship marketing have become customer-oriented rather than product-oriented. That is, as shown in Figure 1, marketing has evolved from a production-centered understanding to a customer-centered understanding of today.

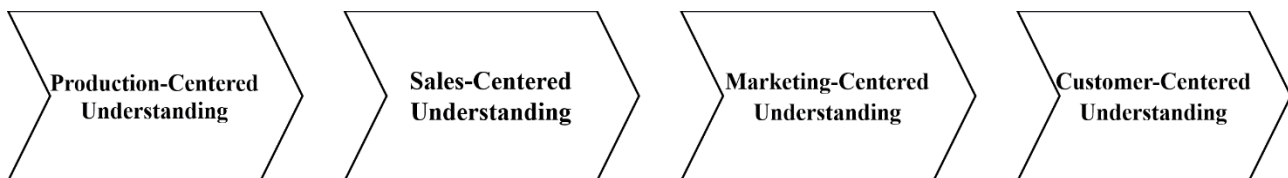


Figure 1. Evolution of Marketing Processes

2.3. Relationship Between Production and Sales & Marketing Systems

In order for companies to provide better quality service, integration between departments is required (Güçlü Hacıoğlu, 2022). Coordination and continuous data exchange is essential for production planning and sales & marketing actions for manufacturing enterprises (Aydın & Dursun, 2022). Therefore, coordination between production and marketing departments is required for many enterprises to continue their activities successfully. It is essential to ensure coordination between these departments in order to provide the right product or service by correctly understanding the demands and requirements of the customers. Communication or lack of communication between these departments directly or indirectly affects customer satisfaction. Although there may be disagreements between all departments of companies, clear differences may be observed between the goals of the production and marketing (or sales) departments (Sezen et al., 2002).

As it is known, the purpose of enterprises is to be active in the market for as long as possible by obtaining maximum profit. In today's market conditions, companies need to constantly improve themselves to exist in the market. In other words, the companies should ensure the production of new products and make them demanded in the market by evaluating the needs and requests of the customers together with the work of the sales & marketing department. The production stage of the product is evaluated by considering the resources

of the production department in order for the process up to this stage to become profitable for the enterprise. In light of the information provided by the sales & marketing department, the production department evaluates the production plans, R&D studies, and the profit margin of the product to be produced for the company. Therefore, the sales & marketing systems should have close relationships with production systems, and there must be a constant information flow between them (Dilek, 1993).

3. IMPLEMENTATION

Although the production and sales& marketing departments of the company operate integrated with each other, it has been decided to make some improvements according to the results of the evaluations made after interviewing the employees in the company.

3.1. Smart Coding for Materials

Unfortunately, one of the biggest problems between the sales & marketing department and the production department is that sales representatives and employees in the production department do not define stocks in the same way. In other words, since the users of the CRM system do not have a good command of the codes of the products defined in the ERP system and are not actually involved in the production processes, communication problems may occur between these departments. Therefore, it was decided to use the smart coding system while opening the product cards and to define the codes of the products using an algorithm that everyone can understand. With the “Smart Code” feature, it has been tried to generate constant stock card codes (in accordance with the previously determined template) and thus to ensure the standardization of the codes.

The following issues are considered while creating a typical smart code system (Kobu, 2003):

- All codes must contain details that may be important to each user who will use the code, and these details must always be provided in a specific order.
- The factors determining the length of the codes should be taken into account.
- The groups specified in the system should be easily separable into subgroups if necessary.
- For preventing confusion in the current coding, the ‘Ø’ sign should be used to omit a breakdown.
- Codes should be separated from each other using the signs such as (.), (-), or (/).
- Codes may be grouped considering reasonable relations.
- Classifications should be made in accordance with international classifications.
- The information provided by the code should be simple enough to be used without needing to look up the prepared guide.

The products were examined in detail by interviewing the ERP officials of the company in line with this information. First of all, the products are classified into the following three basic groups: raw materials, semi-finished products, and finished products. While raw materials are never sold by the company, semi-finished products are mostly not sold. However, all products, except for several ones, are included in the smart coding system.

3.1.1. Codes Created for Raw Materials

The company has raw materials such as paint, wood, plaster, metal, fabric, etc. required for the production of suspended ceilings. Incremental numbers were given to the materials in the inventory while coding them, and detailed information about the inventory is coded in the inventory cards. The details to be specified by the inventory code are determined during the study of the products.

Step 1: Determining the Features of Raw Materials

Typical features that are considered significant in smart coding are as follows:

- Details about the main classification of the raw material (wood, packaging, etc.)
- Details about the model of the raw material

- Color of the raw material
- Size of the raw material

Step 2: Defining the Specified Classification Features by Letters and Abbreviation

Firstly, code ‘HM’ shall be included in the code to indicate that it is a raw material.

Secondly, the details about the main category of raw materials shall be included. Table 1 presents some main categories.

Table 1. Examples of Main Classifications and Abbreviations of the Raw Materials

Main Categories of the Raw Materials	Abbreviation (In Turkish)
MDL METAL	MM
MDL PLASTER	MC
PLASTERBOARD	CP
FABRIC	KM
MDL SFTB	MS
MDL WOOD	MA
GLUE	TT
BEARING ELEMENT	TS
MATERIAL	ML
PACKAGING	AB

In two-word abbreviations, the letter ‘M’ always stands for metal, the letter ‘A’ stands for wood, and the letter ‘C’ stands for plaster.

In the third layer, the model features of the raw materials are coded. Some abbreviations used in coding are shown in Table 2.

Table 2. Examples of Color Features and Abbreviations of the Raw Materials

Model Features of the Raw Materials	Abbreviation (In Turkish)
ROLL	RL
PLATE	LV
CLIP-IN	CL
WOODEN BAFFLE	AB
BAFFLE	BF
SEPARATOR	SP
FABRIC	KM

The fourth layer of the code indicates the details about the color of the product. Some of the raw materials used have RAL color codes. RAL color chart, which has more than 200 shades in its collection, was first published in 1927 by a subsidiary of the German Institute for Quality Assurance and Certification (Çelebi, 2013). The color of the product should be specified using the corresponding code in the RAL color chart. If the product is not included in this chart (wood products such as walnuts, bamboo, etc.), the color should be abbreviated using the first three consonants. If a color has less than three consonants, the existing consonants should be followed by the first vowel after the consonants to adapt to this algorithm. If it is required to specify color shades using multiple words, the initial letter of each word is written then a consonant of this color is added. In addition, the

letters ‘M ‘and ‘Y ‘shall be used to indicate whether the product is matte or semi-matte, respectively, which is important for the company. Some abbreviations used in coding are shown in Table 3.

Table 3. Examples of Color Features and Abbreviations of the Raw Materials

Color Feature of the Raw Materials	Abbreviation (InTurkish)
MAPLE TREE	AKC
WALNUT	CVZ
BLACK	SYH
WHITE	BYZ
CHERRY	KRZ
WENGE	WNG
NATURAL	NTR
PINK	PMB

Finally, the dimensions of the raw materials used shall be added by taking into account their diameters and lengths.

Step 3: Creating the smart code by combining the features of the raw materials (Figure 2)

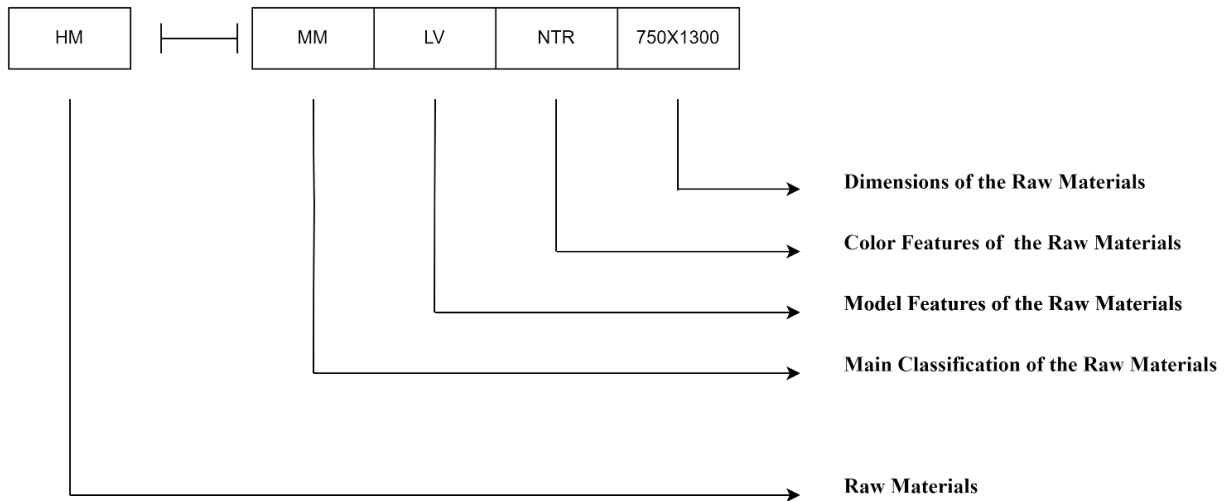


Figure 2. Examples of Raw Materials Coding

Meaning of the Code: Raw material made of MDL metal in the form of a sheet with a natural color and dimensions of 750 x 1300 mm.

3.1.2. Codes Created for Semi-Finished Products

Step 1: Determining the Features of Semi-Finished Products

Typical features that are considered significant in smart coding are as follows:

- Details about the main classification of the semi-finished products (wood, packaging, etc.)
- Model details of the semi-finished products
- Color details of the semi-finished products
- Perforation details of the semi-finished products
- Edge details of the semi-finished products
- Dimensions of the semi-finished products

Step 2: Defining the Specified Classification Features by Letters and Abbreviation

Firstly, the code ‘YM’ shall be included to indicate that it is a semi-finished product.

Secondly, the details about the main category of the semi-finished products shall be included. Table 4 presents some main categories.

Table 4. *Examples of Main Classifications and Abbreviations of the Semi-Finished Products*

Main Classification of Semi-Finished Products	Abbreviation (InTurkish)
MDL METAL	MM
MDL PLASTER	MC
PAINT	BY
FABRIC	KM
MDL SFTB	MS
MDL WOOD	MA
GLUE	TT
BEARING ELEMENT	TS
MATERIAL	ML
PACKAGING	AB

In two-word abbreviations, the second ‘M’ always stands for metal, the second ‘A’ stands for wood, and the second ‘C’ always stands for plaster.

In the third layer, the model features of the semi-finished products are coded. Some abbreviations used in coding are shown in Table 5.

Table 5. *Examples of Model Features and Abbreviations of the Semi-Finished Products*

Model Features of the Semi-Finished Products	Abbreviation (InTurkish)
HOOK-ON	HKO
CLIP-IN	CLI
BAFFLE COVER	BFK
WOODEN SLAT	AHC
T-24 BEARING ELEMENT	24S
FMX BEARING ELEMENT	FMX
EDGE PROFILE	KNP
FMX-5 PANEL	FMP
LAY-ON	OTR
T-15 LAY-IN	15S
HOOK-ON CORRIDOR	HOK
LAY-ON CORRIDOR	OTK
CLIP-IN CORRIDOR	CIK

The fourth layer of the code indicates the details about the color of the product. Since they are classified in the same way as the raw materials, it is not repeated here.

The fifth layer of the code indicates the perforation details of semi-finished products. Metal raw materials are processed under factory conditions, and perforation is the most important of these processes (Güler, 2019). In the production process, perforated products are produced with various hole structures. The types of perforation vary according to the customer's demands and the area where the product will be used. Even if it is thought that there should only be holes in perforated products, designs may sometimes include embossed or embedded items upon request, as seen in Figure 3. Therefore, perforation details are of great importance for suspended ceilings.

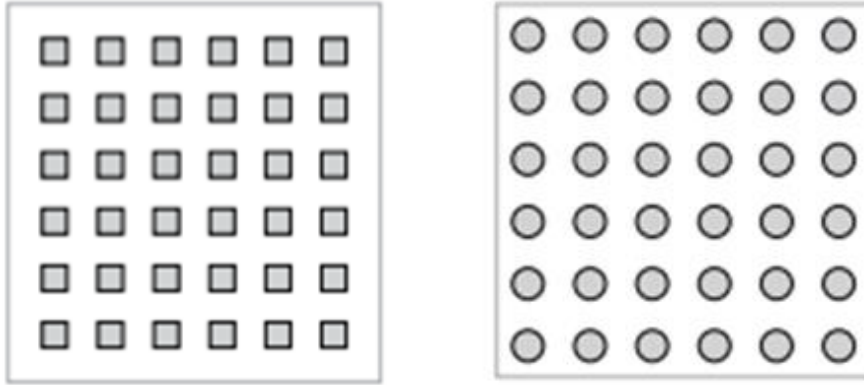


Figure 3. Example of square and circle perforation with full edges in Table 4 (Tacer, 2023)

At this stage, it was decided to take the initial letters of the most used perforation forms of the products. While the first letter stands for the shape, it was decided to write the dimensions of the perforation shape. If the first letter of the perforation shape has previously been used for another shape, the next consonant is used. Table 6 presents some semi-finished product perforation forms and abbreviation details.

Table 6. Examples of Perforation Shapes and Abbreviations of the Semi-Finished Products

Semi-Finished Product Perforation Forms	Abbreviation (InTurkish)
ALIGNED	S
IRREGULAR	G
STRAIGHT	D
ROUND	Y
SQUARE	K
DIAMOND	M
SPECIAL	Ö
OTTOMAN	O
TRIANGLE	Ü

In the seventh layer, the border properties of the products are specified. It refers to the finishes of the perforation holes, that is, how they are finished, on the edges of the ceilings where the perforation process is performed. In this field, the letter "T" shall be written if the standard border finish is to be used; otherwise, the length to be left on the edge of the product shall be written.

Finally, the dimensions of the semi-finished products used shall be added by taking into account their diameters and lengths.

Step 3: Creating the smart code by combining the features of the semi-finished products (Figure 4)

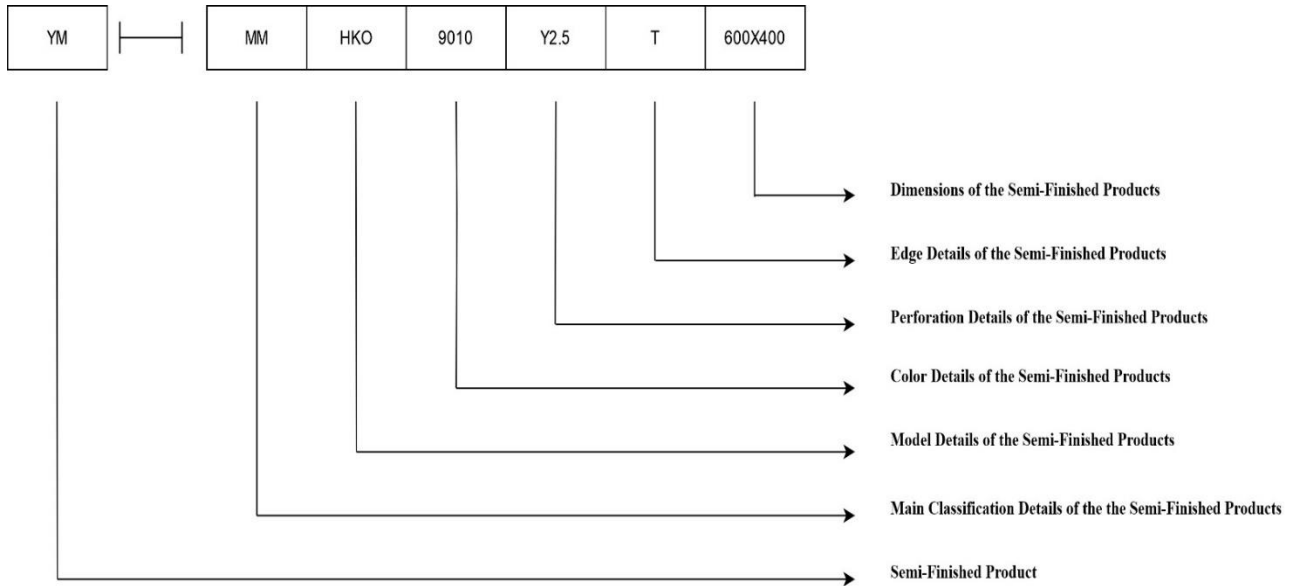


Figure 4. Examples of Semi-Finished Product Coding

Meaning of the Code: Hook-on bearing element suspended ceiling semi-finished product made from MDL Metal with full edges with dimensions of 600 x 400 and color of RAL 9010 with perforation of circles with a diameter of 2.5 mm.

3.1.3. Codes Created for Products

The company produces building products such as suspended ceilings and acoustic wooden ceilings. In this study, a smart coding algorithm was developed by examining the criteria that are considered essential to be known in the final products of the company.

Step 1: Determining the Features of Products

Typical features that are considered significant in smart coding are as follows:

- Details about the main classification of the products (wood, packaging, etc.)
- Model details of the products
- Color of products
- Perforation details of the products
- Edge details of the products
- Dimensions of the products

Step 2: Defining the Specified Classification Features by Letters and Abbreviation

Firstly, the code 'M' shall be included to indicate that it is a product.

Secondly, the details about the main category of the products shall be included. Table 7 presents some main categories.

In general, these codes are used in the main classification process. The factor to be considered here is that the abbreviations have a certain algorithm. For example, as in the coding of raw materials, the second 'C' always stands for plaster, the second 'M' stands for metal, and the second 'A' stands for wood.

In the third layer, the model features of the finished products are coded. Some abbreviations used in coding are shown in Table 8.

Table 7. Examples of Main Classifications and Abbreviations of the Products

Main Classification of the Product	Abbreviation (InTurkish)
MDL METAL	MM
ACCESSORIES	AK
MDL WOOD	MA
BEARING ELEMENT	TA
MESH	ME
WAINSCOT WOOD	LA
WOOD	AH
HONEYCOMBS	PE
MDL PLASTER	MC
FABRIC	KU

Table 8. Examples of Model Features and Abbreviations of the Products

Model Features of the Products	Abbreviation (InTurkish)
HOOK-ON	HKO
CLIP-IN	CLI
BAFFLE COVER	BFK
BOX PROFILE	KTP
WOODEN SLAT	AHÇ
T-24 BEARING ELEMENT	24T
FMX BEARING ELEMENT	FMX
T-15 LAY-IN	15S
HOOK-ON CORRIDOR	HOK
LIGHTING BOX	AYK
LAY-ON CORRIDOR	OTK
CLIP-IN CORRIDOR	CIK
RINGS	RNG
WAINSCOT	LMB
HOOK-ON PLANK	HOP
LAY-IN	SRK
HOOK-ON BEARING ELEMENT	HOT
CURVED HOOK-ON CORRIDOR	EHK

The fourth layer of the code indicates the details about the color of the product. If there is no RAL code of the product, the abbreviation of the color of the product should be specified in this field. The colors were abbreviated in accordance with the abbreviation algorithm of the raw materials. More than one color tone can be used together in the products, so the abbreviation has been continued by placing '+' between them. Below are the abbreviations of some of the mostly used product colors.

The fifth layer of the code indicates the perforation details of the products. At this stage, the same algorithm created for semi-finished products was used. While the first letter stands for the shape, it was decided to write the dimensions of the perforation shape. Some abbreviations used in coding are shown in Table 9.

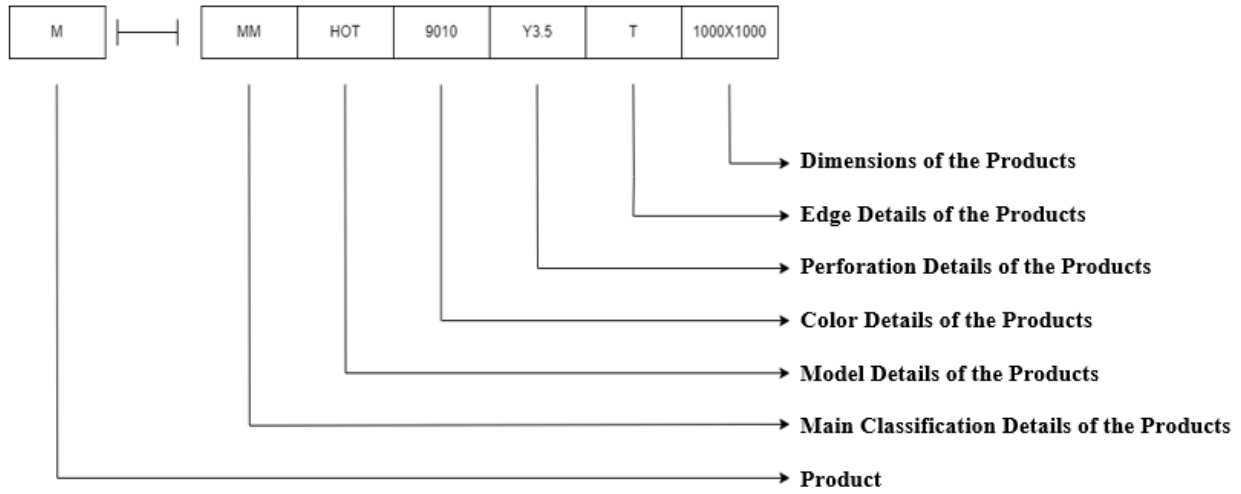
Table 9. Examples of Perforation Shapes and Abbreviations of the Products

Product Perforation Forms	Abbreviation (InTurkish)
ALIGNED	S
IRREGULAR	G
STRAIGHT	D
ROUND	Y
SQUARE	K
DIAMOND	M
SPECIAL	Ö
OTTOMAN	O
TRIANGLE	Ü

In the sixth layer, the border properties of the products are specified. The same border algorithm created for semi-finished products is used.

Finally, the dimensions of the products used shall be added by taking into account their diameters and lengths.

Step 3: Creating the smart code by combining the features of the products (Figure 5)

**Figure 5.** Examples of Products Coding

Meaning of the Code: Hook-on bearing element suspended ceiling product made from MDL Metal with full edges with dimensions of 1000 x 1000 and color of RAL 9010 with perforation of circles with a diameter of 3.5 mm.

3.2. Assigning Roles to Sales Representatives in the Company

Another improvement requested by the company is that the domestic sales representatives should not view the foreign companies and their quotes, and the overseas sales representatives should not view the domestic companies and their quotes. Due to the fact that domestic and overseas orders have radical differences in an order-based production company, the interfaces of the sales representatives have been simplified and any possible confusions have been prevented. Therefore, the ability to view records of the users defined in the CRM role definitions. A new role was created by duplicating the company and quotation role from the roles menu by using a new name. In the new role, permissions on reading and writing fields have been removed so

users can only read and write records that belong to them. Also, 'Object Permissions' is selected so that users can read the records according to the criteria, and only Read and Write permissions have been defined on the add criteria window (Figure 6). On the window that opens after closing this window, the code to be defined is written using the correct button by ticking the checkbox, thus the users are assigned the desired roles (Logo, 2023).

Figure 6. Example window for defining roles where users can see only the companies belonging to the sales representatives assigned to this role

3.3. Ensuring Instant Tracking of Inventory Available to Shipment

One of the biggest problems of the company is that there is a problem in the delivery times of the quotes created due to the fact that the sales representatives do not know the current status of the inventory. Sales representatives are able to follow up with the current inventory in Netsis after its integration with LogoCRM.

Although the actual inventory of the products by the warehouses can be seen on Netsis within LogoCRM (Figure 7), the customers request to be able to view the inventory available for shipment. The reason for this is that sales representatives cannot give a proper deadline to customers because they view the pending inventory during the order stage as included in the warehouse balances. In Netsis, a view was created where the general balance of the products at the order stage was calculated since the transactions are not conducted by leaving stock from the order.

ERP ürünü depolara göre kalanlar
600x600x9,5 mm Otur...

ERP ÜRÜN KODU:
M-5120
ERP ÜRÜN ADI:
600x600x9,5 mm Oturmalı, RAL 9016 Renk, Alçı Plaka

DEPO NO	TANIM	BAKİYE
	Tüm depolar	4.942,00
1	AKYURT FABRİKA	0,00
2	KIRIKKALE FABRİKA	4.942,00
3	İZMİR DEPO	0,00
4	HAVAALANI	0,00
6	NERGİZ	0,00
7	ZİRAAT	0,00
10	HAMMADDE	0,00
11	ALET EDEVAT	0,00
12	KIRIKKALE ALETEDEVAT	0,00
20	KALİTE KONTROL	0,00
21	RED DEPO	0,00
22	HURDA DEPOSU	0,00
23	ŞARTLI KABUL DEPO	0,00

Figure 7. View of actual inventory according to Netsis warehouses in LogoCRM

REATE VIEW [dbo].[_YDS_SIPAYRI] AS

SELECT STOK_KODU,

KUMTOP

FROM**(SELECT STOK_KODU,**

kumtop

FROM (**(SELECT STHAR_HTUR,**

STHAR_FTIRSIP,

STOK_KODU,

Company_DOVTUT,

(SELECT sum(x.sthar_gcmik-FIRMA_DOVTUT)**FROM TBLSSIPATRA AS x****WHERE x.STOK_KODU=s.stok_kodu) AS kumtop,**

STHAR_GCMIK

FROM TBLSSIPATRA AS s**WHERE STHAR_HTUR='h'****AND STHAR_FTIRSIP='6'****GROUP BY STHAR_HTUR,**

STHAR_FTIRSIP,

STOK_KODU,

FIRMA_DOVTUT,

STHAR_GCMIK-FIRMA_DOVTUT,

STHAR_GCMIK)) AS x) AS KML

GROUP BY STOK_KODU,

kumtop

In YDS_SIPAYRI view, the inventory that has not been converted into waybills is calculated cumulatively from the TBLSSIPATRA table where the order items are kept.

CREATE VIEW [dbo].[_YDS_SEVKEDILEBILIR] AS**SELECT PH.STOK_KODU,**

PH.DEPO_KODU,

PH.TOP_GIRIS_MIK,

PH.TOP_CIKIS_MIK,

YDS.KUMTOP,

(CASE

WHEN YDS.KUMTOP IS NULL THEN PH.TOP_GIRIS_MIK-PH.TOP_CIKIS_MIK

ELSE PH.TOP_GIRIS_MIK-PH.TOP_CIKIS_MIK-YDS.KUMTOP

END) AS SIPAYRIBAK

FROM TBLSTOKPH PH

LEFT JOIN _YDS_SIPAYRI YDS ON PH.STOK_KODU=YDS.STOK_KODU

WHERE ph.depo_kodu='0'

In the `_YDS_SEVKEDILEBILIR` view, the inventory available for shipment is found by subtracting the remaining order balances from the `TBLSTOKPH` table where the total quantities of the inventory are kept. The reason for selecting `depo_kodu='0'` as a constraint in this field is that the total balance is kept in an imaginary warehouse number '0' to cover all warehouses, as well as the total balances are kept separately for each warehouse. The quantity of the inventory available for shipment for each warehouse is not important at this stage.

In the next stage, the inventory balances available for shipment in the `_SEVKEDİLİRLİSTOK` view should be visible to the sales representatives for each product while adding the products to the quote on the LogoCRM interface. At this stage, a new balance field can be defined on the quoted products window, or a field that is considered unused may be selected among the existing ones and edited for this operation. In the study, an extra field from the extra fields in the inventory cards was defined (Figure 8).

The screenshot shows the configuration page for an extra field in LogoCRM. The field is named 'SEVK EDİLEBİLİR MİKTAR' and is associated with the 'SVKSTOK' column. The configuration includes the following details:

- BAŞLIK:** SEVK EDİLEBİLİR MİKTAR
- AD:** SVKSTOK
- LAYOUT SIRASI:** 6
- Görünüm Seçenekleri:**
 - Giriş ekranında ön değer olarak görünür
 - Lookup liste ekranında ön değer olarak görünür
 - Listede ön değer olarak görünür
 - Giriş anında gönder
- GÖRÜNÜM FORMATI:** 1
- MOBİL SIRASI:** 0
- Mobilde Göster
- Mobilde Özet Göster

The 'Aktif' checkbox is checked, and the 'Double' option is selected under 'VERİ TÜRÜ'. The 'LOOKUP GÖRÜNEN ALAN' is set to 'SVKSTOK'.

Figure 8. Defining an extra field for the inventory available for shipment in LogoCRM

The defined area is kept in the 'SVKSTOK' column in the 'MT_Product' table in the LogoCRM database, therefore, the fields are matched by writing the update sentence below. The 'COLLATE' command was used due to language incompatibility between the Netsis database and the LogoCRM database.

UPDATE LOGOCRML.. MT_Product

SET logocrm..MT_Product.SVKSTOK=_YDS_SEVKEDILEBILIR.SIPAYRIBAK

FROM_YDS_SIPAYRIBAK

INNER JOIN LOGOCR.M.. MT_Product **ON** _yds_sipayribak.STOK_KODU= Logocrm.. MT_Product.ProductCode

After completing the definitions, the reliability of the field was tested on a randomly selected stock.

As can be seen Figure 9, although the actual inventory of the product in LogoCRM system is zero, the inventory available for shipment seemed to be '-8'.

ORÜN KODU	TANIM	ORÜN TÜRÜ	ERP FİİLİ STOK	SEVK EDİLEBİLİR MİKTAR	BÖLÜM	AÇIKLAMA
M-9376	240X70mm, AL, 0.6mm, Troyaline (TM) Ticari mal		0,00	-8,00	PAKETLEME	Yatay Baffle için

Figure 9. Viewing the inventory available for shipment for a randomly selected stock using LogoCRM

As can be seen Figure 10, the transaction report of the product generated by the Netsis system shows that the balance of the product is '0'.

A	B	C	D	E	F	G	H	I	J	K	L
1	Stok Kodu	M-9376	Ölçü Birimi	AD							
2	Stok Adı	240X70 mm, AL, 0.6mm, Troyaline Kapak, Ahşap Görünümlü TEAK (TCR-AD-10 003) (Yatay Baffle)									
3	Tarih	Fiş No	Tip	Fiyat	Giren Miktar	Giren Tutar	Çıkan Miktar	Çıkan Tutar	Kalan Miktar	Kalan Tutar	Açıklama
4					0,000	0,00	0,000	0,00	0,000	0,00	
5											
6											
7											

Figure 10. Transaction breakdown report of selected stock in Netsis

As can be seen Figure 11, in the detailed order report of the products generated by Netsis, there are 8 orders waiting for the shipment of the same stock. This confirms the reliability of our system.

A	B	C	D	E	F
1	Stok Kodu	Stok Adı	Cari Kodu	Cari İsim	Sipariş Miktarı
2	M-9376	240X70 mm, AL, 0.6mm, Troyaline Kapak, Ahşap Görünümlü TEAK (TCR-AD-10 003) (Yatay Baffle)	120-10-03642	BAREKS POLİETİLEN FİLM EKSTRUZİYON SAN.TİC.A.Ş.	8,000
3	Bakiye Miktarı		0,000	Toplam	8,000
4					0,000
5					
6					

Figure 11. Detailed order report of the selected stock in Netsis

The controls revealed that the process worked accurately; however, since the process consists of constantly changing data, a trigger has been added so that the 'MT_Product' table can be revised in accordance with the update written above after creating each order.

3.4. User-Friendly Interface Customizations

Another problem of the company was that the sales representatives could not view the technical specifications of the products conveniently while entering the product quotes. This problem has been solved by preparing a user-friendly and customized interface. The interface designs to be created are simple, they should be easy and understandable. (Yazar & Akpınar, 2022) Therefore, the fields in the LogoCRM interface have been arranged to make them user-friendly according to the demands of the sales representatives. Then, useless fields have been cleaned from the interface.

In Tacer company, the products are sold in two units: 'piece' and 'meter'. Therefore, in order to reduce the probability of sales representatives' making errors, the company requested to customize the interface according to the unit of the selected product. After opening the products on the ERP system and entering their unit of measure, they are integrated directly into the CRM system. Therefore, the units of the products sold can be confused by the sales representatives in some cases. In this section, the products from ERP were customized accordingly based on their units of measure on the interface in order to minimize the error. Tables containing the units of measure of the product cards were found in the database, and a trigger was written according to the data received from this table. In the product card, the value of the field 'Product Category-01' was arranged to write 'M2', i.e. square meters, for products with a unit of measure of area, and 'piece' for products with a unit of measure of number (Figure 12).

The figure displays two side-by-side screenshots of the LogoCRM product card interface. Both cards show the 'Temel bilgi' (Basic information) section with fields for ÜRÜN KODU (Product Code), TANIM (Description), BİRİM SETİ (Unit Set), ÜRÜN TÜRÜ (Product Type), GRUP (Group), and KULLANIMDA (In Use). The left card shows 'h-010904' as the product code and 'Adet' (piece) as the unit set. The right card shows 'ARM BP313051A PRELUDE CROSS TEE 1200mm' as the product code and 'Öndeğer birim seti' (Default unit set) as the unit set. Below the 'Temel bilgi' section, the 'Kategoriler' (Categories) section is visible, showing 'ÜRÜN KATEGORİSİ-01' (Product Category-01) with the value 'Adet' on the left and 'M2' on the right. Red boxes highlight the 'Kategoriler' section in both screenshots.

Figure 12. Displaying the different units as 'm²' and 'piece' on product cards on LogoCRM interfaces.

With this algorithm, the selected quote is displayed in units of measure customized. For these customizations, the necessary rules were created by defining criteria in the BO Model field and entering the AppearanceRules from the MT_Proposal_Product field through the ModelEditor (Figure 13).

With these customizations, the users were enabled to view the quoted products in their specific units of measure.

As can be seen Figure 14, the user enters the length and quantity details in order to m^2 calculate the measure of products whose units are selected as meters. The 'Length X Pieces' field is passive for users, and its value is automatically assigned by calculating the values of the length and quantity fields.

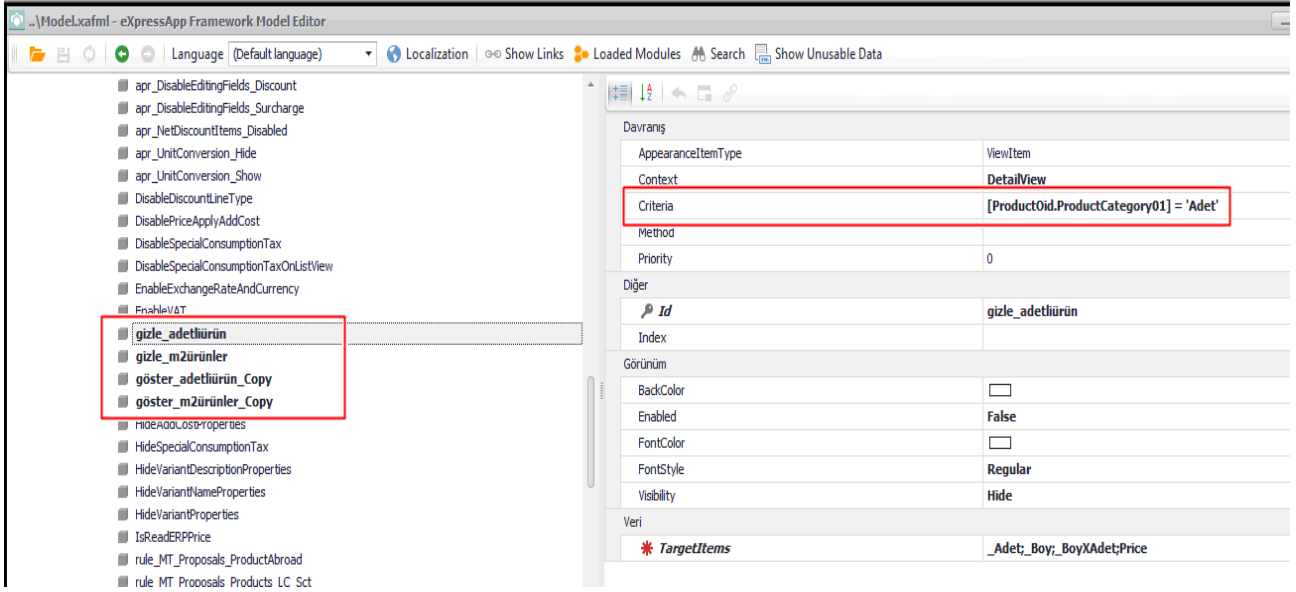


Figure 13. Examples of customizations made on the model editor interface

Figure 14. Displaying the selected quoted products in units of meters

As can be seen Figure 15, the products with a unit of measure of 'piece' only have the quantity field. As a result of these customizations, a user-friendly interface was created.

Figure 15. Displaying the selected quoted products in units of piece

4. CONCLUSION AND ASSESSMENT

The purpose of all enterprises is to maximize their profits and increase their production. Therefore, enterprises are in unending competition with each other. Today, enterprises that cannot adapt to technological transformation cannot survive in this competitive environment. Therefore, the Customer Relationship Management (CRM) system has to be used so that company managers can control customers and prospects to make it easier to manage transaction processes, product management, flagship projects and promotions for customers (Rahayu et al., 2022)

This study is conducted in Tacer company, which produces suspended ceilings in Ankara. Some problems in the company's ERP and CRM systems, which are used as a bridge between production and sales & marketing departments, have been eliminated after making assessments in line with the requirements of the company.

One of the biggest problems in the company is that sales representatives do not have a good command of the product cards because they are not involved in the production stages. Therefore, smart coding has been implemented for the products. A modeling study was carried out based on the most important features of the products required for the sales department. The LogoCRM interface is customized for sales representatives in a simple and uncomplicated way. In this way, human errors that may occur in the orders to be sent to production have been minimized. Moreover, users were allowed to get rid of unnecessary details by restricting their access to data under the control of the management.

The sales representatives were allowed to access the warehouse data in terms of inventory available for shipment and actual inventories. Thus, they were enabled to inform the customers correctly with realistic deadlines.

The study aimed to establish healthier relationships with the customers by making improvements in the processes between the departments of the company. As it is known, companies can increase their productivity only by applying CRM strategies, working continuously with their customers and having a high level of trust (Richards & Jones, 2008). The company aimed to increase customer satisfaction and get superiority in the competitive environment by establishing strong relationships with customers. After solving communication problems between the production and sales & marketing departments, the company has been recommended to purchase and use the Logo Flow workflow management software to follow the company's workflow processes in detail and to facilitate coordination not only between these two departments but also between all departments.

In the studies carried out to eliminate the communication problems between the sales & marketing and production departments in the enterprise, the dependence of these two departments on the purchasing department has been sufficiently understood. Therefore, suggestions have been made regarding the necessity of making improvements in the ERP and CRM systems by re-evaluating the connections between purchasing, production, and sales departments in the enterprise.

CONFLICT OF INTEREST

The authors declare no conflict of interest.

REFERENCES

- Aydin, A., & Dursun, C. (2022). Pazarlama ve Üretim Planlaması İlişkisi (Mobilya İmalatçısı Kobi'lere Yönelik Bir Araştırma) [Relationship of Marketing and Production Planning: A Research for Furniture Manufacturer SMEs]. *Karadeniz Araştırmaları Enstitüsü Dergisi*, 8(14), 9-23. doi:[10.31765/karen.1032462](https://doi.org/10.31765/karen.1032462)
- Bagdat, A., & Can, A. V. (2023). Esnek Üretim Sisteminde Grup Teknolojisi Kullanılarak Faaliyet Tabanlı Maliyetleme Yöntemi ile Birim Maliyetlerin Hesaplanması [Calculation of Unit Costs by Activity-based Costing Method Using Group Technology in a Flexible Production System]. *Muhasebe ve Denetim Bakış*, 22(68), 201-226. doi:[10.55322/mdbakis.1102412](https://doi.org/10.55322/mdbakis.1102412)
- Başkak, M., & Tanyaş, M. (2006). *Üretim Planlama ve Kontrol*. İrfan Yayıncılık, İstanbul.

- Çelebi, N. (2013) *Tekstilde Renk Kombinasyonları [Color Combinations in Textile]*. MSc Thesis, Marmara University.
- Demirkapı, E. (2013). Ticari İşletmenin Tespiti Açısından Esnaf İşletmesi Kavramının Değerlendirilmesi [Evaluating the Concept of Enterprise of Tradesman to Determine Commercial Enterprise]. *Gazi Üniversitesi Hukuk Fakültesi Dergisi*, 17(2), 371-442.
- Demirel, M. Y., & Karaagaç, I. (2014). Bilgisayar Destekli Üretim Süreçlerine Genel Bir Bakış [An Overview of Computer Aided Manufacturing Process]. *Mühendis ve Makina*, 55(652), 51-61.
- Dilek, N. (1993). *Çok Ürünli İşletmelerde Üretim-Pazarlama Sistemlerinin Entegrasyonu [Integration of Production-Marketing Systems in Multi-Product Enterprises]*. MSc Thesis, Yıldız Technical University.
- Doğan, I. B., & Başgelen N. (2008). *Arkeolojik ve Etnografik Kanıtlar Işığında Tarih Öncesinde Ticaret ve Değiş Tokuş [Trade and Exchange Before History in the Light of Archaeological and Ethnographic Evidence]*. Arkeoloji ve Sanat Yayınları.
- Güçlü, B., & Hacıoğlu, G. (2022). Pazarlama ve Lojistik Departmanları Arasında Paylaşılan Bilgi Kalitesinin İş Birliği ve Çatışma Üzerindeki Etkisi [The Affect of Quality of Information Shared Among Logistics and Marketing Departments on Cooperation And Conflict]. *Girişimcilik ve Kalkınma Dergisi*, 17(2), 1-12.
- Güler, M. B. (2019). *Asma Tavan Sistemlerinin İşlevsellik Açısından İncelenmesi [Investigation of Suspended Ceiling Systems in Terms of Functionality]*. MSc Thesis, İstanbul Kültür University.
- Kaya, T. (2023). Nevşehir Hacı Bektaş Veli University “Marketing Definitions and Changing Marketing”, Lecture Notes.
- Kecek, G., & Yıldırım, E. (2009). Kurumsal Kaynak Planlaması (ERP) ve İşletme Açısından Önemi [Enterprise Resource Planning (ERP) and the Importance for Company]. *Elektronik Sosyal Bilimler Dergisi*, 8(29), 240-258.
- Kobu, B. (2003). *Üretim Yönetimi*. Avcıol Basım Yayın, İstanbul.
- Kurgan, N. (2023). 19 Mayıs University “Production Management and Organization”, Lecture Notes.
- Liu, K., Bi, Y., & Liu, D. (2020). Internet of Things based acquisition system of industrial intelligent bar code for smart city applications. *Computer Communications*, 150, 325-333. doi:[10.1016/j.comcom.2019.11.044](https://doi.org/10.1016/j.comcom.2019.11.044)
- Laverty, J. P. (2022, 2-5 November). A New ERP Curriculum to Integrate Computer Technologies, Accounting and Data Analytics. In: Proceedings of the EDSIG Conference 2022 (v8 n5793).
- Logo (2023). Logo Products Knowledge Repository. (Accessed:02/02/2023) [URL](#)
- Morgan, R. M., & Hunt, S. D. (1994) The Commitment-Trust Theory of Relationship Marketing. *Journal of Marketing*, 58(3), 20-38. doi:[10.1177/002224299405800302](https://doi.org/10.1177/002224299405800302)
- Oxford Learner's Dictionary (2023). “Business” Word Meaning in English. (Accessed:10/02/2023) [URL](#)
- Rahayu, S., Cakranegara, P. A., Simanjorang, T. M., Syobah, S. N., & Arifin. (2022). Implementation of Customer Relationship Management System to Maintain Service Quality for Customer. *Enrichment: Journal of Management*, 12(5), 3856-3866.
- Richards, K. A., & Jones, E. (2008). Customer relationship management: Finding value drivers. *Industrial Marketing Management*, 37(2), 120-130. doi:[10.1016/j.indmarman.2006.08.005](https://doi.org/10.1016/j.indmarman.2006.08.005)
- Rinaldy, R. A., & Juarna, A. (2022). Implementation of Enterprise Resource Planning (ERP) and Customer Relationship Management (CRM) Systems to Support Business Operations in PT. Wira Pratama. *International Research Journal of Advanced Engineering and Science*, 7(1), 208-211.
- Saadet, N. C. (2012). *Üretim Sistemlerinde Otomasyon [Automation in Production Systems]*. MSc Thesis, İstanbul Technical University.
- Sağlam, S. (2008). *ERP Sistemleri ve Üretim Planlama Kontrol Faaliyetleri İlişkisi [Relationship Between ERP Systems and Production Planning Control Activities]*. MSc Thesis, Yıldız Technical University.

Savasci, İ., & Ventura, K. F. (2001, 28 June-1 July). *İlişkisel Pazarlamanın Üniversite Öğrencilerinin Hizmet Algulamaları Üzerindeki Etkisi*. In: Proceedings of the 6th National Marketing Congress (pp 39-52), Erzurum.

Sevim, A., & Bulbul, S. (2016). Kurumsal Kaynak Planlaması (Enterprise Resources Planning-ERP) Sistemlerinin Muhasebe Bilgi Sisteminin Verimliliğine Etkileri [Efficiency Effects of Accounting Information Systems on Enterprise Resources Planning (ERP)]. *ASSAM Uluslararası Hakemli Dergi*, 3(6), 54-70.

Sezen, B., Yılmaz, C., & Gezgin, G. (2002). Lojistik İşlevinin Pazarlama ve Üretim Birimleri Arasındaki Bağlayıcı Rolü ve İşletme Performansı Üzerindeki Etkileri [Binding Role of the Logistics Function between Marketing and Production Units and Its Effects on Business Performance]. *Dokuz Eylül Üniversitesi İktisadi İdari Bilimler Fakültesi Dergisi*, 17(2), 133-146.

Tacer (2023). Tacer Company Official Website. (Accessed:02/02/2023) [URL](#)

Yazar, T., & Akpınar, Y. (2022). Mobil Uygulamalarda İnteraktif Sayısal Arayüz Tasarımı ve Bir Etkileşimli Sayısal Arayüz Aplikasyon Örneği [Interactive Digital Interface Design in Mobile Applications and an Interactive Digital Interface Application Example]. *Uluslararası Disiplinlerarası ve Kültürlerarası Sanat*, 7(15), 101-125.

JOURNAL OF SCIENCE

PART A: ENGINEERING AND INNOVATION



| Correspondence Address |

Gazi University
Graduate School of Natural and Applied Sciences
Emniyet Neighborhood, Bandırma Avenue
No:6/20B, 06560, Yenimahalle - ANKARA
B Block, Auxiliary Building

| e-mail |

gujsa06@gmail.com

| web page |

<https://dergipark.org.tr/tr/pub/gujsa>

e-ISSN 2147-9542